Dimensional metrology at the nanoscale: quantitative characterization of nanoparticles by means of metrological atomic force microscopy

Original
Dimensional metrology at the nanoscale: quantitative characterization of nanoparticles by means of metrological atomic force microscopy / Ribotta, Luigi. - (2022).

Doctoral Dissertation
Doctoral Program in Metrology (34th Cycle)

Dimensional metrology at the nanoscale: quantitative characterization of nanoparticles by means of metrological atomic force microscopy

By

Luigi Ribotta

******

Supervisor(s):
Dr. Massimo Zucco, Supervisor
Dr. Gian Bartolo Picotto, Supervisor

Doctoral Examination Committee:
Dr. Fabrizio Sordello, Referee, Università degli Studi di Torino
Dr. Gaoliang Dai, Referee, Physikalisch-Technische Bundesanstalt
Dr. Marco Pisani, Istituto Nazionale di Ricerca Metrologica
Prof. Gianfranco Genta, Politecnico di Torino
Prof. Renato Gonnelli, Politecnico di Torino

Politecnico di Torino
20th July 2022

Declaration

I hereby declare that the contents and organization of this dissertation constitute my own original work and does not compromise in any way the rights of third parties, including those relating to the security of personal data.

Luigi Ribotta

Turin, 20th July 2022

* This dissertation is presented in partial fulfillment of the requirements for **Ph.D. degree** in the Graduate School of Politecnico di Torino (ScuDo).

Acknowledgments

The research activity discussed in this dissertation was carried out within the framework of the EMPIR 15SIB09 project “Traceable three-dimensional nanometrology - 3DNano”. The EMPIR programme co-financed by the Participating States and from the European Union’s Horizon 2020 research and innovation programme.

I wish to thank several people who have collaborated with me and enriched my activities during these years.

At first, I wish to thank Gian Bartolo Picotto, who has been my mentor since my arrival at INRiM. From him I have learned the rigour for the work and the passion for metrology, and working with him has allowed me to grow professionally.

Afterwards, I would like to acknowledge Massimo Zucco, Sandro Balsamo and Marco Pisani, who helped and advised me in my work after the retirement of Gian Bartolo.

Then, a special thanks to Roberto Bellotti, who helped me several times with the lab work and for his unparalleled teachings.

Subsequently, a heartfelt thought goes out to all colleagues of the INRiM building 7 (Laura, Carla, Aline, Milena, Elisabetta, Marco B., Lele, Leonardo, Mattia, Andrea E., Andrea G., Andrea L., Marco P., Mauro, Stefano, Davide) for both the working times and the convivial occasions. Thanks also to all the other colleagues and PhD students I have met over the years.

After, I acknowledge Professor Valter Maurino of the Department of Chemistry of the University of Torino both for the teaching I received during my university studies and for the collaboration in this work (a big thank also to Francesco Pellegrino).

Next, I want to acknowledge Marta Vallino from Istituto per la Protezione Sostenibile delle Piante – Consiglio Nazionale delle Ricerche (IPSP–CNR) for her availability and the interesting discussions.

Finally, I wish to thank my loved ones who have been close to me during these years, who gave me strength in difficult times due to health issues.

Abstract

3D nanometrology supports nanoscience and nanotechnology through new standards and traceable methodologies of measurement and data treatment. The development of candidate reference nanomaterials for dimensional nanometrology will reduce uncertainties and improve traceability at the nanoscale. For this purpose, in my PhD project inorganic nanoparticles (NPs) and bio-plant viruses are studied using the INRiM metrological atomic force microscope (mAFM).

AFM topographies result from the dilation of the probe shape, the sample shape and the tip-sample-substrate interactions. Among other errors, accurate measurements of patterned surfaces and NPs are affected by errors due to probe shape and size. In order to reduce the uncertainty of measurements, the Tobacco Mosaic Virus (TMV) is studied as a tip characterizer.

Tip shape characterization is necessary for many applications, including dimensional, electrical, and magnetic measurements. TMV is chosen for characterizing commercial AFM tips because of (i) its simple geometry, (ii) its stable diameter, and (iii) its availability worldwide in nature.

The TMV is a cylindrical nanostructure with a circle-base diameter of about 18 nm as quoted in the literature by X-ray diffraction measurements, which represents a reference at the nanoscale. The diameter of the TMV is obtained from AFM images as the top height of the cross-section profile of isolated nanostructures. Since the mean diameter by mAFM is (16.5 ± 0.2) nm (smaller than the X-ray-based reference value), the tip-sample-substrate interactions are studied to correct the mAFM measurement and greatly reduce the deviation of the TMV top-height diameter by the mAFM and its reference value.

By assuming the TMV cross-section is undeformed, the tip shape is obtained from lateral measurements taking into account the enlargement, achieving a good repeatability for subsequent images.

Nowadays, quasi-spherical NPs are measured accurately by mAFM, through the determination of the mean diameter as the top-height of the cross-section profile. However, in most real-world, industrial nanomaterials have shapes that are much more complex than the spherical one. Non-spherical NPs represent a challenge regarding AFM measurements, because their particular geometries emphasize the limitations associated with finite tip size and shape.

Traceable measurement of non-spherical shapes and dimensions requires the development of new measurement methods. Through new geometrical approaches which consider the nominal crystal structure and the conditions in which the TiO_2 particles have been synthesized, the critical sizes of bipyramids (~ 60 nm length × ~ 40 nm width) and nanosheets (~ 10 nm thickness × ~ 75 nm lateral) are robustly and accurately reconstructed by the mAFM images and data treatment. In this study, critical sizes like bipyramids breatdth and length, thickness and roughness of platelets, are quantitatively determined providing an uncertainty budget for each measurand. It is worth noting that the critical sizes of these NPs have resulted stable with low dispersion of values and with a monomodal distribution. It follows that they are suitable as potential candidate reference materials in dimensional nanometrology.

Pre-normative works on measurements of 3D nanostructures by AFM require a clear and unambiguous description of the sample to be measured with a consistent and easily understood terminology. The 'quality characteristics' that should be first regulated are intrinsic properties, *e.g.* critical sizes and shapes and descriptors. For this reason, non-spherical NPs characterisation included the quantification of morphological descriptors, that qualify the synthetized batches. In particular, bipyramids are described by shape descriptors, *e.g.* the elongation of about 1.4 indicates a perfect truncated shape, while nanosheets are described by roughness and texture parameters in order to qualify the anatase crystals synthetized.

Summary

List of Symbols and Acronyms

Symbols

%	percentage
©	Copyright
™	trademark
€	euro
°	degrees of angles
°C	Celsius degrees
~	about
$\oplus$	mathematical operator of dilation
$\ominus$	mathematical operator of erosion
α	coefficient of thermal expansion
$\alpha_{tip-sam}$	tip-sample elastic deformation
$\alpha_{sam-sub\,Ch}$	sample-substrate adhesive deformation by Chaudhury *et al.* approach (cylinder on a plane)
$\alpha_{sam-sub\,DMT}$	sample-substrate plastic deformation by DMT model (sphere on a plane)
$\alpha_{sam-sub\,JKR}$	sample-substrate plastic deformation by JKR model (sphere on a plane)
$\alpha_{sam-sub\,MP}$	sample-substrate plastic deformation by MP model (sphere on a plane)
$\alpha_{tip-sub}$	tip-substrate elastic deformation
δ	zero statistical mean errors (error due to random effects)
δX_{hom}	error term due to the homogeinity of the material
δX_{lts}	error term due to the long-tem stability of the material
δ_{dil}	tip dilation
δ_{lay}	correction for bipyramid laying

δ_{lev}	levelling
δ_{int}	tip-sample-substrate interactions
δ_{pl}	reference plane
δ_{str}	mechanical drifts
ϑ	interfacial angle of anatase TiO_2 crystals
2ϑ	SAXS scattering angle
$\lambda/2$	half-wave plate
$\lambda/4$	quarter-wave plate
λ	optical wavelenght
ρ_{lever}	cantilever density
ν	cantilever resonant frequancy
ν	optical frequency
ν	Poisson's ratio
ν_i	degrees of freedom
γ	supplementary angle of the titania interfacial angle ϑ
γ_L	surface energy of the liquid phase
γ_S	surface energy of the solid phase
γ_{SL}	interfacial surface tension
γ_1	surface tension of liquid 1
γ_2	surface tension of liquid
γ_{12}	interfacial tension at the interface between liquids
γ_S	surface energy of the particle
γ_S	surface energy of the substrate
χ^2	thermal noise
$\Delta\nu_{\mathrm{Cs}}$	Caesium frequency
a	major semiaxis of the ellipse in TMV analysis
a_{Chaud}	radius of the circle of contact in Chaudhury theory

a_{DMT}	radius of the circle of contact in DMT theory
a_{Hertz}	radius of the circle of contact in Hertz theory
a_{JKR}	radius of the circle of contact in JKR theory
a_{MP}	radius of the circle of contact in MP theory
A	area
A	oscillation amplitude
A_0	free oscillation amplitude
AR	aspect ratio
B	Builkiness
BW	cantilever bandwidht
b	breadth of the bipyramid
c	length of the bipyramid
c	speed of light in vacuum
c_i	sensitivity coefficient
cmp	Compactness
C_z	factor considering the uncertainty due to instrument calibration, profile noise, resolution of D/A converter
d	diameter of spherical nanoparticle
d	diameter of TMV
dil	tip dilation
e	tip enlargement
e	elliptical chord of the circle in TMV analysis
E	Young's modulus
El	Elongation
el	enlargement segments
E_n	degree of equivalence
E_{red}	reduced Young's modulus
F	Force
f	segment dependent on ϑ on nanosheet analysis

h	nanosheet height
I_s	image of the sample characterizer
k	coverage factor
k	cantilever constant or spring constant
k_B	Boltzmann constant
K	equivalent elastic modulus
l	nanosheet lateral side
l_{top}	constant segment of the nanosheet
L	length of a rectangular cantilever
L	sampling length or cut-off value
L_{20}	length at the temperature for dimensional metrology (20°C)
L_t	length measured at the temperature t
$L[f(x)]$	Legendre transform of a function $f(x)$
n	minor semiaxis of the ellipse in TMV analysis
nm	Nanometer
P	tip shape
P_r	reconstructed tip shape
P	applied force
P	intersection of two linear regression lines fitting the top and the left/right sidewall of a nanosheet
Q	tip quality factor
r	tip-sample distance in Lennard-Jones potential
r_{tip}	nominal tip radius
r_{TMV}	TMV radius
$R*$	equivalent radius
Ra	average roughness of a profile
Rku	kurtosis of a profile
Rq	root mean square roughness
Rsk	skewness of a profile

Rz	maximum height of the roughness profile
Rnd	Roundness
s	semi-chord of the circle in TMV analysis
S	surface tropography
S_r	reconstructed surface
Sa	average texture of a surface
Sdr	surfaces area ratio
Sku	kurtosis of a surface
Sq	root mean square height within the surface
Ssk	skewness of a surface
Sz	maximum height of a surface
t	difference between the height of the top ellipse and the height of the chord in TMV analysis
U	tip-sample interaction Lannard-Jones potential
U	expanded uncertainty
$u(x_i)$	standard uncertainty of the quantity x_i
$u_i(y)$	uncertainty contribution to the estimated quantity y
$u_c(y)$	combined standard uncertainty
u_{CRM}	uncertainty of candidate reference materials
u_{hom}	uncertainty due to homogeneity
u_{lts}	uncertainty due to long term stability
x_i	estimated quantity of the term X_i
X_i	uncertainty term that influences the quantity Y
X_{CRM}	property value of a CRM
X_{char}	property value experimentally measured of a CRM
X_{mean}	repeatability of the generic quantity X
Y	yield point
Y	measurand
y	estimated quantity of the measurand Y

w	cantilever widht
w_a	work of adhesion
z	sample-substrate interaction radius

Acronyms

1D	Mono-dimensional
2D	Bi-dimensional
2.5D	Two-and-a-half dimensional
3D	Three-dimensional
3DNano	“Traceable three-dimensional nanometrology” EMPIR project
AE	Auger Electrons
AFM	Atomic Force Microscopy
APTES	(3-Aminopropyl)triethoxysilane
ASTM	American Society for Testing and Materials
A*STAR	Agency for Science, Technology and Research
BAM	Bundesanstalt für Materialforschung und -prüfung
BIPM	International Bureau of Weights and Measures
BR	Blind Reconstruction (algorithms)
BS	Beam Splitter
BSE	Backscattered Electrons
BSP	Polarizing Beam-Splitter
c-AFM	calibrated AFM by NIST
C-AFM	Conductive Atomic Force Microscopy
CD	Critical Dimension
CEN	European Committee for Standardisation
CL	cathodoluminescence
CLS	Centrifugal Liquid Sedimentation
CMC	Calibration Measurement Capability
CMI	Czech Metrology Institute

CMS/ITRI	Center for Measurement Standards/Industrial Technology Research Institute
CNT	Carbon NanoTubes
COMAR	Code d'Indexation des Matériaux de Référence
CRM	Certified Reference Material
CS	Critical Size
CTE	Coefficient of Thermal Expansion
DFM	Danish National Metrology Institute
DLS	Dynamic Light Scattering
DOI	Digital Object Identifier
DMA	Differential Mobility Analyzer
DMT	Derjaguin, Muller, Toporov
e.g.	*exempli gratia*, for example
EDTA	Ethylenediaminetetraacetic acid
EDX	Energy Dispersive X-ray
EFM	Electrostatic Force Microscopy
EM	Electron Microscopy
EMN	European Metrology Network
EMPIR	European Metrology Programme for Innovation and Research
FMM	Force Modulation Microscopy
FMT	Institute of Manufacturing Metrology, Germany
GCI	Global Calibration Initiative
GPS	Geometrical Product Specification
HOPG	Highly Oriented Pyrolytic Graphite
He-Ne	Helium-Neon
HS	High Speed
i.e.	*id est*, that is
IEC	International Electrotechnical Commission
IES	Incoherent Elastic Scattering
ILC	Interlaboratory Comparison

INRiM	Istituto Nazionale di Ricerca Metrologica
IOP	Institue of Physics
IS	Inelastic Scattering
ISO	International Organization for Standardization
IRMM	Institute for Reference Materials and Measurements
JKR	Johnson, Kendall, Roberts
KCDB	BIPM key comparison database
KIS	Key Industrial Sector
KPFM	Kelvin Probe Force Microscopy
KRISS	Korea Research Institute of Standards and Science
LGC	Laboratory for the Government Chemist
LMS	Least mean squares
LNE	Laboratoire National de métrologie et d'Essais
LR	Large Range
MATLAB	"MATrix LABoratory" programming language and numeric computing environment
M^3	molecular measuring machine by NIST
mAFM	metrological Atomic Force Microscope
mSTM	metrological Scanning Tunnelling Microscopy
METAS	Federal Institute of Metrology
MeP	Mise en Pratique
MFM	Magnetic Force Microscopy
MP	Maugis, Pollock
MRA	Mutual Recognition Arrangement
NIM	National Institute of Metrology of China
NIST	National Institute of Standards and Technology
NMI	National Metrology Institute
NMIA	National Metrology Institute of Australia
NMIJ	National Metrology Institute of Japan
NMM	nanomeasuring machine

nPsize	“Improved traceability chain of nanoparticle size measurements” EMPIR project
NP	Nanoparticle
NPL	National Physical Laboratory
NRC	National Research Council Canada
NTRM	Traceable Reference Material
PDF	Probability Distribution Function
PhD	*Philosophiae Doctor*, Doctor of Philosophy
PID	Proportional-Integral-Derivative controller
PFM	Piezoresponse Force Microscopy
PTB	Physikalisch-Technische Bundesanstalt
QC	Quality Control
RAM	Random-access memory
RCF	relative centrifugal force
RH	relative humidity
RM	Reference Material
rms	root mean square
rpm	round per minute
Si	silicon
Si_3N_4	silicon nitride
SI	International System of Units
SAXS	Small-angle X-ray scattering
SCM	Scanning Capacitance Microscopy
SE	Secondary Electrons
SECM	Scanning Electrochemical Microscopy
SEM	Scanning Electron Microscopy
SETNanoMetro	“Shape-engineered TiO_2 nanoparticles for metrology of functional properties: setting design rules from material synthesis to nanostructured devices” EU project
SMD	DG Quality and Safety, Belgium Metrology Division of Belgium

SNOM	Scanning Near-Field Optical Microscopy
SPIP	Scanning Probe Image Processor
SPM	Scanning Probe Microscopy
SRM	Standard Reference Material
STM	Scanning Tunnelling Microscopy
SVM	Scanning Voltage Microscopy
TC	technical commitee
TE	Transmitted Electrons
TEM	Transmission Electron Microscopy
TiO_2	Titanium Dioxide
TMV	Tobacco Mosaic Virus
UK	United Kingdom
USA	United States of America
VAMAS	Versailles Project on Advanced Materials and Standards
VIM	International Vocabulary of Metrology
VNIIMS	The D.I. Mendeleev All-Russian Institute for Metrology
VSL	Dutch Metrology Institute
VTT	Technical Research Centre of Finland

List of Figures

List of Tables

Introduction

The objectives of this dissertation are mainly (i) the study of a bio-based nanostructure as an AFM tip characterizer and (ii) the dimensional characterization of complex shape nanoparticles which may apply as candidate reference materials by means of a metrological AFM.

This dissertation is divided into four chapters.

Introductory Chapters:

- Chapter 1 covers all the aspects related to dimensional nanometrology, focusing on the importance of metrological traceability, reference materials, and nanoparticle characterization.
- Chapter 2 describes the technique used for the measurements carried out in this thesis (the Atomic Force Microscope), with particular attention to the importance of metrological AFMs (mAFMs).

Experimentally Chapters:

- Chapter 3 reports the study of Tobacco Mosaic Virus by mAFM, with particular emphasis on the characterization of its circular diameter and its use as tip characterizer.
- Chapter 4 concerns the mAFM-based study of critical sizes and morphological descriptors of complex-shaped nanoparticles (titania bipyramids and nanosheets) that may apply as reference materials. Please note that at the end of the thesis the two annexes report the MATLAB code implemented for the analysis of the non-spherical nanoparticle critical sizes.

This dissertation is based on the work that I performed at INRiM Nanometrology Laboratory from November 2018 to March 2022, that led to the publication of the following peer-reviewed papers, of which I am corresponding author:

[1] G. B. Picotto, M. Vallino, L. Ribotta, Tip–sample characterization in the AFM study of a rod-shaped nanostructure, *Meas. Sci. Technol.,* 31 (2020) 084001 (12 pp), DOI: 10.1088/1361-6501/ab7bc2

[2] V. Maurino, F. Pellegrino, G. B. Picotto, L. Ribotta, Quantitative three-dimensional characterization of critical sizes of non-spherical TiO_2 nanoparticles

Introduction

by using atomic force microscopy, *Ultram.* 234 (2022) 113480 (13 pp), DOI: 10.1016/j.ultramic.2022.113480

[3] R. Bellotti, G. B. Picotto, L. Ribotta, AFM Measurements and Tip Characterization of Nanoparticles with Different Shapes, *Nanomanuf. Metrol.* (2022) (12 pp), DOI: 10.1007/s41871-022-00125-x

Chapter 1. Dimensional Nanometrology

1.1 Metrology and Length Unit

The term “metrology” is defined by the International Vocabulary of Metrology (VIM) as the “science of measurement and its application” [4]. «Metrology covers three main activities:

1. the definition of the seven internationally accepted SI units;
2. the realisation of units of measurement by scientific methods;
3. the establishment of traceability chains by determining and documenting the value and accuracy of a measurement and disseminating that knowledge» [5], discussed in Section 1.3.

Moreover, fundamental metrology is supported by basic and applied research in several areas, *e.g.* space, food, quantum optics, medicine, and nanoscience.

Length, along with mass and time, is one of the fundamental units used since the earliest ancient societies. With the advancement of knowledge and technology, increasingly stringent requirements were placed on the definitions of units of measurement, culminating in one of the first international treaties addressing technical issues, the *Convention du Mètre*, signed in Paris on 20 May 1875. The definition of the metre has evolved over time, with the latest revision that was mainly a re-formatting of the wording to align with the other definitions of the base units in what is called the *explicit-constant* formulation [6]. The current definition is “the metre, symbol m, is the SI unit of length. It is defined by taking the fixed numerical value of the speed of light in vacuum, c, to be 299 792 458 when expressed in the unit m·s^{-1} , where the second is defined in terms of the caesium frequency $\Delta\nu_{\mathrm{Cs}}$” [7].

The practical realisation of the metre is done through the use of a frequency comb or, following the *Mise en Pratique*, by one or more frequency stabilized lasers, *e.g.* the 633 nm iodine-stabilized helium-neon laser. The most precise length measurements are usually made by using interferometers with a laser light source.

Due to the problems in subdividing the wavelength of laser light (*i.e.* non-linearity in the optical detection and sub-fringe interpolation), for providing traceability at the sub-nm scale (pico-metrology for nanoscale engineering) the revision of the SI in 2019 included the silicon lattice constant as a secondary realisation of the meter, using as primary instrument the X-ray interferometer [6,8].

The SI-traceable measurable length scale now covers 24 orders of magnitude, from 10 pm (subatomic distance measurable through X-ray interferometry) to over 2.1×10^{10} km (astronomical distance measurable through light transient time) [6]. At the nanoscale, «several institutes use a high-precision differential interferometer for measuring the stage motion of Atomic Force Microscopes which are the workhorse of the dimensional nanometrology world. By measuring the lateral X and Y motion of the sample stage and mounting a third interferometer on the vertical Z axis to monitor the cantilever deflection, the AFM becomes a Metrology AFM, where measurements are traceable to the metre». [8] Metrological AFMs will be deeply discussed in Section 2.2.

1.2 Nanotechnology and Nanometrology

In 1959 in the lecture entitled "There's plenty of room at the bottom", Feynman predicted the possibility of miniaturization and forecast the potential of nanotechnology [9]. Nanotechnology was firstly defined by professor Taniguchi in 1983, and this sector is of great relevance as the global market generated 1.60 billion € in 2020, and by some estimates will grow to 31 billion € by 2030 [10].

Nanotechnology covers various fields of science and study systems with dimensions in the nanoscale range. When we refer to the nanoscale, we describe nanomaterials with one or more dimensions in the range (1 – 100) nm [11].

The push towards the nanotechnology industry arises from (i) the ability to exploit new physical-chemical properties of matter and (ii) the need of the semiconductor industry to miniaturize. To support this emerging market, a significant investment is needed from industry, universities, national metrology institutes (NMIs), regulatory and standardisation bodies. Metrology supports nanosciences by (i) developing transfer standards and reference materials, (ii) reducing uncertainty of measurements and (iii) defining new methodologies to ensure traceable measurements.

The term "nanometrology" appeared for the first time in a peer-reviewed publication in 1983, and most often it indicates the metrological activities related to nanoscience and nanotechnology [12]. Due to the multidisciplinarity of nanotechnology, nanometrology covers several areas with specific metrological needs. This implies that new reference systems can make nanoscale measurements results traceable and thereby comparable. According to Leach *et al.* [13], nanometrology can be divided in the subsequent fields:

1. dimensional nanometrology, discussed below in detail;
2. chemical nanometrology, which refers to (i) the study of the composition of chemical species [14], chemical states or structural properties, and (ii) the development of certified reference materials (CRMs) [15];
3. thin film nanometrology, which control of thickness and composition of semiconductor fabrication and microelectronics [16], photovoltaics and optical components [17];
4. mechanical nanometrology, which measures the mechanical properties of materials, including nanoindentation [18] and nanotribology [19];
5. nanometrology for structured materials, related to engineered nanostructures incorporated in a product, *e.g.* food packaging [20] and composite materials [21];
6. electrical nanometrology, related to quantum electrical metrology of micro- and nanoelectronics [22];
7. biological nanometrology, related to biomedicine [23], pharmaceutical industry, biotechnology [24], clinical diagnostics and imaging technology [25].

«The ability to measure at the nanoscale depends on many factors: improvements in scientific and technical knowledge, in instrumentation, in documentary standards (standard test methods), and in physical standards (reference materials)» [26]. The crucial role of nanometrology is to produce accurate and reliable nanomaterials and nanodevices. Moreover, material measures and reference materials guarantee good measurements and provide a firm basis for production, in the context of mutual recognition of certificates and products, as reported in detail in Section 1.4.

The dimensional nanometrology is a subfield of nanometrology related to the quantitative measurements of dimensions, sizes, shape, form, texture, location, orientation, and alignment of nano-objects.

Almost all nanotechnology applications require precise size control for achieving the desired functional property. In this framework, dimensional nanometrology instrumentations, reported in the Stedman chart [27] (Figure 1. 1), play a leading role [28]. The amplitude–wavelength chart, early introduced by Margaret Stedman (from NPL), provides a precious guide specifying capabilities of instrumentation for surface metrology. Such a graph provides the working resolution of an instrument, reporting on the abscissae axis the lateral range, *i.e.,* waviness/wavelength of the components of the surface texture, and on the ordinate axis the vertical range, *i.e.*, the amplitude of the spatial components of surfaces.

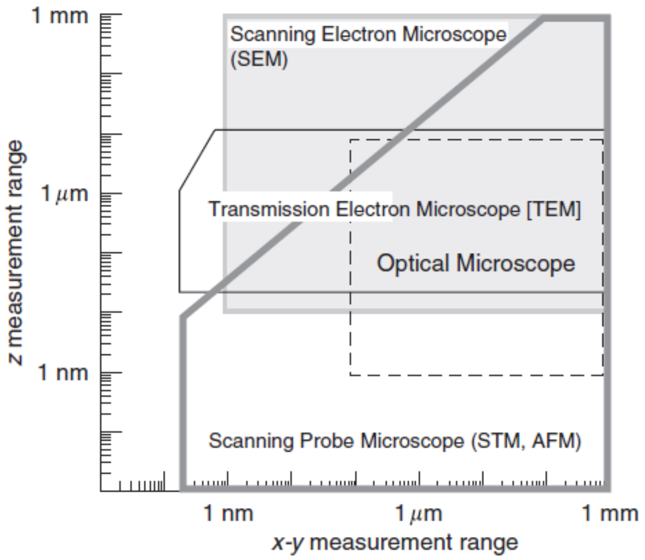

Figure 1. 1 Stedman chart reporting the microscopes used for dimensional nanometrology measurements.
Reprinted with permission from [29]. Copyright © 2018 Elsevier. All Rights Reserved.

Dimensional nanometrology covers several aspects of measurements, from the definition of measurand, measurement procedures and uncertainty evaluation. Moreover, of great importance is the development of new instruments, setups, and displacement sensors. Dimensional nanometrology also deals with the secondary realisations of the length unit at the nanometre and sub-nanometre scale, based on the silicon lattice spacing.

Dimensional nanometrology is also applied outside NMI environment presenting new challenges, such as extending the practical SI length scale to bio applications and to the semiconductor industry.

Many governments support of pre-normative and standardization work on nanomaterials production, and manufacturer or supplier must guarantee the quality infrastructure, according to ISO 17025 [30] (see next Section). In this framework, nanometrology helps in ensuring quality control or conformity assessment (process that demonstrate if a product or service meets specifications).

1.3 Metrological Traceability

The concept of metrological traceability is the backbone of the modern system of measurements, which must be ensured by the National Metrology Institutes (NMIs). VIM defines metrological traceability as the “property of a measurement result whereby the result can be related to a reference through an unbroken chain of calibrations, each contributing to the measurement uncertainty”. Therefore, metrological traceability requires an established calibration hierarchy, which ensures that measuring instruments provide reliable results. The purpose of a metrological traceability chain is the ability to assign uncertainty to measurements of interest, to understand whether the measurement made is satisfactory for the application [31].

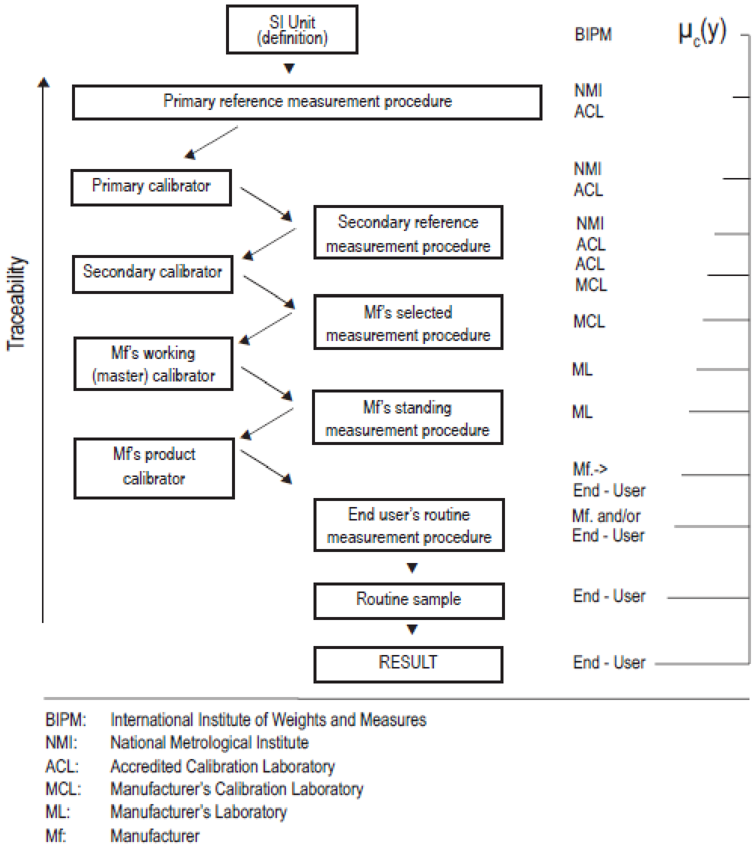

Figure 1. 2 Calibration hierarchy and traceability.
Reprinted with permission from [32]. Copyright © 2007 PubMed Central. All Rights Reserved.

«The international standard ISO/IEC 17025:2017 requires laboratories to establish and maintain metrological traceability of their measurements by means of a documented unbroken chain of calibrations, each contributing to the measurement uncertainty, linking them to an appropriate reference. Furthermore, it requires that measurements results be metrologically traceable to the SI» [31].

A value assigned to a routine or control material can be made traceable by several comparative measurements using RMs (see next Section) and validated measurement procedures in a chain of ascending hierarchical order. Metrological traceability requires a measurement infrastructure consisting of three distinct hierarchical levels, namely NMIs, reference (calibration) laboratories and routine (resting) laboratories, as shown in Figure 1. 2 [32].

Figure 1. 3 depicts the traceability chain for nanometrology measurements.

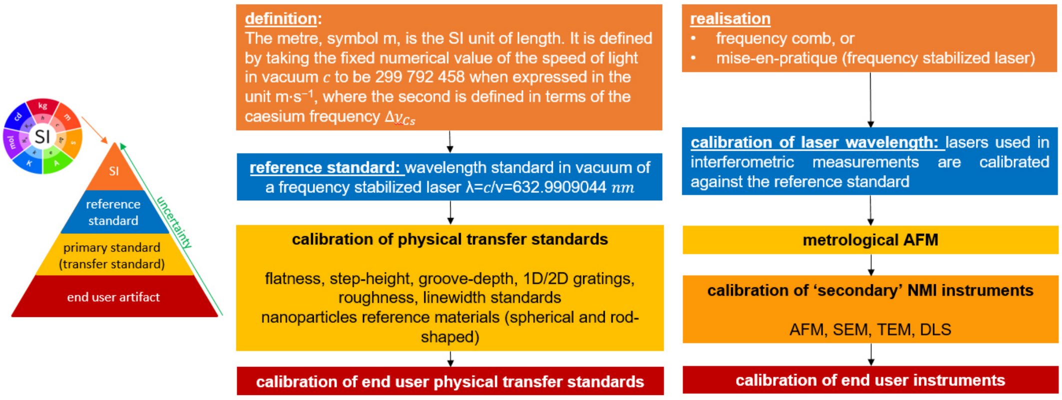

Figure 1. 3 Traceability chain for dimensional nanometrology.
On the left is depicted the measurement traceability 'pyramid'. In the centre, the SI definitions and the transfer standards are reported. On the right, the instrumental chain that allows the traceability to the SI by using the physical transfer standards is reported.

When talking about the length unit, the direct traceability of the wavelength of the laser or laser interferometer is used to transfer the SI length scale from a wavelength (or frequency) to a physical transfer standard [6]. The physical transfer standards (nano-dimensional standard and/or reference materials) permits to calibrate secondary NMI instruments and also end user instruments.

The traceable calibration of 3D geometry of complex nanostructures still remains as a challenging task today. New traceable routes are developed by applying two complementary methods, which traceability chains are quite different, as summarized below [33,34,35]:

(a) secondary realisation of the metre → lattice constant Si single crystal TEM lamella → X-ray interferometry in Si bulk material → optical interferometry → primary He-Ne stabilized laser → optical wavelength → metre definition SI $\lambda = \frac{c}{v}$;
(b) m-AFM sample stage position → laser interferometry → primary He-Ne stabilized laser → optical wavelength → metre definition SI $\lambda = \frac{c}{v}$.

1.4 Reference Materials

In the previous Section we have seen the definition of metrological traceability. Since measurements results must be traceable to appropriate references to be comparable worldwide over time, Reference Materials (RMs) and Certified Reference Materials (CRMs) are fundamental in implementing the concept of metrological traceability of measurements in chemistry, material science, physics and biology. According to VIM, a RM is a “material sufficiently homogeneous and stable with respect to one or more specified properties, which has been established to be fit for its intended use in measurements or in examination of nominal properties”, and a CRM is a RM “accompanied by a certificate that provides the value of the specified property, its associated uncertainty, and a statement of metrological traceability” [4].

The fundamental difference between the two definitions is that while RM is a generic phrase and the property can be quantitative or qualitative, a CRM quantitively certify a property with metrologically valid procedures and provides a traceability statement (to known references) [36].

Below, are reported the «different types of RMs:

- Pure substances, characterised for chemical purity and/or trace impurities;
- Standard solutions and gas mixtures, often prepared gravimetrically from pure substances and used for calibration purposes;
- Matrix reference materials, characterised for the composition of specified major, minor or trace chemical constituents. Such materials may be prepared

from matrices containing the components of interest, or by preparing synthetic mixtures;
- Physico-chemical reference materials, characterised for properties such as melting point, and viscosity;
- Reference objects or artefacts characterised for functional properties, such as taste, odour, and hardness. This type also includes microscopy specimens characterised for properties ranging from microbiological samples to reference nanoparticles» [37].

RMs and CRMs can be used for [38]:

1. Calibration: RMs ensures the relation between the measured signal and the property to be measured. These materials can be used for (i) calibrating instrument parameters (*e.g.*, temperature), or (ii) generating calibration curves of the target property (*e.g.*, particle size vs instrumental response);
2. Statistical quality control (QC): QC-RMs supplement the use of CRMs for controlling the quality of measurements, especially in analytical chemistry, when validated methods are unavailable or the matrix is unstable;
3. Interlaboratory comparisons (ILC): RMs permit to verify the measurement capability, technical competence and uncertainty statement by comparing measurement results between laboratories.

In the following, are listed the major suppliers of RMs:

- NIST – National Institute of Standards and Technology [47];
- BIPM JCTML – Database of higher-order reference materials, measurement methods/procedures and services [39];
- COMAR – Code d'Indexation des Matériaux de Référence: International database for certified reference materials [40] ;
- BAM – Bundesanstalt für Materialforschung und -prüfung – German Federal Institute for Materials Research and Testing [41,42];
- IRMM – Institute for Reference Materials and Measurements [43];
- VSL – Dutch Metrology Institute [44];
- LGC – UK Laboratory of the Government Chemist [45];
- NMIJ – National Metrology Institue of Japan [46].

Please note that NIST has two particular types of RMs, that are:

- «Standard Reference Material (SRM®) - A CRM issued by NIST that also meets additional NIST-specific certification criteria and is issued with a certificate or certificate of analysis that reports the results of its characterizations and provides information regarding the appropriate use(s) of the material» [47];

- «Traceable Reference Material (NTRM^{TM}) - A commercially produced reference material with a well-defined traceability linkage to existing NIST standards for chemical measurements. This traceability linkage is established via criteria and protocols defined by NIST to meet the needs of the metrological community to be served. A NIST NTRM may be recognized by a regulatory authority as being equivalent to a CRM» [47].

The ISO 17034:2016 written standard (formerly ISO Guide 34:2009) specifies the general requirements for the competence and continued proper operation of RM producers. This standard deals with all production requirements, including production planning and control, material handling, manipulation and storage, RM documents and labels, distribution service, and quality management service and audits [48].

This standard also has technical requirements, such as (i) RM definition, (ii) evaluation of homogeneity and stability according to the ISO/Guide 35:2017 [49], (iii) qualitative and quantitative characterisation, and (iv) metrological traceability of certified values.

The study of homogeneity gives rise to an uncertainty component that must be considered in the budget for the certified value of relevant property of the RM or CRM. Since many RMs are prepared as batches of units (bottles, vials, etc.), homogeneity can refer not only to the variation of a property within each unit (within-unit homogeneity), but also between separate units (between-unit homogeneity). Such evaluation is necessary to ensure that each RM unit carries the same value for each property [50].

A reference material should be sufficiently stable for its intended use, which means that the end user can rely on the signed value at any point within the period of validity of the certificate. The stability has not only to be accessed but also monitored in a reliable way, since the value of each property could change during the time for different reasons at different rates, according to material nature.

Stability studies can be classified according to [50]:

(i) the condition of measurements; the classical stability studies, or isochronous studies, ensures repeatability conditions when measuring samples just prepared or exposed to the same degradation condition (like storage and times);

(ii) duration of the study, that can be a real-time study, in which the storage and/or the transport conditions are those intended for the RM, or an accelerate study, in which the study is performed under extreme conditions. The stability should be monitored during the entire lifetime of the RM;

(iii) specific objectives, like expected transport conditions, packaging, lifetime and shelf life of the RM.

In the RM production, an extremely important step is the characterisation of the specific property, which can be done using different approaches according to the type of the measurand or the RM. These approaches are (i) single method, in which a single laboratory adopts a reference measurement procedure sufficiently well understood, (ii) a network of competent laboratories, in which a single procedure is used for the determination of an operationally defined measurand, (iii) multiple methods in one or more competent laboratories, that use different procedures for determining a non-operationally defined measurand, and (iv) by value transfer from a primary CRM to a secondary CRM using a single measurement procedure performed by one laboratory [50].

The value assignment is the process of combining the results obtained from the characterisation with those deriving by homogeneity and stability assessment. These values are those issued on certificates or product information sheets, and comprises also the development of an accurate uncertainty budget, the calculation of the uncertainty associated with each property value, and a statement of metrological traceability [50].

Industry, manufacturers and accredited calibration need standards for the nanoscale. Various samples are commercialized [51], such as transfer standards (step-height and groove samples, 1D and 2D gratings, line width samples) and mono and multimodal spherical and cylindrical nanoparticles in stabilized suspensions (Figure 1. 4).

As described in this Section, «RMs are needed for the traceable calibration and characterisation of measurement instruments to enable the valid comparison of measurement results and to establish a solid basis for the design of objects with traceable nanoscale dimensions and tolerances. Furthermore, new types of reference materials are needed for probe characterisation and 3D measurement of shape and size» [52]. For this purpose, in Chapter 3 a bio-based characteriser for AFM tip is described, while in Chapter 4 is reported the study of complex-shaped NPs that can be applied as candidate RMs at the nanoscale is reported. Please note that a "candidate reference material needs to be investigated to determine if it is sufficiently homogeneous and stable with respect to one or more specified properties" [53].

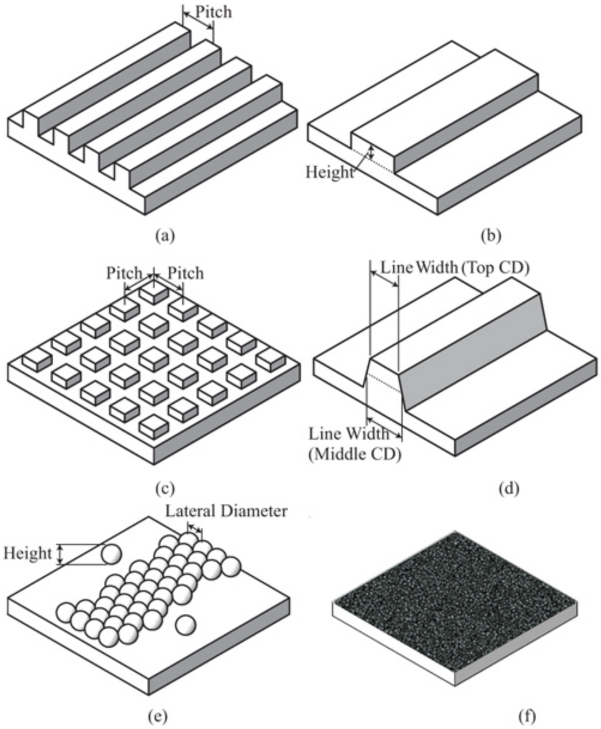

Figure 1. 4 Transfer standard at the nanoscale. For each standard, the typical measurand is reported.
(a) 1D grating standard.
1D pitch: lateral distance between two lines center or between two line edges.
(b) Step-height standard.
Height/thickness: vertical distance between the baseline and the center of a step/groove.
(c) 2D grating standard.
2D pitch: lateral distance between two grating elements in the X-Y directions.
(d) Line width standard.
Line width: lateral distance between two sidewalls of a step/groove. This critical dimension (CD) can be at the top or in the middle of a step/groove.
(e) Quasi-spherical NPs.
Height: distance between the top of the sphere and the substrate baseline for an isolated NP.
Lateral diameter: lateral distance between two NPs in a closely-packed arrangement.
(f) Surface roughness standard.
It is used for texture/roughness calibration and for tip diameter evaluation.
Reprinted with permission from [54]. Copyright © 2021 IOP Publishing. All Rights Reserved.

In the dimensional characterisation of RMs NPs there are several challenges [38], such as (i) the difficulty in the exact definition of the measurand (there are more than 200 definitions of "size" related to NPs [8]), (ii) not clear definition of acceptable uncertainty by potentially customers and industries and difficulties in reliable uncertainty determination by the laboratories, and (iii) the lack of documented and validated methods and qualified laboratories.

In the next Section, the instrumental techniques for dimensional characterization of nanoparticles RMs are investigated.

1.5 Measurement Techniques for the Dimensional Characterization of Nanoparticles Reference Materials

Nanoparticles can exhibit unique properties depending on their size. For understanding the different properties of NPs, reliable size measurements should be made. In this regard, the use of RMs, quality control, and calibration materials is crucial.

Size and size distribution measurements are essential to understand the relevant properties of NPs. Many techniques permit the analysis of size and size distribution of NPs in a suspension. Most of these techniques attempt to quantify the size of the particle with a diameter, thus simplifying the reality. Since in the real world it is very rare for particles to be perfectly spherical, most techniques give result as an "equivalent spherical diameters".

«Different techniques may result in different particle diameters due to the different measurement principles used for establishing the particle diameter» [55].

Table 1. 1 reports the CRM spherical nanoparticles available in the market. These NPs are supplied by American and European institutions, and each of them is accompanied by a certificate of analysis, a certification report, and a safety data sheet.

The certificate of analysis is a document that reports the certified value with its uncertainty budget.

Table 1. 1 CRMs spherical nanoparticles available on the market.

NP reference material	mean diameter nominal values	institution	Identifier
Gold	10 nm, 30 nm, 60 nm	NIST	RMs 8011 [56], 8012 [57], 8013 [58]
silver	75 nm	NIST	RM 8017 [59]
polystyrene	60 nm, 100 nm	NIST	SRM 1964 [60], SRM 1963 [61]
silicon dioxide	20 nm, 40 nm, mixture 20 nm and 80 nm	IRMM	ERM-FD100 [55], ERM-FD304 [62], ERM-FD102 [63]

The certification report is a detailed file which describes the nature and the purpose of the RM, the certified value with its uncertainty, the expiration of the value assignment, the analytical methods used for certification, the metrological traceability, the participants who studied the RM, the instruction for handling and storage, the instructions for use, preparation and analysis, homogeneity and stability assessment, and legal notice.

The safety data sheet is divided into several parts, that are «substance and source identification, hazards identification, composition and information on hazardous ingredients, first aid measures, firefighting measures, accidental release measures, handling and storage, exposure controls and personal protection, physical and chemical properties, stability and reactivity, toxicological information, ecological information, disposal considerations, transportation information, regulatory information and other information» [[64]].

Table 1. 2 reports the different instrumentations present in the certificates of the RMs in Table 1. 1. The following is a brief description of the different techniques, focusing on the different nature of measurands and their resolution.

Table 1. 2 Measurands and resolution of the different instrumental techniques for the analysis of reference material nanoparticles.

Technique	**Measurand**	**Resolution/ Detection limits**	**Reference**
AFM	thickness lateral sizes	0.1 nm (Z) 1 nm (X-Y)	[[65]]
SEM	mean area-equivalent diameter	1 nm	[[65]]
TEM	mean area-equivalent diameter	0.1 nm	[[65]]
DLS	scattered light intensity-weighted mean hydrodynamic diameter	3 nm	[[65]]
CLS	intensity-based Stokes particle diameter	20 nm	[[66]]
DMA	electrical mobility mean diameter	1 nm	[[67]]
SAXS	volume-weighted mean diameter	1 nm	[[68]]

A first classification is based on the different nature of the instruments, dividing the counting from the ensemble methods.

The various microscopes (AFM, SEM and TEM) are defined as "direct techniques", since they allow the shape and size of the particles to be measured directly, compared to "non-imaging methods" such as DLS, CLS, DMA and SAXS, which analyze the distribution of a large number of NPs but are unable to distinguish shapes of individual particles and thus calculate the size indirectly.

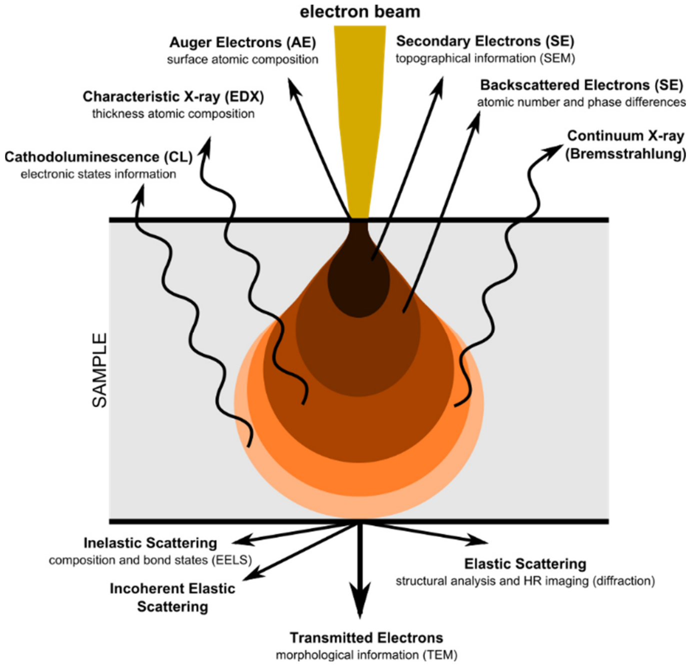

Figure 1. 5 Sketch illustrating the typical electron-solid interactions occurring in electron microscopy. Image from [69]. This image is licensed under the Creative Commons Attribution-Share Alike 4.0 International license.

Electron microscopy (EM) uses accelerated electron beams to visualize samples. The pear shape interaction (Figure 1. 5) depicts the various phenomena that occur from the electron-matter interaction. In this volume, it is observed that the lost energy due to the beam-sample interaction is converted into alternative forms, typically elastic (AE, EDX, CL, SE, BSE, Bremsstrahlung) and inelastic (IS, IES, TE) interactions, which gives signals related to surface topography and its chemical composition.

Both SEM and TEM produce 2D projection of 3D particles. EM can handle polydisperse samples because the size of individual particles can be detected, and this allow to build the size distribution plot [66].

Since most of EM is performed under high vacuum, measurements require the use of dry samples. Moreover, for organic NPs or NPs with organic surface coating cryo-TEM and environmental SEM are available, since the interaction between the electron beam and the vacuum can cause issues in image formation [66].

The basic operation of electron microscopes is described by several written standards. ISO 29301:2010 [70] deals with the calibration of the image magnification, and ISO 13322-1:2004 [71] describes the protocol for features size determination through static image analysis. It is possible to quantitatively define particle size through EM measurements in several ways, such as the minimum and maximum Feret diameter or the projected area-equivalent circular diameter [72]. However, there is no standard describing the NP sample preparation for reliable particle size analysis by EM.

Scanning Electron Microscope (SEM) enables information on the physical nature of surfaces to be obtained with very high resolution. The instrumentation is shown in Figure 1. 6 and consists of a filament source that, by thermionic effect or field emission, causes the ejection of electrons, accelerated with an energy between 1 and 30 keV.

A system of electromagnetic lenses collimates the electrons into a coherent beam, and after the beam passes the obejctive lens it strikes the sample surface. SEM scanning is performed by electromagnetic coils that deflect the beam along the X and Y axes. The image can be recorded using different detectors, for instance, the secondary electron detector and the backscattered electron detector. The secondary electron detector (SE) gives morphological information, by detecting the sample low energy electrons ejected because of the excitation caused by the electron beam. Due to its position, the image from these electrons can provide shadows. The backscattered electron detector (or backscattered electron BSE), which detects electrons from the beam that undergoes elastic collisions, provides less information from the morphological point of view but provides chemical information, because the number of electrons bouncing on the detector is directly proportional to the main quantum number, and the more an atom is large, the more electrons are detected and the image is brighter [70].

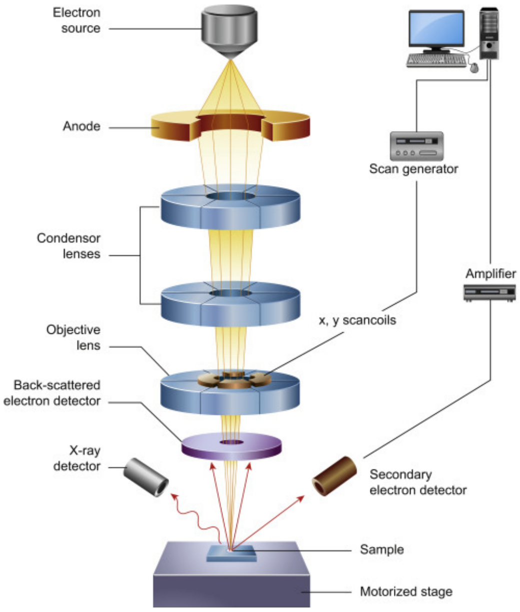

Figure 1. 6 Arrangement of the Scanning Electron Microscope (SEM) components. Reprinted with permission from [73]. Copyright © 2016 Elsevier. All Rights Reserved.

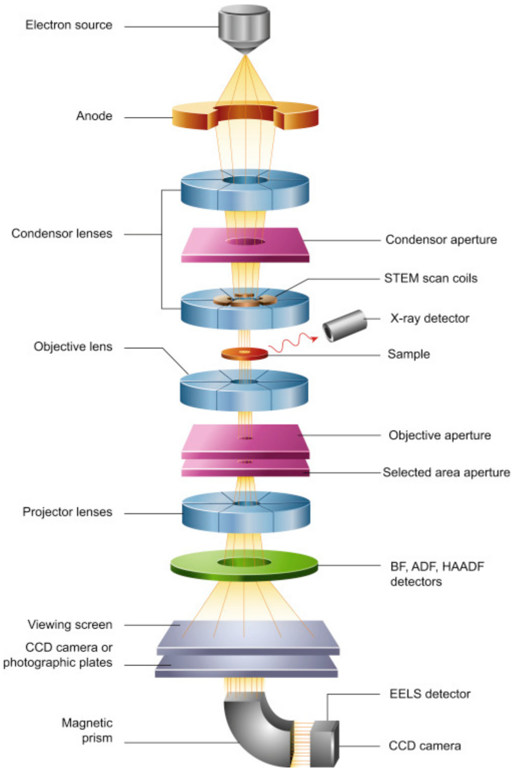

Figure 1. 7 Arrangement of the Transmission Electron Microscope (TEM) components. Reprinted with permission from [73]. Copyright © 2016 Elsevier. All Rights Reserved.

Transmission electron microscopy (TEM) is an imaging technology in which are collected the electrons transmitted through a sample, that can be a suspension on a grid or a section less than 100 nm thick. The detector can be a fluorescent screen or a sensor, such as a charge-coupled device (Figure 1. 7) [73].

Dynamic Light Scattering (DLS) is a technique used to determine the size distribution of suspended particles. It has a high statistical value since an average measurement is taken over the entire sample mass.

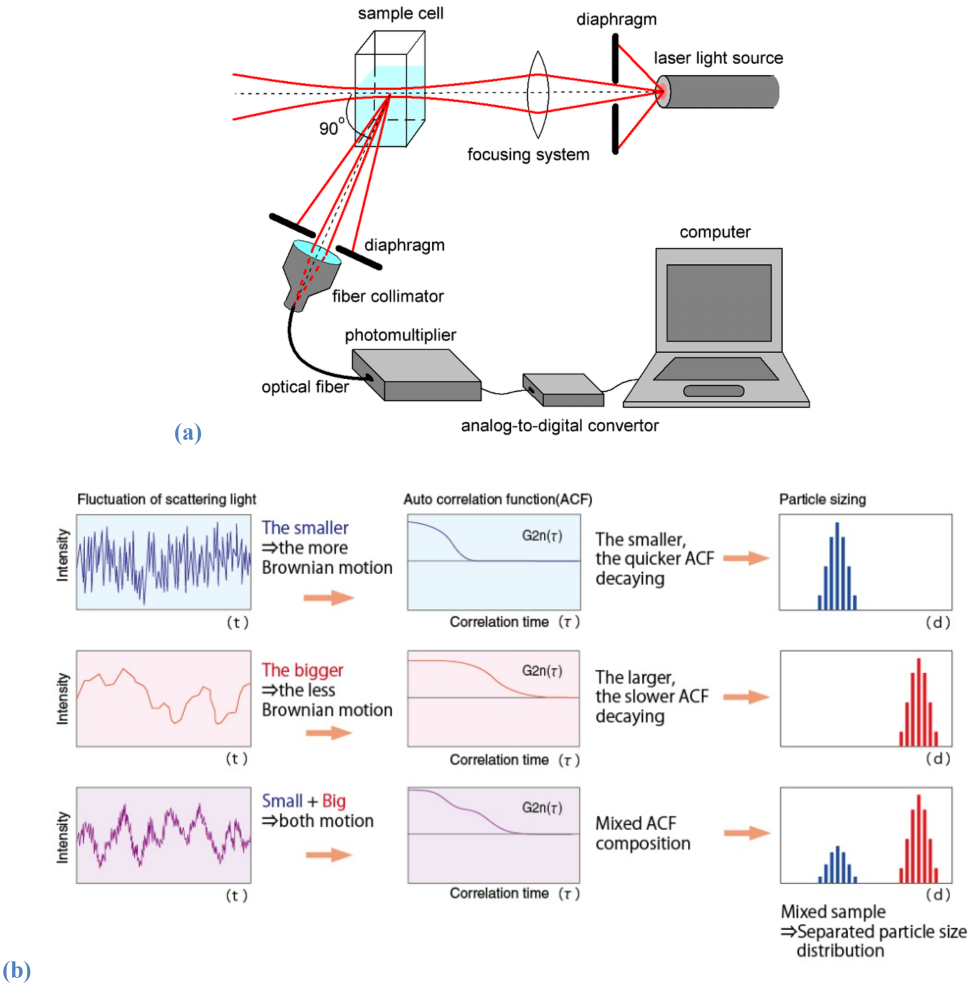

Figure 1. 8 (a) Scheme of a Dynamic Light Scattering (DLS) spectrometer.
(b) Schematic illustration of (left) intensity measurement, (centre) the corresponding autocorrelation function, and (right) particle size distribution plot. The figure illustrates dispersion composed of small, large and polydisperse samples.
Figure (a) reprinted with permission from [74]. Copyright © 2020 PubMed Central. All Rights Reserved.
Figure (b) reprinted with permission from [75]. Copyright © Otsuka Electronics Co., Ltd. All Rights Reserved.

This instrument measures how the intensity of the scattered light varies over time and this depends on the Brownian motion. The light intensity is registered by a highly sensitive photodetector at an angle of about 90° to the incident light beam (Figure 1. 8 (a)).

The bandwidth of the intensity spectrum as a function of time is proportional to the scattering coefficient. The instrument uses what is called an autocorrelation function to obtain the decay time τ, which is inversely proportional to the half-height amplitude of the spectrum.

From the autocorrelation function we get the diffusion coefficient and then from Stoke-Einstein equation goes back to hydrodynamic radius giving as output a particle size distribution. The hydrodynamic radius is the radius of a rigid sphere that diffuses with the same velocity of the particle in question. Since real particles are not perfect spheres, the hydrodynamic radius obtained via DLS gives an estimate of particle size. Moreover, this radius also depends on the type of interactions that the particle has with the solvent.

DLS works well with monodisperse samples of suspended NPs with a size range (1 to 500 nm) and known refractive index.

To account for polydispersity, «the autocorrelation function must be fitted by a sum of functions, each corresponding to monodisperse nanoparticles of the same properties. It should be noted, however, that the resulting size distribution plot is highly dependent on the algorithm used» [[66]].

Centrifugal liquid sedimentation (CLS) exploits the concept that nanoparticles, when subjected to a centrifugal force, will sediment at different velocities according to the size, *i.e.* larger particles sediment faster than smaller ones of the same density.

The measurand is the Stokes diameter, defined as an equivalent diameter of a sphere with uniform and known density with the same sedimentation time. CLS is a technique capable of separating different size fractions in polydisperse materials prior to the detection/quantification step [[66]].

CLS instruments can have two different setups, in which the suspension is contained in a disc or a cuvette (Figure 1. 9).

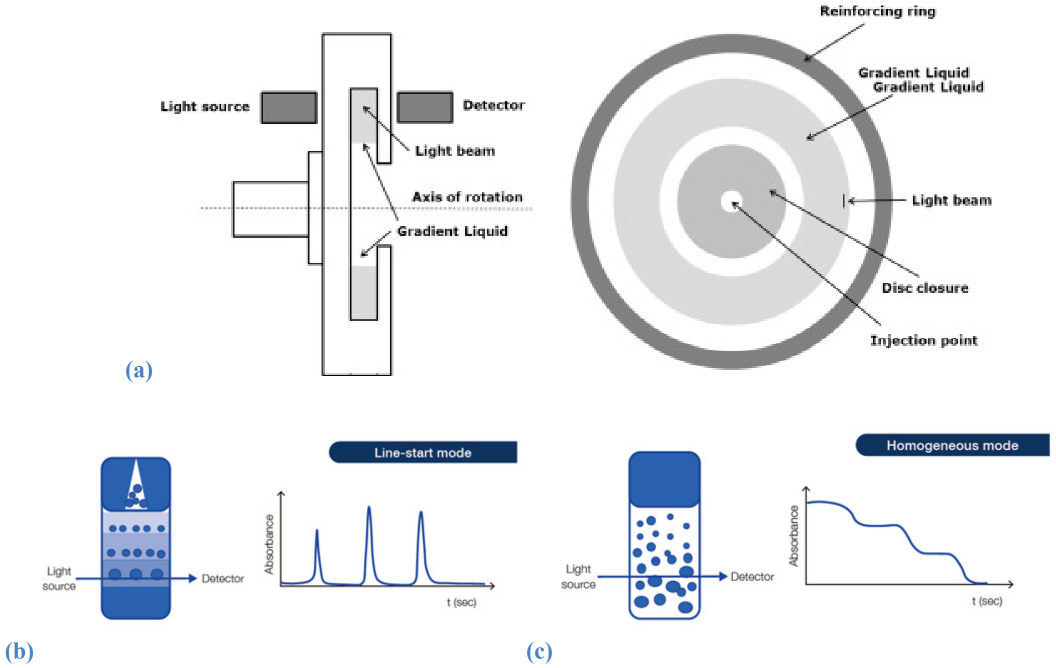

Figure 1. 9 (a) Top view and side-view of a CLS spinning disc.
(b) CLS line start method, spinning disc and absorbance plot.
(c) CLS homogeneous method, cuvette and absorbance plot.
Figures (a) from [76]. Copyright © 2020 Elsevier. All Rights Reserved.
Figures (b) and (c) reprinted with permission from [77]. Copyright © HORIBA, Ltd. All Rights Reserved.

In the “CLS line-start method”, «a small volume of a dilute suspension of particles is injected into the centre of a spinning disc, which is filled with a sucrose solution that has a slight density gradient» [55]. A laser light or X-ray beam passes through the liquid, and particles passing the beam reduce the light intensity in proportion to their concentration. «The measured time is then converted to an equivalent particle size using Stokes’ law of sedimentation and assuming an effective particle density» [63].

In order to determine intensity-based modal Stokes diameter in a correct way, the general guidelines in ISO 13318-1:2001 [78] and ISO 13318-2 [79] written standards are applied.

In the “CLS homogeneous method” the particle suspension is contained into a cuvette. The distribution of sedimentation is determined by measuring the difference in refractive index between the sample and a reference. The particle size distribution obtained from the initial sedimentation distribution is mass-based, since the refractive index directly matches the mass of the detected particles [63].

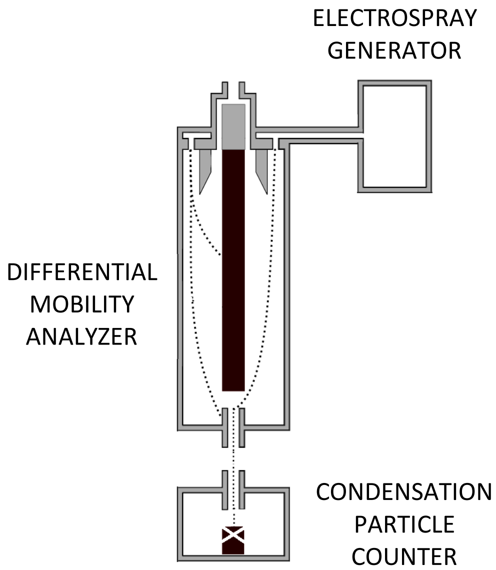

Figure 1. 10 DMA equipment scheme.
Adapted with permission from [80]. Copyright © 2008 Songklanakarin Journal of Science and Technology. All Rights Reserved.

Differential mobility analysis (DMA) or electrospray-differential mobility analysis is a powerful technique for the measurement of nanoparticle size distributions in colloidal suspensions. This technique can also produce monodisperse aerosols of charged or neutralized aerosol particles [81].

The instrument typically consists of three units (Figure 1. 10): (i) a charge reduced electrospray generator, that neutralise the incoming aerosol; (ii) a differential mobility analyzer (DMA) that selects particles according to their electrical mobility equivalent diameter; and (iii) a condensation particle counter, that counts selected particles within minutes to seconds [82].

Note that the electrical mobility equivalent diameter is the diameter of a spherical particle with the same mobility (defined as the particle velocity produced by a unit external force) as the particle in question [83].

The DMA can be described as an assembly of two concentrically cylindrical electrodes with an air gap between the walls. A negative electric field is applied to the inner electrode: negatively charged particle are repelled, neutral charge exits the instrument, while positively charged particles will be accelerated until they reach a certain constant limiting velocity, depending on on the magnitude of the electricfield and on the electrical mobility and charge of the particle. By adjusting the magnitude of the electric field within the DMA, particles having a specific mobility exit through a small slit located at the bottom towards the condansator particle counter [80, 84].

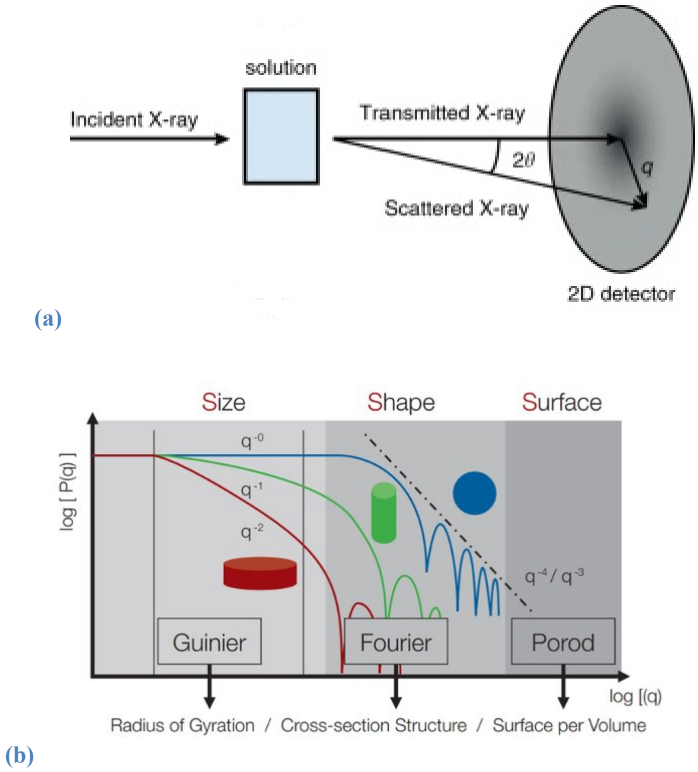

Figure 1. 11 (a) SAXS equipment scheme and (b) intensity pattern.
Figure (a) adapted with permission from [85]. (c) Copyright © 2014 Nature. All Rights Reserved.
Figure (b) adapted with permission from [86]. Copyright © 2015 Taylor & Francis. All Rights Reserved.

Small Angle X-ray Scattering (SAXS) measures the size of NPs by exploiting the elastic scattering of the radiation that pass through a suspension of nanoparticles at small angles (θ<4°). X-rays with wavelengths between 0.1 nm and 1 nm are scattered by particles in the range between 1 nm and 100 nm [66].

The scattering pattern is done by the interference of different waves generated by the elastic scattering of X-rays in all directions (Rayleigh scattering) at the interfaces between particles and dispersant.

The scattered intensity is detected at the “scattering angle” 2θ (Figure 1. 11 (a)), which depends on the light wavelength and the NP size.

From the fit of the scattered radiation versus the scattering angle, the size and shape of NPs are obtained. According to the different regions of a SAXS pattern, one can obtain information about the size (Guinier zone), shape (Fourier zone) and surface (Porod zone) of monodispersed NPs, expressed as radii of spheres, cylinders or discs of equivalent scattering properties (Figure 1. 11 (b)) [63].

Among the various techniques previously described there is the Atomic Force Microscopy, that will be extensively discussed in Chapter 2.

Chapter 2. Atomic Force Microscopy

2.1 The Microscopy Technique

2.1.1 Scanning Probe Microscopy

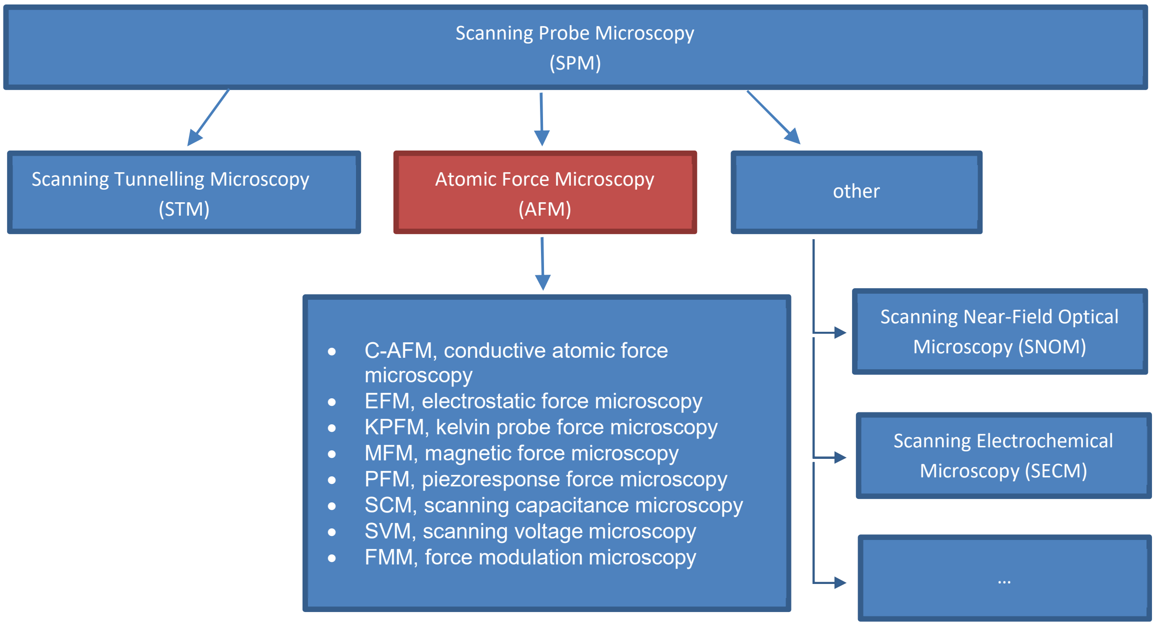

Figure 2. 1 The Scanning Probe Microscopy family tree.

Scanning Probe Microscopy (SPM) is a general term which describes all microscopic techniques in which a probe scans the surface in a bustrophedic way. These techniques can be divided into several branches (Figure 2. 1), depending on (i) the different nature of the probe and the sample in the analysis, and (ii) the different physical interactions that occurs between them [87].

Scanning Tunnelling Microscopy (STM) was developed by Gerd Binnig and Heinrich Rohrer at IBM Research in Zurich in 1981 [88]. This instrument can measure the electron tunneling current between a metallic needle probe and a conductive specimen, obtaining images with atomic surface resolution. Note that a similar microscope, called topographiner, was developed by Russell Young in 1971 [89]. This last exploited the electron field emission current between a surface and a sharp metal probe, but since its resolution suffered from instrument vibrations, the topographiner was supplanted by STM, for which Binning and Rohrer won the Nobel Prize in Physics in 1986.

In the same year, Gerd Binning, Calvin Quate, and Christoph Gerber developed atomic force microscopy (AFM), a microscope that exploits the interaction forces between a silicon tip and the sample [90]. Since AFM can operate in air, vacuum, or liquid, various types of samples (conductive, insulators, inorganic, organic, biological, etc.) can be characterised in 3D. Because of its versatility, AFM can be hyphenated with other techniques using specific hardware and probes with a metallic coating (*e.g.*, magnetic force microscopy (MFM), conductive atomic force microscopy (C-AFM)).

The other SPM techniques investigate specific surface properties, such as optical properties (fluorescence, photoluminescence) in scanning near-field optical microscopy (SNOM) [91], or the electrochemical properties in Scanning Electrochemical Microscopy (SECM) [92]. The peculiarity of these techniques is the nature of the probe, which is a glass fiber in SNOM and a pipette with an electrochemical solution in SECM.

2.1.2 Atomic Force Microscopy

As the name implies, Atomic Force Microscopy permits to measure a surface by exploiting the interaction forces between the atoms at the tip apex with the outermost atoms of a surface. These interactions are modelled by the Lennard-Jones potential (Figure 2. 2), which describes interatomic and intermolecular interaction. The blue curve represents a short-range repulsive interaction, due to the Pauli exclusion principle which prohibits the superposition of electron clouds. The red curve represents the attractive contribution, the so-called Van der Waals forces, that arises from dipole-dipole interactions (Keesom forces), permanent dipole-induced dipole interactions (Debye forces), instantaneous dipole-induced dipole interactions (London Dispersion Force) [93].

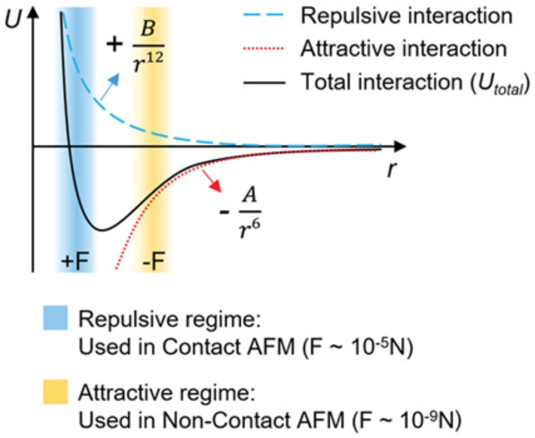

Figure 2. 2 Plot reporting the tip-sample interaction potential U as a function of the distance r. The black curve describes the Lennard-Jones potential, that combines the long-range attractive (dashed red curve) and short-range repulsive (dashed blue curve) interactions.
Adapted with permission from [93]. Copyright © Park Systems. All Right Reserved.

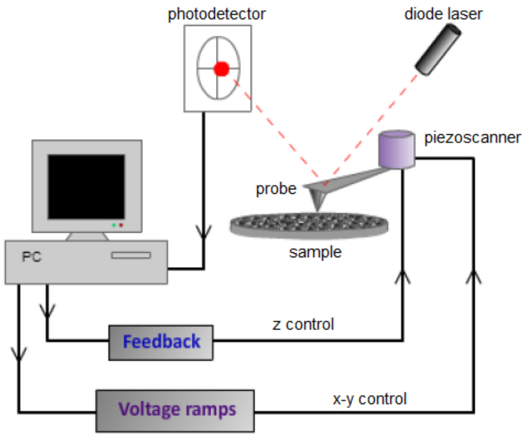

Figure 2. 3 Main components of the AFM microscope.
Adapted from [94]. The figure is under Creative Commons licence "Attribution-Non-Commercial-Share Alike 2.0 UK: England & Wales".

As depicted in Figure 2. 3, the main components of the microscope are [94]:

1. the probe, consisting of a cantilever on which is mounted a tip;
2. a laser diode, whose beam is focused on the cantilever;
3. a four-quadrant photodetector, that monitors the deflection of the lever as it interacts with the sample;
4. a piezoelectric, that precisely adjusts the tip-sample distance, which movement is controlled by a feedback system (in Z direction) and by voltage ramps (in X and Y directions).

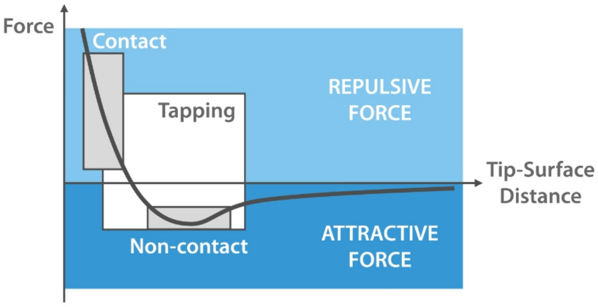

Figure 2. 4 Illustration of the three topography modes, depending on the tip-sample force. Reprinted with permission from [95]. Copyright © NanoandMore. All Rights Reserved.

Depending on (i) the interaction forces between the AFM tip and the surface (Figure 2. 4) and (ii) the morphology and surface characteristics of the sample in analysis, there are three different topography modes [95]:

1) contact mode: the deflection of the cantilever, proportional to the tip-sample interaction forces, provides sample topography [96].

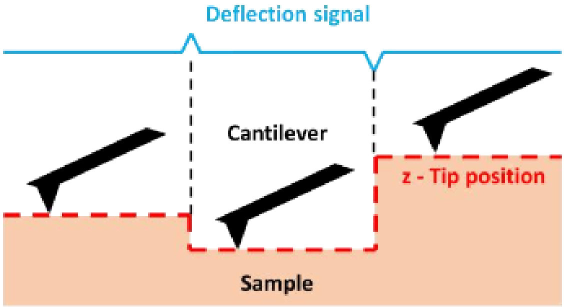

Figure 2. 5 Sketch of an AFM cantilever operating in contact mode. Reprinted with permission from [96]. Copyright © 2018 Université Grenoble Alpes. All Rights Reserved.

2) non-contact mode: during measurements the cantilever vibrates, and there are two modes for measuring the interaction forces [96]:

   - amplitude modulation: the cantilever oscillates at a frequency close to the resonance one, and the oscillation amplitude modifications produce topographic information and are used as a feedback to keep the tip-sample distance constant;

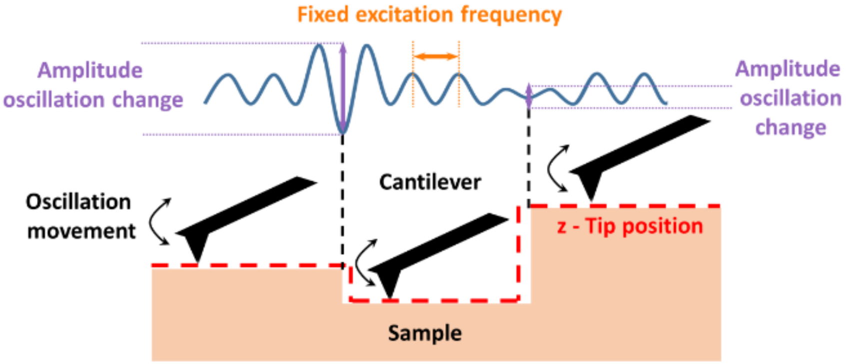

Figure 2. 6 Sketch of an AFM cantilever operating in non-contact amplitude modulation mode. To keep a constant tip-sample distance, the oscillation amplitude is employed as feedback signal.
Reprinted with permission from from [96]. Copyright © 2018 Université Grenoble Alpes. All Rights Reserved.

- frequency modulation: the oscillation amplitude of the cantilever is kept fixed at the set point, and the change in oscillation frequency is used as a feedback signal to adjust the tip-sample distance;

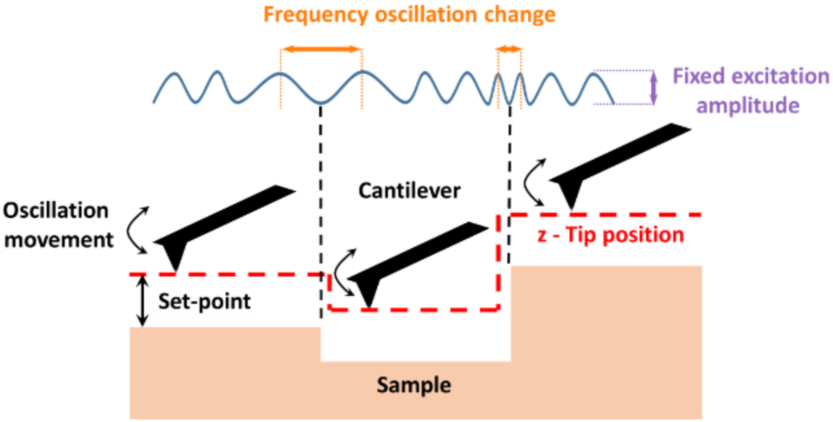

Figure 2. 7 Sketch of an AFM cantilever operating in non-contact frequency modulation mode. For maintaining a constant tip-sample distance, the oscillation frequency is employed as feedback signal.
Reprinted with permission from from [96]. Copyright © 2018 Université Grenoble Alpes. All Rights Reserved.

3) intermittent contact mode or tapping: the cantilever oscillates so that it can contact the sample cyclically, and then the force required to detach the tip

from the sample is applied. This mode is used to detect short-range interatomic forces, while at the same time preventing the tip from getting stuck on the surface. The resonance shifts to lower frequencies and exhibits a drop in amplitude [96].

The scanning motion is generated in almost all AFMs by means of piezoelectric actuators. A piezoelectric is a non-centrosymmetric material that polarizes by generating an electrical potential difference when subjected to a mechanical deformation (direct piezoelectric effect), and it deforms elastically when subjected to an electrical voltage (inverse piezoelectric effect). This piezoelectric effect occurs only along a certain direction and the deformations associated with it are on the order of nanometers.

Typically, commercial AFMs use a piezo tube, in order to allow X, Y and Z movements with one single element. Other actuators used are piezo stacks and flexure-guided nanopositioning stages, these last usually used in closed loop operation (see below) [97].

Depending on the position of the piezoscanner in the instrumentation, AFM can have several scanning configurations, depicted in Figure 2. 8, which are:

- sample scanner, when the piezoelectric is under the sample, and this last is moved along the XYZ directions;
- hybrid scanner or decoupled XY and Z scanning system, when the sample is scanned in the XY horizontal directions and the tip is controlled by the Z scanner. This is the configuration mostly used in Park Systems AFMs [98], that develop it because «first generation AFM based on piezoelectric tubes (...) suffers from poor repeatability and accuracy due to background curvature and crosstalk between the XYZ axes» [99];
- tip scanner, when the piezoelectric moves the tip in the XYZ directions.

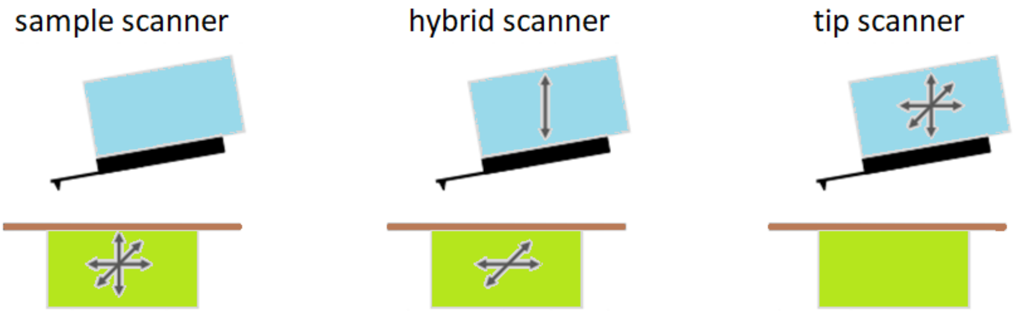

Figure 2. 8 AFM scanning configurations depending on the piezoscanner position.

All topography modes have a feedback circuit connected to the Z piezoelectric. As seen above, this circuit tries to keep the tip–sample interaction constant, protecting them from damaging [100]. Figure 2. 9 explains what would ideally happen with and without feedback control.

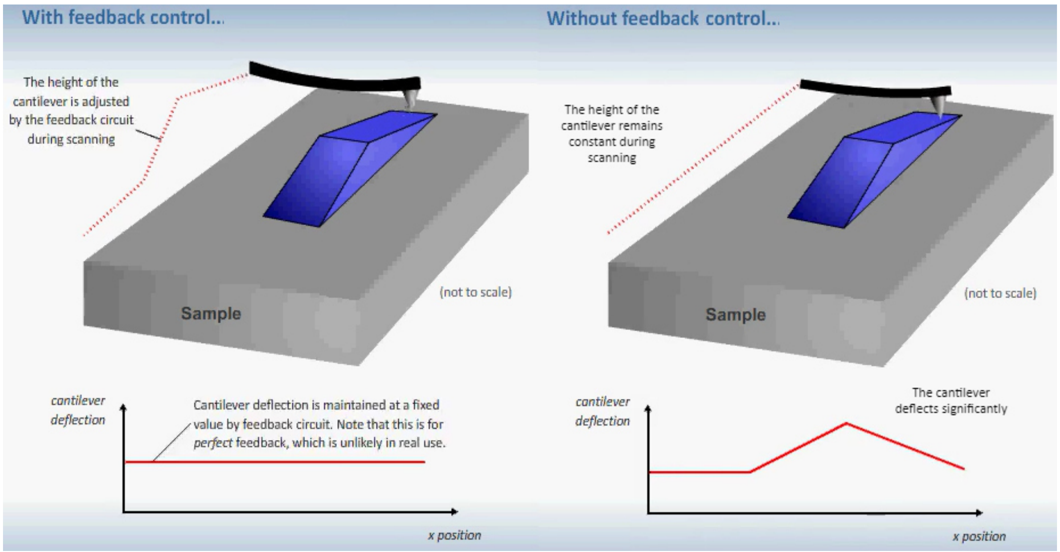

Figure 2. 9 Sketch of cantilever height and deflection with and without the use of the Z piezoelectric feedback control.
Adapted from [100]. The figure is under Creative Commons licence "Attribution-Non-Commercial-Share Alike 2.0 UK: England & Wales".

The feedback system is influenced by the following parameters [100]:

- Setpoint: «value of the cantilever deflection (in static mode) or oscillation amplitude (in dynamic mode) that the feedback circuit attempts to maintain. This is usually set such that the force on the cantilever is small, but the probe remains engaged with the surface» [100];
- Feedback gain: value indicating the reaction speed of the feedback system;
- Scan rate: value that indicates the time given to the tip for scanning.

The X-Y lateral movements are electronically controlled by a voltage ramp, at which is associated a relative displacement [101], and according to the on-board metrology[1] AFMs can be divided into three groups: open loop, closed loop, or metrological AFMs [[102]].

In open loop systems, the position comes directly from the drive voltage of the piezoelectric without feedback. This mode provides very good imaging resolution, but the measured position does not match the actual tip position because of the absence of positional feedback. This leads to images distortions, typically due to nonlinearities caused by phenomena such as creep, hysteresis and ageing effects, which originate from the piezoelectric scanners (see Section 2.4) [[63]].

In the closed-loop modality, the actual position of the tip is monitored by position sensors (capacitive, inductive, encoders, resistive strain gauges…) attached to the piezoscanner. The sensor applies a voltage to the piezoelectric to correct and keep its position at the desired location. The feedback compensates for the hysteresis and nonlinear behaviour of the piezo, which is particurarly relevant for large scanning areas [[63]].

«The most accurate type of AFM is metrological AFMs, which have position measurement with integrated laser interferometers. The interferometric position measurement is directly traceable to the metre via the laser wavelength» [[102]] (see next Section).

Although with closed-loop the exact position of the displacement actuator is known, metrological AFMs are advantageous for quantitative measurements because the position is directly related to the movement of the sample.

2.2 Metrological Atomic Force Microscopes

NMIs activities related to dimensional measurements are critical dimensions' measurements on transfer standard, NPs, and RMs. NMIs use and develop instruments directly traceable to the SI, called metrological Atomic Force Microscopes (mAFM), in order to calibrate these samples.

---

[1] On-board metrology: set of sensors that measure a specific quantity. In this case, since dimensional measurements are considered, on board metrology refers to displacement actuators.

Table 2. 1 Metrological AFMs in the world (in alphabetical order).
The principal mAFM types are X-Y interferometric and Z capacitance controls, 3D (three-dimensional), CD (Critical Dimension), tip-tilting, HS (High Speed), and LR (Large Range).
Tables inspired to [102] and [103]. Adapted with permission. Copyright © 2014 University of Helsinki. Copyright © 2011 IOP Publishing. All Rights Reserved.

NMI association	Country	NMI	mAFM Type	Displacement Range (X × Y× Z)	Reference
America (SIM)					
	Canada	NRC	LR	(40×40×6) mm	[104]
	USA	NIST	M^3	(50×50) mm ×5 µm	[105]
			c-AFM	(100×100) µm	[105]
			CD	-	[105]
Asia-Pacific (APMP)					
	Australia	NMIA	3D	(100×100×25) µm	[106,107,108]
	China	NIM	3D	(50×50×2) mm	[109]
	Korea	KRISS	X-Y interferometric Z capacitive sensor	(100×100×12) µm	[110]
			LR	200 mm × 200 mm × 38 µm	[111]
	Japan	NMIJ	tip-tilting	(12×12×8) µm	[112]
	Singapore	A*STAR	LR	(25×25×5) mm	[113]
	Taiwan	CMS/ITRI	LR	(250×250×100) µm	[114]
Euro-Asian Cooperation (COOMET)					
	Russia	VNIIMS	3D	(3×3×1) µm	[115]
Europe (EURAMET)					
	Belgium	SMD	3D	(100×100×100) µm	[116]
	Czech Republic	CMI	LR	1 cm × 1 cm × 35 µm	[117]
	Denmark	DFM		(70×70×6) µm	[103]
	Finland	VTT	3D	(100×100×16) µm	[118]
	France	LNE	3D	(60×60×15) µm	[119]
	Germany	PTB	mSTM	(100×100×10) µm	[120]
			ZEISS Veritekt A	(70×15×15) µm	[121]
			ZEISS Veritekt B	(70×15×15) µm	[122]
			ZEISS Veritekt C	(70×15×15) µm	[123]
			CD/tip-tilting	(12×12×8) µm	[124,125,126]
			HS LR	(25×25×5) mm	[127,128]
	Italy	INRiM	X-Y interferometric Z piezoscanner	(30×30×2) µm	[129]
	Netherlands	VSL	3D	(1×1×1) mm	[130,131]
	Switzerland	METAS	LR	(380×380×5) µm	[132]
			3D	(800×800×200) µm	[133]
	UK	NPL	3D	(100×100×5) µm	[134,135]
			HS	-	[136]
Non-NMI					
AFM head integrated in a nanomeasuring machine (NMM), Institute of Manufacturing Metrology (FMT), Germany [137]					
Automated AFM Metrology in industrial instruments for semiconductor applications [138,139]					

Direct traceability of AFM results can only be achieved through built-in interferometers to measure the tip–sample relative position. These instruments are fully characterized to establish an uncertainty budget, which is taken into account into the uncertainty of measurement results.

The development of more metrologically advanced setups began few years after AFM invention. Table 2. 1 reports all the mAFM present worldwide, describing the type of instrumental configuration, and the displacement range.

All mAFM have sample scanner configuration. None of the instruments use a piezo tubes to generate the scanning motion, but most mAFMs use linear piezoelectric actuators because they are «fast, mechanically simple, have a relatively high stiffness and are capable of sub-nn movements» [140].

Another characteristic common to almost all mAFMs is the use of a commercial AFM head, since it has «a cantilever deflection measurement system with sufficient resolution, built-in signal processing electronics, and a user-friendly software» [140].

Fundamental principles of dimensional measurements that mAFMs must undergo are metrology loop, mechanical stability, thermal stability, and minimisation of the Abbe error and cosine error.

The metrology loop is the closed path that connects the measurand within the measuring equipment (Figure 2. 10). Any uncorrected variation in length or position of any part of the metrology loop will affect the measurement result [8].

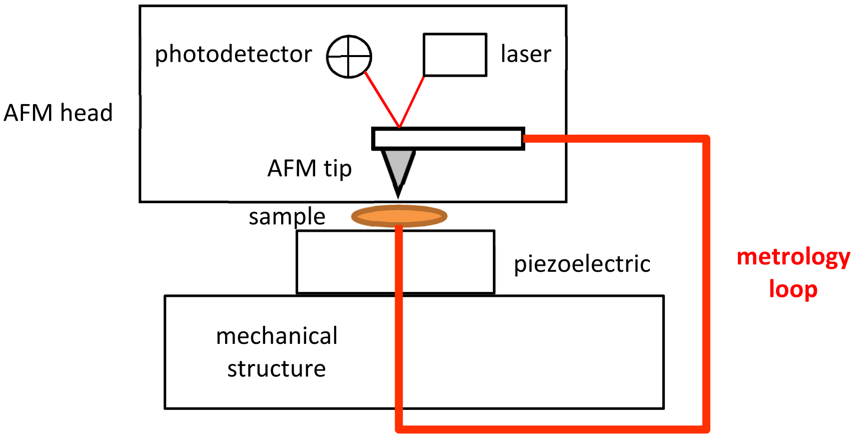

Figure 2. 10 Example of a metrology loop for an AFM.

Mechanical stability is achieved by the presence of kinematic mounting and mechanical stiffness.

The object to be measured must be mechanically stable during the measurement, so the instrumental setup must have kinematic mounting. A stable three-point contact can be done by the Kelvin clamp (cone, vee, flat) or by the Boyes clamp (three balls in three vee with axes aligned to a common centre point) [8].

In terms of designing a measuring system for mechanical stability, the aim should be to achieve a high resonance frequency throughout the whole metrology loop and to place the instrument in a low vibration environment [8].

The majority of components that require dimensional measurements are generally made of metal that change size with temperature unless they have a zero coefficient of thermal expansion (CTE). ISO 1 [141] defines the reference temperature for dimensional metrology to be 20°C, and as a consequence the temperature has to be corrected according to the equation $L_{20} = L_t\big(1 + \alpha(20°\mathrm{C} - t)\big)$, where t is the temperature, L_t is the length measured at the temperature t and α is the CTE of the material [8].

For measuring instruments (which have all metal components), thermal compensation «can be in the form of using compact and thermally compensated instruments (short metrology loops), fast measurements (drift minimisation), low and constant power consumption» [8].

Drift is the gradual uncontrolled movement of the measuring system over time, which affects the positioning of the tip with respect to the sample in the three spatial axes. Short-term thermal drift causes the distortion of the individual image. Long-term thermal drift is the net movement of the probe from the indicated position after the time required to take at least two images [101].

Thermal drift compensations are usually applied post-measurements, but also real-time methodologies are used.

Online correction methods measure drift during the scanning and correct the measurement by adding offset to the scanner displacements. These methods can be performed (i) by using additional sensors, such as an inverted optical microscope [142] or flexible electronics to be connect to AFM [143], or (ii) by the AFM itself, as in the case of the compensation system reported by Yang *et al* [144], in which consecutive images are recorded, and a neural network algorithm estimates and corrects the drift.

Offline methods correct thermal drift in raw datasets after the measurement is finished. Several methods exist, and among them of relevant interest there are (i) correction methods of Z-drifts and (ii) correction of 3D drifts.

Marinello *et al.* [145] correct Z-drift by the alignment of two topographies taken with mutually orthogonal scanning directions, while Meyer *et al.* [146] propose a method that uses self-intersicating scan path to correct thermal drifts along Z axis, and distinguish it from topographic features.

The method proposed by Degenhardt *et al.* [147], which reconstruct and correct non-linear drift in all three dimensions based on data fusion using the point-to-plane iterative closest point algorithm, compared to other 3D drift correction methods has high temporal drift resolution and without data redundancy.

The non-correct alignment and positioning of the sample can lead to respectively and cosine and Abbe errors.

The cosine error can occur when (i) the scale is not parallel to movement (scale cosine error), (ii) the artefact is not parallel to movement artefact (artefact cosine error) and (iii) the artefact is not parallel to the scale (artefact cosine error) [8].

«Abbe error, or parallax error, occurs when the measuring point of interest is separated laterally from the actual measuring scale location (reference line or axis of measurement) and when angular error motions exist in the positioning system. Abbe error causes the measured displacement to appear longer or shorter than the true displacement, depending on the direction of angular motion. The spatial separation between the measured point and reference line is known as the Abbe offset» [148].

As seen in Table 2. 1, there are several types of mAFM, which are (i) X-Y interferometric and Z capacitance controls mAFM, (ii) 3D mAFM, (iii) CD mAFM, (iv) tip-tilting mAFM, (v) LR mAFM, and (vi) HS mAFM. In the following, the peculiar characteristics of several different instrumental configurations are reported. Remember that these considerations are general, since the principle is unambiguous, but each NMI instrument differs from each other.

The first mAFMs built in the late 1980s - early 1990s were M^3 (molecular measuring machine) and c-AFM (calibrated AFM) by NIST.

The M^3 is an ultra-high precision coordinate measuring machine equipped with an AFM tip and a X-Y interferometric motion control. It allows a wide scanning range and atomic scale resolution [105].

The c-AFM (calibrated AFM) is an instrument with a scanning system made by flexure stage piezo transducer and an on-board metrology done by X-Y heterodyne interferometers and Z capacitance sensor controls [105]. With the same principle, KRISS mAFM [110] and also the first INRiM mAFM setup were built [129].

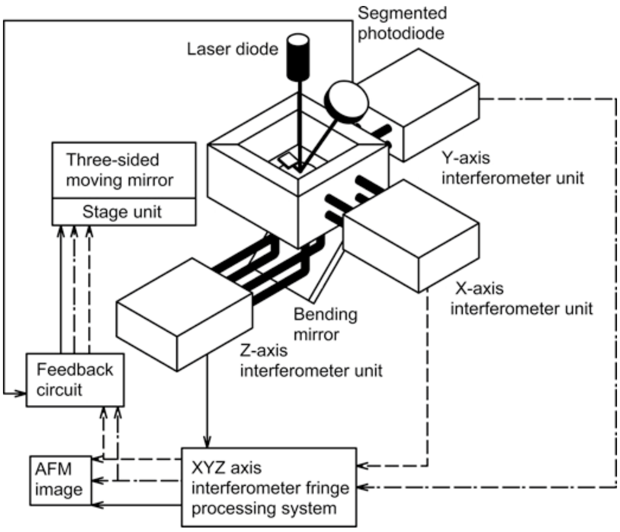

Figure 2. 11 Scheme of the equipment of a 3D mAFM.
Reprinted with permission from [54]. Copyright © 2021 IOP Publishing. All Rights Reserved.

A large number of NMIs built a three-dimensional (3D) mAFM, the peculiarity of which is the tip-sample relative movement is servo-controlled in time by using the signal from the three interferometers along the X, Y, and Z axes (Figure 2. 11). The advantage of this setup is that the movements in all directions are directly traceable to the SI.

Step height is a one-directional measurement which is not affected by the tip shape. On the contrary, line width is a bidirectional measure strongly affected by the tip shape. Critical Dimension (CD) mAFM are developed for measuring lateral sidewalls of line patterns. These instruments use a flared CD probe-tip of known width, and the CD line width is obtained through the subtraction of the effective tip shape to the measured profile [149]. To date, these instruments permit to perform the most accurate measures of line width, as demonstrated by the comparison between PTB and NIST [35].

This technique has the advantage of measuring both the sidewalls in only one measurement, but struggles in the determination of the footing of structures.

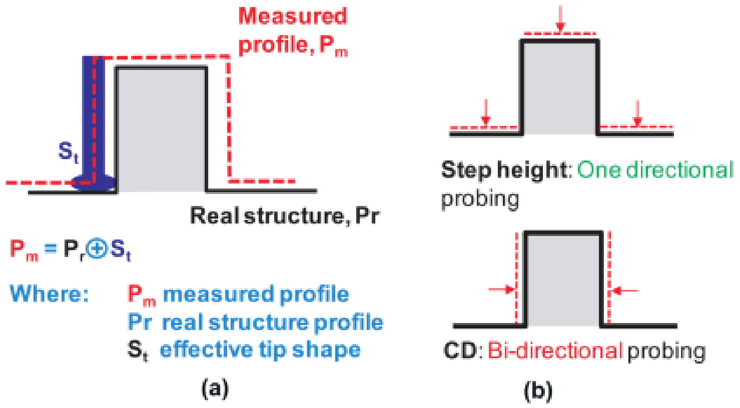

Figure 2. 12 (a) Sketch of the CD mAFM width measurements.
(b) Difference between one-directional and bi-directional measurements.
Reprinted with permission from [35]. Copyright © 2017 IOP Publishing. All Rights Reserved.

Since the radius of the CD tip is larger than that of ordinary tips (typically tens to hundreds of nanometres), tip-tilting mAFM has been developed to measure finer shapes and/or dense patterns. This kind of instrument uses super sharp conical tips that must be tilted along the rotation around the vertical axis; this operation allows the measurement the corner rounding and footing of dense patterns. For measure a step, two sets of measurements on the left and right sidewalls are performed, and the tip or the sample has to be rotated for determining the CD. Consequently, the topographies obtained at different tilting have to be subjected to stitching, which strongly influence the measurement accuracy [126].

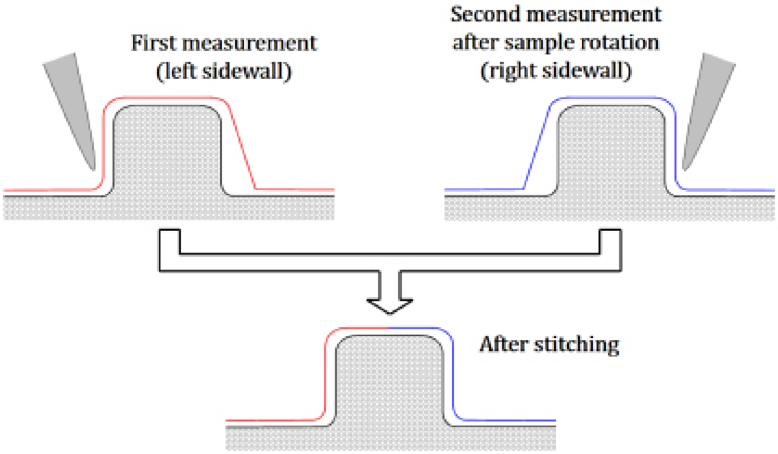

Figure 2. 13 Stitching of the right and left sidewall in tip-tilting mAFM.
Reprinted with permission from [150]. Copyright © 2019 IOP Publishing. All Rights Reserved.

Large range (LR) mAFM are instruments that permit highly accurate dimensional metrology of nanostructures and ultra-precision surfaces.

LR mAFMs couple an AFM with a long-range sample displacement stage [111,132] or a nanopositioning and nanomeasuring machine [128], thus providing both a large motion range and a high dynamic positioning capability with subnanometre resolution. These instruments are capable of high image quality obtainable at a scan speed of 500 µm·s^{-1} with a good repeatability (Figure 2. 14).

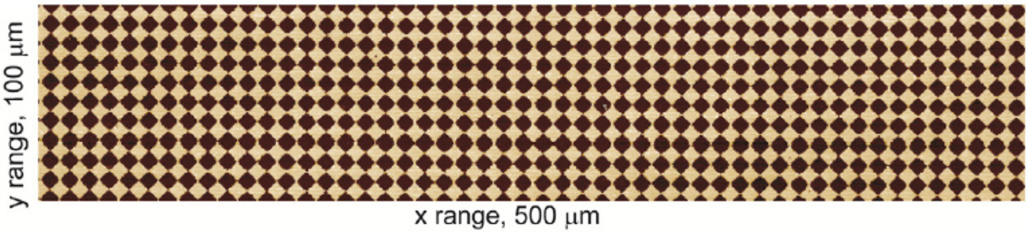

Figure 2. 14 AFM topography measured with LR mAFM at PTB.
Reprinted with permission from [128]. Copyright © 2015 IOP Publishing. All Rights Reserved.

The largest manufacturers in the world developed AFMs with automated metrology in industrial instruments for failure detection in semiconductor applications [138,139]. The new research frontier is the development of traceable High-Speed Scanning Probe Microscopy (HS-SPM) for the application in industrial measurements in semiconductor, nano-optics and bioscience fields [151].

Some effort in this direction saw the development of a traceable high-speed AFM both for short-range video rate images and large-area scans by using optical interferometry [136].

2.3 INRiM mAFM

In my PhD I performed measurements of nanoparticles and nanostructures by using INRiM mAFM. It is a customised instrument with an AFM head placed on a sample-moving mechanical structure. Tip-sample movements while scanning the sample are monitored by interferometers, ensuring a direct traceability to the SI.

The instrumental setup has been developed over the years by Dr. Gian Bartolo Picotto and Dr. Marco Pisani, and it consists of (Figure 2. 15):

1. a commercial AFM head - Veeco “Multimode 5”;
2. a compact stainless steel mechanical structure built in INRiM, which guarantees a metrology loop;
3. a metrological closed-loop interferometric control made in INRiM, which guarantees the traceability of measurements to the SI;
4. an electronic control of interferometric signals made in INRiM;
5. a piezoelectric feedback loop control system by A.P.E. Research [152] for topography measurements only.

The AFM head has a laser diode inside it, whose beam is directed towards the back of the cantilever (in proximity of the tip position) and then reflected onto an internal 4-quadrant photodetector.

The microscope operates with two separate devices for the lateral scanning, given by two micro-nano positioning stages (one for the X axis and the other for the Y axis) with a working range of about (30 x 30) μm.

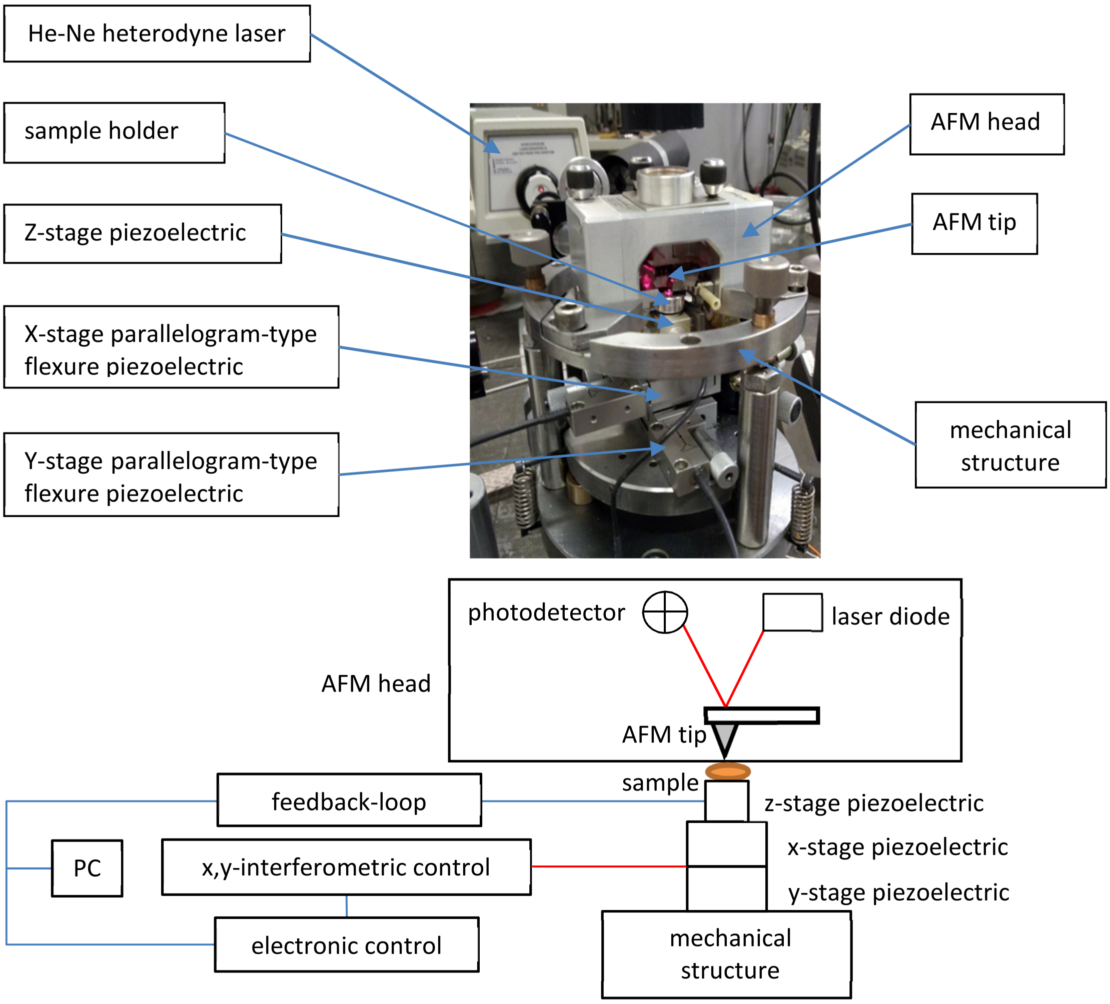

Figure 2. 15 Photo and sketch of INRiM mAFM.
The instrumental setup is made by (i) a commercial AFM head, (ii) a compact stainless steel mechanical structure, (iii) X- and Y- stage parallelogram-type flexure piezoelectric actuators, which movements are controlled by a metrological closed-loop interferometer with a He-Ne heterodyne laser, (iv) an electronic control of X-,Y-interferometric signals, and (iv) a Z-stage piezoelectric, which movement is controlled by a piezoelectric feedback loop.

In a previous configuration, «the Z-stage uses a novel design based on three pairs of capacitive sensors and piezo bimorph plates driving a kinematic sandwich-like assembling of two plates, the upper one supports the sample and can be easily removed and precisely repositioned for sample handling. Capacitive sensors have the double purpose to guarantee a pure parallel movement, namely Z displacements free of pitch and roll tilts, and to deliver a measurement of the displacement itself» [153].

Today, the Z stage is equipped with a piezotranslator with 2 µm working range.

Instrument traceability is achieved through in-situ interferometric calibration of the vertical scanning device (Z-axis) and interferometric measurement (metrological closed loop control) of lateral displacements (X- and Y-axes) during relative tip/sample movement.

The wavelength of the He-Ne heterodyne laser Zeeman modulation type source of the interferometer (633 nm) is calibrated with respect to the MeP sample length laser He-Ne every 5 years.

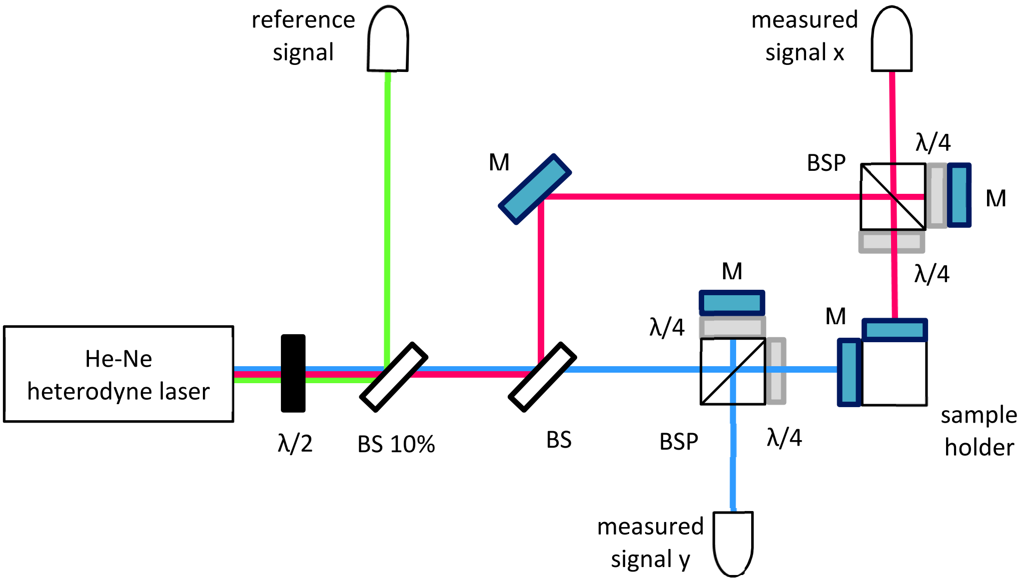

Figure 2. 16 Sketch of the heterodyne Michelson interferometers for the X axis (pink line) and the Y axis (blue line).

In Figure 2. 16 the Michelson-type interferometric system on the X and Y axes is shown.

The laser radiation is reflected in small part by a first beam-splitter (BS), so that it can be used for the heterodyne reference signal phase, while the other beam continues in the initial direction. The optical system is based on a configuration of corner cube/mirrors (M), polarizing beam-splitter (BSP) separators and quarter-wave retarding plates.

The sample movements along the X-, Y-axes are then measured through two phasemeters as the phase difference between the measured signal and the reference signal of the heterodyne interferometer. The signal is processed by an electronic control circuit.

In this circuit (Figure 2. 17), the phase difference measured by the phase-meter is an analogic signal, which is converted and incremented by a 12 bit A/D converter and a 16 bits counter. The bits represent the number of wavelengths that reveal how far the piezoelectric has shifted, and are converted via a D/A converter in an analog signal to be used for a PID closed-loop control.

The output of each phase-meter of the X-, Y-stages is a voltage proportional to the displacement. This signal is compared to the driving signal generated by the A.P.E. Research control unit when scanning the surface to be imaged; the difference between the two is integrated, amplified and sent to the piezo actuator, thus realizing a closed control loop configuration [129].

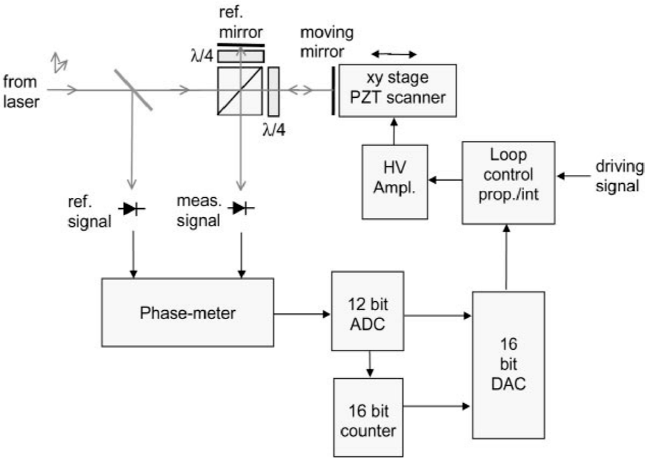

Figure 2. 17 Block diagram of electronic control of INRiM mAFM.
Reprinted with permission from [129]. Copyright © 2001 Elsevier. All Rights Reserved.

A laser can be used to measure an optical path L, given by the product of the physical path l and the index of refraction n. The refractive index n of a material depends on pressure, temperature, humidity, so these environmental parameters variations must be evaluated.

The mAFM is located in INRiM building 8 “impianto Galleria Metrologica”, that houses INRiM’s Length and Mass laboratories. The air-conditioning system was developed in 1970 [154], and its special feature is that the underground building is less impacted by environmental vibrations from city traffic, and that the temperature and humidity can be set at T = (20.0 ± 0.1) °C and RH ~ (50 ± 15) % respectively, according to ISO 1 [141].

The temperature is measured with a digital thermometer with a measurement uncertainty of at least 0.05 °C, while pressure and humidity are evaluated with an uncertainty of 20 Pa for pressure and 20% for relative humidity.

Instrumental improvements are ongoing, in fact we are developing a new Z interferometer setup, in order to build up a 3D mAFM.

In addition, we are going to put in operation a new AFM head, which is able to perform the Kelvin probe force microscopy (KPFM), electrical force microscopy mode (EFM), and piezoresponsive force microscopy (PFM) hyphenated techniques. The goal is to develop a "multipurpose 3D mAFM", which links functional measurements to dimensional measurements directly traceable to the SI.

2.4 Critical Aspects in AFM-Based Measurements of NPs

The previous Sections present the operating principle of the AFM, together with the different instrumental configurations to make AFM measurements directly traceable to the SI. This Section leads us towards the experimental work done, describing the critical aspects related to the measurement of an AFM topography, specifically those related to the dimensional quantification of NPs and nanostructures.

Surface topographies are achieved by scanning a surface in a bustrophedic way using a probe. The tip movement is described by two main directions, namely, the "fast scan direction" X and the "slow scan direction" Y. Each profile is normally scanned twice: once forward, referred to "scan" or "trace", and once backward, indicated as "back-scan" or "retrace" [101].

An AFM image is commonly referred to as a 3D representation, although it is more correct referred to as a 2.5D reconstruction. The topography is a mapping of the heights given by a 2D array of numbers, which corresponds to the deflection of the cantilever as the tip scans the sample surface. Therefore, a 3D reconstruction is identified, albeit limited by the tip geometry, which is not complete but is limited only to the exposed surface, and it does not consider the portion of the sample in contact with the substrate [3].

Table 2. 2 Main distortions and relative sources in AFM images.
Table based on [101]. Adapted with permission. Copyright © 2007 University of Padova. All Rights Reserved.

Source	Distortion
scanning system	• non-linearity • hysteresis • ageing • creep • bow
metrology loop	• noise • vibration
probing system	• drifts • overshoots • unsampled parts • height shifts • tip artefacts • convolution • tip geometry • tip-sample interaction
image processing	• filtering • levelling

In order to make quantitative dimensional measurements, as the first thing to consider there is that a good AFM image must be registered. Unfortunately, several sources of error mainly due to the instrument (classified in Table 2. 2) can lead to distortions and artifacts in images. Moreover, Table 2. 3 reports other sources that directly impact AFM dimensional reconstruction of shape, size and roughness of nanostructures.

In the following a brief explanation of each point of these two tables is reported.

Since the scanning systems are based on piezoelectric, the distortions that the images may have are due to issues related to it.

As seen before, for open-loop instruments based on tube or stack piezo-actuators the measured position does not correspond to the effective tip position. This leads to a distortion that is generally proportional to the scanning range, because the positioning accuracy is significantly reduced due to non-linear hysteresis effects. The linear model is applicable to closed-loop scanners, usually controlled by capacitance sensors whose non linearity is about 0.01% [101].

The sensitivity of a piezoelectric is defined by the ratio of the movement to the voltage applied to the piezoelectric. Piezo scanners have higher sensitivity at the end of the scanning range, implying that there is hysteresis between the two scanning directions [101].

In addition, piezoelectric materials suffer from ageing, as their sensitivity decreases exponentially with time [101].

Creep is the drift of the piezoactuator after the application of an offset voltage, due to a non-immediate response. Creep appears as the stretching of image features in the offset direction [101].

Bow is a non-linear image artifact, which appears as a false curvature superposed on the real sample topography. Bow is due to the fact that the lateral bending of the piezo-tube is not horizontal but follows a trajectory with a radius of curvature of the order of a few tens of millimetres, and its influence is not negligible when measurements are made in large scanning fields [101].

The metrology loop has to minimize errors due to noise and vibration. They are stochastic effects that can be due to environmental changes of temperature and pressure, or to electrical, acoustical, mechanical changes that impact the instrumental setup.

The probing system is one of the main error sources in AFM images. The probing system can lead to several distorsions; among them, there are thermal drifts, described in Section 2.2.

Poor hysteresis and creep compensation in the Z direction can cause edge overshoot. This appears as an over-extension of a step in the proximity of the edge, and a reduction of this distortion can be obtained by adjusting the gain of the feedback loop. Excessive gains bring instability, with appearent overlapping vibrations, whereas low gains cause the image to be smoothed [101].

The height shifts distortions can be considered as stochastic jumps due to repulsive to attractive interactions. When a jump occurs during imaging, the feedback loop responds by retracting the tip from the sample for increasing the suddenly decreased amplitude to the set-point level. This results in an upward shift in the height level, *i.e.* the structures seem buried [101].

The pick-up of dust or tip fractures may further alter the alignment of the profiles.

The effects due to convolution, tip geometry, and tip-sample interaction in AFM measurements will be investigated in Chapter 3.

The AFM image is the result of the dilation of the sample and probe shapes and tip–sample–substrate interactions. In AFM measurements, height is obtained with sub-nanometer accuracy and very high resolution, while the lateral resolution is influenced by the tip shape and size, so it is very important to characterize it (see Chapter 3).

The critical aspects in image pre-processing include the leveling of the image because a tilt that is not actually present on the sample surface is found, but it depends on sample mounting, since the plane which contains the sample surface is not perfectly parallel to the scan plane on which the AFM tip moves. Linear plane fit corrections can be applied to remove any artifacts of consequence [3].

Image filtering is a tool that permits to detect and eliminate outliers, unwanted features or artifacts by using statistical, Gaussian, or Fourier filters. Elimination of AFM image distortions can be done by using off-line correction methods implemented in commercial software packages (e.g. [155]), or by applying algorithms (e.g. [156,157]).

Table 2. 3 Critical aspects in the dimensional analysis of NPs with AFM

Source	critical aspects
sample preparation	• substrate • protocols
instrumental parameters	• on-board metrology • scan size, pixel size and speed • cantilever oscillation amplitude set point • PID feedback parameters
image distorsions	• see Table 2. 2
dimensional measurements	• sizes reconstruction and distribution • morphological parameters

Table 2. 3 reports the critical aspects that influence the dimensional measurements of nanostructures with AFM.

NPs to be analyzed with AFM must be prepared onto an ultraflat substrate, which has subnanometric roughness. Three materials are ideal candidates, and are SiC wafer, HOPG, and mica.

The SiC wafer has a roughness of about 0.13 nm, but it is a large sample and it is too expensive for daily use analysis [158].

HOPG (Highly Ordered Pyrolytic Graphite) is a form of synthetic graphite consisting of layered monocrystal grains from 1 μm to 10 μm slightly disoriented with respect to each other. The best HOPG samples have a mosaic spread angle value of less than 1° [159].

HOPG is an excellent substrate for STM measurements or calibration standards at atomic resolution levels, since single steps have the well-defined height of 0.34 nm [160]. It is an inert and hydrophobic substrate used for studying the growth of metal NPs [161] or Fe/Au/Pt NPs by electrochemical deposition [162].

Muscovite mica is a commonly used substrate because it is atomically flat, with a layer height of (0.37 ± 0.02) nm [163]. It is also easily cleaned by removing the top layer using an adhesive tape, making sample preparation easy because its crystal structure consists of silica tetrahedral sheets weakly bonded to one another.

Muscovite is negatively charged, and it is therefore quite hydrophilic. In addition, based on the sample to be analyzed, mica can be used as it is or functionalized with 3-aminopropyltriethoxysilane (APTES) or poly-L-lysine to change the surface charge.

Different protocols can be used in the preparation of NP samples. Based on the intrinsic nature of the nanostructure (interparticle and particle–solvent interactions), different deposition techniques (*e.g.*, drop evaporation, spin coating, and dip coating) are used. Moreover, characterization must be considered. Based on the type of analysis (*i.e.*, top-height or lateral pitch), different concentrations of suspensions can be prepared (respectively diluted or concentrated) [3].

In this dissertation, NPs are deposited onto freshly- cleaved mica substrates from diluted suspensions. Mica is commercially found as disk-shaped and/or square supports. One face of the disk/square is glued with a cyanoacrylate-based quick glue to a nickel-plated steel diskette. In this way, the specimen can be fixed on the magnetically sealed sample holder of the INRiM mAFM.

The setting of instrumental parameters is crucial to record a good AFM topography for quantitative measures.

Intrinsic errors due to on-board metrology are cosine error, deviation from the reference plane (straightness), and calibration of displacement sensors. Recall that normally calibration is used for quantifying and correcting systematic deviations of the measuring instrument [101].

Based on the requested relative height accuracy and radius of the tip used, the number of pixels in the image should be adjusted. Moreover, the operator must optimize the scan speed based on the scan size, and measurements must be performed using the right cantilever oscillation amplitude set point in non-contact mode and PID (proportional–integral–derivative) feedback parameters [3].

Finally, in order to reconstruct critical sizes, size distribution and morphological parameters of NPs and candidate reference material nanostructures in a quantitative way, robust and traceable procedures must be developed (see Chapter 4 and the Annexes).

The distortions and critical aspects described in Table 2. 2 and Table 2. 3 contribute to the uncertainty of AFM measurements. Quantitative measurements do not have a numerical value in their own right, but this value is provided within a measurement range. A first approach is to report the standard deviation, which gives the repeatability of the measurement; however, for truly quantitative measurements, it is necessary to report uncertainty budgets, which identify and quantify the various sources of error. A measurement without uncertainty cannot be compared either with other measurements or with reference values or legal limits.

In Chapters 3 and 4 several uncertainty budgets for the nanostructure and nanoparticles measurands are reported. The intent is to estimate the different sources of error for obtaining a more reliable and consistent result, that also considers any systematic errors and the uncertainty associated with their corrections.

Uncertainty evaluation depends on the measurand in consideration. For each measurand Y in the analysis that is influenced by X terms, a model for the estimated quantity $y = f(x)$ is reported, which takes into account all the contributions x that affect the estimated quantity y.

Each uncertainty budget, according to the GUM reference guide [164], reports:

(i) the quantity x_i, which is the source of uncertainty that contributes to the uncertainty of the estimated quantity y;

(ii) the type of uncertainty, which can be experimentally evaluated through a statistical analysis on a series of observations (A-type), or based on previous measures, certificate values or on theoretical assumptions of statistics that characterize a measurement process (B-type);

(iii) the probability density function (PDF), which is the mathematical function describing a continuous quantity, whose integral over an interval gives the probability that the value of the variable lies within that interval. There are different PDFs, which can be normal (indicated with N), which is present when the source of uncertainty has a Gaussian distribution, or rectangular (indicated with R), if the source of uncertainty has the same probability of being contained within an interval;

(iv) the standard uncertainty $u(x_i)$, equal to the square root of the variance, which gives the uncertainty of the measurand expressed as a standard deviation. To convert the uncertainty values into standard uncertainties $u(x_i)$, it must be used the 'divisor' appropriate to the PDF, which is 1 for N distribution and $\sqrt{3}$ for R distribution;

(v) the sensitivity coefficient $c_i = {}^{\partial f}/_{\partial x_i}$, that describes the extent to which the source of uncertainty influences the overall uncertainty;

(vi) the uncertainty contribution to the estimated quantity $u_i(y)$, which gives the final contribution from a given source of uncertainty to the overall uncertainty;

(vii) the degrees of freedom ν_i, which give information about the reliability of the uncertainty value. In all budgets reported in this thesis, the degrees of freedom for A-type uncertainty depend on the observations, while for the B-type ν_i is set equal to 100 if is available in calibration certificates or equal to 50 if it derives from previous knowledge or published reports;

(viii) the combined standard uncertainty $u_c(y)$, that is the overall uncertainty of the estimated quantity y calculated by combining the individual values $u_i(y)$ according to the law of propagation of uncertainty;

(ix) the expanded uncertainty U, obtained by multiplying the combined standard uncertainty $u_c(y)$ with the coverage factor k, chosen on the basis of the desired level of confidence to be associated with the interval

In the budgets, all contributions x_i are assumed to be not correlated each other, and δ terms are the so called zero statistical mean errors (errors due to random effects).

Chapter 3. Biological Samples as Tip Characterizer

The next two Chapters report the experimentally work done at INRiM Dimensional Nanometrology laboratory.

Both Chapters are divided into an introductory part explaining the state of the art, followed by the explanation of the work performed.

Part of the study described in this Chapter was previously published in [1,3]. Before dealing with the study of TMV samples as tip characterizers, there is an introductory part describing the different AFM probes, the various models used for characterizing the tip shape and size, and the literature models describing the tip-sample interaction.

3.1 AFM Probe Description

According to the definition of the Encyclopedia of Nanotechnology, «AFM probes are transducers that convert the interaction force with a sample surface into a deformation or a change of the vibrational state of the probe. (…)

A typical AFM probe consists of a sharp tip, which determines the lateral resolution, and a microcantilever, which plays the role of a force transducer and provides the force sensitivity. In this case, the interaction force between the tip and sample deflects the cantilever. (…) Assuming that the deflection and the spring constant of the cantilever are Δz and k, respectively, the interaction force F is given by $F = k\Delta z$» [165].

Proper selection of a probe is important to obtain good quality sample surface images. There are several types of probes with different cantilever and tip characteristics, which depends on the type of analysis, on the sample nature and on the SPM technique.

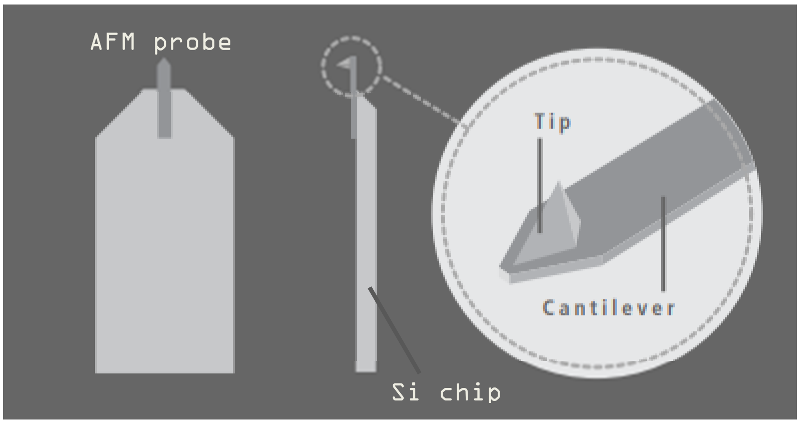

Figure 3. 1 AFM probe elements: a silicon chip, a cantilever hanging from the chip, and a tip attaching at the cantilever extremity.
Adapted with permission from [166]. Copyright © Park Systems. All Right Reserved.

As seen in Section 2.1.1, the probe composition differs depending on the type of SPM measurement, but for the family of AFM measurements the probes are usually made of Si or Si_3N_4.

The cantilever deflection can be detected by optical systems, which is the most widely used conventional configuration usually given by the reflection of a laser beam, or by self-sensing and self-actuating cantilevers, such as quartz cantilevers, piezoresistive cantilevers, piezoelectric cantilevers, capacitive cantilevers. These last type of probes offer the possibility of use more compact systems or AFM in SEM setup [167], but the achievable resolution is lower than laser detection system [168].

The cantilevers are mounted onto a metallic holder chip of about (1.6 x 3.4) mm, and it is possible to have one-, two-, three-, or four-lever configurations [169].

The cantilevers can have different geometries, usually rectangular or triangular. Their length can vary in the range of (20 – 400) µm, the width from 1 µm to 120 µm, and the thickness of about (0.2 – 7) µm [170]. The shape and size of cantilevers relates to performance; it must be borne in mind that probes have to deal with a sensitivity on the scale of atoms and forces commensurate with atomic bonds. Short cantilevers have better deflection sensitivity of the laser spot and lower hydrodynamic drag in liquid [171].

For enhancing the reflectivity of the laser spot in the detection of the cantilever deflection, the cantilevers can have a backside coating of few nm of Al or Au. Furthermore, depending on the different kinds of measurements, they can have tipside coating of gold (bio-compatible), platinum (electric measurements), platinum/iridium (electric measurements), cobalt alloy (magnetic measurements), silicon nitrite (biocompatible), diamond (nanoindentation) [170].

The important characteristics of cantilevers are [171]:

- spring constant k (N·m^{-1}), that relates to imaging force as seen in the Encyclopedia of Nanotechnology definition;
- resonant frequency f_{res} (kHz), that indicates the speed to reach equilibrium oscillation, tipicaly ranging from 100 kHz up to 10MHz in measurements performed in air;
- quality factor Q, that indicates the number of cycles to reach cantilever equilibrium;
- cantilever bandwidth $BW \propto \frac{f_{res}}{Q}$, that determines the imaging speed for the amplitude modulation mode.

The spring constant is directly proportional to the third power of the thickness and inversely proportional to the third power of the length of the cantilever, so to maintain low tip sample forces AFM cantilevers must be short and thin [171].

According to the type of measurements to be done, different characteristics must be chosen [171]:

- contact mode: low spring constant (< 1 N·m^{-1}) and low resonance frequency (< 200 kHz);
- non-contact mode: high spring constant (> 1 N·m^{-1}) and high resonance frequency (> 200 kHz).

Generally, soft sample must be analyzed by using soft cantilevers (spring constant of about 0.1 N·m^{-1} to 5 N·m^{-1}), while for hard sample must be used hard cantilevers (spring constant of about 1 N·m^{-1} to 100 N·m^{-1}).

The elastic spring constant k can be determined in several ways:

1. Theoretical methods, that involves the use of expressions that require accurate knowledge of the cantilever properties and dimensions:

  - Euler beam equation: $k = \frac{Et^3w}{4L^3}$, where E is the elastic modulus, t the thickness, w the width and L the length of a rectangular cantilever [172];
  - Cleveland formula: $k = 2\pi^3 wL^3 \left(\frac{\rho_{lever}^3}{E}\right)^{\frac{1}{2}} \nu^3$, where ρ_{lever} is the density and ν is the resonant frequency [172];
  - Sader hydrodynamic method: $k = 0.19Lw^2\rho_f Q_f \Gamma_i (2\pi\nu_f)^2$, where ν_f and Q_f are the resonant frequency and the quality factor in air, and Γ_i is the imaginary part of the hydrodynamic function. This last parameter defines a universal dimensionless function for describing cantilevers with different geometries [173];
  - thermal noise method: $k = \frac{k_B T}{\chi^2}$, where k_B is the Boltzmann constant, T is the absolute temperature, $\chi^2$is the thermal noise [174].

2. Static methods, in which a trial cantilever is pressed against a reference one [175, 176];
3. Dynamic methods, which require knowledge of the cantilever resonance behavior [177];
4. Global Calibration Initiative (GCI) tool: $k = AQf_R^{1.3}$, where the A-coefficient is universal for a particular cantilever geometry and given by $A = \frac{1}{N}\sum_{i=1}^{N} A_i = \frac{1}{N}\sum_{i=1}^{N} \frac{k_{ref,i}}{Q_{ref,i}\, f_{R\,ref,i}^{1.3}}$ where N is the total number of independent measurements on different reference cantilevers, and $f_{R\,ref,i}^{1.3}$ is the resonant frequency of a reference cantilever. This equation combines Sader and thermal methods for describing in a universal way cantilevers with different geometries.

   The GCI allows damage-free cantilever calibration through direct comparison of calibration results between AFM users worldwide [178].

The tips can have different shapes, such as 3- or 4- sided pyramidal, super sharp, carbon nanotube (CNT) tips, rounded, colloidal or flared, as we have seen in Section 2.2 for CD measurements [170]. The height they can have is about 20 µm, with cone angle in the range of 20°-40° and radius from 5 nm to 50 nm.

Tip shape and dimensions determine lateral resolution, in particular the tip radius influence the measurements of sample features, while the cone angle influence the measurement of steep edges. «Sharper tips with small half-angle provide high-resolution for single molecule imaging. Blunter tips with larger half angle provide low pressure needed for live cell imaging» [171].

To summarize, «the measurement of the lateral distance between two points on a surface is limited by the measurement capability of the laser interferometer, any Abbe offsets, noise, stray light effects of the detection system used, and by the tip shape and tip stability. The last point also includes the effects of the interaction of the SFM tip with the sample» [168].

Tip shape changes over time because of physical effects and dynamical interactions, and the deterioration is due to wear phenomenon [101]. This can influence the step-height value up to 1% [168]. Since tip sharpness is not constant, errors in the order of few nm can occur if the probe profile is not frequently controlled.

The methods developed in this thesis for critical sizes determination reconstruct the tip shape for each individual image, minimizing these errors.

3.2 Elastoplastic Interactions between Tip-Sample-Substrate

Contact mechanics is the branch of mechanical engineering that studies the deformation of solids that touch each other at one or more points [179].

The elastoplastic interactions acting between the tip and the sample, the sample and the substrate and the tip and the substrate regard stresses acting perpendicular to the surfaces of the bodies in contact.

It should be noted that there are different forces that play at different distances [180]:

- electrostatic interactions dominate at large tip-sample separations;
- Van der Waals forces dominate at tip-sample distances of the order of several nanometers (tip out of contact);
- elastic interactions dominate when the tip and the sample are in contact.

In the middle range between these two last scenarios, it is not possible to determine the interaction force between the entire probe and the sample because both attractive and repulsive interactions simultaneously act between some probe-sample molecule pairs. Moreover, in this region from the short-range molecular forces arises the adhesion. «Adhesion is a nonconservative process. Forces acting during the cantilever-to-sample approach differ from the forces during the probe retraction. Such an operation requires some work to be done which is called the work of adhesion» [181]. According to the Duprè's expression, the reversible thermodynamic work that is needed to separate the interface from the equilibrium state of two phases to a separation distance of infinity for a liquid–solid combination is $w_a = \gamma_{\mathrm{L}} + \gamma_{\mathrm{S}} - \gamma_{\mathrm{SL}}$, where γ_{L} is the surface energy of the liquid phase, γ_{S} is the surface energy of the solid phase, γ_{SL} is the interfacial surface tension [182]; for two contacting liquids, the work of adhesion is $w_a = \gamma_1 + \gamma_2 - \gamma_{12}$, where γ_1, γ_2, and γ_{12} are the surface tensions of the liquids and the interfacial tension at the interface between the liquids, respectively [183]. When two solids are in contact, as the case of NP-substrate interaction, the work of adhesion is calculated as $w_a = 2 \cdot \sqrt{\gamma_{\mathrm{P}} \cdot \gamma_{\mathrm{S}}}$, where γ_{P} is the surface energy of the particle and γ_{S} is the surface energy of the substrate [184].

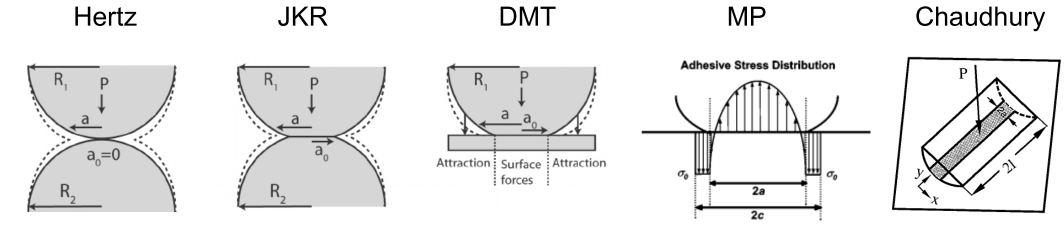

Figure 3. 2 Interaction models between two bodies in contact. The cross-sectional illustrations report the different radiuses of the circle of contact *a* that arise from the Hertz, JKR (Johnson, Kendall, Roberts), DMT (Derjaguin, Muller, Toporov), MP (Maugis, Pollock), and Chaudhury models.

In the Figures reporting Hertz, JKR, and DMT models, R_1 and R_2 indicates the radiuses of the spherical bodied in contact, P indicates the external force exerted on the particle, a_0 is the contact radius at zero load, a is the contact radius after P is applied, the continuous lines refer to the situation before P is applied, dotted lines describe the particles deformation after P is applied.

In MP Figure, 2a refers to the contact area (which is the seat of an adhesive stress distribution), while 2c is the process zone that takes into account a theoretical adhesive stress value σ_0 over a ring shaped zone outside the contact area.

In the Chaudhury Figure, P indicates the external force exerted in the Z direction on the cylinder parallel to a flat substrate, and the contact zone is a grey strip lying parallel to the Y axis with length 2l and width 2a.

Figures reprinted with permission from [185], [186] and [187].

Several types of models have been developed studying the interactions between objects in contact to each other. In Figure 3. 2 are reported the main models.

The first model was developed by Hertz in 1896, and its theory considers a purely repulsive elastic interaction without considering adhesion and/or surface forces [188].

Hertz contact relates to the stress near the contact area between two spheres of different radius (Figure 3. 2), and the radius of the circle of contact is $a_{Hertz} = \sqrt[3]{\frac{F \cdot R^*}{K}}$, where F is the indenter load, R^* is the equivalent radius given by $R^* = \frac{R_1 \cdot R_2}{R_1 + R_2}$ and $K = \frac{4}{3} \cdot \left[\frac{1-\nu_1^2}{E_1} + \frac{1-\nu_2^2}{E_2}\right]^{-1}$ is the reduced (or effective) elastic modulus, that include into the elasticity modulus the deformation between the material 1 and the material 2 (1 and 2 can be two spheres or a sphere and a plane) [189].

In Hertz model, the deformation is elastic and adhesion is not considered. Without F no deformation can occur, so this theory is not directly applicable to the particle adhesion problems, but it is incorporated in other theories [190].

Johnson, Kendall, and Roberts found a similar solution for the case of adhesive contact. JKR theory of adhesive contact balances stored elastic energy and surface energy loss, considering both compressive and adhesive tractions only within the area of contact. The contact area for the JKR model is greater than the Hertian area [190].

The radius of contact at zero external force is $a_{JKR} = \sqrt[3]{\frac{6 \cdot \pi \cdot w_a \cdot R^2}{K}}$, where w_a is the work of adhesion, R is the radius of the sphere, and K is the reduced elastic modulus [191].

This theory was rejected by Derjaguin, Muller and Toporov, which develop the DMT model. In this model, the contact area is the same as in the Hertzian model; inside the area, only repulsive forces are considered, while outside attractive Van der Waals interactions are taken into account.

The radius of contact between a sphere and a plane is $a_{DMT} = \sqrt[3]{\frac{2 \cdot \pi \cdot w_a \cdot R^2}{K}}$, where w_a is the work of adhesion, R is the radius of the sphere, and K is the reduced elastic modulus [192].

Maugis and Pollock (hereafter called MP) generalized the JKR model for including plastic deformations [193]. This model assumes the contact profile of pressure Hertian, but with the radius of curvature changed due to plastic deformation [190].

The radius of contact is $a_{MP} = \sqrt{\frac{2 \cdot w_a \cdot R}{3 \cdot Y}}$, where w_a is the work of adhesion, R is the radius of the sphere, and Y is the yield strenght of the material [194].

Chaudhury model describes the adhesive deformation by contact of parallel cylinders or a cylinder parallel to a flat plate. The radius of contact $is\ a_{Chaud} = \sqrt[3]{\frac{128 \cdot w_a \cdot R^2}{3 \cdot \pi \cdot K}}$, where w_a is the work of adhesion, R is the radius of the sphere, and K is the reduced elastic modulus [187].

These interactions are strictly related to the geometry of the bodies. As it will be reported in Section 3.4.1 and 4.4, in the tip-sample-substrate calculations the tip is considered as a sphere, the nanoparticles are considered as spheres or cylinders, while the substrate is considered as a flat surface. For Hertian elastic contact between different geometries, the formulas from Puttock and Thwaite [195] are considered.

3.3 Tip Characterizers

We have seen that AFM technique provides high-resolution height values with sub-nanometric accuracy. The uncertainties for step height and pitch measurements are now in the nanometre and picometre range respectively. In both cases the measurements are independent of the tip shape as long as the structure is not too small and the tip is stable [168].

The lateral resolution, instead, is influenced by several factors (as seen in Section 3.1); the most impacting are pixel size and tip shape. Pixelization affects resolution because it cannot resolve features smaller than the pixel size of the image [3]. The tip shape has a great impact on the measured profiles of line width (critical dimension CD), NPs shape, and surface roughness. «To estimate the true shape, width and profile of a surface it is necessary to know the tip shape or, more correctly, the effect of the tip shape on the image» [168]. For this reason, several methodologies have been proposed to construct the morphology of the probe tip, that can be divided into *ex situ* and *in situ*.

Ex situ methods do not use AFM for the tip shape reconstruction but use electron microscopes. Some studies show that accurate 3D morphology of the tip is difficult to obtain because of the (i) different experimental conditions and probe–sample dilation effects [196], and (ii) EM techniques that give only a 2D projection shape [197].

In situ tip shape reconstruction is better because of the same experimental conditions used for performing measurements. These methods extract the tip shape by using three different approaches, that are (i) mathematical procedures, (ii) blind reconstruction (BR) algorithms, and (iii) the use of a known tip characterizer [168].

Mathematical techniques that determine the tip shape can be divided into (i) slope-matching techniques and (ii) envelope reconstruction [168].

Slope-matching techniques assume that the slopes of the tip and the sample at the point of contact are identical. This can be described mathematically by the Legendre transform, where the Legendre transform of a function $f\ (x)$ is defined as the intercept on the y axis of the line tangent to $f\ (x)$ at point x, $L[f\ (x)]\ \equiv\ b(m)\ =\ f\ (x(m))\ -\ mx(m)$, where $x = x(m)$ is expressed as a function of the slope m. It is worth noting that the Legendre transform of the sample surface is the sum ofof the Legendre transforms of the image surface and the tip surface $L[s(x)]\ =\ L[i(x')]\ +\ L[t\ (\Delta x)]$ [198]. The limitations of this method are (i) the sensitivity of the Legendre transform to image signal noise, and (ii) the impossibility of reconstruct the tip shape in areas where the tip cannot reach all surface points or is contacting two points at once [168].

To overcome the drawback due to the noise, an alternative technique called envelope reconstruction was developed; this methodology exploits the mathematical morphology, that use the language of the set theory [168]. The two main operations of mathematical morphology are dilation and erosion. AFM images refer to the tip and the sample dilation $I_s\ =\ S\ \oplus\ P$, where I_s is the image of the sample characterizer, S is the actual surface topography of the characterizer, P is the tip shape and it is the reflected form of the tip ($P = -T$), and $\oplus$ denotes the mathematical operation of the dilation. It has to be borne in mind that AFM topographies are frequently defined as tip and sample convolution, but this term is not strictly correct since it represents a linear mathematic process, while dilation is a non-linear process because the image is created by the physical interaction between tip and sample [168].

The erosion operation, expressed as $\ominus$, is used to (i) reconstruct the surface S_r given a measured image I and an estimate for the tip shape P, $S_r = I \ominus P$, or for (ii) reconstruct the tip shape P_r if the sample geometry S is known, $P_r = I \ominus S$. However, note that «erosion is not the exact inverse of dilation, since there are points on the tip that may not come into contact with the sample and points of the sample that may not come into contact with the tip» [168].

Blind reconstruction (BR) algorithms are able to obtain information of the tip shape even if the sample shape and topography are unknown. This method is based on the concept that all points in a surface image can be considered as an image of the tip enlarged by the sample surface. Because the topography of the sample is unknown, the method cannot estimate the actual shape of the tip, only that of the bluntest tip that might have been used to record the image. Three inputs are requested for the operation of blind reconstruction, that are (i) the AFM image, (ii) an initial upper bound for the tip shape (usually a "square pillar" with a flat top is used), and (iii) a threshold value for the noise on the scan signal [168].

These algorithms were first proposed by a few groups working independently (Villarrubia [199], Williams [200]), and then have been studied and improved over the years. In 1994 Villarrubia et al. developed a methodology for accelerating the evaluation of the blind tip algorithm by relying on neighborhood information of feature points. Afterwards, Dongmo et al. [201] completed the tip modeling by verifying BR efficiency. Later, Todd et al. [202] studied the noise of BR algorithm and suggested a method to eliminate it. Then, Abdelhady et al [203] used BR algorithm for estimating the tip shape by adopting gold NPs and analyzed tip influence on biomolecules images. Subsequently, Tranchida et al. [204] examined the effect of image noise and sampling resolution on tip shaping and proposed a proper parameter setting. In 2014, Flater et al. [205] studied a robust methodology for choosing the threshold parameter in order to obtain an optimal reconstruction of the tip shape once the image is provided.

«BR algorithms reconstruct a deconvoluted image to identify the deepest penetration of the tip, but if the tip geometry is not appropriate or the sample does not contain sharp features, then errors may occur during the reconstruction of tip and sample geometries [206]» [3]. Moreover, the main drawbacks of BR algorithms are the large amount of calculation, low efficiency and sensitivity to noise [207].

In addressing these issues, another *in situ* method is the tip morphology calibration through the scan of a known tip characterizer. [208]. This methodology is based on reconstructing the tip shape from experimentally measured data, so exact *a priori* knowledge of the geometric shape of the characterizer is required. These tip characterizers consist of elements with lower or comparable sharpness to AFM tips. When the tip is scanned on the sample, the reverse image of the tip is obtained.

The key feature of this method is the use of sample containing delta-like or well-known structures. Based on inverse imaging, several attempts have been made to determine the shape of the tip by using samples containing small holes, tip-like structures, calibration patterns, random structure with sharp features (e.g. 'TipCheck'), dense and sharp needles (e.g. 'Nioprobe'). These characterizers can determine either the tip radius or the opening angle or both [168].

Sharply pointed features are commercially available, but these characterizers lack traceability, which can lead to damage of tips [209]. Over the years, several new physical artifacts for tip characterization have been presented, including nanospheres [210] and cylindrical nanostructures [211,1].

3.4 Bio-sample as Tip Characterizer

To overcome the issue of tip damaging by using samples containing metallic sharp structures, soft samples are to be used as tip characterizers. The power in use Tobacco Mosaic Virus for this purpouse is that is nanostructure available worldwide in nature, it has a simple geometry, and a stable measurand.

Novelties reported in this work are the metrological characterisation of TMV measurand diameter, the quantitative investigation of tip-sample-substrate (Si-TMV-mica) deformations, and the calibration of several commercial tips.

As is usual practice in INRiM Nanometrology laboratory, no high-resolution tips are used, but standard tips are used to perform such demanding measurements. The tips used in this thesis are commercial n-type silicon tips by μMasch [169], having a rectangular support chip with a rectangular cantilever, which has a nominal resonance frequency of 325 kHz (frequency range (265 – 410) kHz) and a nominal force constant of 50 $N{\cdot}m^{-1}$ (force constant range (20 – 80) $N{\cdot}m^{-1}$). The nominal cantilever geometrical characteristics are a length of (125 ± 5) μm, a width of (35 ± 3) μm, a thickness of (4.0 ± 0.5) μm and a cone angle of 40°. The tip attached to the cantilever apex has a height of (20 – 25) μm with a nominal radius of 8 nm.

All measurements are performed in non-contact mode with amplitude modulation, so as not to ruin and pollute the tip. 120 mAFM images from (300 × 300) nm to (500 × 500) nm with resolution (512 × 512) pixels centred on isolated viral nanostructures are measured.

3.4.1 Tobacco Mosaic Virus and its Characterization with mAFM

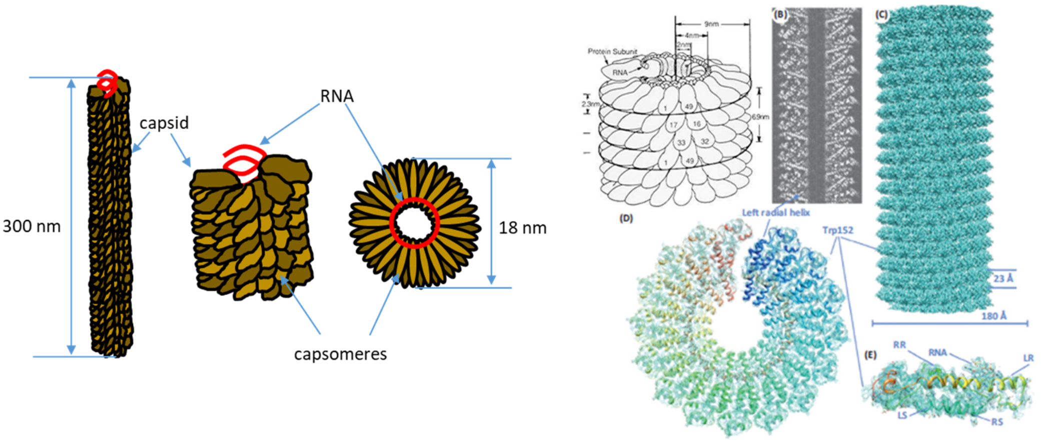

Figure 3. 3 Sketch and helical structure of the Tobacco Mosaic Virus.
Reprinted with permission from [212] and [213].
Copyright © 1996 The University of Texas Medical Branch at Galveston. All Rights Reserved.
Copyright © 2013 Elsevier. All Rights Reserved.

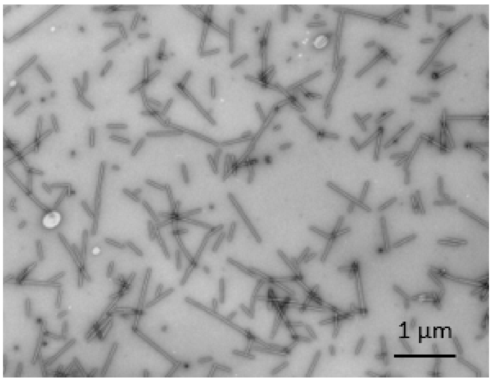

Figure 3. 4 TEM micrography of TMV. Image with courtesy of CNR-IPSP.
Reprinted with permission from [1]. Copyright © 2020 IOP Publishing. All Rights Reserved.

The term virus, derived from the Latin "vīrus, -i" (venom), denotes an acellular microorganism with characteristics of an obligate parasite, because it replicates and proliferates exclusively within the cells of other organisms that it will then infect. Specifically, Tobacco Mosaic Viruses (TMVs) are RNA viruses that belong to the *Tobamovirus* family, and their name is due to the characteristic "mosaic-like" mottling and discoloration they cause in infected tobacco leaves.

The coat protein (capsid) self-assembles into the rod-like helical structure around the RNA. TMVs are characterized by a cilindrical structure long 300 nm, with a diameter of (18.00 ± 0.36) nm, as reported by fibre diffraction studies in several studies (Figure 3. 3) [214,215,216,217].

The viruses analyzed were provided by Dr. Marta Vallino from CNR–IPSP (Consiglio Nazionale delle Ricerche – Istituto per la Protezione Sostenibile delle Piante), and the preparation takes approximately one month as described in the following.

An aliquot of dried leaves of *Nicotiana benthamiana* is taken from the collection and crushed with a mortar and pestle in 50 mM phosphate buffer, pH 7.0, containing 1 mM Na EDTA, 5 mM Na DIECA and 5 mM Na thioglycolate, added with activated charcoal.

The homogenate is used for mechanical inoculation on *N. benthamiana* leaves previously dusted with carborundum powder as an abrasive.

After viral symptoms appeared (about one week), symptomatic leaves were collected and stored at - 80 °C. For TMV particle purification, 20 g of leaves were used. Leaves are crushed in liquid nitrogen using a mortar and pestle and then homogenized in 80 ml (1:4 w:v) of extraction buffer (0.25 M potassium phosphate buffer, pH 7.0, 0.5% thioglycolic acid and 10 mM EDTA). The homogenate is filtered through a gauze, mixed with an equal volume of chloroform and stirred for 15 min at 4 °C. After centrifugation at 10 000 rpm (corresponding to 16 319 RCF using a Sorvall GSA rotor) for 10 min at 4°C, the supernatant was layered onto a 10 ml 20% sucrose cushion prepared in the extraction buffer and centrifuged for 60 min at 40 000 rpm at 4°C (corresponding to 151 693 RCF using a Ti55 Beckman rotor). The resulting pellet was dissolved in 2 ml of the extraction buffer and centrifuged for 1 min at 16 000 rpm (corresponding to 41 775 RCF using a Sorvall GSA rotor). The supernatant was layered on a 10 to 50% sucrose gradient in extraction buffer and centrifuged for 2 h at 36 000 rpm (corresponding to 122 871 RCF using a Ti55 Beckman rotor). A large band was collected and centrifuged at 100 000 rpm for 1 h (corresponding to 424 480 RCF using a TLA100.3 Beckman rotor). The pellet was dissolved in 0.05 M K-phosphate buffer, pH 7.0 and centrifuged for 1 min at 15 000 rpm (corresponding to 21 130 RCF using a FA-45-24-11 Eppendorf rotor). Please note that RCF is the relative centrifugal force, also known as g force. The supernatant is recovered and stored at - 20 °C. To check for purity and for viral particle integrity and quantity, the extract is observed under an electron microscope. A drop of the purification is allowed to adsorb for 1 min on carbon and formvar-coated grids and then rinsed several times with water. The grids are negatively stained with 0.5% uranyl acetate and excess fluid is removed with filter paper. Serial dilutions of the purification are prepared in water and observed, in order to reach a concentration in which viral particles are abundant but well separated and not overlapping. The instrumentation used for qualitative analysis of the TMV batches is the CM 10 Philips TEM with a fluorescence detector, using an electronic beam energy of 60 kV (Figure 3. 4).

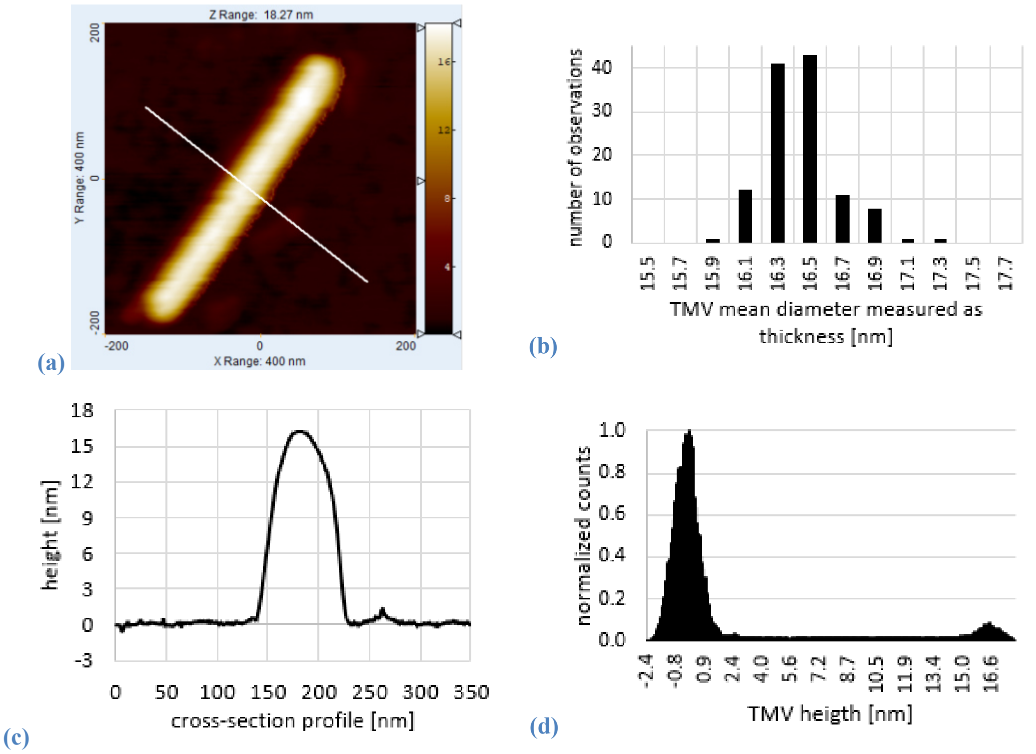

Figure 3. 5 (a) TMV topography measured with mAFM, (b) TMV diameters measured as thicknesses of the virus cross-section profile from 120 mAFM images, (c) TMV cross-section profile, (d) TMV normalized height histogram.
Reprinted with permission from [1]. Copyright © 2020 IOP Publishing. All Rights Reserved.

A drop of 20 ml of the diluted suspension without organic residues, prepared in MilliQ water, is then deposited on freshly cleaved mica and allowed to air evaporation [1].

During sample preparation, TMV may break and so change its length, but the diameter size is not altered and thus can be used as a reference size for tip calibration because the virus appears to be stable under air conditions [211] once deposited on the mica substrate.

Figure 3. 5 (a) reported the topography of a TMV measured by using INRiM mAFM set-up with the following measurement conditions: µMasch NSC15/AlBS tip, 1.5 V free amplitude, set point at 60%, (512 × 512) pixel density, (400 × 400) nm measurement area, 20% oversize, scanning speed at 200 $\mathrm{nm \cdot s^{-1}}$, measurement time of 40 minutes, and laboratory temperature of 20.0 °C and humidity of 55%.

Since in AFM vertical measurements are the most robust and accurate, the diameter of the TMV is evaluated as cross-sectional height of the isolated virus by using SPIP [155] software. After image levelling (Figure 3. 5 (a)), an average cross-section profile is extracted along all the virus length; top-height of an individual virus is evaluated by cursors tool, by placing one cursor into the top of the cross-section profile (Figure 3. 5 (c)) and the other on the right/left side of the virus on the mica substrate, and then averaging the right-side height and left-side height.

Furthermore, the TMV height is obtained by the histogram tool, which describes how many pixels are present in the image at a certain height. This histogram (Figure 3. 5 (d)) presents two peaks, the higher refers to the baseline level and is centred at 0 nm, the smaller identifies the TMV top. Histogram height is calculated by the difference between the modal values of the two peaks.

The measurand analysed is the mean diameter of 120 indepented TMVs measured by 120 independent images recorded using six different tips on three different samples deposited on mica. As reported in Figure 3. 5 (b), the average TMV diameter value from INRiM mAFM measurements is (16.5 ± 0.2) nm. The results of independent diameter measurements by the cursor and histogram methods are in agreement within 1%.

It should be appreciated that this diameter measurement looks robust and repeatable, and is also stable over time, as reported in Figure 3. 6. This characteristic is a mandatory requirement in the definition of reference material, but is also important for a tip calibrator.

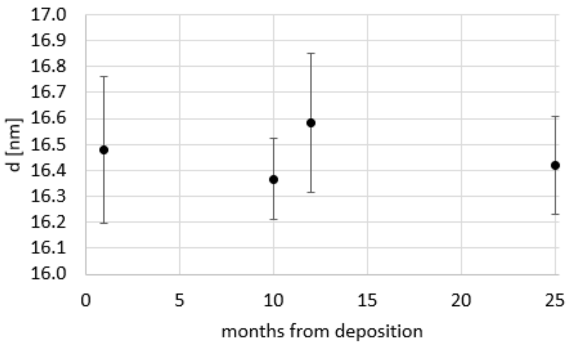

Figure 3. 6 TMV diameter analysis of the same sample after 1, 10, 12, and 25 months from deposition of the virus suspension on the mica substrate. Error bars refer to the standard deviation of measurements.

Note that after deposition, the samples are stored in plastic boxes to avoid contamination and kept in a laboratory cabinet under stable environmental conditions.

Table 3. 1 TMV diameter values reported in literature.

average height TMV [nm]	cited values [nm]	environment	substrate	imaging mode	Authors
16.2	-	air	mica	-	Finch et al. [218]
16.5	16.5 ± 0.2	air	mica	tapping	Trinh et al. [211]
16.7	16.65 ± 0.17	air	mica	tapping	Lin et al. [219]
16.8	16.80 ± 0.24	air	mica	tapping	Godon et al. [220]
16.2	16.2 ± 0.8	air	mica	tapping	Sinitsyna et al. [221]
16.6	16.6 ± 0.2	air	glass	non-contact	Zhang et al. [222]
14	-	air	O_2 plasma treated silicon	tapping	Stitz et al. [223]
18.2	18.2 ± 1	liquid	mica	tapping	Schabert et al. [224]
18.4	18.42 ± 0.19	liquid	mica	peak force	Godon et al. [220]

The average TMV diameter value from INRiM mAFM measurements is smaller than the reference value from X-ray diffraction measurements. Furthermore, it should be noted that TMV diameter values smaller than the nominal value are also reported in the literature from AFM-based measurements on isolated viruses, with values that are strongly dependent on the imaging environment and the substrate (Table 3. 1) [1].

The difference between the cross-sectional height diameter by AFM and the X-ray nominal value is due to the interaction between the AFM tip, the sample, and the substrate.

This assumption is firstly supported by the elastic moduli of the various materials, which differs of orders of magnitude. In fact, TMV is a soft material with a low Young's modulus, while mica and the silicon tip are hard materials (E_{mica} = (190 ± 20) GPa [225] and E_{Si} = (170 ± 5) GPa [226])[3].

Recall that Young's modulus is a mechanical property that measures the tensile strength of a solid material. Instead, Poisson ratio measures the deformation of a material in directions perpendicular to the direction of loading. The Poisson ratio values are ν_{TMV} = 0.48 [227], ν_{Si}= (0.22 ± 0.01) [228], and ν_{mica}= (0.25 ± 0.01) [225].

In literature are present several values for TMV Young modulus (Table 3. 2). Since there is a wide dispersion of these elasticity moduli, the estimate I have made together with an uncertainty budget is given below.
It was not possible to measure Young's modulus experimentally by force spectroscopy because the current mAFM system is affected by piezoelectric hysteresis and does not allow a quantitative measurement. Therefore, the elasticity modulus was estimated from the topographic measurements performed.

To evaluate the true mechanical properties of biomaterials, standardized data evaluation including the well-known Oliver-Pharr model is actually only valid for elastoplastic materials. This model is based on Hertian theory and, in fact, it assumes that deformations are elastic.

The reduced (or effective) elastic modulus $E_{red} = \frac{1}{2} \cdot k_{tip} \cdot \sqrt{\frac{\pi}{A}}$ is a combination of the sample material and tip elastic deformations [229].

For separating the tip elastic deformation term from the sample material elastic modulus is needed the inverse reduced modulus, according to $\frac{1}{E_{red}} = \frac{1-{\nu_{tip}}^2}{E_{tip}} +$

$\frac{1-\nu_{TMV}{}^2}{E_{TMV}}$. By this last formula, it is derived the TMV Young's modulus as $E_{TMV} = \frac{E_{red} \cdot E_{tip} \cdot (1-\nu_{TMV}^2)}{E_{tip} - E_{red} \cdot (1-\nu_{tip}^2)}$.

Table 3. 2 TMV Young's modulus values from literature.

TMV Young's modulus [GPa]	evaluation method	Authors
1.1	manipulation with the AFM silicon nitrite tip (i.e. rotations and bendings) of TMV viruses deposited onto a graphite substrate	Falvo et al [230]
3	measurements of indentation on TMV deposited on mica substrate	Kiselyova et al [231]
6.8 ± 2.4	static method, in which the TMV is deposited onto a polycarbonate substrate and it is trapped in a solvent bubble	Schmatulla et al [232]
5.0 ± 2.8	dynamic method, in which the TMV lays at one end on the mica substrate and at the other end on another virus	
	indentation measurements on viruses deposited onto mica, by means of a silicon nitride tip with a radius of about 15 nm in an open liquid cell in contact mode; these measurements are processed in two different ways obtaining two different modulus values:	Zhao et al [227]
1.0 ± 0.2	Hertz model	
0.92 ± 0.15	finite element analysis	
	indentation measurements by using a silicon tip with a radius of 12 nm on a 2D hexagonal packed rod-like superlattice structure assembled from TMVs; these measurements are processed in two different ways obtaining two different modulus values:	Wang et al [233]
2.14	application of JKR model to experimental data	
2.00 – 4.38	finite element analysis on different indenting locations	

By using the Global Calibration Initiative tool (Section 3.1), a cantilever constant k_{tip} = 47.8 Nm^{-1} is evaluated, once set the brand, nominal resonance frequency, and quality factor of the tip. This value has an error of 11%, derived from the values of AFM worldwide microscopists that used the GCI tool.

Since the Young's modulus value is strongly influenced by the interaction area, considering 8 nm (nominal tip radius) and 20 nm (blunt tip radius) as the limit of a rectangular distribution of the radius of the tip-sample interaction area, a mean value E_{TMV} = 1.3 GPa is obtained, with an expanded uncertainty of 0.5 GPa as reported in Table 3. 3.

Table 3. 3 Uncertainty budget of the estimated elastic modulus E_{TMV}.

quantity X_i	estimate x_i	standard uncertainty $u(x_i)$	unit	PDF	degrees of freedom ν_i	sensitivity coefficient c_i	standard uncertainty $u_i(E_{TMV})$ [Pa]
reduced Young's modulus E_{red}	1.6E+09	2.8E+0.8	Pa	N	95	7.8E-01	2.2E+08
TMV Poisson ratio ν_{TMV}	0.48	0.05	-	N	50	-1.5E+09	-7.4E+07
tip Poisson ratio ν_{tip}	0.24	0.02	-	N	50	5.6E+06	9.7E+05
tip Young's modulus E_{tip}	1.7E+11	1.7E+10	Pa	N	50	6.5E-05	1.1E+06
					combined standard uncertainty $u_c(E_{TMV})$		**2.5E+08**
					degrees of freedom ν_{eff}		115
					coverage factor k		2
					expanded uncertainty $U(E_{TMV})$		**5.0E+08**

All contributions have a Gaussian probability distribution function, and the tip and TMV Poisson ratios and tip Young's modulus are assumed to have a 10% relative standard uncertainty. The main contribution to the budget is made by the reduced Young's modulus E_{red}, due to the uncertainty from the radius of the tip.

TMV elastic modulus estimation is needed for the tip-sample-substrate quantitative investigation, by using the models introduced in Section 3.2. Note that for all deformations α an uncertainty with rectangular distribution calculated as $u_c(\alpha) = \frac{\Delta\alpha}{2} \cdot \frac{1}{\sqrt{3}}$ is reported.

Elastic deformations are calculated by using the Puttock-Thwaite [195] reported below.

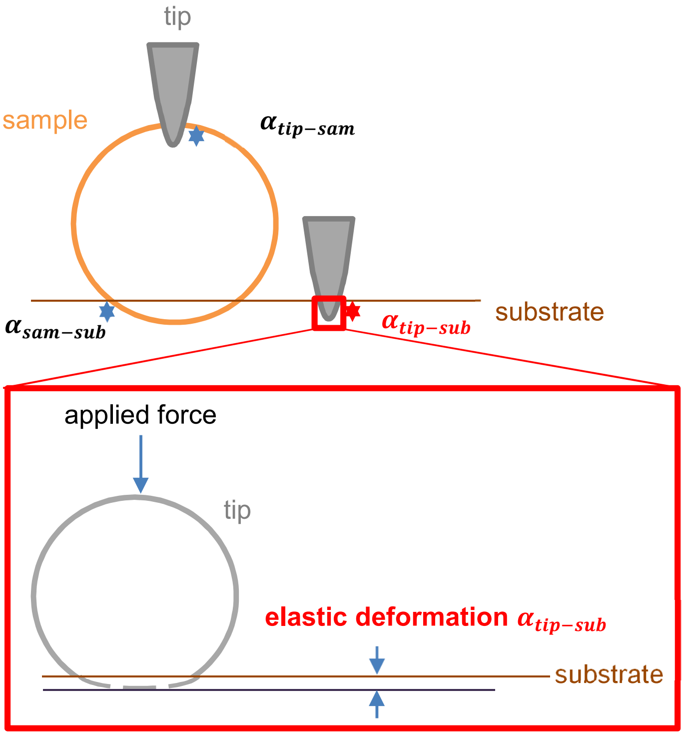

Figure 3. 7 Not-to-scale sketch of tip-substrate (Si-mica) interaction.

The interaction between the tip and the mica substrate is analysed considering the Hertzian model of contact mechanics between a sphere (representing the tip apex) and a plane (representing the mica substrate) [1]. The calculation is made by using the $\alpha_{tip-sub} = \frac{(3\pi)^{2/3}}{2} \cdot P^{2/3} \cdot (V_{tip} + V_{sam})^{2/3} \cdot \left(\frac{1}{D_{tip}}\right)^{1/3}$, where P is the applied force, $V = \frac{1-\nu^2}{\pi E}$ and D is the tip diameter [195].

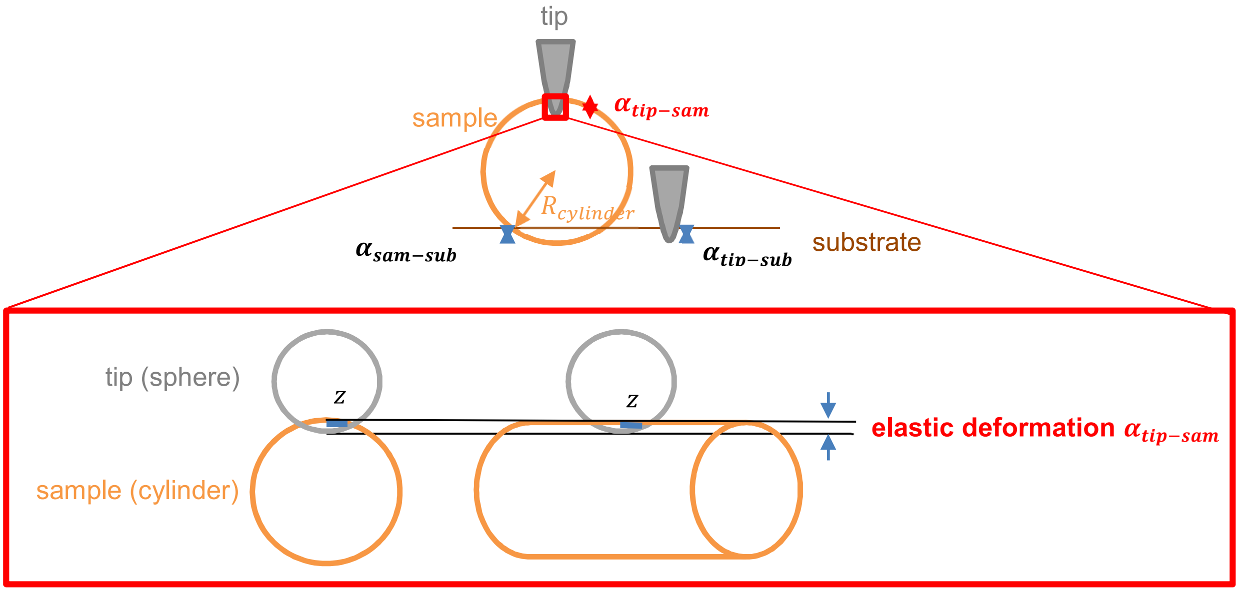

Figure 3. 8 Not-to-scale sketch of the tip-sample (Si-TMV) interaction.

To calculate the tip-TMV elastic deformation, the interaction of a sphere (representing the tip apex) with a cylinder (representing the TMV) is considered [1]. The elastic compression α_{el} is calculated as $\alpha_{tip-sam} = \frac{2QPK}{z}$, where P is the applied force, $Q = \frac{3}{4}(V_1 + V_2)$, the interaction radius $z = \sqrt[3]{\frac{2QP}{A} \cdot -\frac{1}{e}\frac{dE}{de}}$. The elliptic integrals K and $-\frac{1}{e}\frac{dE}{de}$, where E is the Young's modulus and e is the contact ellipse eccentricity, are calculated from the appropriate $\frac{A}{B}$ value. Therefore, the factor $\frac{A}{B} = \frac{\frac{1}{D_1}}{\frac{1}{D_1}+\frac{1}{D_2}}$ is calculated, where D_1 is the sphere diameter and D_2 is the cylinder diameter [195].

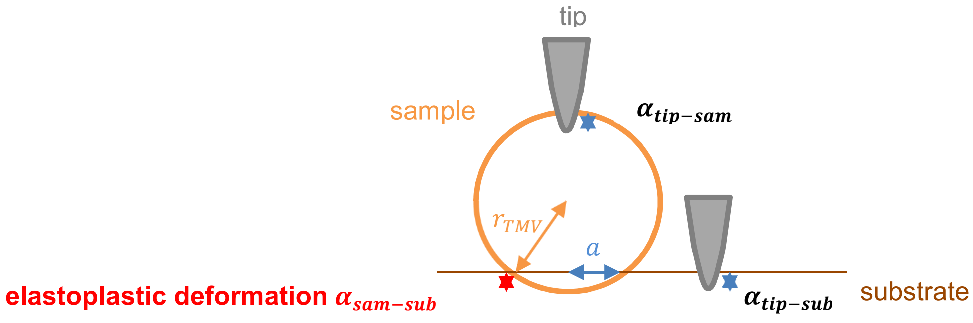

Figure 3. 9 Not-to-scale sketch of the sample-substrate (TMV-mica) interaction.

The sample-substrate elastoplastic deformations are calculated as $\alpha_{sam-sub} = r_{TMV} - \sqrt{r_{TMV}{}^2 - a^2}$ [184], where a are the radiuses of contact calculated by using the different models described in Section 3.2.

It must be remembered that the Hertzian model considers a purely elastic interaction without the presence of any forces, the JKR theory considers both compressive and adhesive tractions inside the area of contact, while DMT considers only repulsive forces inside the contact area [234]. MP considers elastoplastic or full plastic contact [194], so its contribution is higher compared to the other models [3].

Table 3. 4 reports all deformations calculated as explained above, and the values are calculated by considering a nominal tip radius $r_{tip} = 8$ nm, and an applied force $P = 1.2$ nN.

Throughout the thesis, measurements were performed in non-contact mode, and the applied force $P = 1.2$ nN was calculated by using the equation $P = k \cdot \frac{\sqrt{A_0 - A}}{2 \cdot Q}$ [211], where A_0 is the free oscillation amplitude, A is the oscillation amplitude when imaging, Q is the quality factor equal to 580, k the cantilever spring constant. The amplitude oscillation is recorded in volts ($A = 0.9$ V and $A_0 = 1.5$ V); therefore, the conversion factor $c_{ampl} = 217$ nm·V^{-1} was calculated by measuring the pitch of the screw that adjusts the laser beam on the photodiode is measured, and correcting the calculated factor for the amplification due to the optical lever of the laser beam on the photodiode.

The overall deformation is calculated by $\alpha_{TOT} = \alpha_{tip-sam} + \alpha_{\mathrm{sam}-sub\ Chaud} - \alpha_{tip-sub} = 0.4 + 0.8 - 0.02 = 1.2$ nm; thus, the TMV diameter taking into account the average diameter of the mAFM measurements and all the tip-sample-substrate deformations is approximately 17.7 nm.

Even if for the calculation of the overall deformation only the Chaudhury model is considered because of the cilindrical geometry, in Table 3. 4 are also reported JKR, DMT and MP models (usually used in literature for elastoplastic deformation calculations).

Table 3. 4 Calculation of the tip-sample-substrate interactions for the silicon tip-TMV-mica system.

Interaction	**Model**	**Parameter name**	**Deformation** α **[nm]**	**Uncertainty** $u_c(\alpha)$ **[nm]**
Tip-substrate (Si-mica)	Hertz (sphere-plane)	$\alpha_{tip-sub}$	0.02	0.01
Sample-substrate (TMV-mica)	JKR (sphere-plane)	$\alpha_{\mathrm{sam}-sub\ JKR}$	1.0	0.3
	DMT (sphere-plane)	$\alpha_{\mathrm{sam}-sub\ DMT}$	0.5	0.1
	MP (sphere-plane)	$\alpha_{\mathrm{sam}-sub\ MP}$	1.8	0.6
	Chaudhury (cylinder-plane)	$\alpha_{\mathrm{sam}-sub\ Chaud}$	0.8	0.2
Tip-sample (Si-TMV)	Hertz (sphere-cylinder)	$\alpha_{tip-sam}$	0.4	0.1

Table 3. 4 reports all deformations calculated by considering a nominal tip radius r_{tip} = 8 nm, but since the real tip radius may significantly deviate from its nominal value, by considering 20 nm (blunt tip radius) as the upper limit of a rectangular distribution of the radiuses, a maximum difference of 26% can be appreciated for both tip-substrate and tip-sample interactions. In fact, tip-sample deformation varies from 0.35 nm, when considering the nominal tip radius of 8 nm, to 0.26 nm, when

considering a blunt tip radius of 20 nm. Tip-substrate deformation is equal to 0.020 nm when considering the nominal tip radius of 8 nm, while it is equal to 0.015 nm considering a radius of 20 nm (blunt tip radius). However, it can be stated that the tip-substrate is negligible in any case.

Table 3. 5 Uncertainty budget of the TMV diameter measured as cross-section top height.

quantity X_i	**estimate** x_i	**standard uncertainty** $u(x_i)$	**unit**	**PDF**	**degrees of freedom** vi	**sensitivity coefficient** c_i	**standard uncertainty** $u_i(d)$ **[nm]**
repeatability d_{mean}	16.5	0.1	nm	N	120	C_z	0.1
C_z factor	1	0.03	-	N	50	d_{mean}	0.5
mechanical drifts δ_{str}	0	0.2	nm	R	50	1	0.2
tip-sample interaction $\alpha_{tip-sam}$	0.4	0.1	nm	R	20	1	0.1
sample-substrate interaction $\alpha_{sam-sub}$	0.8	0.1	nm	R	10	1	0.1
					combined standard uncertainty $u_c(d)$		**0.6**
					degrees of freedom ν_{eff}		70
					coverage factor k		2.025
					expanded uncertainty $U(d)$		**1.2**

For a quantitative determination of the diameter descriptor by mAFM measurements, an uncertainty budget is evaluated (Table 3. 5). The measurand is the diameter of the TMV measured as mean height $d_{mean} = \frac{1}{n}\sum_{i=1}^{n} d_i$, and the model equation that takes into account all the error sources that affect the measurements is $d = C_Z \cdot d_{mean} + \delta_{str} + \alpha_{tip-sam} + \alpha_{sam-sub} + \alpha_{tip-sub}$. Note that the overall average TMV diameter is $d = 1 \cdot 16.5$ nm + 0 nm + 0.4 nm + 0.8 nm + 0 nm = 17.7 nm. For the sake of completeness of the measurand equation d, the term $\alpha_{tip-sub}$ is listed, although it is not considered in the uncertainty budget because it is a negligible contribution.

The repeatability d_{mean} considers the standard deviation of the mean of the 120 isolated TMV analyzed.

The C_z factor considers (i) the calibration, that takes into account the interferometric calibration of the Z axis including cosine errors ($0.5 \times 10^{-4}L$), (ii) the piezoelectric non-linearity (0.5 nm), (iii) the profile noise (0.3 nm), measured as Rq of mica along the X-direction profile, and (iii) the resolution of the D/A converter (0.1 nm) on the piezoelectric stroke of 2 µm; this last contribution is negligible. Note that the previous values reported in brackets refer to normal and rectangular distributions resulting in a combined standard uncertainty of the C_z factor of $3 \cdot 10^{-2}$.

The uncompensated mechanical drifts are described by straightness, which is the error on Z-axis that occurs when the tip scans an ideally flat surface, evaluated by measuring Rt of the substrate only along Y-direction.

The sample-substrate interaction contribute as described in Table 3. 4, while the standard uncertainty $u(x_i)$ due to tip-sample interaction term $u(\alpha_{tip-sam})$ is calculated by the square root of the quadratic sum of the uncertainties of deformation values $u_c(\alpha)$ calculated by using the nominal tip radius $r_{tip} = 8$ nm and the blunt tip radius $r_{tip} = 20$ nm.

3.4.2 Tip Characterisation by using TMV

In order to fully characterize TMVs, the lateral sizes are also analysed. Specifically, in the analysis of various cross-section profiles from topographies recorded with the same tip, points at various heights (0 nm, 8 nm, 12 nm, 14 nm, 15 nm, 16.5 nm from the bottom of the profile) are taken into account. As reported in Figure 3. 12 (a), for each tip are considered the average points from the analysis of subsequent TMVs. Figure 3. 12 (b) shows the results obtained for the 6 tips used for imaging the viruses over a period of more than 1 year.

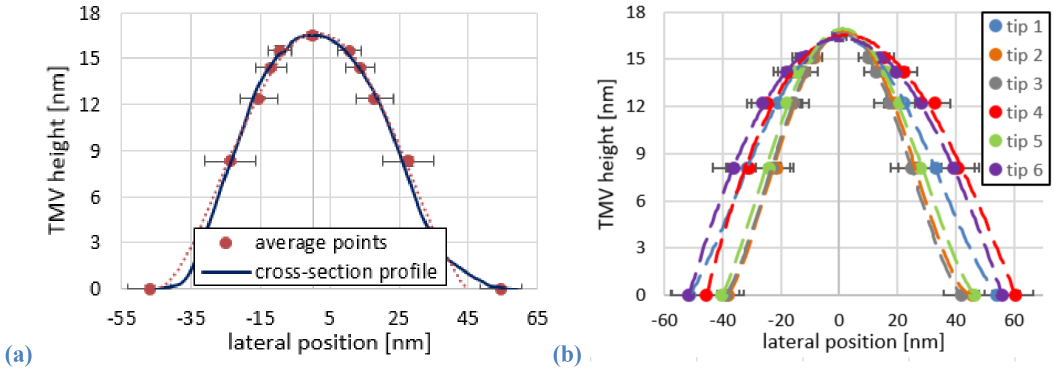

Figure 3. 10 (a) Comparison between a cross-section profile and average points from several subsequent images registered with the same tip (tip 1). (b) Reconstruction of TMV cross-section mean profiles from the lateral measurement of 120 images measured by 6 different tips; the error bars refer to measurements' standard deviation.
Reprinted with permission from [1]. Copyright © 2020 IOP Publishing. All Rights Reserved.

AFM images suffer from errors in reconstructing the actual lateral shape of the surface, which become significant especially when the tip size is comparable with the critical size of the sample under investigation. The lateral measurements reported above are useful for characterizing the apex tip geometry. Since the TMV diameter is a stable measurand, it is developed a geometric approach to estimate the dilation of the tip.

Given the known circular shape and size of the base of the rod virus (Figure 3. 11 (a)), the semi-chord of the circle by $s = \sqrt{t(2r_{TMV} - t)}$ is calculated, where t is the difference between the top circle height to the height of the chord at which the dilation is calculated.

Notably, the shape of the virus affects the accuracy of tip characterization. In real measurements, the shape of the virus is not ideally cylindrical because of (i) the sample– substrate interaction $\alpha_{sam-sub}$ and (ii) the AFM probing force that affects the tip–sample interaction $\alpha_{tip-sam}$. Considering these interactions, an elliptical geometry of the TMV cross-sectioncross-section is reported (Figure 3. 11 (b)); the elliptical semi-chord is calculated by $e = \frac{a}{n}\sqrt{t(2n - t)}$, where t is the difference between the top ellipse height to the height of the chord at which the dilation is calculated, and a and n are the major and minor semiaxis of the ellipse, respectively.

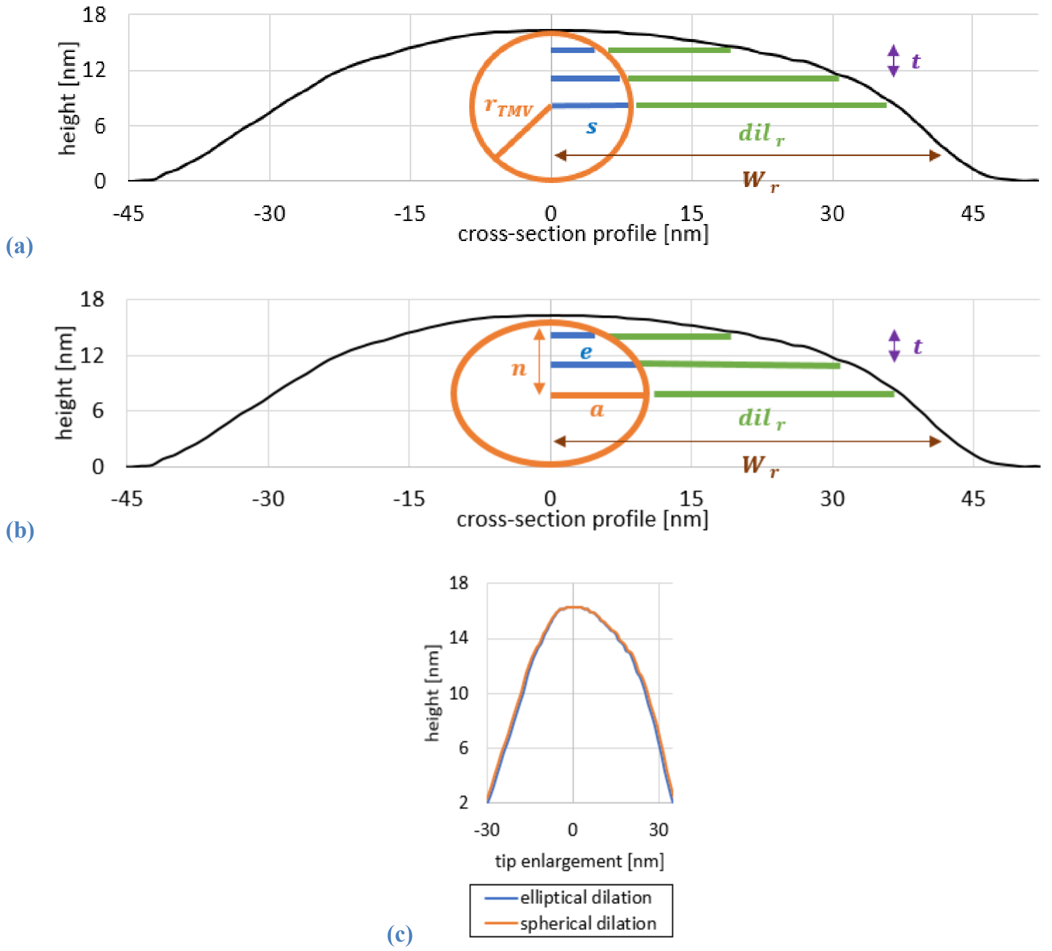

Figure 3. 11 (a) Spherical geometric approach to determine the tip dilation "dil" from the TMV cross-section profile. (b) Not-to-scale sketch illustrating the elliptical geometric approach to determine the tip dilation "dil" from the TMV cross-section profile. (c) Comparison of the tip dilation profile between spherical and elliptical methods.
These profiles are registered with tip 5.
Reprinted with permission from [3]. Copyright © 2022 Springer Nature. All Rights reserved.

Figure 3. 11 (a) and (b) show the right dilation dil_r, which is calculated by the difference between the right width W_r and the semi-chord s/e based on the model used.

The same calculation is performed for the left side of the profile to calculate dil_l, and the sum of the right and left dilation is calculated to obtain the overall tip dilation profile.

Figure 3. 11 (c) reports the comparison between the spherical and elliptical models, showing a lateral difference of 3%. Notably, the cylinder is primarily deformed in the part that is in contact with the substrate, but we expect that for the upper semi-cylindrical section of the virus, slightly deformed by the tip–sample elastic interaction, the approximation with a circle is consistent [3].

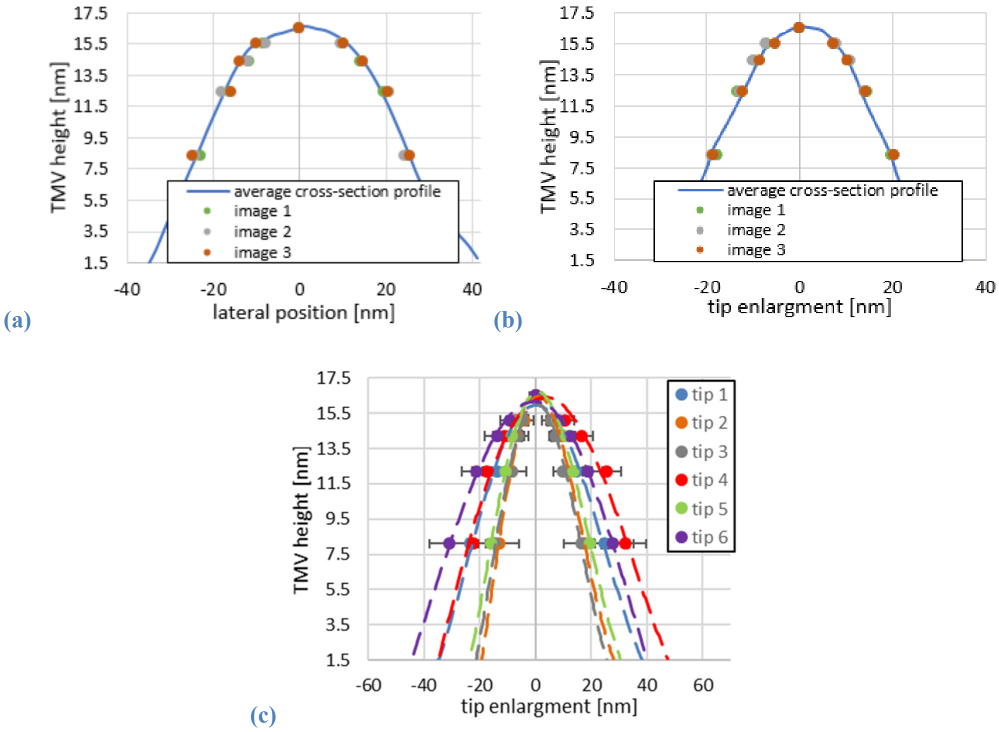

Figure 3. 12 (a) Average TMV cross-sectioncross-section profile from the analysis of 3 independent images measured with the same tip. (b) Enlargement profile of a tip used for the analysis of 3 independent TMVs. (c) Mean dilation profiles of the 6 tips used for analysing the TMV; the error bars refer to measurements' standard deviation.
Reprinted with permission from [1]. Copyright © 2020 IOP Publishing. All Rights Reserved.

Figure 3. 12 (a) and (b) show the comparison between a mean cross-section profile and the profile of the enlargement for a case study on three subsequent images measured with the same tip (tip 3).

Figure 3. 12 (c) shows the tip enlargement mean values of the three samples measured by six different tips at heights of about 8 nm, 12 nm, 14 nm, 15 nm and 16.5 nm from the mica substrate. Note that the bottom 10% is excluded from all profiles of Figure 3. 12 (a), (b), and (c), because it can contain non-tip artefacts [[149]][[1]]. Remember that the tip dilation profile from the geometrical approach gives as result the reflected form of the tip dilation.

Chapter 4. Non-Spherical Nanoparticles to be applied as Candidate Reference Materials for Dimensional Nanometrology

Chapter 4 describes the dimensional characterization of complex geometry nanoparticles, after an introduction regarding nanoparticle nanometrology and the AFM study on spherical NPs. Some of the work described in this chapter has been previously published in [2,3].

It is worth to be noted that a punctual description of the programs developed for NPs' critical sizes determination is reported in the two Annexes.

4.1 Nanoparticle Nanometrology

Nano-objects can be divided into (i) nanofibers, materials with only one dimension in the nanoscale, *e.g.* nanotubes (hollow nanofibers), nanorods (solid nanofibers), nanowires (electrical conducting nanofiber), (ii) nanoplates, objects with two dimensions in the nanoscale [2], and (iii) nanoparticles (NPs), which have all three dimensions in the nanoscale range (1 nm to 100 nm) [235].

Nanoparticles are defined as «minute piece of matter with defined physical boundaries» [236], and have two particularly important features:

1. they have a very high surface/volume ratio, meaning that any interaction with the external environment occurs through the atoms on the surface;
2. their properties depend not only on their chemical composition, but primarily on their size and shape (they can be spherical, cylindrical, star-shaped, hollow...).

NP can originate both naturally (such as sand suspensions, volcanic eruptions) and anthropogenically (industrial emissions, automobile traffic, cigarette smoke).

Over the last thirty years, however, new nanoparticles of widely varying size, geometry, and chemical composition have been produced; these are called engineered nanoparticles, that are designed and produced for specific purpose or function [236]. Nanoparticles are widely used as they are highly interesting in various research fields, including health (*e.g.* drug delivery, toxicity studies), environmental (abatement of pollutants), quantum nanoscience (semiconductor nanoparticles for quantum devices), and various industrial sectors, such as cosmetics (NPs in sunscreams), food (antimicrobial polymer sheet with silver/additive NPs), and energy (*e.g.* TiO_2 NPs is the Grätzel solar cell) [237].

Within this framework, metrology supports nanoscience to (i) develop reference materials and (ii) define quantitative measurements to strengthen the reliability, safety and competitiveness of products.

Dimensional nanometrology is important because at the nanoscale all properties of a material are strongly dependent on its size and surface area, and these properties may be different from the properties of the same material at the macroscopic scale, where the physical and chemical properties are given by the solid structure. In particular, particle nanometrology relates to particles chemical/mechanical/electrical or biological functional properties, but all these chacteristics are strictly linked to dimensional nanometrology, in particular to shape, size, size distribution, and morphological parameters.

For this reason, it is important to clearly define methods for measuring NPs critical sizes. Note that critical sizes are those descriptors that unambiguosly characterize the shape of a NP.

Since so many industrial NPs are characterised by irregular shapes and a wide size distribution, it is difficult to follow European regulations for identifying a nanomaterial. In addition, it is difficult to measure the size of NPs with complex geometry in a traceable way. Given these new requirements, in order to perform robust and traceable 3D measurements, in this thesis I have focused on studying new methodologies to perform quantitative measures of critical sizes of complex geometry NPs having non-monodisperse size distributions by using mAFM.

These new measurement methodologies on complex shape nanoparticles have relevance, as they could impact (i) many industries dealing with nanoparticles in a high volume which all require accurate and reliable characterisation of their nanoparticulate products, (ii) standardisation committees, such as ISO/TC229 (nanotechnologies), European Committee for Standardization CEN/TC 352

"Nanotechnologies", and pre-normative committee VAMAS (Versailles Project on Advanced Materials and Standards), and (iii) the newly approved European Metrology Network for Advanced Manufacturing (EMPIR EMN AdvManu) [238], that will drive the high-level coordination of the metrology community in this field and will foster the impact of metrology developments for advanced manufacturing in several Key Industrial Sectors (KIS), including micro- and nano-technology.

4.2 Quantitative Dimensional Characterization by mAFM

Nanomaterials have peculiar properties due to their small size. Accurate depiction of nanomaterials using dimensional techniques is critical for product development and quality control. Metrology of nanoscale materials depends on the capacity to traceably measure samples with 3D nanoscale resolution.

Regarding the NPs, the fundamental dimensional descriptors are shape, size, size distribution, and morphological parameters.

The NP shape is related to the geometry, that can be spherical, ellipsoid, granular, blocky, flaky, platy, prismodal, rod-like, acicular, and needle-shaped. Particle shape strongly influences its interaction with the surrounding ambient and determine its possible application fields.

The NP size can be described as the distance between the boundaries of the particles. These boundaries can be described in various ways, and according to their definition, different sizes could be obtained for the same NP. As an example, if we consider the water layer attached to the NP when moving in solution, the hydrodynamic size is measured, while if we consider the distance between two tangents to the physical interface of the particle in a well-defined orientation, the Feret diameter is measured. We have seen in Section 1.5 that the definition depends strictly on the instrumental method, and according to the technique used (direct or non-direct) different interfaces and different shapes (often approximated as spherical) can be considered.

The size distribution describes the dispersion of the nanoparticles, and it can reveal for example if there are aggregates present in the solution.

Morphological parameters are numerical descriptors that are related to the shape and size of a NP or to the finiture and texture of the surface (that can be smooth, rough, porous, with cracks).

In the following paragraphs, the descriptors studied for the quantitative characterisation of non-spherical NPs are introduced.

4.2.1 Critical Size Determination

The first dimensional characterisation of a NP regards the quantitive determination of size and size distribution, that depends by the instrumental technique used. Furthermore, it must be noted that, especially for direct microscopy techniques, various methods can be used for the size determination for NPs with different geometries.

Sections 4.3 and 4.4 describe the different methodologies for the determination of the sizes of spherical and complex geometry nanoparticles measured with mAFM.

4.2.2 Morphological Parameters

Monitoring NPs morphology is of paramount importance to exploit their properties and use them in various emerging technologies. Although the study of NPs morphology is of great importance, it is often not well characterized due to lack of documentations.

In order to support pre-normative works on measurements of 3D nanostructures by AFM, it is important to clearly define some parameters in a terminology easily understandable. NP morphology can be described by several parameters, and in this thesis I focused on descriptors based on surface roughness and texture and shape.

4.2.2.1 Roughness and Texture

Geometrical Product Specification (GPS) [239] is a set of ISO standards, whose goal is the development of a language for specifying the macrogeometry (size, shape, orientation, location) and microgeometry (surface texture) of products, so that it can be adopted consistently throughout the world.

ISO written standard on roughness measurement refers to profiles from 80 μm up to hundreds of mm. The primary profile measured with stylus and/or optical profilometer instrumentations can be divided into a waviness profile, by removing the short-wavelength component from the primary profile, and a roughness profile, by removing the long-wavelength component from the primary profile. The roughness profile refers to a curve in which only high frequency components of the primary profile are recorded through a phase-correct high-pass filter (sampling length or cut-off value L) [240]. Please note that for nanometric profiles measured by AFM L (present in the equation describing the parameters in Table 4. 1) is referred to the total length of the profile analyzed, without further cut-off filters.

Surface characterisation regards the analysis of the roughness of the profiles, according to the ISO 21920:2021 [241], and the texture of an area, according the ISO 25178:2021 [242]. Please note that ISO 21920-2:2021 transposes and replaces ISO 4287:1997, ISO 13565-2:1996, ISO 13565-3:1998, while ISO 25178-2:2021 replaces ISO 25178-2:2012. These written standards are divided into several parts, and in part 1 are reported symbols and indications, while in part 2 are reported the description of parameters.

Roughness parameters can be divided into (i) amplitude parameters, that characterize the surface based on the Z-axis deviations of the roughness profile from the average line, (ii) hybrid parameters, which calculations are based on local Z-slopes, (iii) functional parameters, *e.g.* characterizing bearing and fluid retention properties, and (iv) spatial parameters, based on the dominant texture in the image [155]. As reported by Marinello et al. [243] on the study of food packaging at the nanoscale, more than 65% of considered papers investigate roughness parameters, and the 55% of publications concentrate on root mean square texture and/or roughness (S_q or rms or R_q). In this study, I decided to report also other main amplitude roughness parameters, such as average value, peak parameter, skewness, and kurtosis, reported in Table 4. 1 for roughness profile texture parameters and in Table 4. 2 for areal surface texture parameters. The areal surface texture parameters, reported in Table 4. 2, are the roughness profile texture parameters extended to a surface. The parameters are calculated as double integrals across the whole surface.

Table 4. 1 Profile (roughness) texture parareasonablemeters.
Figures reprinted with permission from [244]. Copyright © Keyence Corporation. All Rights Reserved.

Profile (roughness) texture parameters	**Equation**	**Explanation**
average roughness	$R_a = \frac{1}{L}\int_0^L \lvert Z(x)\rvert dx$ 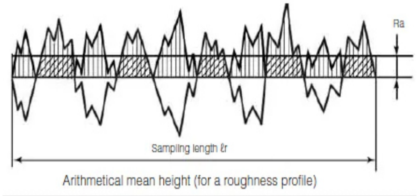 Arithmetical mean height (for a roughness profile)	this parameter is the arithmetical mean height of the absolute values; describes the profile divergence from the average line calculated along the total length of the profile L.
root-mean-square (rms) roughness	$R_q = \sqrt{\frac{1}{L}\int_0^L \lvert Z^2(x)\rvert dx}$ 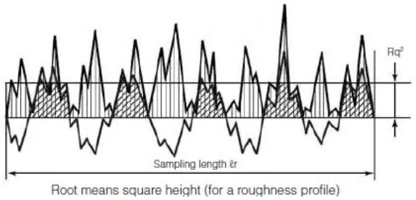 Root means square height (for a roughness profile)	this parameter represents the root mean square height, which is affected by the presence of peaks more than R_a.

maximum height of the roughness profile	$R_z = R_p + R_v$ 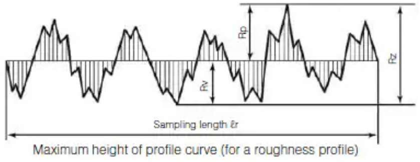 	this parameter sums the highest peak R_p with the deepest valley R_v.
roughness skewness	$R_{sk} = \frac{1}{R_q^3}\left[\frac{1}{L}\int_0^L Z^3(x)dx\right]$ 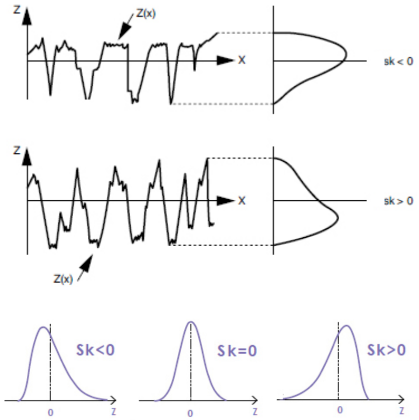 	this parameter relies on the asymmetry of the roughness profile distribution: • if $R_{sk} < 0$, height distribution is skewed above the mean plane (the distribution is deviated to the upper side); the mode is minor than the mean value of the height distribution. Negative skewness refers to profiles prevalent in deep valleys [245]; • if $R_{sk} = 0$, peaks and valleys are equally distributed around the mean plane, and the height distribution is symmetrical (mode = mean); • if $R_{sk} > 0$, height distribution is skewed below the mean plane (the distribution is deviated to the lower side); the mode is greater than the mean value of the height distribution. Positive skewness refers to profiles prevalent in high peaks [245].

roughness kurtosis	$R_{ku} = \frac{1}{R_q^4}\left[\frac{1}{L}\int_0^L Z^4(x)dx\right]$ 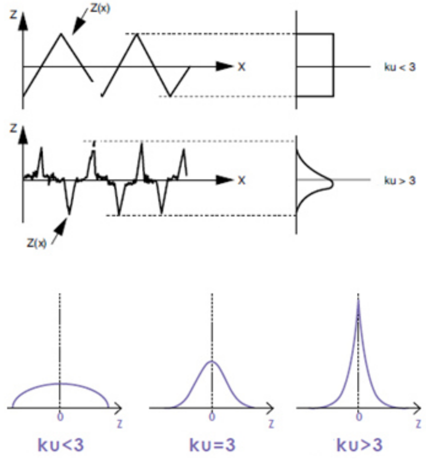	this parameter measures the sharpness of the roughness profile: • if $R_{ku} < 3$, peaks and valleys are very broad (platykurtic distribution [245]); • if $R_{ku} = 3$, peaks and valleys are normally distributed (Gaussian distribution); • if $R_{ku} > 3$, peaks and valleys are very sharp (leptokurtic distribution [245]).

Table 4. 2 Areal surface texture parameters.
Figures reprinted with permission from [246]. Copyright © Olympus. All Rights Reserved.

Areal surface texture parameters	**Equation**	**Explanation**
average roughness area	$S_a = \frac{1}{A} \iint_A \lvert Z(x,y) \rvert \, dxdy$ 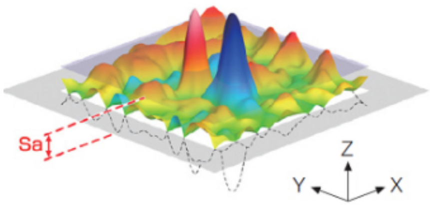	this parameter reveals the height deviation of each point from the arithmetical mean of the surface.

root-mean-square (rms) of the roughness area	$S_q = \sqrt{\frac{1}{A}\iint_A \lvert Z^2(x,y)\rvert \, dxdy}$ 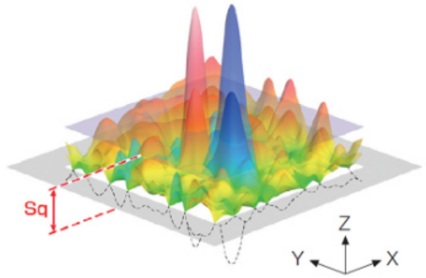 	this parameter represents the root mean square height within the area in examination, thus providing an idea of the amplitude of peaks and valleys recognizable in the surface. Compared to S_a, S_q is more sensitive to large peaks or deep valleys and it is therefore appropriate for quantifying localized changes in the surface.
maximum height of the roughness area	$S_z = S_p + S_v$ 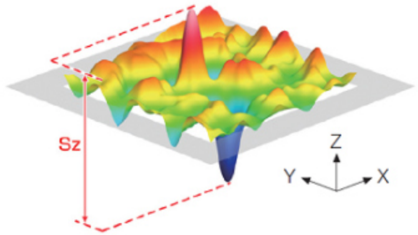 	this parameter sums the maximum peak height value S_p with the maximum pit depth value S_v.

areal skewness	$S_{sk} = \frac{1}{S_q^3}\left[\frac{1}{A}\iint_A Z^3(x,y)dxdy\right]$ 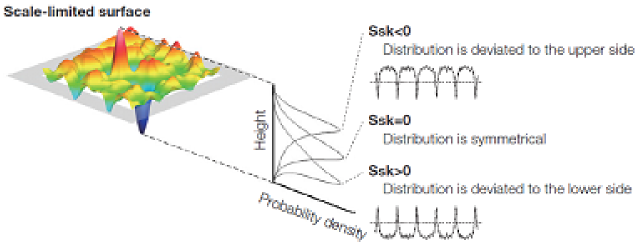 	this parameter represents the surface asperity: - if $S_{sk} < 0$, the height distribution is skewed above the mean plane; - if $S_{sk} = 0$, the height distribution (formed by all the peaks and valleys) is symmetrical around the mean plane; - if $S_{sk} > 0$, the height distribution is skewed below the mean plane.
areal kurtosis	$S_{ku} = \frac{1}{S_q^4}\left[\frac{1}{A}\iint_A Z^4(x,y)dxdy\right]$ 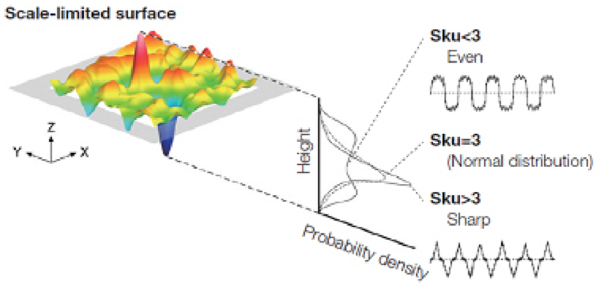 	this parameter measures the sharpness of the roughness profile: - if $S_{ku} < 3$, the surface presents broad peaks and valleys; - if $S_{ku} = 3$, the height distribution is Gaussian, with the coexistence of sharp and indented portions; - if $S_{ku} = 3$, the surface presents sharp peaks and valleys.

4.2.2.2 Shape Descriptors

Other morphological information can be obtained by shape descriptors, that are parameters depending on the NP shape and size, such as sphericity and aspect ratio. The development of these descriptors is increasingly required by companies and standardisation bodies to unambiguously characterise NPs.

The next paragraphs describe how quantitative dimensional characterisation is performed for NPs with different geometries measured with mAFM.

4.3 Spherical Nanoparticles

NPs can assume different shapes, depending on the fabrication methods, the starting material, and the physical/chemical interactions acting during the synthesis. The most common shape is spherical, easily obtained for energy-favourable reasons.

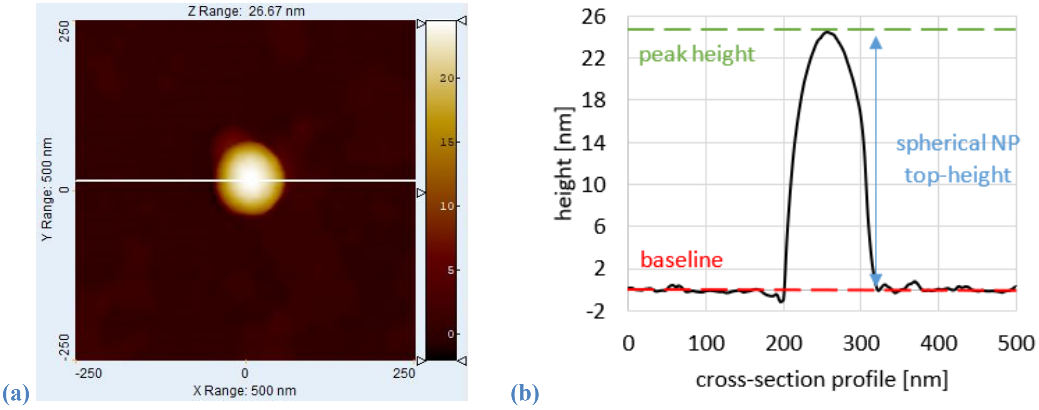

Figure 4. 1 (a) AFM image of a gold spherical NP and (b) its cross-sectioncross-section profile. (b) Diameter of an isolated spherical NP as the height of the profile at the top. Reprinted with permission from [3]. Copyright © 2022 Springer Nature. All Rights Reserved.

As reported in the American ASTM E2859-11 [247] and the NPL GPG 119 [248] guides, two methods can be used to measure the diameter of spherical nanoparticles: (i) height of isolated NPs dispersed onto a flat substrate and (ii) lateral distance of NPs in a closely packed monolayer arrangement. Considering that the second method could be a source of errors because of tip dilation and a perfect closely packed monolayer arrangement of nanoparticles can be difficult to achieve, the first method is preferable [3]. Note that for both methods the measurand is the mean diameter of a population of NPs.

Calibration of the mean diameter of nanoparticles deposited on an ultra-flat substrate (mica) starts by reconstructing the polar cross-sectioncross-section of the quasi-spherical particle and measuring the pole height relative to the flat substrate (Figure 4. 1). In nanoparticle measurements, the shape is commonly assumed to be perfectly spherical.

The nanoparticle sample is usually stored in a phosphate buffer suspension. From the nominal concentration, the diluted suspension is prepared by dilution with ultra-pure water and sonication of the suspension, for disaggregating any accumulation of nanoparticles. A few drops of the diluted suspension are deposited on the mica disc and the acqueous solvent is let to evaporate.

NMIs demonstrate the international equivalence of their measurement standards and measurement certificates within the Mutual Recognition Arrangement (MRA) framework. «The outcomes of the MRA are the internationally peer-reviewed and approved Calibration and Measurement Capabilities (CMCs) of the participating institutes. A CMC is characterized by the measured quantity and associated measurement uncertainty (generally given at a 95% level of confidence) for a given range, the method or instrument used, the values of influencing parameters and any other relevant information» [249].

INRiM is able to emit calibration certificates thanks to its CMCs, which are published on the BIPM key comparison database (KCDB). In order to demonstrate a CMC, one has to participate to at least one intercomparison. There are two types of intercomparisons: (i) round robin test, which is an intercomparison between different laboratories which perform the measurements independently, and (ii) interlaboratory comparison (ILC), which consists in intercomparison of measurement results between a laboratory and a NMI. The goal is to verify the technical competence and validate the measurement methodologies and the uncertainty statement of the laboratory.

In the INRiM Nanometrology laboratory there are two CMCs, one for 1D and 2D gratings and the other for spherical NPs.

The measurement capabilities of the mean diameter of quasi-spherical nanoparticles of gold, silver, silica, and polystyrene have been fully attested through participation to international comparisons (European iMERA-Plus project 'Traceable

Characterisation of Nanoparticles', a comparison among European metrology institutes (2011) [250], and APMP.L-S5 – Supplementary Comparison on Nanoparticle Size (2012) [251]). These ILCs support the newly assigned INRiM CMC for spherical NPs in the measurement range from 5 nm to 500 nm with an expanded uncertainty between 1.8 nm and 12 nm. The equation that describes the uncertainty is 1.8 nm + 0.02 d, and it is given by a constant term, which is primarily influenced by the repeatability of measurements and reference plane definition, and a proportional term, which is measured by the interferometric calibration of the Z-axis and sample leveling [252].

The CMC related to spherical NPs is based on comparisons prior to this doctoral work. I performed measurements on ERM-FD304 silica nanoparticles and NIST RM8012 gold nanoparticles within the framework of a round robin between NMIs into the EMPIR project 15SIB09 3DNano – Traceable three-dimensional nanometrology [253].

In determining the consistency of results from different participants, the degree of equivalence E_n is calculated. The results are consistent if the absolute value of E_n is smaller than 1. Moreover, the Birge ratio is evaluated, and for the consistency of results, this parameter must be less than a critical value depending on the number of participating laboratories. Based on these statistical tests, which are smaller than 1 for all participants, all the results are considered valid to calculate a reference value and associated uncertainty (Figure 4. 2) [3].

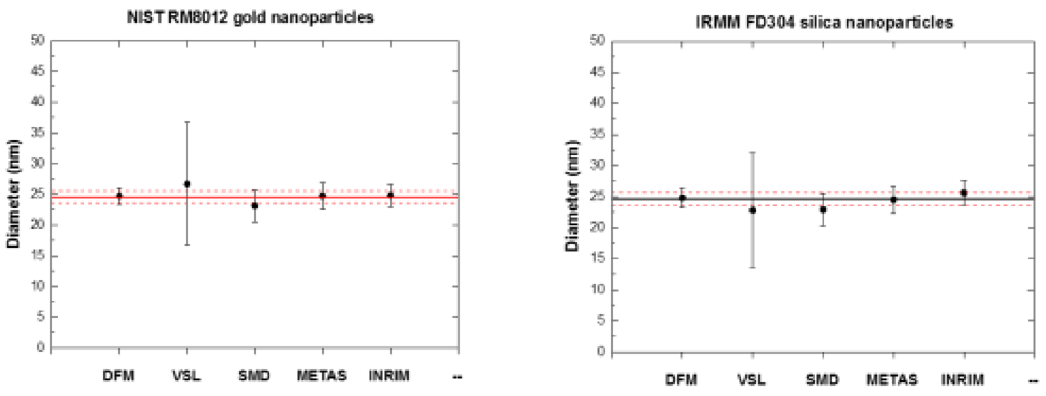

Figure 4. 2 Plots representing the measurement results compared to the reference value in gold and silica NPs. Note that the error bars indicate a 95% level of confidence. Reprinted with permission from [253]. Copyright © 2019 EURAMET. All Rights Reserved.

4.4 Complex Geometry Nanoparticles

We have seen that spherical NP is measured sufficiently accurately by AFM, through the determination of the mean diameter as the top height of the cross-section profile of isolated NP or as the pitch of packed NPs. To date, only RMs based on spherical geometry NPs certified by NIST and IRMM are commercially available (Section 1.5).

As reported in Section 1.4, a variety of samples are available on the market at the nanoscale, such as step-height and groove-depth samples, 1D and 2D gratings, line-width samples, spherical and cylindrical mono- and multi-modal nanoparticles stored in aqueous and/or stabilised suspensions [51]. New nano-samples are continuously being developed in laboratories and NMIs to fully meet new measurement needs, which require the cost-effective dissemination and traceable 3D characterization of shapes and sizes.

Traceability and dissemination of nanoscale RMs is of considerable interest, as demonstrated by several completed European projects like 3DNano [254], SETNanoMetro [255], and nPsize [256].

The "3D Nano – Traceable three-dimensional nanometrology" project overall goal of this project is to (i) establish new routes for traceability, (ii) develop new calibration artefacts and made them available to industry as traceable reference standards to enable valid comparison of fabrication and measurement results, and (iii) establish a robust basis for design of objects with traceable nanoscale dimensions and tolerances. Moreover, the project aims to further develop SPM instrumentation, measurement procedures, data interpretation and reference materials to bridge the gap between SPMs and the rest of 3D metrology, as proper understanding of probe-sample interactions is crucial for the reduction of measurement uncertainty [254]. As reported in Chapter 3, within this project I studied TMVs as tip characterizers, and I theoretically investigate tip–sample–substrate interactions by using different models of contact mechanics.

The "SETNanoMetro – Shape-engineered TiO_2 nanoparticles for metrology of functional properties: setting design rules from material synthesis to nanostructured devices" project develops well defined and controlled protocols for the production of TiO_2 NPs, and determine NPs properties with various measurements techniques by establishing the correct metrological traceability chain in order to ensure the reliability of the results [255].

Titanium dioxide (TiO_2) is a material widely employed in several fields, such as the production of varnishes and paints, food colouring, cosmetic dye, and sun filter. Moreover, due to its photoinduced antibacterial and hydrophilic properties, it is used to produce self-cleaning surfaces [257], with commercial applications in automotive, medical equipments and protective clothing. Furthermore, because of its thermodynamic properties, TiO_2 is a semiconductor widely used as a water splitting photocatalyst for hydrogen production [258].

The lack of international measurement standards for calibration is an aspect of particular relevance in nanotechnology, as it is difficult to select a universal calibration artefact to achieve repeatability at nanoscale. The materials produced according to such procedures, will be hence sufficiently characterised and homogeneous in their properties to become candidate Certified Reference Materials to be used in various applications where the lack of metrological traceability in (i) environment, for improving the photocatalytic properties for the treatment of pollutants in air and water, (ii) energy, for improving the traceability of DSSC measurements, and (iii) health, for improving traceable production of TiO_2 nanostructured coatings in orthopaedic and dental prostheses [255].

The "nPsize – Improved traceability chain of nanoparticle size measurements" project develop methods, reference materials and modelling to improve the traceability chain, comparability and compatibility of nanoparticle size measurements to support standardization by using SEM, TSEM, TEM, AFM and SAXS techniques. Moreover, the project develop validated nanoparticle reference materials with (i) non-spherical shapes, (ii) non monodisperse size distributions and (iii) accurate concentrations [256].

Within this framework, the novel element reported in this dissertation is the development of new methods for traceable dimensional characterization of NPs with complex geometry. For non-spherical particles, the only techniques that can be used to robustly reconstruct critical dimensions are microscopic ones, because non-imaging methods (Section 1.5) give indirectly only an equivalent spherical diameter.

In my thesis, I used a metrological AFM that gives direct traceability to critical sizes. AFM measures of complex-shaped NPs are non-trivial because complex geometries highlight the limits caused by the finite tip shape. To make traceable measurements of 3D sizes new methods are required, which must be easily translatable for measuring bulk nanostructures with different shapes. Anatase bipyramids and nanosheets are complex shape NPs which have particular geometries that allow them to be potential reference for their critical sizes (CSs) [259]. These shape-controlled anatase TiO_2 NPs [260,261] were synthesized by the group of Professor Valter Maurino of the "Università degli Studi di Torino".

Shape-controlled TiO_2 anatase NPs with different shapes (nanosheets and bipyramids) are obtained by tuning the parameters used in the synthesis. These nanoparticles. TiO_2 anatase bipyramids and nanosheets are studied here as candidate reference materials [261].

TiO_2 anatase nanoparticles are synthetised by hydrothermal methods using a 200 mL Teflon lined stainless-steel reactor. More specifically, nanosheets are obtained by using titanium butoxide as precursor in an acid environment at 250°C for 24 h, as described in [260,261]. Truncated bipyramids are fabricated by using a complex of Ti(IV) with triethanolamine as precursor, in basic condition with a temperature of about 220°C, for 50 hours with a method similar to that reported in [262]. The post-synthesis treatment to obtain nanopowders is made by dialysis plus freeze-drying, in order to wash the NPs and eliminate the solvent [262].

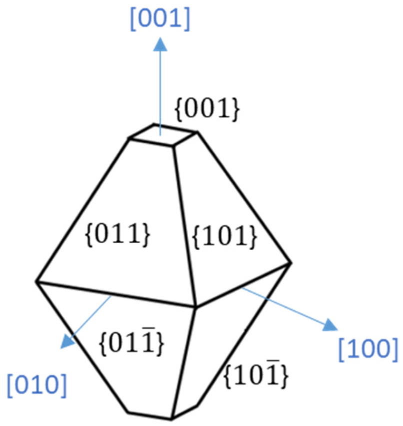

Figure 4. 3 Equilibrium shape using the Wulff construction for TiO_2 anatase crystals. Note that in blue square brackets are reported the crystalline axes, while in curly brackets are given the anatase crystalline facets.
Reprinted with permission from [2]. Copyright © 2022 Elsevier. All Rights Reserved.

In Figure 4. 3 the equilibrium shape is sketched using Wulff construction, that considers the surface energies of the crystal surfaces in the growth medium, for TiO_2 anatase crystals [263]. For the anatase phase, the equilibrium shape is a slightly truncated tetragonal bipyramid enclosed by eight thermodynamically stable {101} facets and two {001} facets, with an interfacial angle ϑ = (68.3 ± 0.3)° from X-ray diffraction measurements [264].

By tuning the synthesis parameters, anatase crystals with different characteristics are obtained. In fact, nanobipyramids have an elongated truncated tetragonal bipyramidal shape, while nanosheets are squashed along the [001] axis. This difference in shape is also expressed in the orientation in which they are arranged on the mica substrate, and consequently also in the way in which the CSs are calculated (Section 4.4.1).

For preparing the samples to be analyzed by mAFM, the nanopowder is dispersed into MilliQ water creating a suspension of 3 $mg{\cdot}L^{-1}$, which is put in an ultrasonic bath for 5 hours for disagglomerating the NPs. For a sample with isolated nanoparticles well dispersed onto an ultraflat substrate, a drop of 20 μL of suspension is deposited onto a freshly cleaved mica support, with 10 mm diameter, and let it dry to air and stabilize for at least 12 hours. The samples are then stored into plastic boxes and kept at a stable temperature of (20.0 ± 0.1) °C. Once the sample is mounted on the mAFM sample holder, a few hours of thermal stabilization are needed before any measurement is taken [2].

In the next two Sections, the description of the geometric model for critical sizes and morphological parameters determination and quantification for both bipyramids and nanosheets are reported. Please note that the sizes are quantitatively analyzed, together with an uncertainty budget.

4.4.1 Bipyramids

In Figure 4. 4 a sketch of the anatase bipyramid nanoparticle with a squared base and a truncated geometry, the interfacial angle ϑ, and the critical sizes are reported.

The sizes descriptors of TiO_2 bipyramids are b, that corresponds to the “breadth” of the particle, and c, which is the “length” of the NP.

Figure 4. 5 displays a topography focused on an isolated bipyramid as reconstructed by the mAFM. The 3D images at the top show the critical sizes in examination. The topography is measured by using INRiM mAFM set-up with the following measurement conditions: μMasch NSC15/AlBS tip, 1.5 V free amplitude, set point at 60%, (512 × 512) pixel density, (300 × 300) nm measurement area, 20% oversize, scanning speed at 100 nm·s^{-1}, measurement time of 60 minutes, and laboratory temperature of 20.05 °C and humidity of 50%.

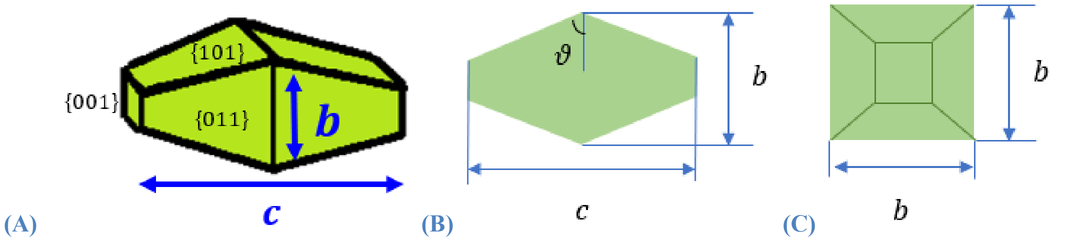

Figure 4. 4 (A) Not-to-scale 3D sketch, (B) side and top views, and (C) front-view of a TiO$_2$ bipyramid. Adapted with permission from [2]. Copyright © 2022 Elsevier. All Rights reserved.

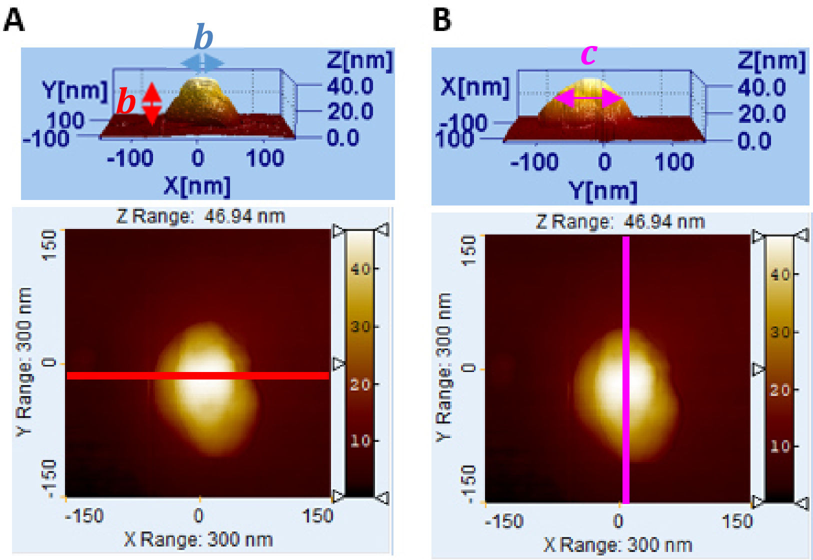

Figure 4. 5 2D and 3D images of a bipyramid made with mAFM, with (A) ‘b’ and (B) ‘c’ sizes. Reprinted with permission from [2]. Copyright © 2022 Elsevier. All Rights Reserved.

The geometrical model is based on two assumptions: (i) the bipyramid, due to its intrinsic nature, has a square base, and (ii) the tip has an isotropic shape at the apex. The tip has an anisotropic shape (trihedral) if we consider its global size (on the order of tens of micrometres), but at its very end of tens of nanometers at the tip apex, its shape is assumed to be isotropic.

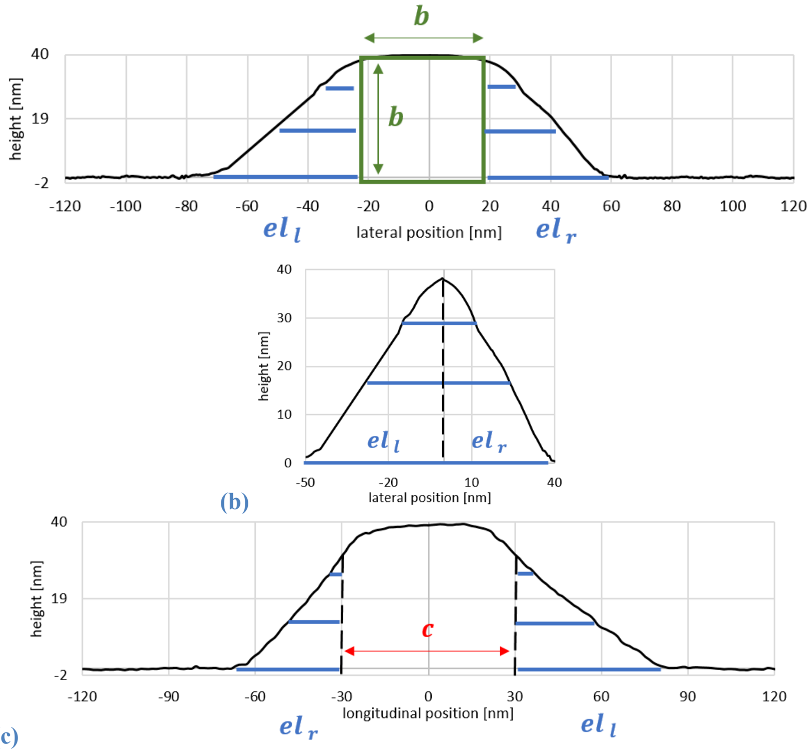

Figure 4. 6 Not-to-scale sketches illustrating the geometric approach to determine the bipyramid critical sizes.

(A) Cross-section profile along the minor bipyramid axis reporting the square base with side length "b" and the left/right tip enlargement el_l and el_r
(B) Tip dilation profile obtained by deleting the square of Figure 4. 6 (a)
(C) Cross-section profile along the major bipyramid axis reporting the determination of the critical size "c"
Reprinted with permission from [3]. Copyright © 2022 Springer Nature. All Rights Reserved.

As reported in the sketch in Figure 4. 6, from the analysis of the cross-section top profile along the X axis is defined the square side b, as the thickness and lateral length at the center of the profile (Figure 4. 6 (A)). The blue segments outside the square describe the dilation based on the tip, and a tip dilation profile can be extracted on the basis of the union of the right and left enlargement segments el_r and el_l (Figure 4. 6 (B)). Instead, the size c is obtained by deleting the tip enlargement segments el_r and el_l from the cross-section top profile along the Y axis (Figure 4. 6 (C)).

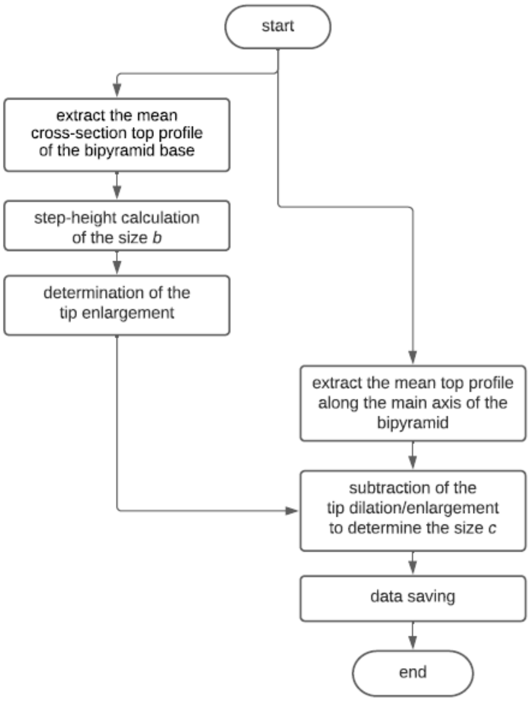

Figure 4. 7 Flowchart describing the main steps in calculating the critical sizes of the bipyramid. Reprinted with permission from [2]. Copyright © 2022 Elsevier. All Rights Reserved.

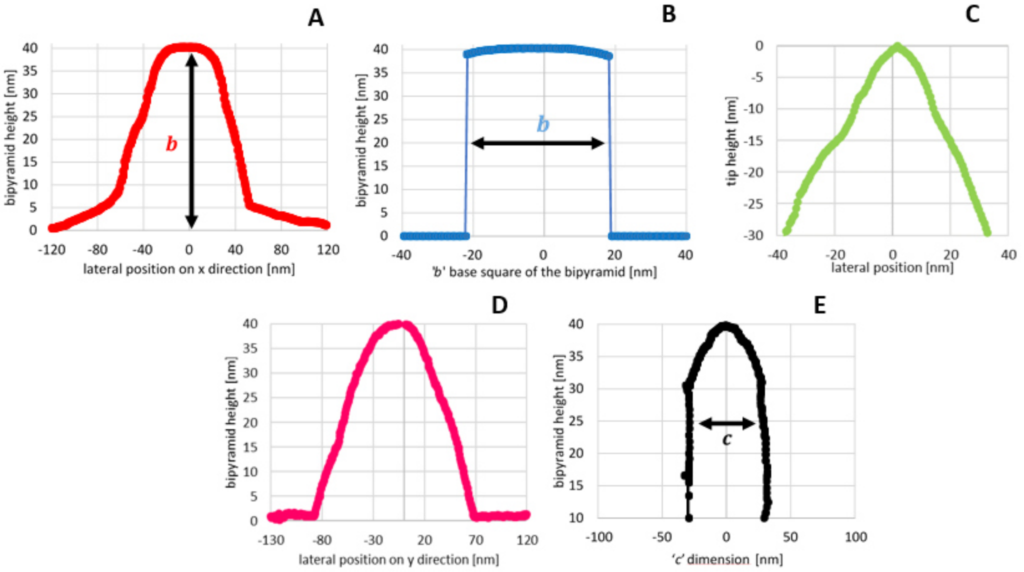

Figure 4. 8 Process steps in the determination of bipyramid critical sizes:
(A) Mean cross-sectional top profile at the bipyramid base;
(B) The size b of the square base of the bipyramid;
(C) Tip enlargement as estimated by A and B;
(D) Mean longitudinal profile along the axis of the bipyramid;
(E) The size c as obtained by subtracting C from D.
Reprinted with permission from [2]. Copyright © 2022 Elsevier. All Rights Reserved.

The process outlined in the flowchart in Figure 4. 7 is implemented and tested in a new own developed program, discussed in detail in Annex A. To let the operator know if the process steps in the calculation of bipyramid CSs are properly made, the “A” to “E” profiles in Figure 4. 8 are subsequently calculated and displayed.

After tilting removal and rotation of the image to have the NP’s axis along the Y-axis of the image, the maximum z-height of the NP’s topography is searched along the X-lines of the image in order to find and build the top cross-section profile of the NP. To minimize the influence of spikes, five X-lines around the maximum z-heights of the image are averaged in a single profile (Figure 4. 8 (A)), from which the size b, i.e., the step-height of the profile, is calculated according to the ISO 5436 [265].

Since the bipyramids have a square base, a length b of the profile at the top of the cross-section (Figure 4. 8 (B) is taken, while all the other parts of the cross-section are set equal to the mean z-height of the baseline (clean mica surface) if it has not yet removed its z-offset. In this way, the profile of the square base of the bipyramid is achieved, which is not dilated by the tip geometry.

This geometric approach also permits the determination of the tip enlargement (Figure 4. 8 (C)). To depict it, the length b of the profile in correspondence of the bipyramid base in Figure 4. 8 (A) is simply deleted; in other words, the base of the square b is not considered from the profile in Figure 4. 8 (A).

After that, the longitudinal section profile along the axis of the bipyramid (Figure 4. 8 (D)), *i.e.* the Y-axis of the image, is extracted. Again, five Y-lines of the image are averaged to minimize noise and spike effects. In order to obtain the size **c** (Figure 4. 8 (E)), the tip dilation profile (Figure 4. 8 (C)) up to the z-heights of the bipyramid terminations is subtracted to the mean longitudinal profile (Figure 4. 8 (D)).

The choice to not consider the last 10 nm in Figure 4. 8 (C) and at Figure 4. 8 (E) is due to the fact that non-tip artefacts may be present in these regions [149].

Please note the Figure 4. 6 (B) and Figure 4. 8 (C) are equivalent, as they depict the profile due to the tip dilation.

Once more, one has to consider the inclined lying of the bipyramid on the mica substrate. Since the bipyramid lays on a $\{101\}$ facet (Figure 4. 9 (A)), the measured size b_{meas} of the base is corrected according to the sine of the interfacial angle of the anatase crystal, which value is ϑ = (68.3 ± 0.3)° from crystallographic measurements. The lying of the bipyramid is confirmed by AFM measurements of the angle between the ascent segment and the top constant segment of the bipyramid profile along the Y scan axis direction, resulting in 2ϑ = (136.9 ± 10.2)° as (mean value ± standard deviation).

Similarly, the measured c_{meas} is corrected for the cosine of the angle γ, as reported in Figure 4. 9 (B).

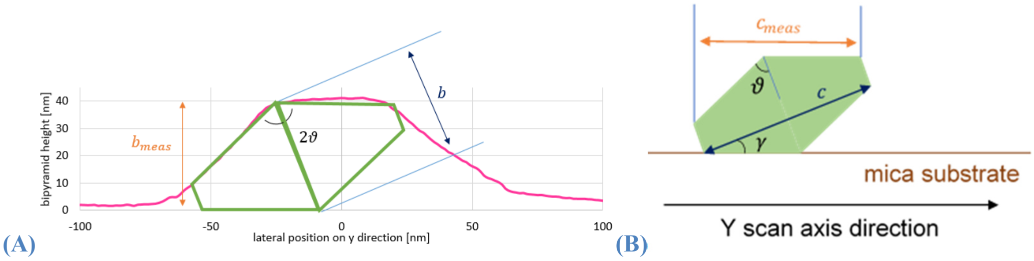

Figure 4. 9 (A) Profile along the Y scan axis direction with a side-view sketch of bipyramid laying onto substrate highlighting the correction of the size ‘b’. (B) Not-to-scale side-view sketch of nanobipyramid laying onto mica substrate substrate highlighting the correction of the size ‘c’. Reprinted with permission from [2]. Copyright © 2022 Elsevier. All Rights Reserved.

The analysis on 106 images (106 bipyramids) gives the sizes b = (43.2 ± 3.4) nm and c = (58.2 ± 5.2) nm as (mean value ± standard deviation). These results are in good agreement with the analysis performed in a similar sample, but of a different batch [266]. Figure 4. 10 shows the histogram distribution for the two bipyramids measurands. It is worth noting that both bipyramid CSs have a dispersion that is narrow and monomodal, and so b and c dimensions are sufficiently homogeneous, to be applied as candidate reference material.

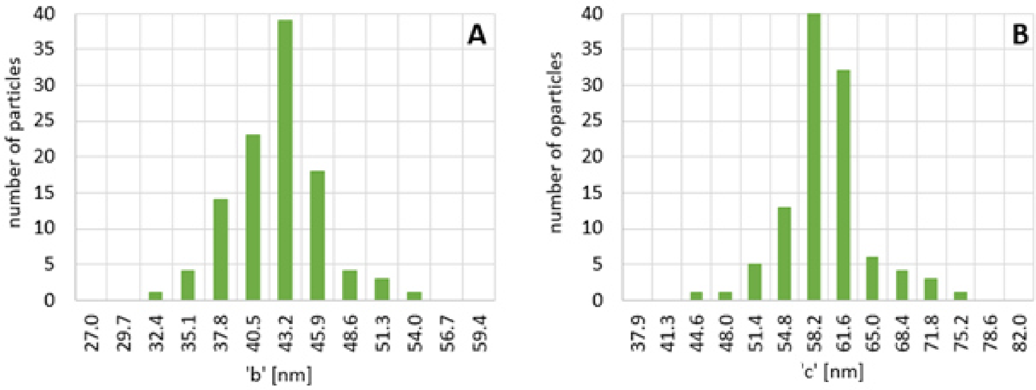

Figure 4. 10 Critical sizes of bipyramids: (A) size ‘b’ and (B) size ‘c’. Reprinted with permission from [2]. Copyright © 2022 Elsevier. All Rights Reserved.

Table 4. 3 Uncertainty budget of the bipyramid 'b' size.
Adapted with permission from [2]. Copyright © 2022 Elsevier. All Rights Reserved.

quantity $\boldsymbol{X_i}$	**estimate** $\boldsymbol{x_i}$	**standard uncertainty** $\boldsymbol{u(x_i)}$	**unit**	**PDF**	**degrees of freedom** $\boldsymbol{\nu_i}$	**sensitivity coefficient** $\boldsymbol{c_i}$	**standard uncertainty** $\boldsymbol{u_i(b)}$ **[nm]**
repeatability b_m	43.2	0.3	nm	N	106	C_z	0.3
C_z factor	1	0.01	-	N	50	b_m	0.4
reference plane δ_{pl}	0	1.2	nm	R	20	1	1.2
levelling δ_{lev}	0	0.3	nm	R	50	1	0.2
tip-sample-substrate interactions δ_{int}	0.4	0.1	nm	R	50	1	0.1
correction for bipyramid laying δ_{lay}	0	0.8	nm	R	50	1	0.8
mechanical drifts δ_{str}	0	0.3	nm	R	50	1	0.3
					combined standard uncertainty $\boldsymbol{u_c(b)}$		**1.6**
					degrees of freedom ν_{eff}		75
					coverage factor k		2.025
					expanded uncertainty $\boldsymbol{U(b)}$		**3.2**

Table 4. 4 Uncertainty budget of the size of the bipyramid ‘c’.
Adapted with permission from [2]. Copyright © 2022 Elsevier. All Rights Reserved.

quantity X_i	**estimate** x_i	**standard uncertainty** $u(x_i)$	**unit**	**PDF**	**degrees of freedom** ν_i	**sensitivity coefficient** c_i	**standard uncertainty** $u_i(b)$ **[nm]**
repeatability c_m	58.2	0.5	Nm	N	106	C_X	0.5
C_X factor	1	0.02	-	N	50	c_m	1.4
correction for bipyramid laying δ_{lay}	0	0.9	Nm	R	80	1	0.9
tip dilation size δ_{dil_b}	0	1.6	Nm	R	50	1	1.6
tip dilation wear δ_{dil_w}	0	1.6	Nm	R	50	1	1.6
					combined standard uncertainty $u_c(c)$		**2.8**
					degrees of freedom ν_{eff}		110
					coverage factor k		2
					expanded uncertainty $U(c)$		**5.6**

Table 4. 3 reports the uncertainty budget of the bipyramid b measured as the thickness of the X-axis cross-section profile. The adopted model equation is $b = C_z \cdot b_m + \delta_{pl} + \delta_{lev} + \delta_{int} + \delta_{lay} + \delta_{str}$. Note that the overall size is $b = 1 \cdot 43.2$ nm + 0 nm + 0 nm + 0.4 nm + 0 nm + 0 nm = 43.6 nm.

The uncertainty associated to the measurement repeatability b_m is the standard deviation of the mean thickness calculated on 106 samples. The standard deviation of the mean is calculated by dividing the standard deviation of the population ($s =$

3.4 nm) by the square root of the number of samples (N = 106), so $u(b_m) = \frac{s}{\sqrt{N}} = \frac{3.4\text{ nm}}{\sqrt{106}} = 0.3$ nm. I considered the mean as the unknown parameter of the population with the hypothesis that the distribution is normal.

This repeatability term also considers the rotation of the structures.

The C_z factor considers (i) the calibration, that takes into account the interferometric calibration of the Z axis including cosine errors ($0.5 \times 10^{-4}L$), (ii) the piezoelectric non-linearity (0.5 nm), (iii) the profile noise (0.3 nm), measured as Rq of mica along the X-direction profile, and (iii) the resolution of the D/A converter (0.1 nm) on the piezoelectric stroke of 2 μm; this last contribution is negligible. Note that the previous values reported in brackets refer to normal and rectangular distributions resulting in a combined standard uncertainty of the C_z factor of $1 \cdot 10^{-2}$, including constant and proportional terms calculated at the nominal b size of 43.2 nm of the bipyramid base.

The reference plane correction δ_{pl} assumed with zero mean value refers to the error in the definition of the substrate plane. Since b is defined as top-height measurement, one has to be careful to define the height of baseline, *i.e.* the mica surface. This contribution was evaluated by repeating five times the baseline definition in the same image for ten different images.

The levelling of the substrate δ_{lev} is evaluated through a method that considers the variation of the thickness value b after the tilting of the substrate orientation for an angle of 1°. More precisely, starting from a position in which the substrate is levelled, the thickness variation is studied by varying the angle from -0.5° to 0.5°.

The correction δ_{int} due to the interactions between the tip, the sample and the substrate is assumed with an uncertainty contribution calculated from the maximum error. Tip-sample and tip-substrate interactions are elastic terms, while sample-substrate deformation is elastoplastic. Note that tip-substrate and tip-sample deformations are calculated by using the Hertzian model [195] considering the silicon tip apex as a sphere with a radius of 8 nm, the mica substrate as a plane, and approximating the NP resting on the mica to a cylinder with a radius equal to the bipyramid size b and a length equal to the size c. Note that these negligible elastic interactions (~ 0.02 nm) compensate to each other.

The adhesion interaction between the bipyramid and the mica is calculated using the Chaudhury model [187], which describes the interaction between a cylinder (the bipyramid) and a plane (the mica), obtaining a deformation δ_{int}= 0.4 nm.

Please note that these models do not consider complex geometries, but we have reasonably approximated the bipyramid by using its critical sizes in order to estimate the entity of the interactions. In fact, contributions due to tip-sample-substrate interactions are not so relevant, since both TiO_2 anatase NPs and Si tip are stiff/hard materials.

Note that the parameters used in the calculations are (i) the elastic moduli E_{TiO_2}= (237 ± 3) GPa [267], E_{Si} = (170 ± 5) GPa [226], E_{mica} = (190 ± 20) GPa [225], and (ii) the Poisson ratios ν_{TiO_2}= (0.27 ± 0.02) [268], ν_{Si}= (0.22 ± 0.01) [228], and ν_{mica}= (0.25 ± 0.01) [225].

The bipyramid laying onto mica substrate is corrected as previously described, while the uncertainty of the correction is evaluated by varying the interfacial angle ϑ of ± 5°.

The uncompensated mechanical drifts refer to the straightness, that reports the variation of Rt profile along Y axis onto mica before and after line-wise correction tool. It is assumed with a zero mean value and an uncertainty equal to the straightness, as mentioned above.

Table 4. 4 reports the uncertainty budget for the bipyramid c size, which model equation is $c = C_X \cdot c_m + \delta_{lay} + \delta_{dil_b} + \delta_{dil_w}$. Note that the overall size is $c = 1 \cdot 58.2$ nm + 0 nm + 0 nm + 0 nm = 58.2 nm.

The repeatability considers the standard deviation of the mean of the 106 bipyramids analyzed.

The X-size factor C_X deals with (i) the interferometric calibration of the X axis, optical non-linearity of 1 nm («the nonlinearity of interferometer, which is caused by the interferometer structure and the nonlinearity of optical and electrical components» [269]), Abbe (parallax) error of $5 \times 10^{-3}L$, where L is the lateral displacement of the stage, dead-path error of 0.5 nm, «caused by an uncompensated length of the laser beam between the interferometer and the retroreflector» [270], that can occur when environmental conditions vary during the measure, (ii) the uncertainty of the image side, that considers the pixel size (1 nm), depending by the resolution and dimensions of the images, and (iii) the resolution of the D/A converter (<0.1 nm), this latter negligible. Note that the values reported in brackets refer to normal and rectangular distributions resulting in a combined standard uncertainty of the C_X factor of $2.3 \cdot 10^{-2}$, including constant and proportional terms calculated at the nominal c size of 58.2 nm of the bipyramid length.

The uncertainty of the correction for bipyramid laying δ_{lay} is evaluated by varying the interfacial angle ϑ of ± 5°.

The uncertainty of the tip dilation correction takes into account (i) the uncertainty due to the size b, δ_{dil_b}, which is used for calculate c according to the assumptions made in the geometrical approach, and (ii) the tip wear δ_{dil_w}, evaluated through the analysis of the lateral enlargement of the dilation profile taken by the same tip on subsequent images. In fact, size c is calculated by taking the average profile Y and subtracting the tip, whose geometry depends on size b. At a height of 20 nm, the tip dilation has a value of about 10 nm, and his uncertainty contribution is evaluated as a rectangular maximum error.

In Section 1.4 the main characteristics of a reference material are described, that are homogeneity and stability evaluated according to the ISO Guide 35:2017 [49]. The model equation for a certified reference material is $X_{CRM} = X_{char} + \delta X_{hom} + \delta X_{lts}$, where X_{CRM} is the property value, X_{char} is the property value obtained from its experimental characterisation, δX_{hom} is the error term due to the homogeneity of the material, and δX_{lts} is the error term due to the long-tem stability of the material. Assuming the indepence of the variables, the combined standard uncertainty associated with the property value of a CRM is expressed as $u_{CRM} = \sqrt{u_{char}^2 + u_{hom}^2 + u_{lts}^2}$.

Being a guide and not a written standard, the indications in ISO Guide 35:2017 may not be followed rigidly, as it only provides guidelines. This is because this Guide is manly intended for chemical-based characterisations, in fact, some examples reported regards the homogeneity study of a CRM for chromim in soil and anions in river water. The uncertainty associated with heterogeinty is given by $u_{homog} = \sqrt{u_{wb}^2 + u_{bb}^2}$, where the estimated standard deviation of the within-bottle term is $s_{wb}^2 = s_r^2$, where s_r is the repeatability standard deviation, while the between-bottle term u_{bb}^2 depends on the number of observations for each group.

In my study, I analyzed physical quantities (critical sizes) for complex-shaped non-spherical nanoparticles candidate reference materials, and I did not consider the term due to homogeneity in the combined standard uncertainty formula u_{CRM}. This is because homogeneity is included in the term due to repeatability of the measurements in the previously reported uncertainty budgets (Table 4. 3 and Table 4. 4), since in sample preparation I started from a mother suspension and I deposited them onto mica substares, so the homogeneity studied is always linked to the homogeneity in mother suspension (within-bottles homogeneity). Another reason for my choice is due to the fact that I analyzed a single batch; to make a more rigorous evaluation, measurements from different batches should be compared.

Regarding the uncertainty due to long-term stability, it is evaluated as a rectangular distribution for both bipyramid sizes (Figure 4. 11).

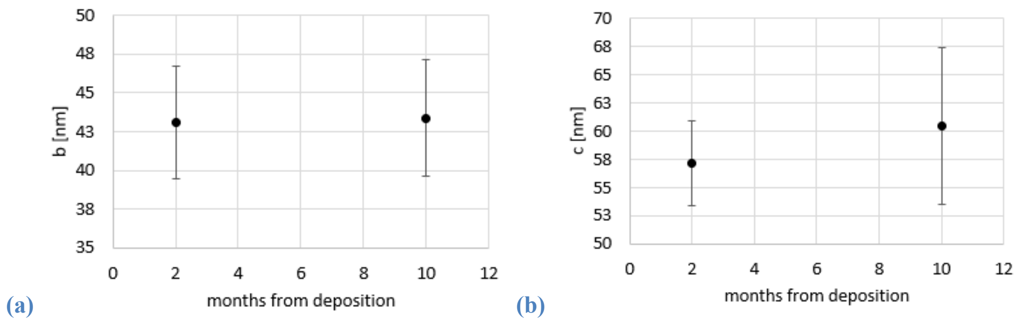

(a) (b)

Figure 4. 11 Stability plot for the analysis of bipyramid 'b' size (plot (a)) and 'c' size (plot (b)) of the same sample after 2 and 10 months from the deposition of the suspension on the mica substrate. Error bars refer to the standard deviation of measurements.

So, the combined standard uncertainty accounting for homogeneity and stability for bipyramid critical sizes evaluated as $u_{CRM} = \sqrt{u_{char}^2 + u_{lts}^2}$ is $u_{CRM\ b} = 1.5$ nm and $u_{CRM\ c} = 3.3$ nm.

It is worth recalling that at the nanoscale uncertainty components can be of the same order of magnitude of the measurand, while for example in macroscale measurements the uncertainty can be 5-6 orders of magnitude smaller than the measurand value.

The morphological parameters chosen for describing the bipyramids are the shape descriptors presented in Table 4. 5. These parameters are some of the descriptors early reported in an interlaboratory comparison by TEM measurements performed on a different batch of anatase bipyramids [[271]]. These shape parameters facilitate the identification and quantitative comparison of the same feature from data taken by different instruments, as seen in Section 4.4.2.

Table 4. 5 Shape descriptors for bipyramid analysis.
Adapted with permission from [2]. Copyright © 2022 Elsevier. All Rights Reserved.

Morphological parameters	Equation	Explanation
Elongation	$El = \frac{c}{b}$	ratio of the maximum to the minimum size
aspect ratio	$AR = \frac{b}{c}$	inverse of the elongation
projection area	$A = \pi \cdot \frac{b}{2} \cdot \frac{c}{2}$	bipyramid projection area calculated as elliptical area by using the two available CSs
Roundness	$Rnd = \frac{A}{\pi \left(\frac{c}{2}\right)^2}$	ratio of the bipyramid area to the circular area, it describes the resemblance to a circle 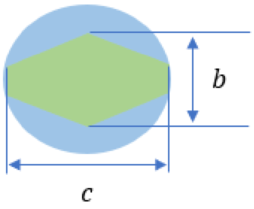
Bulkiness	$B = \frac{A}{c \cdot b}$	ratio of the bipyramid area to the rectangular area defined by the CSs, it describes the resemblance to a rectangle 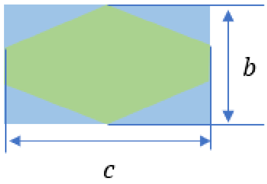
Compactness	$cmp = \frac{d}{c} = \frac{\sqrt{\frac{4 \cdot A}{\pi}}}{c}$	ratio of the equivalent circular diameter to the size c, it describes the resemblance of the NP diameter to that of circle with the same area 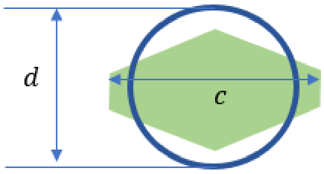

In Table 4. 6 are reported the shape descriptors calculated by the analysis of all 106 bipyramids. It can be noticed that these nanoparticles resemble for the 80% to a rectangular area (bulkiness ~ 0.8), for the 80% to a diameter of a circle with the same area (compactness ~ 0.8), and they resemble for the 70% to a circle (roundness ~ 0.7). Moreover, an elongation ~ 1.4 (and so and aspect ratio of about 0.7) indicates a bipyramid with a perfect truncated shape [262], so the study of these two descriptors is very important to understand the quality of the batch synthetized. In fact, through these shape descriptors, it is possible to know if bipyramids from different batches can be able to be applied as reference materials [2].

Table 4. 6 Shape descriptors calculated for 106 bipyramids. Values are reported as (mean value ± standard deviation).
Reprinted with permission from [2]. Copyright © 2022 Elsevier. All Rights Reserved.

Descriptor		**Unit**	**AFM measurements**
projected area	A	[nm^2]	1970 ± 220
aspect ratio	AR	-	0.7 ± 0.1
elongation	El	-	1.4 ± 0.2
roundness	Rnd	-	0.7 ± 0.1
bulkiness	B	-	0.8 ± 0.1
compactness	cmp	-	0.8 ± 0.1

4.4.2 Nanosheets

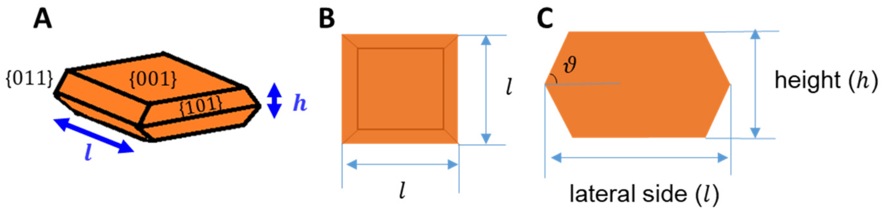

Figure 4. 12 Not-to-scale 3D sketch of a TiO_2 nanosheet (A), its view from above (B), and side-view (C). Reprinted with permission from [2]. Copyright © 2022 Elsevier. All Rights Reserved.

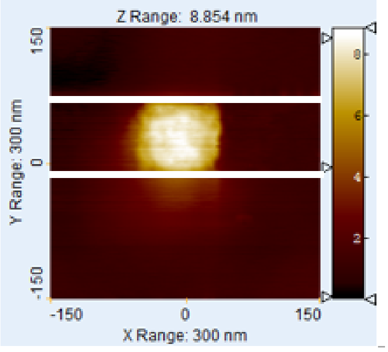

Figure 4. 13 Nanosheet imaged by mAFM.
Reprinted with permission from [2]. Copyright © 2022 Elsevier. All Rights Reserved.

In Figure 4. 12 (A) is reported a 3D sketch of a TiO_2 nanosheet, which highlights the presence of a large {001} crystalline facet. Nanosheets also have a bipyramid shape but with a truncated "length" along the [001] axis, now called height h, and a square base of side l, as illustrated in Figure 4. 12 (B, C).

These anatase nanoparticles have a truncated tetragonal bipyramidal shape squashed along the [001] axis; the peculiarity of these NPs is a height much smaller than the lateral size of the two end {001} facets, one exposed and the other laying onto the mica substrate.

Figure 4. 13 displays a topography centered on a single nanosheet. The topography is measured by using INRiM mAFM set-up with the following experimental conditions: μMasch NSC15/AlBS tip, 1.5 V free amplitude, set point at 60%, (512 × 512) pixel density, (300 × 300) nm measurement area, 20% oversize, scanning speed at 100 $nm \cdot s^{-1}$, measurement time of 60 minutes, laboratory temperature of 20.0 °C and humidity of 45%.

The geometric approach for the study of the lateral sizes is based on two assumptions depending on the crystalline structure of the anatse: (i) truncated tetragonal bipyramidal shape squashed along the [001] axis, and (ii) known interfacial angle $\vartheta = (68.3 \pm 0.3)°$ from X-ray measurements.

The geometric model for processing the nanosheets is outlined on the sketch in Figure 4. 14. The flowchart in Figure 4. 15 reports the main steps for the calculation of the critical sizes; a more detailed description of the program implemented in MATLAB environment is found in Annex B. The blue line represents the mean cross-section profile of the nanosheet, which is calculated as the mean of the X-line profiles within the white lines in Figure 4. 12, *i.e.*, the part of the image with the exposed facet area of the nanosheet.

In order to find the critical sizes, the edge points $\mathrm{P_l}$ and $\mathrm{P_r}$ are determined as the intersection of linear regression lines fitting parts of the top and of the left/right sidewalls of the mean cross-section profile. The fitting line at the top part of the profile considers all points with Z-heights from 90% to 100% of the maximum height of the profile, while the points with heights from 60% to 80% are taken for the fitting lines of the left/right sidewall parts of the profile. A repeatability better than 95% has been determined for the edge points P position, varying by 10% the Z-heights of the left/right sidewall to be taken for the fitting lines.

The height h of the nanosheet is therefore assumed as the mean of the Z-heights of the two edge points P, providing that the mean height of the profile in correspondence of the mica substrate is at zero height. The size of the top base of the nanosheet l_{top} is given by the lateral (X) distance between the edge point and the center of the nanoparticle.

To further check the consistency of these sizes, the segment $f_i = \frac{h-h_i}{\tan\vartheta}$ is calculated at various heights h_i between ${}^{h}/_{2}$ and h, and the left lateral size $\left({}^{l}/_{2}\right)_{\mathrm{l}}$ of the nanosheet is obtained by the sum of $l_{top\,l} + f$ at the half-height ${}^{h}/_{2}$. Again, use is made of the known interfacial angle ϑ = (68.3 ± 0.3)°.

Thus, the left side tip enlargement e_l at various heights can be obtained as the difference between the measured lateral position along the cross-section profile $X_{l\ i}$ and the sum of the segments $l_{top\,l}$ and f_i.

The same calculation is performed for the right side of the profile, for obtaining the right lateral side $\left({}^{l}/_{2}\right)_{\mathrm{r}}$ and the tip enlargement e_r at the right side of the nanosheet.

The lateral dimension l is defined as the sum of $\left({}^{l}/_{2}\right)_{\mathrm{l}}$ and $\left({}^{l}/_{2}\right)_{r}$, while the tip enlargement profile is obtained by the sum of the segments $e_{l\ i}$ and $e_{r\ i}$ at the same height h_i.

In addition, image processing and the calculation of sizes are repeated for the Y-axis cross-section profile of the nanosheet. Therefore, the height h and size l are the average values of those calculated from the X and Y cross-section profiles of the nanosheet.

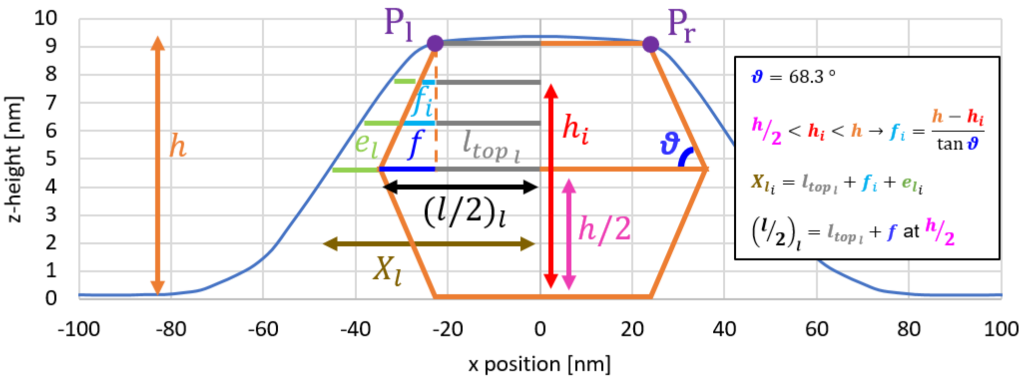

Figure 4. 14 Not-to-scale sketch illustrating the geometric approach to determine nanosheet sizes. The blue line indicates the mean cross-sectional profile, the orange figure pictures a side view of a nanosheet, and the rows represent the segments involved into the geometrical analysis. Reprinted with permission from [2]. Copyright © 2022 Elsevier. All Rights Reserved.

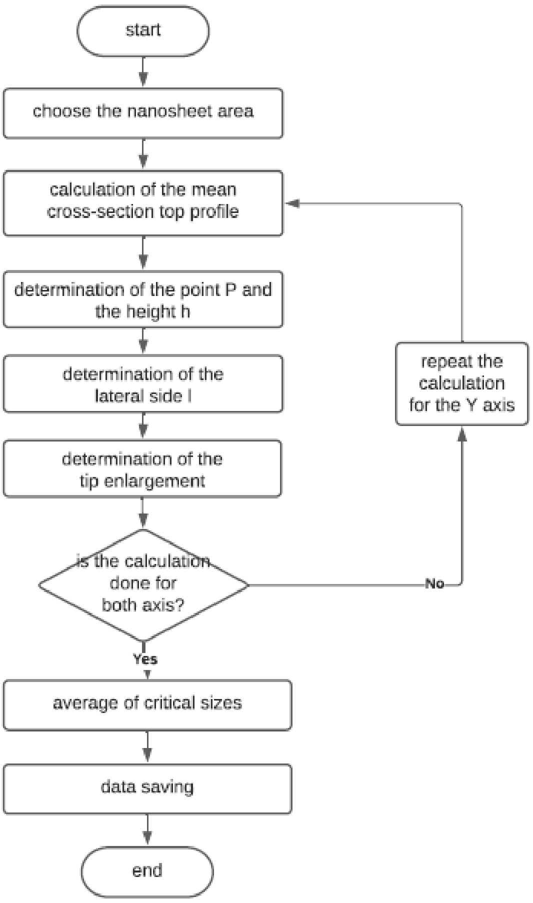

Figure 4. 15 Flowchart describing the calculation of the nanosheet critical sizes. Reprinted with permission from [2]. Copyright © 2022 Elsevier. All Rights Reserved.

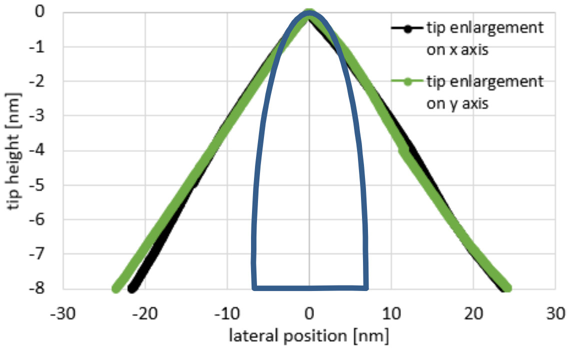

Figure 4. 16 Tip dilation profiles on the X and Y axes of a nanosheet. The blue line represents a tip with nominal radius of 8 nm. Reprinted with permission from [2]. Copyright © 2022 Elsevier. All Rights Reserved.

Figure 4. 16 compares the enlargement of the tip for X and Y profiles obtained by the analysis of a nanosheet, showing a good agreement between the two profiles. This figure supports the assumption of AFM tips with an isotropic shape at the apex, also assumed with the AFM images of the bipyramids (Section 4.4.1).

By assuming the nominal half-angle of 20° at the tip apex and the crystalline angle of nanosheets of 68.3°, a small area of interaction between the tip and the surface is expected when scanning {001} facet, while a large area of interaction can occur at the edges of the nanosheets.

Thus, the reconstructed tip enlargement profile (obtained with the geometrical approach) reflects such a lateral tip-sample interactions preventing a proper reconstruction of the tip shape. For comparison, the tip shape with a nominal radius of curvature of the has been added in Figure 4. 16. However, it must be remembered that the geometrical approach reconstructs the profile of the enlargement due to the tip and not the tip shape, since to estimate the true shape and critical sizes of a particle, it is necessary to know the effect of the tip shape on the image, rather than the tip shape [168].

A final consideration that can be made is that the advantage of using such a geometrical model is the ability to analyze quantitatively selected measurands of isolated non-spherical NPs in a robust, repeatable and fast way. soft easily modified for determining some crucial sizes of isolated NPs with other non-spherical geometries, such as nanorods and/or nanocubes, therefore also the programs developed in MATLAB can be easily modified.

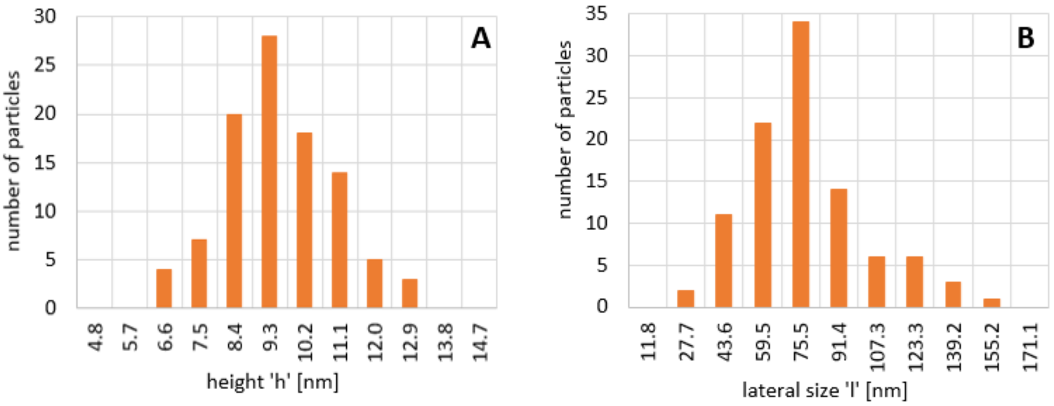

Figure 4. 17 Critical sizes of nanosheets: (A) height ‘h’ and (B) lateral size ‘l’. Reprinted with permission from [2]. Copyright © 2022 Elsevier. All Rights Reserved.

100 nanosheets are imaged with the mAFM. The results, displayed in Figure 4. 17, are h = (9.3 ± 1.4) nm and l = (75 ± 26) nm. The large standard deviation of the size l is due to the inhomogeneity of the synthetic process.

The results of the mAFM measurements are well in agreement with those of the same batch analyzed by means of TSEM, by which height value h = (9.4 ± 1.6) nm and lateral values l = (75 ± 25) nm were reported [261]. Please note that all the above values are given as (mean value ± standard deviation).

As shown in the histroygrams, the distributions of both CSs of the nanosheets are monomodal, but while the height h has a narrow dispersion, the lateral dimension is more dispersed (the standard deviation of l is very large) due to the growth of the crystals during the synthesis.

For this reason, only the height h can be applied as a reference size at the nanoscale.

The model equation for the height of the nanosheets is $h = C_z \cdot h_m + \delta_{pl} + \delta_{lev} + \delta_{int} + \delta_{lay} + \delta_{str}$, and in Table 4. 7 the uncertainty budget table is given. Note that the overall thickness is h = 1 · 9.3 nm + 0 nm + 0 nm + 0.3 nm + 0 nm = 9.6 nm.

The repeatability, Z-heights, substrate levelling, reference plane, and uncompensated drifts uncertainty sources are evaluated as reported for the budgets previously described in Table 4. 3.

The tip-substrate interaction is equal to that reported in Section 4.4.1, while the elastic tip-sample interaction is $\alpha_{tip-sam}$ = 0.02 nm whether the interaction is calculated between a spherical tip and a nanosheet considered as (i) a plane or (ii) a cylinder with a very large diameter.

Table 4. 7 Budget of uncertainty of the nanosheet height ‘h’.
Adapted with permission from [2]. Copyright © 2022 Elsevier. All Rights Reserved.

quantity X_i	**estimate** x_i	**standard uncertainty** $u(x_i)$	**unit**	**PDF**	**degrees of freedom** ν_i	**sensitivity coefficient** c_i	**standard uncertainty** $u_i(b)$ **[nm]**
repeatability h_m	9.3	0.1	nm	N	100	C_z	0.1
C_z factor	1	0.05	-	N	50	b_m	0.4
reference plane δ_{pl}	0	0.5	nm	R	50	1	0.5
levelling δ_{lev}	0	0.3	nm	R	50	1	0.3
tip-sample-substrate interactions δ_{int}	0.3	0.1	nm	R	50	1	0.1
mechanical drifts δ_{str}	0	0.2	nm	R	50	1	0.2

combined standard uncertainty $u_c(h)$	**0.8**
degrees of freedom ν_{eff}	150
coverage factor k	2
expanded uncertainty $U(h)$	**1.5**

Sample-substrate adhesion are equal to $\alpha_{sam-sub\ \mathrm{Chaudhury}} = 0.30$ nm, considering the nanosheet as a cylinder with radius equal to the height h and length equal to the lateral side l. The same considerations done for the bipyramids are also valid for the nanosheet, and we have demonstrated that tip-sample-substrate deformations are not so relevant; moreover, it must be considered that the adhesion terms are always overestimated.

Table 4. 8 Budget of uncertainty of the nanosheet lateral side 'l'.
Adapted with permission from [2]. Copyright © 2022 Elsevier. All Rights Reserved.

quantity X_i	**estimate** x_i	**standard uncertainty** $u(x_i)$	**unit**	**PDF**	**degrees of freedom** ν_i	**sensitivity coefficient** c_i	**standard uncertainty** $u_i(b)$ **[nm]**
repeatability l_m	75	2.6	nm	N	100	C_X	2.6
C_X factor	1	0.02	-	N	50	c_m	1.3
tip dilation isotropy $\delta_{dil\,iso}$	0	2.0	nm	N	20	1	2.0
tip dilation wear $\delta_{dil\,w}$	0	1.6	nm	R	20	1	1.6
					combined standard uncertainty $u_c(l)$		**3.7**
					degrees of freedom ν_{eff}		140
					coverage factor k		2
					expanded uncertainty $U(l)$		**7.4**

Table 4. 8 reports the uncertainty budget of the nanosheets lateral dimension l, in which is considered the repeatability in the analysis of 100 nanosheets. The X-size contribution is evaluated as described for the budget in Table 4. 4, while the dilation of the tip is due to (i) the tip wear $\delta_{dil\,w}$, evaluated as explained above, and (ii) the isotropy of the tip, evaluated through the analysis of the lateral enlargement of the dilation profile taken by the same tip on subsequent images along the X and

Y scan axes. Note that the model equation is $l = C_X \cdot l_m + \delta_{dil_w} + \delta_{dil_{iso}}$, and the overall lateral size $l = 1 \cdot 75$ nm + 0 nm + 0 nm = 75 nm.

The combined standard uncertainty that accounts for homogeneity and stability (Figure 4. 18) for nanosheets critical sizes, evaluated as described in Section 4.4.1, is $u_{CRM\ h}$ = 0.8 nm and $u_{CRM\ l}$ = 9.4 nm.

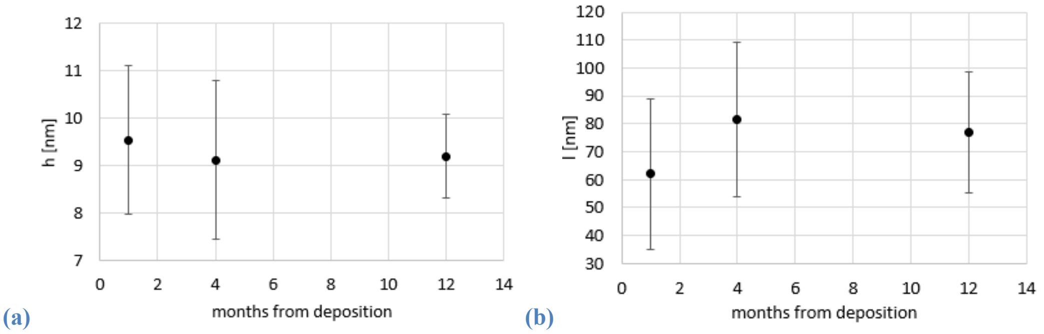

Figure 4. 18 Stability plot for the analysis of nanosheet 'h' size (plot (a)) and 'l' size (plot (b)) of the same sample after 1, 4 and 12 months from the deposition of the suspension on the mica substrate. Error bars refer to the standard deviation of measurements.

For characterizing nanosheets with surface texture descriptors, the roughness of the {001} exposed crystalline facet, either by profile [241] and areal texture parameters [242] (Section 4.4.2), is quantitatively studied.

I decided to study the roughness of a candidate reference nanoparticle because it is important to have a material used as parameter reference. In fact, at the nanoscale level, roughness is very important in the AFM study in various fields, such as in tribology, in the correlation between friction coefficient and roughness height-amplitude parameters [272], and in material science, in the study of the performance and behavior of a material to a specific treatment [273].

The roughness of anatase TiO_2 is extensively studied in literature for polycrystalline films, which rms (Rq) values range from a few to tens of nanometers depending on the sample thickness [274]. A functional characteristic of TiO_2 films depending on nano-roughness is the wettability, that strongly depends on the texture and size of crystalline domains [275].

In studying the surface roughness and texture of nanosheets, I made use of amplitude parameters, calculated on the length/size of the profile/area of the nanosheet surface without further cut-off filters, and a hybrid parameter, which calculation is based on local Z-slope. For comparison, both profile roughness R and areal texture S parameters texture are reported.

Table 4. 9 Roughness parameters of 100 nanosheets, calculated as (mean value ± standard deviation). Reprinted with permission from [2]. Copyright © 2022 Elsevier. All Rights Reserved.

descriptor	**profile**	
	mica	**nanosheet**
Ra [nm]	0.14 ± 0.04	0.3 ± 0.1
Rq [nm]	0.17 ± 0.05	0.4 ± 0.1
Rz [nm]	0.6 ± 0.3	1.4 ± 0.4
Rsk	0.1 ± 0.6	-0.6 ± 0.6
Rku	2.5 ± 0.7	2.6 ± 0.7

Table 4. 10 Texture parameters of 100 nanosheets, reported as (mean value ± standard deviation). Reprinted with permission from [2]. Copyright © 2022 Elsevier. All Rights Reserved.

descriptor	**areal**	
	mica	**nanosheet**
Sa [nm]	0.14 ± 0.04	0.3 ± 0.1
Sq [nm]	0.17 ± 0.05	0.4 ± 0.1
Sz [nm]	1.0 ± 0.4	2.1 ± 0.6
Ssk	0.1 ± 0.5	-0.6 ± 0.5
Sku	3.2 ± 0.9	3.1 ± 0.7
Sdr [%]	0.05 ± 0.03	0.2 ± 0.1

In addition, a quantitative characterisation of the surface texture parameters on the nanosheets {001} exposed facet and on mica substrate is presented in Table 4. 9 and Table 4. 10. To determine these parameters, the mAFM image of each nanosheet is tilted to minimize the inclined plane of the image. After that, an area and a profile are extracted both onto mica substrate and in the centre of the nanosheet, to analyze only the {001} facet.

Moreover, a line-wise offset correction (LMS fit of degree zero) is made for each area extracted using the SPIP tool. Line-wise distortions are typical scanning artefact like steps between subsequent scan lines occurring when changing from outward to inward direction of the tip scanning or by some tip contaminations along scanning.

In Table 4. 9 and Table 4. 10 the parameters calculated on the NPs and substrate surfaces are compared, and it can be noticed that the profile roughness parameters Ra and Rq are practically the same as the areal parameters Sa and Sq, since both are isotropic surfaces.

Mica has a Rq (rms) roughness of about 0.2 nm, as reported in literature [276], while the nanosheets' surface presents a larger roughness also in agreement with those in the range of 0.22 nm to 0.88 nm given for anatase single crystals [277].

Compared to average values, the rms Rq and Sq values are more sensitive to the presence of local surface peaks and valleys, which are even more highlighted by the Rz and Sz peak parameters. To understand if these surface variations are peaks or valleys, that can be broad or sharp, skewness and kurtosis parameters are investigated.

The skewness Rsk and Ssk rely on the asymmetry of the profile and areal texture. Skewness with positive or negative values means that peaks or valleys are present, while a null (zero) skewness characterizes a symmetrical texture around the mean plane.

The kurtosis Rku and Sku measure the sharpness of the surface texture. A kurtosis greater or lower than three represents sharp or broad textures, while if equal to three the height distribution is Gaussian, with the coexistence of sharp and indented portions.

With the nanosheets, the kurtosis is around three for the areal parameters (normal distribution of peaks and valleys), while the profiles show the presence of broader peaks and valleys.

Skewness is slightly positive for the mica substrate, while for the nanosheets is slightly negative. The negative skewness, confirming the presence of valleys, can be due to the possible presence of lattice vacancies on the anatase crystals [260,278]. These vacancies can lead to the presence of larger space defects on the nanosheet surface, since each nanoparticle is a single crystal. Please note that the behavior of a crystal at the boundaries can be different from the behavior at bulk. This because grain boundaries have a lower density, as in the same volume unit the number of atoms is reduced, and the probability to have crystalline defects on the surface is higher.

The surfaces area ratio Sdr is an index of the "complexity" of the surface, since it expresses the increment of the interfacial surface area (the real surface) relative to the area of the projected plane (that is, the reference planar surface). Sdr = 0% for a totally flat surface, since the real surface and the reference area are the same, while is greater if gradient components of several degrees are present. Nanosheets have a value of Sdr = 0.2%, which indicates, together with low Sa and Sq values, that the nanosheets have a roughness low enough to be used as a reference in nanometrology.

4.5 Tip Dilation Determination

When the AFM tip interacts with the sample, the surface height at the apex of the tip is recorded, whereas the true surface of the sample may lie at a different location. Dilation arises from the finite size and geometry of the tip, and it is pronounced when the sizes of the sample and tip are similar.

For the estimation of the tip shape by using the BR method implemented in MATLAB by Flater et al. [205], a square pillar with a flat top is selected as the initial estimate. After initializing the parameters, the algorithm iterates through all possible contact points to estimate the best shape of the tip. Optimizing the tip matrix size and the threshold value parameters is important to obtain the best estimate of the tip shape. The tip matrix size must have the same lateral dimension as the largest object imaged in the topography. The threshold parameter establishes a tolerated level of inconsistency between the image and the tip estimate. These values are proportional to the image z-range; if they are too low, then the tip reconstruction is dominated by the image noise, whereas if they are too high, then no features on the image are sharp enough to be applied in the calculation of the tip shape.

The comparison on the estimation of the shape of a commercial tip between BR software, which is proposed by Flater et al. [205], and the geometric approach developed in this work is shown in Figure 4. 19. These reconstructions refer to the analysis of the same bipyramid image.

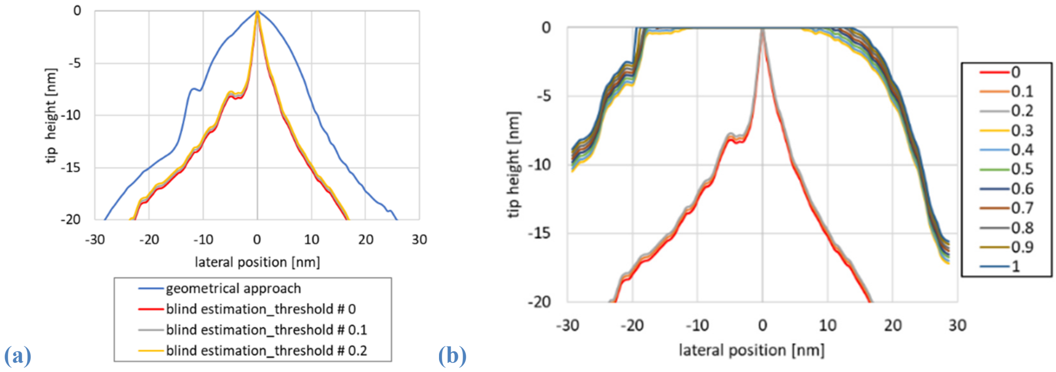

Figure 4. 19 (a) Comparison between BR and geometric approach for tip shape estimation (b) Tip shape estimation profiles after threshold refinement (in the legend, the refined threshold numbers are reported).
Reprinted with permission from [3]. Copyright © 2022 Springer Nature. All Rights Reserved.

In estimating the tip shape, the parameters set in the Flater software include (i) a tip matrix size of 100 pixels, (ii) a number of thresholds of 20, and (iii) a threshold step size of 0.05. The tip shape is equal to 5% of the NP height, obtaining a threshold step size of 2.35 nm. Then, a refinement of thresholds is made to obtain a threshold step size of 0.235 nm. Figure 4. 19 shows three profiles obtained with a smaller step size.

As shown in Figure 4. 19 (a), the BR method estimates a shape sharper than the shape obtained by the geometric approach (lateral difference of about 30%), but the two methods analyze the same nanoparticle in a reasonable way because both methods reconstruct the same image artifact (small peak at the left side). Notably, BR software struggles during the erosion of the initial square pillar (Figure 4. 19 (b)). For threshold numbers higher than 0.3, the tip shape estimate is not significantly different from the original square pillar, whereas for smaller threshold numbers, tip reconstructions are dominated by image noise and tend to be unrealistically sharp in the absence of a more realistic reconstruction of the tip shape. The lateral offset (Figure 4. 19 (a)) is due to the different reconstruction methods. Using the geometrical approach, a conical shape is reconstructed, and the outcome of the BR may transform from a square pillar-like shape to an unrealistic sharp shape. Scanning a known tip characterizer is advantageous because the sample sizes can be reconstructed by correcting the sampled image with the known shape. On the contrary, the BR method reveals an upper boundary of the tip geometry only, but in reality, tip characterizers are not infinitely sharp.

Moreover, the BR method consumes a high computation time (the reconstruction takes about 24 h using a personal computer with 8 GB RAM and a 3.40 GHz processor because of the high number of pixels and threshold for the estimation of the tip shape).

Therefore, based on tip shape analysis from AFM topographies centered on single NPs deposited onto flat substrates, the geometric approach is a suitable option. On the contrary, in the analysis of AFM images with a rougher substrate and several NPs, the BR method is recommended. The geometric method is developed primarily to study critical sizes of isolated NP, following the reconstruction of the tip dilation profile [3].

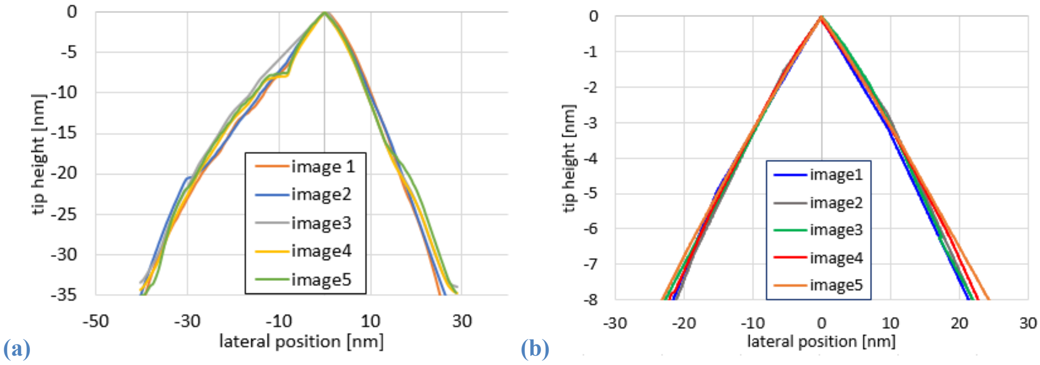

Figure 4. 20 Tip dilation profiles of 5 subsequent measurements performed on (a) bipyramids and (b) nanosheets.

Finally, in Figure 4. 20 (a) is reported a comparison between the enlargement profiles of the same tip scanning 5 subsequent independent images of bipyramids, with a maximum lateral dispersion of about 5 nm. Analogous results are obtained from the nanosheets measurements, as reported in Figure 4. 20 (b).

Conclusion and Future Perspectives

Nanometrology plays a key role in nanoscience and nanomanufacturing, since it allows to produce traceable and accurate results, ensuring the quality of products down to the nanoscale. Developments in nanomanufacturing, particularly in the nanoelectronics industry, pose increasing challenges in measuring nanostructures with ever smaller sizes and more complex 3D shapes. The dimensional parameters being measured include critical dimensions, size and shape, film thickness, and surface texture, that relates to chemical/physical/biological functional properties of patterned surfaces and nanomaterials.

Nanometrology enables the characterization of materials at the nanoscale by means of a large range of techniques. Among the various instrumental techniques, AFM directly provides a 2.5D reconstruction of NPs and nanostructures.

In this thesis, isolated NPs of different nature and shapes (quasi-spherical synthetic NPs, complex-shaped synthetic NPs, and cyilindrical biological nanostructures) are imaged by metrological AFM using standard tips, then analyzed by *ad-hoc* models to determine traceable measurements of their critical sizes.

Height measurements can be achieved with sub-nanometer accuracy and high resolution. Once the cross-sectioncross-section of the NPs is extracted, the average substrate baseline is subtracted from the peak height to find the top-height of NPs.

INRiM calibration measurement capability (CMC) on quasi-spherical NPs demonstrates our ability to measure cross-sectional top-height mean diameter. It is worth noting that our CMC is consistent with the capabilities of other NMIs for NPs with spherical shape.

Another shape studied is the cylindrical one, that of the Tobacco Mosaic Virus nanostructure. Since its cross-sectional diameter has a stable value, it is used as calibrator for reconstructing the dilation caused by the tip in lateral measures.

Note that the TMV diameter is $d = (17.7 \pm 1.2)$ nm, reported as (overall average diameter ± U). The overall average diameter comes from the mean top-height cross-section measurementcross-section of 120 TMVs performed by means of mAFM corrected for the tip–sample–substrate interactions evaluated by using different models of contact mechanics, while U is the expanded uncertainty of the mean at

95% confidence level. The total correction for the elastoplastic deformations is approximately 1.2 nm; thus, the difference between the X-ray and the overall average diameter is about 0.3 nm.

Then, my study focused on complex-shape NPs sizes made of TiO_2 in forms of bypiramids and platelets, which may be applied as candidate reference materials. Determining the size of non-spherical NPs by AFM is challenging because of the finite shape of the tip and the complex geometry of the NP. In this study, an approach based on intrinsic characteristics of the NP crystalline structure is presented.

The geometric approach developed for the analysis of bipyramid breadth b and length c is based on two assumptions: (i) the presence of a square base bipyramid caused by the anatase crystal, and (ii) the isotropy of the tip shape at its apex.

With the bipyramid lying on a $\{101\}$ facet onto the mica substrate, the side of its base is reconstructed from the AFM image as the top-height of the bypiramid cross-section, resulting on b = (43.6 ± 3.2) nm from 106 nanoparticle images. It is worth noting that the expanded uncertainty of the mean is primarily affected by the extraction from the cross-section of the reference baseline.

Besides, a mean length c = (58.2 ± 5.6) nm, *i.e.*, the size that lies on the major bipyramid axis, was determined with an expanded uncertainty of the mean influenced by the uncertainty of b, the correction of tip dilation, and the X-size term.

Nanosheet geometric analysis is based on the anatase interfacial angle, by which "slicing" the cross-section profile into various segments of known length is possible, describing the nanosheet lateral dimension and tip dilation.

The nanosheet thickness h = (9.6 ± 1.5) nm was determined from 100 particles, with an expanded uncertainty of the mean primarily affected by the definition of the reference plane and instrumental calibration. The lateral size is l = (75 ± 7.4) nm, and this size is strongly affected by the repeatability and tip dilation.

Please note that all the nanoparticles critical sizes indicated above are reported as (overall average diameter ± expanded uncertainty of the mean at 95% confidence level).

The uncertainties in complex geometric NPs are greater than those of spherical NPs because of the large distribution caused by the synthetic process. Lateral measurements with smaller uncertainties can be achieved by inspection of line width standard with CD-tips.

Notably, all the mean values of the measurands on the non-spherical NPs are consistent with those performed on the same batch by transmission-mode scanning electron microscopy.

Furthermore, study of homogeneity and stability for these complex shape NPs as potential candidate reference materials are performed according to ISO Guide 35. The results obtained as overall expanded uncertainty are ${U_{CRM}}_b = 3.0$ nm, ${U_{CRM}}_c = 6.6$ nm for bipyramids, and ${U_{CRM}}_h = 1.6$ nm, ${U_{CRM}}_l = 19$ nm for nanosheets. Please note that the overall expanded uncertainty U_{CRM} is obtained as $U_{CRM} = k \cdot u_{CRM}$, where $k = 2$ is the coverage factor at 95% confidence level and u_{CRM} is the combined standard uncertainty associated with the critical sizes.

Therefore, the geometric approach developed allows the quantitative analysis of selected measurands of isolated bipyramids and nanosheets in a robust and repeatable way. This geometrical model can be easily adapted to other non-spherical geometries, once the nominal dimensional characteristics based on the synthetic process of non-spherical NPs are known.

Moreover, a quantitative characterization of these complex shape NPs included the study of shape descriptors, which are morphological descriptors depending by CSs, and finiture descriptors depending on surface roughness. It is worth noting that these parameters make easier to quantitatively compare the same characteristic from data taken by different laboratories and/or instrumental techniques.

Further developments will concern the creation of a new “mixed sample” containing isolated spherical and non-spherical NPs and bio-based nanostrucutres deposited onto mica substrate, in order to have the presence of both tip calibrators and reference materials in a single sample.

Furthermore, by using the new AFM head, it will be possible to measure electromechanical properties on nanoparticles, biosamples, and polimers. Moreover, with the development of a new Z interferometer setup, it will be possible to develop a “multipurpose 3D mAFM”, which will link functional characteristics to dimensional measurements directly traceable to the SI.

Annex A. Program Implemented with MATLAB software describing the Geometrical Method for the Analysis of the Critical Sizes of Bipyramids measured by Atomic Force Microscopy

In the following pages, the program, based on the geometrical approach for bipyramid CSs reconstruction described in Section 4.4.1 and implemented in MATLAB software, is described. In order to clarify each step, the number of the code lines is reported together to some experimental plots.

Note that the Step 10 is taken from the software implemented by Flater [205].

%% Step 1: OPENING IMAGE

In this step, the BCRF image of the bipyramid (previously levelled with the SPIP software) is opened according to the instruction reported on `ReadImage` (Figure A. 1). The file ReadImage.m is a `function` which reads the AFM image defined by the parameter filename, which returns the variables `Immagine,xsize,ysize,xlen,ylen,bit2n,` that are an array containing respectively the image pixel intensity, pixel size in x and y directions, and the length of the axes in nm.

```
10  file_path = 'C:\Users\Documents\';          %USER SHOULD ENTER
    CONVIENENT STARTING file_path
11  [file_name,sourcepath] = uigetfile('*.*','Select an image for
    Geometrical Model Tip Reconstruction');
12  [~,name,ext] = fileparts([sourcepath,file_name]);
13  filename=strcat(sourcepath, file_name);

15  [fl,xsize,ysize,xlen,ylen,bit2nm] = ReadImage(filename);
    %opening image
```

Annex A. Program Implemented with MATLAB software describing the Geometrical Method for the Analysis of the Critical Sizes of Bipyramids measured by Atomic Force Microscopy

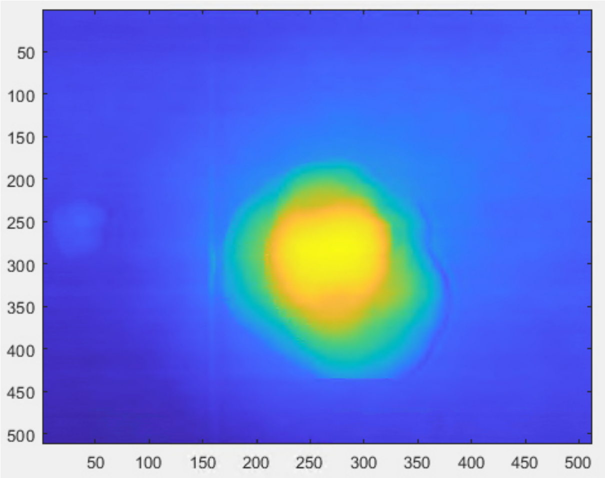

Figure A. 1 Bipyramid image to be analyzed; the x and y axes report the pixels.

The first operation to do is to convert the image axes from pixel to nm.

```
pixel_size = xlen/xsize;                         %pixel size in nm

x_axis_plot_nm=[1:xsize];
x_axis_plot_nm=x_axis_plot_nm/xsize*xlen;    %x axis of plots in nm
```

```
%% Step 2: CROSS_SECTION x profiles AT MAXIMUM POSITION
```

For measuring the mean cross-section top profile at the bipyramid base (along the X axis direction) the following steps are done:

1. Search the position of the maximum peak by finding the maximum for each row of the image;
2. In order to obtain a X cross-section profile that is not influenced by noise, 5 rows are averaged (the row which contains the maximum peak + the 2 rows before and the 2 rows after);
3. Before plotting the X cross-section profile, the minimum is set to zero.

Annex A. Program Implemented with MATLAB software describing the Geometrical Method for the Analysis of the Critical Sizes of Bipyramids measured by Atomic Force Microscopy

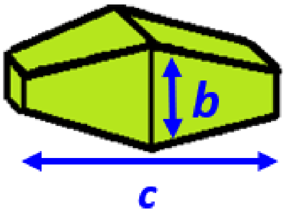

Figure A. 2 Sketch of bipyramids and its critical sizes.

Recall that the images are previously processed with the SPIP software, and they are rotated in order to have the minimum critical size *b* along the X direction, while the maximum critical size *c* is on the Y direction of the AFM image. The two critical sizes are depicted in Figure A. 2.

```
max_rows = max(fl')'; %find maximum for each row of the image
[z_max_rows, x_max_rows] = max (max_rows); %find maximum of maximums --> find position of maximum peak

for i= -2:1:2
    x_lines (i+3,:) = fl(x_max_rows+i,:);
end

profile_x = mean(x_lines);       % mean of 5 lines (the row which contains the maximum peak + the 2 rows before and the 2 rows after)
min_profile_x = min(profile_x);     % this passage is needed to set the minimum at zero
profile_x = profile_x - min_profile_x;

figure
plot(x_axis_plot_nm,profile_x,'LineWidth', 2);
axis ([0 inf 0 inf])
title('x-direction cross-section image profile');
xlabel('profile coordinate (nm)');
ylabel('bipyramid height (nm)');
```

Annex A. Program Implemented with MATLAB software describing the Geometrical Method for the Analysis of the Critical Sizes of Bipyramids measured by Atomic Force Microscopy

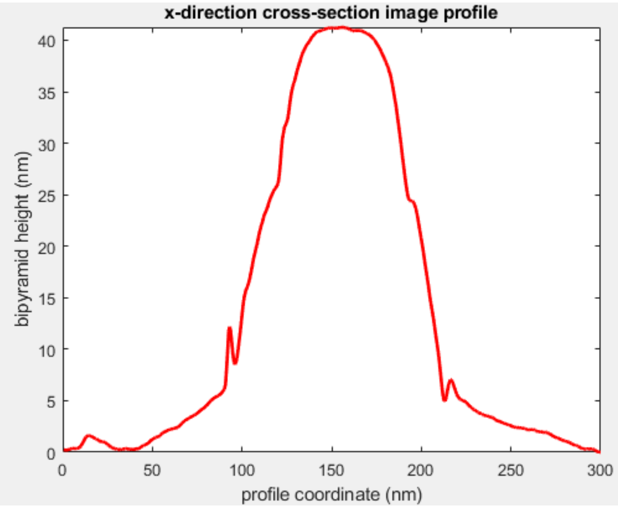

Figure A. 3 Mean cross-sectional top profile at the bipyramid base.

The mean cross-sectional top profile at the bipyramid base (Figure A. 3) is then saved in the first row of a matrix, while in the second row are reported the Z position in nm.

```
matrix_profile_x = (1:xsize) * pixel_size;           % in nm
matrix_profile_x = [matrix_profile_x; profile_x];  % matrix
2x512 --> row1: x position profile_x , row2: z profile_x
```

For obtaining a X cross-section profile centered on zero, the X profile is divided into ascent and descent branches that are subsequently concatenated. In an analogous way, the centered cross-section profile of the bipyramid on the X direction is saved and plotted.

```
[z_max, x_max] = max(profile_x);
profx_asc=profile_x(1:x_max);                        %left side of
the profile_x (ascent)
profx_desc=profile_x(x_max:numel(profile_x));        %right
side of profile_x (descent)
x_axis_profx_asc = [1:numel(profx_asc)]*pixel_size;  % x
position in nm
x_axis_profx_desc = [1:numel(profx_desc)]*pixel_size;  % x
position in nm

x_axis_profx_asc=x_axis_profx_asc-max(x_axis_profx_asc);
%this passage is needed to set the maximum at zero
x_axis_profx= [x_axis_profx_asc x_axis_profx_desc];
%concatenate x profiles of ascent and descent of the
profile_x
```

```
z_axis_profx= [profx_asc profx_desc];          %concatenate
z profiles of ascent and descent of profile_x
matrix_centered_profile_x=[x_axis_profx;z_axis_profx];
%profile x centered

figure
plot(x_axis_profx,z_axis_profx,'LineWidth', 2);
axis ([-inf inf 0 inf])
title('x-direction cross-section image profile');
xlabel('profile coordinate (nm)');
ylabel('bipyramid height (nm)');

x_max_nm=x_max*pixel_size;              %position x_max in nm
```

Please note that hereafter the phrase “ascent branch” refers to left side of the profile (from the beginning to the maximum of the profile), while “descent brasch” refers to the right side of the profile (from the maximum of the profile to its end).

```
%% Step 3: Step-height calculation according to ISO 5436
```

As reported in Section 4.3, the top-height diameter of a spherical nanoparticle is calculated from its cross-section by subtracting the average substrate baseline from the top-height.

ISO 5436 written standard describes how to extract the top-height from a square step or a groove. As depicted in Figure A. 4, the lateral length of the measured step profile must be at least 3 times the width W of the step. The height of the step is expressed as $h = C - \frac{A+B}{2}$, where A, B and C are the average heights of the profile regions that are large $W/_3$ [279].

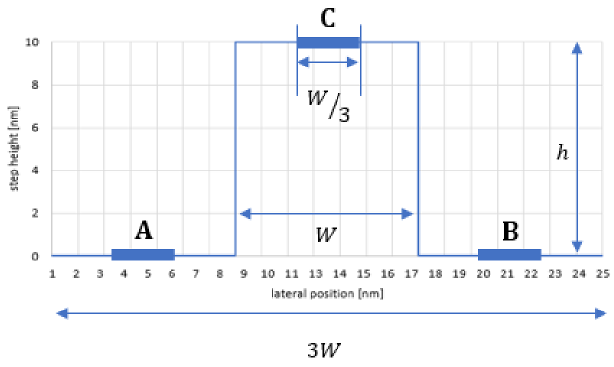

Figure A. 4 Sketch of a perfect step profile, in which the regions A, B and C are used for the calculation of the step-height “h” according to the ISO 5436.

Annex A. Program Implemented with MATLAB software describing the Geometrical Method for the Analysis of the Critical Sizes of Bipyramids measured by Atomic Force Microscopy

In order to calculate the height of a complex shape nanoparticle from its cross-section, an attempt is made to follow the ISO 5436 written standard, but it is not strictly applied because (i) it is not possible strictly follow the W/3 rule, and (ii) the cross-section of nanoparticles are not perfect steps. For this reason, the regions A, B and C are manually selected.

```
%select points for defining maximum
```

The first thing to do, is to manually select the extremes of the segments C from the X cross-section centered profile.

```
plot(x_axis_profx,z_axis_profx)
uiwait(msgbox('Click 2 points for defining the nanoparticle top'));
[x y] = ginput(2);
hold on;
plot(x, y, 'r+', 'LineWidth', 2);
```

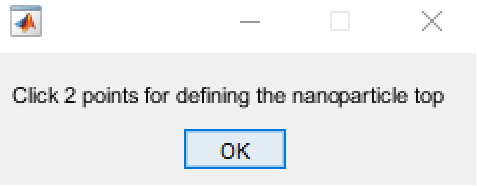

Click 2 points for defining the nanoparticle top

Subsequently, the values of the selected points `x1` and `x2` are estimated.

```
xFitted = x;
x1 = xFitted(1);
diff_x1 = matrix_centered_profile_x(1,:) - x1;     %matrix diff_x1 = matrix_centered_profile_x to which I subtract x1
[minValue_x1,closestIndex_x1] = min(abs(diff_x1));       %x position which value is the closest to the x1, in pixel
z1 = matrix_centered_profile_x(2,closestIndex_x1);
x2 = xFitted(2);
diff_x2 = matrix_centered_profile_x(1,:) - x2;     %matrix diff_x2 = matrix_centered_profile_x to which I subtract x2
[minValue_x2,closestIndex_x2] = min(abs(diff_x2));       %x position which value is the closest to the x2, in pixel
z2 = matrix_centered_profile_x(2,closestIndex_x2);
```

In order to avoid errors, it is checked that `closestIndex_x2` was greater than `closestIndex_x1`, otherwise their values are swapped.

```
if closestIndex_x2<closestIndex_x1
```

```
    temp = closestIndex_x2;
    closestIndex_x2 = closestIndex_x1;
    closestIndex_x1 = temp
end
```

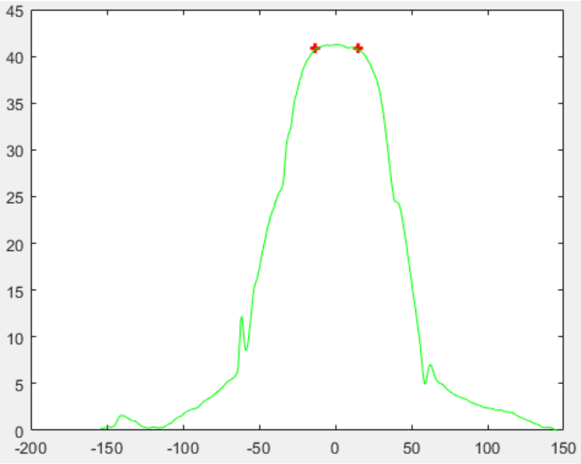

Figure A. 5 Mean cross-sectional top profile along the X axis. Red crosses represent the extremes of the segment that describes the top of the nanoparticle.

Finally, the points between the two extremes `x1` and `x2` are averaged to find the height at the top of the nanoparticle (Figure A. 5).

```
z_max = mean
(matrix_centered_profile_x(2,closestIndex_x1:closestIndex_x2));
```

In an analogous way, the segments A and B describing the substrate are also found.

```
%select points for defining the right minimum
```

```
plot(x_axis_profx,z_axis_profx)
uiwait(msgbox('Click 2 points for defining the right
minimum'));
[x y] = ginput(2);
hold on;
plot(x, y, 'r+', 'LineWidth', 2);

xFitted=x
x1 = xFitted(1);
diff_x1 = matrix_centered_profile_x(1,:) - x1;     %matrix
diff_x1 = matrix_centered_profile_x to which I subtract x1
[minValue_x1,closestIndex_x1] = min(abs(diff_x1));        %x
position which value is the closest to the x1, in pixel
```

```
z1 = matrix_centered_profile_x(2,closestIndex_x1);
x2 = xFitted(2);
diff_x2 = matrix_centered_profile_x(1,:) - x2;     %matrix
diff_x2 = matrix_centered_profile_x to which I subtract x2
[minValue_x2,closestIndex_x2] = min(abs(diff_x2));        %x
position which value is the closest to the x2, in pixel
z2 = matrix_centered_profile_x(2,closestIndex_x2);

if closestIndex_x2<closestIndex_x1
    temp = closestIndex_x2;
    closestIndex_x2 = closestIndex_x1;
    closestIndex_x1 = temp;
end

z_min_right = mean
(matrix_centered_profile_x(2,closestIndex_x1:closestIndex_x2));
```

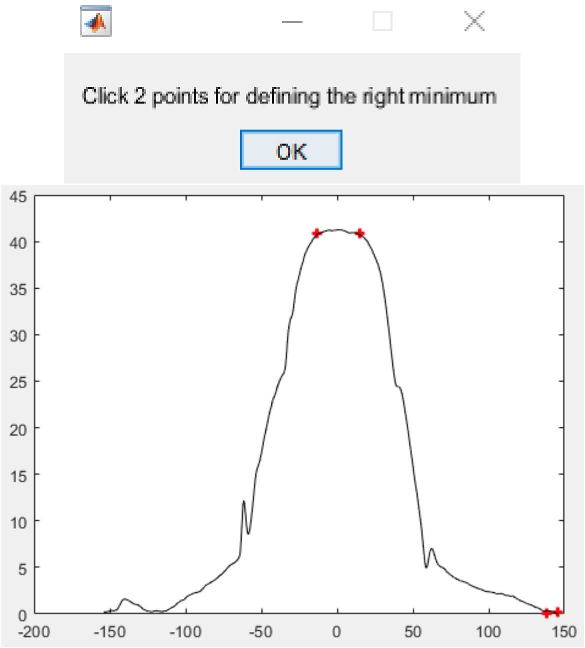

Click 2 points for defining the right minimum

Figure A. 6 Mean cross-sectional top profile along the X axis. The red crosses on the right represent the extremes of the segment describing the right minimum.

```
%select points for defining the left minimum
```

```
plot(x_axis_profx,z_axis_profx)
uiwait(msgbox('Click 2 points for defining the left minimum'));
[x y] = ginput(2);
hold on;
plot(x, y, 'r+', 'LineWidth', 2);
```

```
xFitted = x;
x1 = xFitted(1);
diff_x1 = matrix_centered_profile_x(1,:) - x1;     %matrix
diff_x1 = matrix_centered_profile_x to which I subtract x1
[minValue_x1,closestIndex_x1] = min(abs(diff_x1));        %x
position which value is the closest to the x1, in pixel
z1 = matrix_centered_profile_x(2,closestIndex_x1);
x2 = xFitted(2);
diff_x2 = matrix_centered_profile_x(1,:) - x2;     %matrix
diff_x2 = matrix_centered_profile_x to which I subtract x2
[minValue_x2,closestIndex_x2] = min(abs(diff_x2));        %x
position which value is the closest to the x2, in pixel
z2 = matrix_centered_profile_x(2,closestIndex_x2);

if closestIndex_x2<closestIndex_x1
   temp = closestIndex_x2;
   closestIndex_x2 = closestIndex_x1;
   closestIndex_x1 = temp;
end

z_min_left = mean
(matrix_centered_profile_x(2,closestIndex_x1:closestIndex_x2));
```

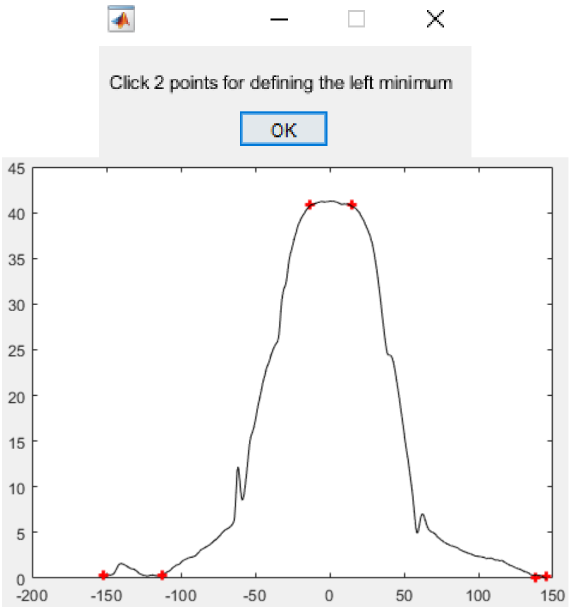

Click 2 points for defining the left minimum

Figure A. 7 Mean cross-sectional top profile along the X axis. The red crosses on the left represent the extremes of the segment describing the left minimum.

The baseline height is calculated as the average heights of the two segments A and B, depicted in Figure A. 6 and Figure A. 7.

```
z_min = (z_min_right+z_min_left)/2 ;
```

Finally, the NP height is calculated as the difference between the top height and the baseline height.

```
h = z_max - z_min ; %bipyramid step-height
```

```
%% Step 4: Set the SQUARE BASE at the bipyramid (size 'b')
% Note that b is the min size of the bipyramid
```

Since the bipyramids have a square base, the height `h` previously calculated is set equal to the lateral critical size `b`.

```
b = h; %Note that we set b = h
```

Sometimes, it happens that the maximum peak does not correspond to the central symmetry point of the square. To find this point, the height `z_cal` is taken into consideration, calculated to be 10 % lower than the maximum height, in order to do the mean of the right and left points in nm. These last two positions are defined as the point in the ascent/descent profile which height z minimizes the difference (in absolute value) between the profile and the value taken into consideration.

```
z_cal= h -(10/100*h);

x_axis_profx_asc = [1:numel(profx_asc)]*pixel_size;  % x
position in nm
diff_z_sx_nm = profx_asc - z_cal;
[minValue_z_sx_nm,closest_z_sx_nm] = min(abs(diff_z_sx_nm));
%closest left point coordinates
x_sx_nm=x_axis_profx_asc(closest_z_sx_nm);
%position x of z_sx_nm

diff_z_dx_nm = profx_desc - z_cal;
[minValue_z_dx_nm,closest_z_dx_nm] = min(abs(diff_z_dx_nm));
%closest left point coordinates
x_dx_nm=x_axis_profx_desc(closest_z_dx_nm);
%position x of z_dx_nm
x_dx_nm=x_max_nm+x_dx_nm;
```

The central symmetry point `x_mean` (Figure A. 8) is important because it permits to define the left and right points of the square. At first are calculated the points in nm, then the closest measured positions (in pixel) are found.

```
x_mean_nm=mean(x_sx_nm:x_dx_nm);    %central simmetry point of the profile_x

point_sx_nm = x_mean_nm - b/2;  %left point of the square in nm
point_dx_nm = x_mean_nm + b/2;  %right point of the square in nm

diff_point_sx_nm = x_axis_plot_nm - point_sx_nm;
[minValue_point_sx_nm,closest_point_sx_nm] = min(abs(diff_point_sx_nm));   %closest left point coordinates
point_sx = closest_point_sx_nm;   %left point of the square in pixel
diff_point_dx_nm = x_axis_plot_nm - point_dx_nm;
[minValue_point_dx_nm,closest_point_dx_nm] = min(abs(diff_point_dx_nm));   %closest right point coordinates
point_dx = closest_point_dx_nm;   %right point of the square in pixel
```

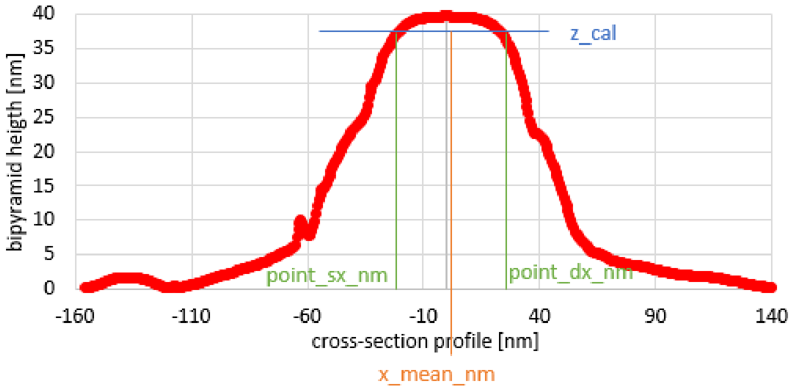

Figure A. 8 Definition of the central symmetry point ‘x_mean’.

`line_x` is the cross-section profile of the bipyramid along the x direction between the right and the left pixel positions of the square; the external points and abscissae axis are set equal to zero.

```
line_x = profile_x;       % base square of the bipyramid
min_line = min(line_x);     % this passage is needed to set the minimum at zero
line_x = line_x - min_line;

line_x(1:point_sx)=0;
line_x(point_dx:xsize)=0;
```

Annex A. Program Implemented with MATLAB software describing the Geometrical Method for the Analysis of the Critical Sizes of Bipyramids measured by Atomic Force Microscopy

```
Figure
plot(x_axis_plot_nm, line_x,'b','LineWidth', 2);
axis ([50 400 0 inf])
title('b critical size - base square of the bipyramid');
xlabel('profile coordinate (nm)');
ylabel('bipyramid height (nm)');
```

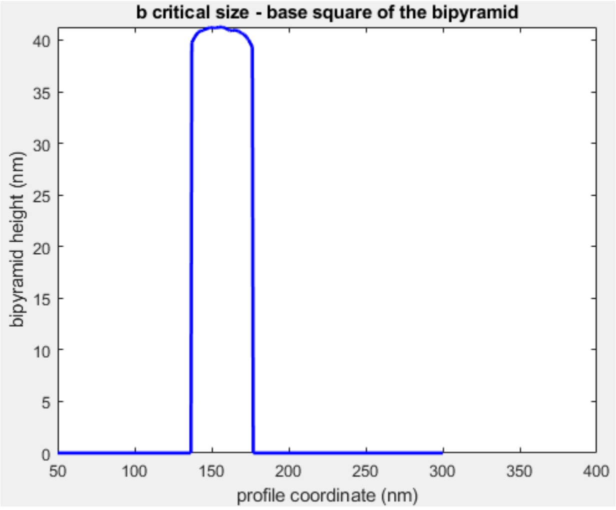

Figure A. 9 Definition of the base square of the bipyramids.

Once `line_x` is saved and plotted (Figure A. 9), the line_x centered with respect to the ordinate axis (Figure A. 10) is find as previously described.

```
matrix_line_x = (1:xsize) * pixel_size;           % in nm
matrix_line_x = [matrix_line_x; line_x];  % matrix 2x512 --> row1: x position profile_x , row2: z profile_x

[z_max_linex, x_max_linex] = max(line_x);
prof_linex_asc=line_x(1:x_max_linex);                  %left side of the line x (ascent)
prof_linex_desc=line_x(x_max_linex:numel(line_x)); %right side of the line x (descent)
x_axis_linex_asc = [1:numel(prof_linex_asc)]*pixel_size;  % x position in nm
x_axis_linex_desc = [1:numel(prof_linex_desc)]*pixel_size; % x position in nm
x_axis_linex_asc=x_axis_linex_asc-max(x_axis_linex_asc); %this passage is needed to set the maximum at zero
x_axis_linex= [x_axis_linex_asc x_axis_linex_desc]; %concatenate x profiles of ascent and descent of the line x
z_axis_linex= [prof_linex_asc prof_linex_desc]; %concatenate z profiles of ascent and descent of the line x
```

```
matrix_centered_line_x=[x_axis_linex;z_axis_linex];    %line x centered

figure
plot(x_axis_linex, z_axis_linex,'b','LineWidth', 2);
axis ([-inf inf 0 inf])
title('b critical size - base square of the bipyramid');
xlabel('profile coordinate (nm)');
ylabel('bipyramid height (nm)');
```

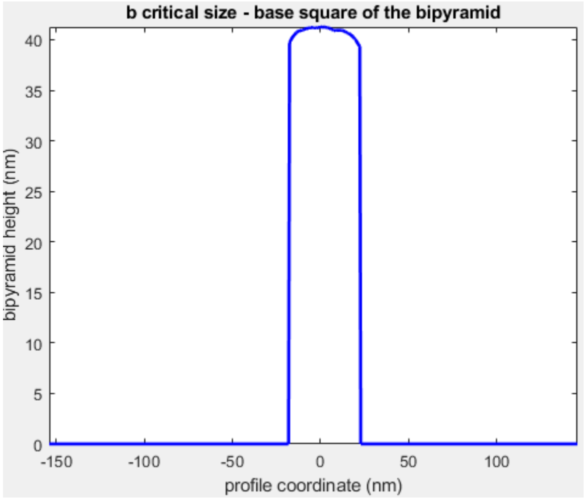

Figure A. 10 Profile describing the base square of the bipyramids centered with respect to the ordinate axis.

%% Step 5: Build the TIP ENLARGEMENT PROFILE

This geometrical method, which is developed to determine the critical sizes of the bipyramid, also permits the determination of the tip enlargement. To determine the profile of the tip dilation (Figure A. 11), the points that describe the `line_x` are excluded from the mean cross-section top profile at the bipyramid base.

```
tip = profile_x - line_x;           %tip profile definition

tip1 = tip;
tip1(point_sx:point_dx)=[];
finalnumber = numel(tip1);
x_axis_plot_tip_nm=[1:finalnumber];
x_axis_plot_tip_nm=x_axis_plot_tip_nm/xsize*xlen;   %x axis of the tip plot in nm
```

```
figure
plot(x_axis_plot_tip_nm,tip1,'g','LineWidth', 2);
axis ([50 450 10 inf])
title('cross-section profile of the tip');
xlabel('profile coordinate (nm)');
ylabel('tip height (nm)');

matrix_tip = (1:finalnumber) * pixel_size;      % in nm
matrix_tip = [matrix_tip; tip1];         % matrix 2x512 -->
row1: x position tip, row2: z tip
```

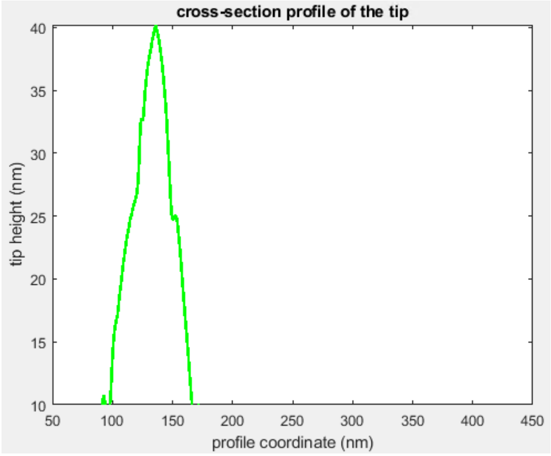

Figure A. 11 Definition of the tip enlargement cross-section.

As previously described, in the following there is the code that permits the construction of the centered tip plot (Figure A. 12). This plot permits the comparison between subsequent images, in order to evaluate the tip wear.

```
[z_max_tip1, x_max_tip1] = max(tip1);
prof_tip1_asc=tip1(1:x_max_tip1);                  %left side
of the tip (ascent)
prof_tip1_desc=tip1(x_max_tip1:numel(tip1));        %right
side of the tip x (descent)
x_axis_tip1_asc = [1:numel(prof_tip1_asc)]*pixel_size;  % x
position in nm
x_axis_tip1_desc = [1:numel(prof_tip1_desc)]*pixel_size;  %
x position in nm
x_axis_tip1_asc=x_axis_tip1_asc-max(x_axis_tip1_asc);
%this passage is needed to set the maximum at zero
x_axis_tip1= [x_axis_tip1_asc x_axis_tip1_desc];
%concatenate x profiles of ascent and descent of the tip
z_axis_tip1= [prof_tip1_asc prof_tip1_desc];
%concatenate z profiles of ascent and descent of the tip
```

```
matrix_centered_tip=[x_axis_tip1;z_axis_tip1];    %tip centered

figure
plot(x_axis_tip1,z_axis_tip1,'g','LineWidth', 2);
axis ([-inf inf 10 inf])
title('cross-section profile of the tip');
xlabel('profile coordinate (nm)');
ylabel('tip height (nm)');
```

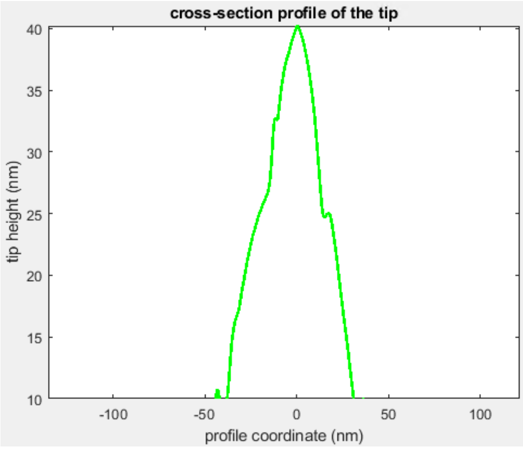

Figure A. 12 Profile describing the tip enlargement cross-sectioncross-section centered respect to the ordinate axis.

For further tip enlargement comparisons, for each tip are calculated the cross-section segment values at height steps of 0.3 nm.

To do that, the following steps are performed for the ascent profile (Figure A. 13):

1. Creation of a `for` loop from the height of 10 nm to the maximum height with steps of 0.03 nm; the choice of 10 nm is due to the fact that at lower heights there can be non-tip artefacts [149];
2. Interruption of the loop if the height calculated is greater than the maximum height (control command);
3. For each height z searched (`z_loop_tip_asc`) find the closest measured value `closestIndex_z_step_tip_`asc in pixel, then find the corresponding height value in nm `closestIndex_z_step_tip_asc_1` and lateral position `closestValue_x_step_tip_asc_1` on abscissae axis;
4. Creation of an `if` block which states that if the measured value `closestIndex_z_step_tip_asc_1` is greater than the z height searched (`z_loop_tip_asc`), I considered for the calculation of the cross-section

segment a value `closestIndex_z_step_tip_asc_2` that is the previous value; on the contrary, is valid what is state in the else, *i.e.*, if the measured value `closestIndex_z_step_tip_asc_1` is minor than the z height searched (`z_loop_tip_asc`), I considered for the calculation of the cross-section segment a value `closestIndex_z_step_tip_asc_2` that is the subsequent value (Figure A. 13);

5. Once considered the previous or the following value, it is calculated the percentage distance of the z value searched compared to z measured value, and the corresponding abscissae position.

```
%calculation of the segments for the ascent tip profile

z_step_tip_asc = 0.03 ; %nm
index=1;
for z_loop_tip_asc = 10:z_step_tip_asc:z_max_tip1 ;

    if z_loop_tip_asc>=z_max_tip1
           break
    end

diff_z_step_tip_asc = prof_tip1_asc - z_loop_tip_asc;
%matrix diff_z_step_c_asc = matrix tip ascent to which I
subtract the z_step_c_asc
    [minValue_z_step_tip_asc,closestIndex_z_step_tip_asc] =
min(abs(diff_z_step_tip_asc));       %z height which value
is the closest to the z_step_c_asc in pixel
    closestValue_z_step_tip_asc_1 =
prof_tip1_asc(closestIndex_z_step_tip_asc); %z height
defined in the line above in nm
closestValue_x_step_tip_asc_1=
x_axis_tip1_asc(closestIndex_z_step_tip_asc);
%value searched (z_loop_tip_asc) between two measured points
if  closestValue_z_step_tip_asc_1>z_loop_tip_asc     %value
measured > value searched
        closestValue_z_step_tip_asc_2 =
prof_tip1_asc(closestIndex_z_step_tip_asc-1); %previous
value
closestValue_x_step_tip_asc_2=
x_axis_tip1_asc(closestIndex_z_step_tip_asc-1) ;
    else
        closestValue_z_step_tip_asc_2 =
prof_tip1_asc(closestIndex_z_step_tip_asc+1);  %following
value
closestValue_x_step_tip_asc_2=
x_axis_tip1_asc(closestIndex_z_step_tip_asc+1) ;
    end
```

Annex A. Program Implemented with MATLAB software describing the Geometrical Method for the Analysis of the Critical Sizes of Bipyramids measured by Atomic Force Microscopy

```
     percent_z = abs((closestValue_z_step_tip_asc_1 -
z_loop_tip_asc) / (closestValue_z_step_tip_asc_2 -
closestValue_z_step_tip_asc_1)*100) ; %percentage distance
of the value searched compared to measured values
     delta_x= abs(closestValue_x_step_tip_asc_2 -
closestValue_x_step_tip_asc_1)*percent_z/100 ;

    if  closestValue_z_step_tip_asc_1>z_loop_tip_asc
        posx_1=closestValue_x_step_tip_asc_1-delta_x ;
    else
        posx_1=closestValue_x_step_tip_asc_1+delta_x ;

    end

matrix_ascent_tip(index,2)=x_axis_tip1_asc
(numel(x_axis_tip1_asc))-posx_1 ;
    matrix_ascent_tip(index,1)=z_loop_tip_asc ;
    index=index+1 ;

end
```

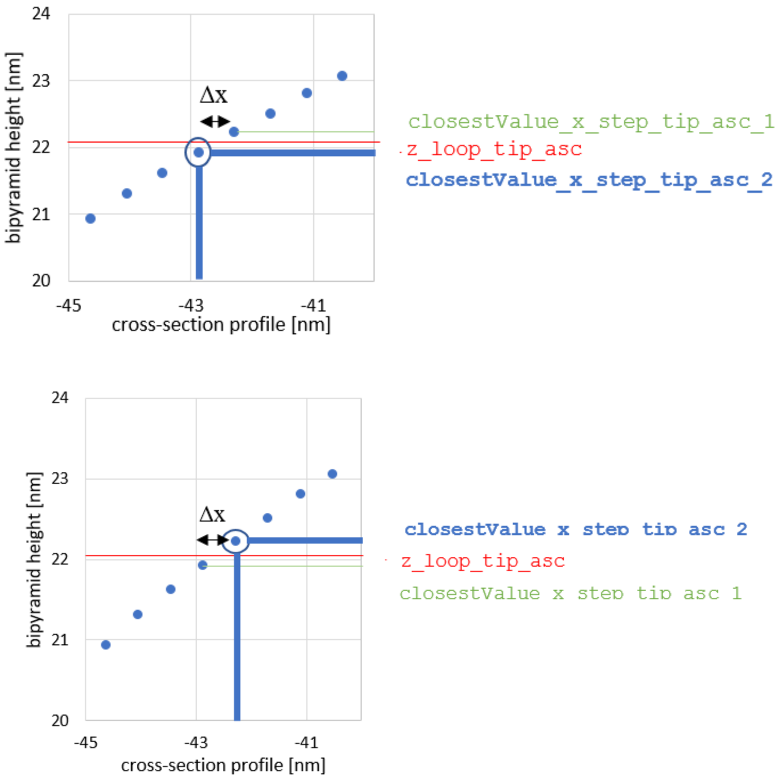

Figure A. 13 Explanation for the calculation of cross-section segments at various heights for ascent profiles.

For the descent profile, the steps are analogous with the previous one, but the choice of the points is the contrary. In fact, if the measured value `closestIndex_z_step_tip_asc_1` is greater than the z height searched (`z_loop_tip_asc`), I considered for the calculation of the cross-section segment a value `closestIndex_z_step_tip_asc_2` that is the following value; on the contrary, is valid what is state in the else, i.e., if the measured value `closestIndex_z_step_tip_asc_1` is minor than the z height searched (`z_loop_tip_asc`), I considered for the calculation of the cross-section segment a value `closestIndex_z_step_tip_asc_2` that is the previous value (Figure A. 14).

```
%calculation of the segments for the descent tip profile

z_step_tip_desc = 0.03 ; %nm
index=1;
matrix_descent_tip(1,1)=0;
matrix_descent_tip(1,2)=0;

% for z_loop_desc = z_max:-z_step_c_desc:10-z_step_c_desc
for i= numel(matrix_ascent_tip)/2:-1:1 ;
    z_loop_tip_desc = matrix_ascent_tip(i,1) ;

    diff_z_step_tip_desc = prof_tip1_desc - z_loop_tip_desc;
%matrix diff_z_step_c_asc = matrix tip ascent to which I
subtract the z_step_c_asc
    [minValue_z_step_tip_desc,closestIndex_z_step_tip_desc]
= min(abs(diff_z_step_tip_desc));       %z height which
value is the closest to the z_step_c_asc in pixel
    closestValue_z_step_tip_desc_1 =
prof_tip1_desc(closestIndex_z_step_tip_desc); %z height
defined in the line above in nm
closestValue_x_step_tip_desc_1=
x_axis_tip1_desc(closestIndex_z_step_tip_desc);
if  closestValue_z_step_tip_desc_1>z_loop_tip_desc
    closestValue_z_step_tip_desc_2 =
x_axis_tip1_desc(closestIndex_z_step_tip_desc+1) ;%following
value
    closestValue_x_step_tip_desc_2=
x_axis_tip1_desc(closestIndex_z_step_tip_desc+1) ;
else
closestValue_z_step_tip_desc_2 =
prof_tip1_desc(closestIndex_z_step_tip_desc-1); %previous
value
closestValue_x_step_tip_desc_2 =
x_axis_tip1_desc(closestIndex_z_step_tip_desc-1) ;
end
```

```
percent_z = abs((closestValue_z_step_tip_desc_1 - z_loop_tip_desc) / (closestValue_z_step_tip_desc_2 - closestValue_z_step_tip_desc_1)*100) ;
delta_x= abs(closestValue_x_step_tip_desc_2 - closestValue_x_step_tip_desc_1)*percent_z/100 ;

if  closestValue_z_step_tip_asc_1>z_loop_tip_desc
    posx_1=closestValue_x_step_tip_desc_1+delta_x ;
else
    posx_1=closestValue_x_step_tip_desc_1-delta_x ;

end

matrix_descent_tip(index,2)= posx_1 ;
    matrix_descent_tip(index,1)=z_loop_tip_desc ;
    index=index+1 ;

end

matrix_descent_tip= flipud(matrix_descent_tip); %the points are reported in a reverse order

matrix_tip_segments=[matrix_ascent_tip(:,1)] matrix_ascent_tip(:,2)+matrix_descent_tip(:,2)] ;
```

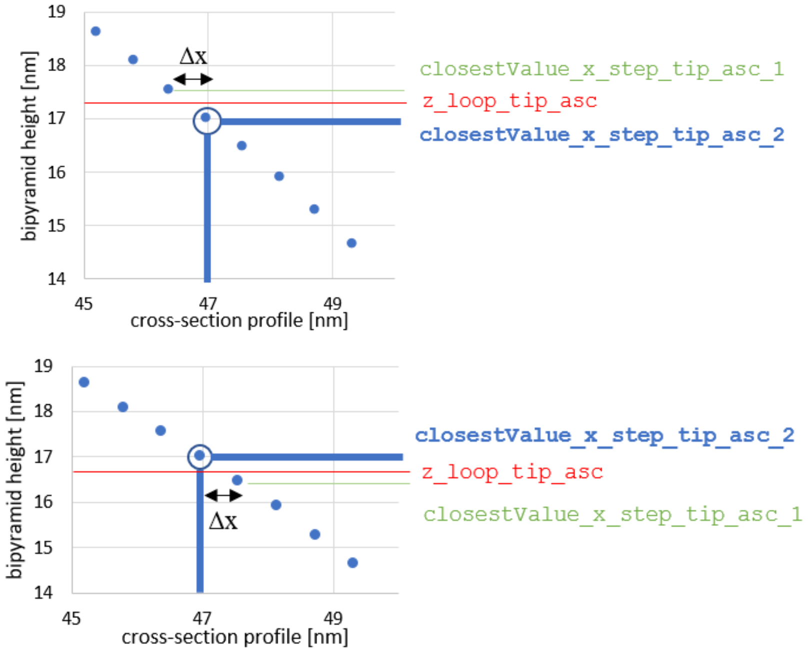

Figure A. 14 Explanation for the calculation of the cross-section segments at various heights for descent profiles.

%% Step 6: CROSS_SECTION y profiles AT MAXIMUM POSITION

In order to find the mean top profile along the main axis of the bipyramid (along the Y axis direction) the same instructions reported in Step 2 are used. The profile of the main bipyramid axis is reported in Figure A. 15 and Figure A. 16.

```
set(0,'DefaultAxesColorOrder',[1 0 0;1 0 1; 0 1 0;0 0 1;0 0 0]);

max_columns = max(fl)'; %find maximum for each column of the image
[z_max_columns, x_max_columns] = max (max_columns); %find maximum of maximums --> find position of maximum peak

for i= -2:1:2
    y_lines(i+3,:)= fl(:,x_max_columns+i);
end

profile_y = mean(y_lines);       % mean of 5 lines (the column which contains the maximum peak + the 2 columns before and the 2 columns after)
min_profile_y = min(profile_y);       % this passage is needed to set the minimum at zero
profile_y = profile_y - min_profile_y;

figure
plot(x_axis_plot_nm, profile_y,'m','LineWidth', 2);
axis ([0 inf 0 inf])
title('y-direction cross-section image profile');
xlabel('profile coordinate (nm)');
ylabel('bipyramid height (nm)');
```

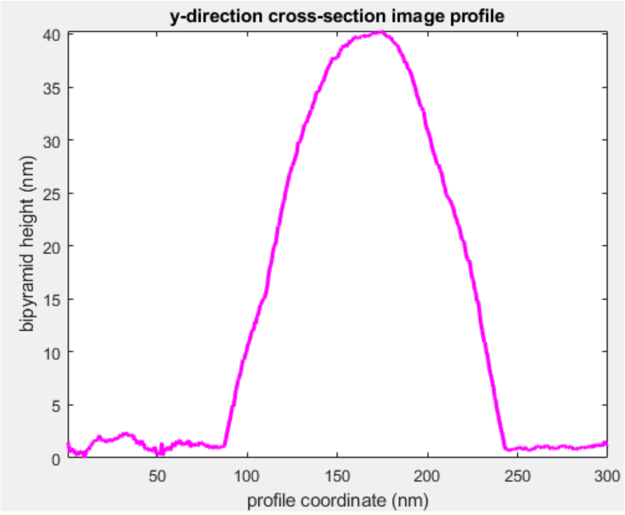

Figure A. 15 Mean cross-sectional top profile along the Y axis.

```
matrix_profile_y = (1:xsize) * pixel_size;             % in nm
matrix_profile_y = [matrix_profile_y; profile_y];  % matrix
2x512 --> row1: x position profile_y , row2: z profile_y

[z_max_profile_y, x_max_profile_y] = max(profile_y);
prof_profy_asc=profile_y(1:x_max_profile_y);
%left side of the profile_y (ascent)
prof_profy_desc=profile_y(x_max_profile_y:numel(profile_y));
%right side of the profile_y (descent)
x_axis_profy_asc = [1:numel(prof_profy_asc)]*pixel_size;  %
x position in nm
x_axis_profy_desc = [1:numel(prof_profy_desc)]*pixel_size;
% x position in nm
x_axis_profy_asc=x_axis_profy_asc-max(x_axis_profy_asc);
%this passage is needed to set the maximum at zero
x_axis_profiley= [x_axis_profy_asc x_axis_profy_desc];
%concatenate x profiles of ascent and descent of the
profile_y
z_axis_profiley= [prof_profy_asc prof_profy_desc];
%concatenate z profiles of ascent and descent of the
profile_y
matrix_centered_profile_y=[x_axis_profiley;z_axis_profiley];
%profile_y centered

figure
plot(x_axis_profiley, z_axis_profiley,'m','LineWidth', 2);
axis ([-inf inf 0 inf])
title('y-direction cross-section image profile');
xlabel('profile coordinate (nm)');
ylabel('bipyramid height (nm)');
```

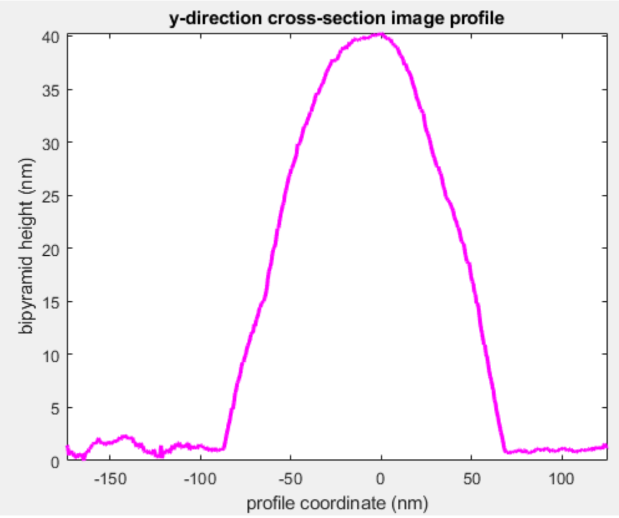

Figure A. 16 Mean cross-sectional top profile along the Y axis, centered with respect to the ordinate axis.

```
%% Step 7: Subtract the TIP PROFILE from the CROSS-SECTION y profile to find the size 'c'
% Note that c is the MAX size of the bipyramid
```

In this step a plot reporting the critical size `c` of the bipyramid is obtained by subtraction of the tip profile (obtained in Step 4) to the mean top profile along the main axis of the bipyramid (obtained in Step 6). This is done by assuming the tip enlargement to be isotropic along the x and y axes.

First of all, the cross-section tip and bipyramid cross-section profile in y direction are divided in their ascent and descent parts; in this way, the calculation of the difference between the profile y and tip can be exactly calculated for the two branches.

```
[max_tip1,cell_max_tip1]=max(tip1);
profA=tip1(1:cell_max_tip1);                   %left side of the tip (ascent)
profB=tip1(cell_max_tip1:finalnumber);         %right side of the tip (descent)

[max_yprof,cell_max_yprof]=max(profile_y);
profC=profile_y(1:cell_max_yprof);           %left side of the profile y (ascent)
profD=profile_y(cell_max_yprof:end);         %right side of the profile y (descent)

x_axis_profA = [1:numel(profA)]*pixel_size;  % x position in nm
x_axis_profB = [1:numel(profB)]*pixel_size;  % x position in nm
x_axis_profC = [1:numel(profC)]*pixel_size;  % x position in nm
x_axis_profD = [1:numel(profD)]*pixel_size;  % x position in nm

min_r=min(numel(x_axis_profA),numel(x_axis_profC));  %set the minor of one of the two matrices
```

To find the eroded profile for the ascent branch (Figure A. 17), a `for` loop is set to calculate the segment length for each height z starting from 1 to the maximum value of the matrix of the ascent tip profile.

The steps in the loop are the following.

1. Find the z height from the ascent profile y;
2. Find the z tip height which value is the closest to the z height of the ascent profile y and the corresponding position in the abscissae axis;

3. Calculate the x distance between tip profile and right ordinate axis border (`distA`);
4. Calculate the x distance between the NP profile and the right ordinate axis border (`distC`);
5. Calculate the segment that describes the NP profile eroded by the tip (`distAC`).

```
for idx_x_axis_profC = 1:numel(x_axis_profC)  %loop for all the z height of the profile y (ascent) --> find the ERODED profile y (ascent)

    z_profC = profC(idx_x_axis_profC);  %z height of the profile y (ascent)
    diffAC = profA - z_profC;    %matrix diffAC = matrix tip ascent to which I subtract the z height of the profile y
    [minValueAC,closestIndexAC] = min(abs(diffAC));      %z tip height which value is the closest to the z height of the profile y
    x_tip_closestValueAC = x_axis_profA(closestIndexAC); %position x of the z height defined in the line above

    distA = x_axis_profA(numel(profA))-x_tip_closestValueAC; %x distance between tip profile and right ordinate axis border
    distC = x_axis_profC(numel(profC))-x_axis_profC(idx_x_axis_profC); %x distance between profile y and right ordinate axis border
    distAC = - abs(distA-distC); %x distance between the two profiles

    x_axis_profC(idx_x_axis_profC) = distAC;   %matrix of distances x of the profile y from the right ordinate axis border

end

matrix_ascent=[x_axis_profC;profC];
matrix_ascent=matrix_ascent';
```

Annex A. Program Implemented with MATLAB software describing the Geometrical Method for the Analysis of the Critical Sizes of Bipyramids measured by Atomic Force Microscopy

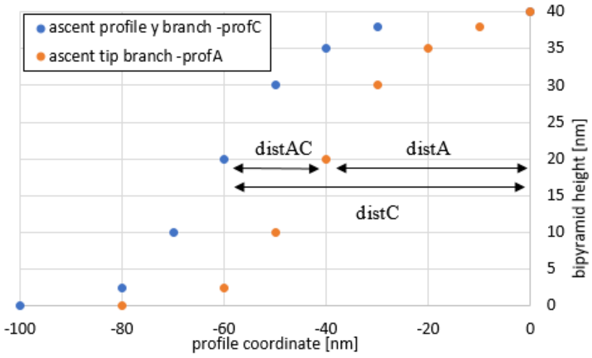

Figure A. 17 Not-in-scale sketch reporting the calculation of the eroded NP ascent profile.

For the descent branch of the eroded profile (Figure A. 18) the code instructions are similar for that one of the ascent one.

```
min_q=min(numel(x_axis_profD),numel(x_axis_profB));  %set
the minor of one of the two matrices

for idx_x_axis_profD = 1:numel(numel(x_axis_profD))  %loop
for all the z height of the profile y (descent) --> find the
ERODED profile y (descent)

    z_profD = profD(idx_x_axis_profD);  %z height of the
profile y (descent)
    diffBD = profB - z_profD;     %matrix diffBD = matrix tip
descent to which I subtract the z height of the profile y
    [minValueBD,closestIndexBD] = min(abs(diffBD));        %z
tip height which value is the closest to the z height of the
profile y
    x_tip_closestValueBD = x_axis_profB(closestIndexBD);
%position x of the z height defined in line above

    distB = x_axis_profB(min_q) - x_tip_closestValueBD; %x
distance between tip profile and left ordinate axis border
    distD = x_axis_profD(min_q) -
x_axis_profD(idx_x_axis_profD); %x distance between profile
y and left ordinate axis border
    distBD = abs(distB-distD); %x distance between the two
profiles

    x_axis_profD(idx_x_axis_profD) = distBD;   %matrix of
distances x of the profile y from the left ordinate axis
border

end

matrix_descent=[x_axis_profD;profD];
matrix_descent=matrix_descent';
```

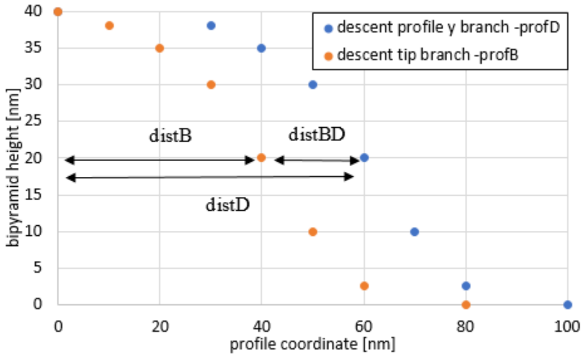

Figure A. 18 Not-in-scale sketch reporting the calculation of the eroded NP descent profile.

Finally, the two branches are concatenated in order to find the eroded y cross-section profile (Figure A. 19), from which the critical size c is obtained.

```
x_fin= [x_axis_profC x_axis_profD];   %concatenate x profiles of ascent and descent eroded profile y
z_fin= [profC profD];                 %concatenate z profiles of ascent and descent eroded profile y
matrix_fin=[x_fin;z_fin];
matrix_fin2=matrix_fin';

figure
plot(x_fin,z_fin,'k','LineWidth', 2);
axis ([-inf inf 10 inf])
title('c critical size - eroded y cross-section profile');
xlabel('profile coordinate (nm)');
ylabel('bipyramid height (nm)');
```

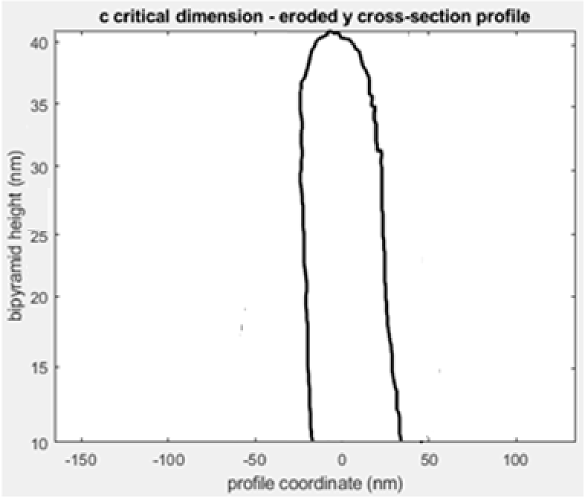

Figure A. 19 Eroded cross-section profile along Y-direction, through which it is possible to calculate the critical size 'c'.

%% Step 8: Calculation of the value "c"

In this step, the cross-section segments for each height of the plot obtained in the previous step are calculated in order to find the value of the `c` critical size; the code instructions are the same reported in Step 5. Please note that the value `c` is calculated as the mean value of the segments between 30% and the 90% in height of the plot obtained in Step 7, as described in the code lines 537 and 538.

```
453  %calculation of the segments c for the ascent profile

455  z_step_c_asc = 0.03 ; %nm
456  index=1;
457  z_max=max(profC);
458  for z_loop_asc = 10:z_step_c_asc:z_max ;

460          if z_loop_asc>=z_max
461             break
462          end

464      diff_z_step_c_asc = profC - z_loop_asc;     %matrix
     diff_z_step_c_asc = matrix tip ascent to which I subtract
     the z_step_c_asc
465      [minValue_z_step_c_asc,closestIndex_z_step_c_asc] =
     min(abs(diff_z_step_c_asc));       %z height which value is
     the closest to the z_step_c_asc in pixel
466      closestValue_z_step_c_asc_1 =
     profC(closestIndex_z_step_c_asc); %z height defined in the
     line above in nm
467  closestValue_x_step_c_asc_1=
     x_axis_profC(closestIndex_z_step_c_asc);
468      if  closestValue_z_step_c_asc_1>z_loop_asc
469          closestValue_z_step_c_asc_2 =
     profC(closestIndex_z_step_c_asc-1) ;
470      closestValue_x_step_c_asc_2=
     x_axis_profC(closestIndex_z_step_c_asc-1) ;
471      else
472          closestValue_z_step_c_asc_2 =
     profC(closestIndex_z_step_c_asc+1);
473    closestValue_x_step_c_asc_2=
     x_axis_profC(closestIndex_z_step_c_asc+1;

475      end

477      percent_z = abs((closestValue_z_step_c_asc_1 -
     z_loop_asc) / (closestValue_z_step_c_asc_2 -
     closestValue_z_step_c_asc_1)*100) ;
478      delta_x= abs(closestValue_x_step_c_asc_2 -
     closestValue_x_step_c_asc_1)*percent_z/100 ;
```

```
    if  closestValue_z_step_c_asc_1>z_loop_asc
        posx_1=closestValue_x_step_c_asc_1-delta_x ;
    else
        posx_1=closestValue_x_step_c_asc_1+delta_x ;

    end

    matrix_ascent_c(index,2)=
x_axis_profC(numel(x_axis_profC))-posx_1 ;
    matrix_ascent_c(index,1)=z_loop_asc ;
    index=index+1 ;

end

%calculation of the segments c for the descent profile

z_step_c_desc = 0.03 ; %nm
index=1;
matrix_descent_c(1,1)=0;
matrix_descent_c(1,2)=0;

for i= numel(matrix_ascent_c)/2:-1:1 ;
    z_loop_desc = matrix_ascent_c(i,1) ;

    diff_z_step_c_desc = profD - z_loop_desc;    %matrix
diff_z_step_c_asc = matrix tip ascent to which I subtract
the z_step_c_asc
    [minValue_z_step_c_desc,closestIndex_z_step_c_desc] =
min(abs(diff_z_step_c_desc));       %z height which value is
the closest to the z_step_c_asc in pixel
    closestValue_z_step_c_desc_1 =
profD(closestIndex_z_step_c_desc); %z height defined in the
line above in nm
closestValue_x_step_c_desc_1=
x_axis_profD(closestIndex_z_step_c_desc);
    if  closestValue_z_step_c_desc_1>z_loop_desc
        closestValue_z_step_c_desc_2 =
profD(closestIndex_z_step_c_desc+1) ;% following
closestValue_x_step_c_desc_2=
x_axis_profD(closestIndex_z_step_c_desc+1) ;
    else
        closestValue_z_step_c_desc_2 =
profD(closestIndex_z_step_c_desc-1); %previous
closestValue_x_step_c_desc_2=
x_axis_profD(closestIndex_z_step_c_desc-1) ;
    end

     percent_z = abs((closestValue_z_step_c_desc_1 -
z_loop_desc) / (closestValue_z_step_c_desc_2 -
closestValue_z_step_c_desc_1)*100) ;
```

```
     delta_x= abs(closestValue_x_step_c_desc_2 -
closestValue_x_step_c_desc_1)*percent_z/100 ;

    if  closestValue_z_step_c_asc_1>z_loop_desc
        posx_1=closestValue_x_step_c_desc_1+delta_x ;
    else
        posx_1=closestValue_x_step_c_desc_1-delta_x ;

    end

    matrix_descent_c(index,2)= posx_1 ;
    matrix_descent_c(index,1)=z_loop_desc ;
    index=index+1 ;

end

matrix_descent_c= flipud(matrix_descent_c);

matrix_c=[matrix_ascent_c(:,1)
matrix_ascent_c(:,2)+matrix_descent_c(:,2)] ;

ix=1;
lim_min = max (matrix_c(:,1))/100*30;  %nm
lim_max = max(matrix_c(:,1))/100*90;   %nm

diff_point_lim_min_nm = matrix_c - lim_min;
[minValue_point_lim_min_nm,closest_point_lim_min_nm] =
min(abs(diff_point_lim_min_nm));
lim_min_pixel = closest_point_lim_min_nm;
lim_min_pixel = lim_min_pixel (1);     %colomn position of
lim_min

diff_point_lim_max_nm = matrix_c - lim_max;
[minValue_point_lim_max_nm,closest_point_lim_max_nm] =
min(abs(diff_point_lim_max_nm));
lim_max_pixel = closest_point_lim_max_nm;
lim_max_pixel = lim_max_pixel (1);     %colomn position of
lim_max

for ix= lim_min_pixel:lim_max_pixel
    matrix_c_2 (ix,:) = matrix_c(ix, :);
end

c = mean (matrix_c_2(:,2));
```

```
%% Step 9: Correction for bipy lying on the substrate
```

As reported in Figure 4. 9 of Chapter 4, the previously calculated values are corrected for the laying of the nanoparticle on the mica substrate.

```
theta = 1.19206; %rad       -->    theta = 68.3°
gamma = 0.37874; %rad       -->    gamma = 90° - theta = 21.7°
b_corr = b/sin(theta);
c_corr = c/cos(gamma);
```

%% Step 10: Save workspace data (.mat) for further analysis

In this last step are reported the instructions needed to choose the folder in which save the MATLAB file for further analysis, *e.g.* in a spreadsheet.

```
%User is prompted to select a destination folder.
destinationpath = uigetdir(file_path, 'Choose output folder for Geometrical Model Tip Reconstruction data');
if destinationpath == 0
    destinationpath = file_path;
end

% Save workspace data (.mat)
k = strfind(file_name,'.');
filetype = file_name(k+1:k+3);
new_file = fullfile(destinationpath,[name '_' filetype '_' datestr(now, 30) 'all.mat']);     %Output name has image name plus date in format YYYYMMDDTHHMMSS
save (new_file) %Outputs all the data in the workspace into "new_file.mat"
```

Annex B. Program Implemented with MATLAB software describing the Geometrical Method for the Analysis of the Critical Sizes of Nanosheets measured by Atomic Force Microscopy

In this Annex, the program implemented in MATLAB environment is described. This program is based on a geometrical method for CDs reconstruction of complex geometry nanoparticles in AFM-based images. In order to clarify each step, some experimental plots are reported.

Recall that topographies are formed by a matrix of N x N pixels, in which each pixel is a point with a specific height value z.

Note that the algorithms reported in Annex A and Annex B are intended as illustrative implementations of the operations discussed in Chapter 4. The main focus of this study is the derivation and correctness of the algorithms, while efficiency is a minor concern.

`%% Step 1: OPENING IMAGE`

In this step, the BCRF image of the nanosheet (previously levelled with the SPIP software) is opened according to the instruction reported in `ReadImage`. The file ReadImage.m is a `function` which reads the AFM image defined by the parameter `filename`, which returns the variables `Immagine,xsize,ysize,xlen,ylen,bit2n`, which are an array containing, respectively, the image pixel intensity, pixel size in x and y directions, and the length of the axes in nm.

```
file_path = 'C:\Users\Documents\';         %USER SHOULD ENTER CONVIENENT STARTING file_path
[file_name,sourcepath] = uigetfile('*.*','Select an image for Geometrical Model Tip Reconstruction');
```

```
[~,name,ext] = fileparts([sourcepath,file_name]);
filename=strcat(sourcepath, file_name);

[fl,xsize,ysize,xlen,ylen,bit2nm] = ReadImage(filename); %opening image
```

Since the nanosheet is oriented so that one side of the square facet {001} is parallel to the X-axis and the other side is parallel to the Y-axis, the operator can decide which axis to analyze first. I decided to introduce this step also to avoid the unnecessary repetition of entire sections of code. In fact, this program calculated both height and lateral size of the nanosheet, and in order to calculate the final critical sizes, the values obtained from the two axes must be averaged.

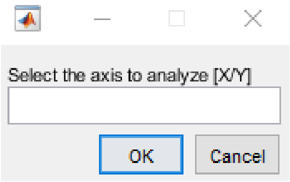
Select the axis to analyze [X/Y]

```
%choosing the profile direction to analyze: X or Y

answer=' ';
prompt = 'Select the axis to analyze [X/Y]';

while answer~='X' && answer~='Y'
     risp = inputdlg(prompt);
     risp = upper(risp);
     answer = char(risp);
end

if answer=='X'
    fl=fl;
else
    fl=fl';
end
```

The user then chooses the platelet area to analyse by tracing in the subsequent order the top left corner and the lower right corner on the displayed image (Figure B. 1).

```
% selecting nanosheet area to analyze: the operator has to choose the particle boundaries in the subsequent order:
% 1) top left corner 2) lower right corner

f=fl;
```

Annex B. Program Implemented with MATLAB software describing the Geometrical Method for the Analysis of the Critical Sizes of Nanosheets measured by Atomic Force Microscopy

```
image(f,'CDataMapping','scaled')
uiwait(msgbox('Select the nanosheet area. Select the top left corner and then the lower right corner'));
[x_left, y_up, but] = ginput(1) ;
x_left=int16(x_left);
y_up=int16(y_up);
f(y_up,:)=0;
f(:, x_left)=0;
image(f,'CDataMapping','scaled')
[x_right, y_down, but] = ginput(1) ;
x_right=int16(x_right);
y_down=int16(y_down);
f(y_down,:)=0;
f(:, x_right)=0;
image(f,'CDataMapping','scaled')
```

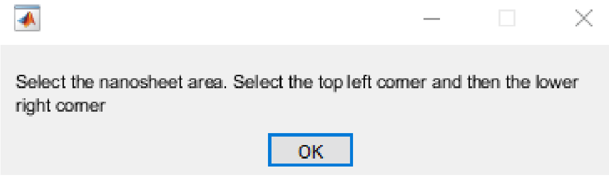

Select the nanosheet area. Select the top left corner and then the lower right corner

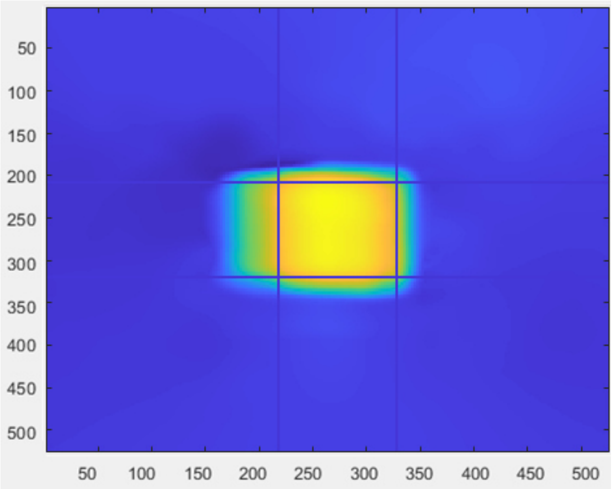

Figure B. 1 Nanosheet image to be analyzed; the x and y axes report the pixels, while the dark blue lines define the boundaries of the NP area considered in the analysis.

The dark blue lines in Figure B. 1 describe the boundaries that define the area of the nanoparticle, within which all cross-section profiles are averaged to obtain the profile used for defining the platelet CDs.

The X-axis of the image is then converted from pixel to nm.

```
pixel_size = xlen/xsize;      %pixel size in nm
x_axis_plot_nm=[1:xsize];
x_axis_plot_nm=x_axis_plot_nm/xsize*xlen;   %x axis of plots in nm
```

%% Step 2: CROSS_SECTION profile IN NANOSHEET AREA

For measuring the nanosheet cross-section profile along the X/Y axis direction, the following steps are done:

1. Search the position of the maximum peak by finding the maximum for each row of the image;
2. Average the various profiles between the upper and lower limits defined in Figure B. 1;
3. Before plotting the cross-sectional profile, the minimum is set at zero.

```
max_rows = max(fl')'; %find maximum for each row of the image
[z_max_rows, x_max_rows] = max (max_rows); %find maximum of maximums --> find position of maximum peak

for i_rows= x_up:x_down
    x_lines (i_rows-y_up+1,:) = fl(i_rows,:);
end

profile_x = mean(x_lines);       % mean of lines between x_up and x_down
min_profile_x = min(profile_x);     % this passage is needed to set the minimum at zero
profile_x = profile_x - min_profile_x;

figure
plot(x_axis_plot_nm,profile_x,'LineWidth', 2);
axis ([0 inf 0 inf])
title('cross-section profile');
xlabel('profile coordinate (nm)');
ylabel('nanosheet height (nm)');
```

Annex B. Program Implemented with MATLAB software describing the Geometrical Method for the Analysis of the Critical Sizes of Nanosheets measured by Atomic Force Microscopy

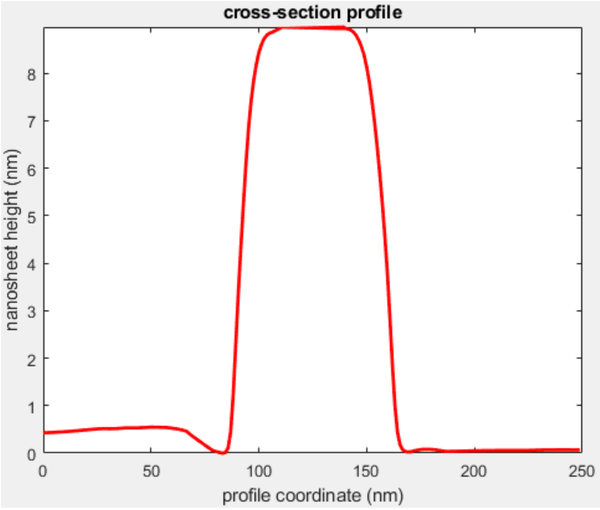

Figure B. 2 Cross-section profile of the nanosheet.

The mean cross-sectional profile (Figure B. 2) is then saved in the first row of a matrix, while in the second row are reported the lateral position in nm.

```
matrix_profile_x = (1:xsize) * pixel_size;
matrix_profile_x = [profile_x ; matrix_profile_x ];  % matrix 2x512 --> row1: z values of profile_x , row2: x position profile_x
```

For obtaining the cross-sectional profile centered on zero, the profile is divided into ascent and descent branches that are subsequently concatenated. In an analogous way as previously described, the centered cross-section profile of the nanosheet is saved and plotted.

```
[z_max, x_max] = max(profile_x);
profx_asc=profile_x(1:x_max);                    %left side of the profile_x (ascent)
profx_desc=profile_x(x_max:numel(profile_x));     %right side of the profile_x (descent)

X_pos = matrix_profile_x(2,:) ;        % x position profile_x in nm
X_pos_asc = X_pos(1:x_max) ;
X_pos_asc = flip(X_pos_asc) ;
X_pos_asc=X_pos_asc - min(X_pos_asc);
X_pos_asc = X_pos_asc * -1 ;
X_pos_desc = X_pos(x_max:numel(profile_x))-X_pos(x_max);

matrix_profile_asc = [profx_asc ; X_pos_asc] ;
```

```
matrix_profile_desc = [profx_desc ; X_pos(x_max:numel(profile_x))-X_pos(x_max)] ;

x_axis_profx= [-X_pos_asc X_pos(x_max:numel(profile_x))-X_pos(x_max)]; %concatenate x profiles of ascent and descent of the profile_x
z_axis_profx= [profx_asc profx_desc]; %concatenate z profiles of ascent and descent of the profile_x
matrix_centered_profile_x=[x_axis_profx;z_axis_profx]; %profile x centered

figure
plot(x_axis_profx,z_axis_profx,'LineWidth', 2);
axis ([-inf inf 0 inf])
title('cross-section profile');
xlabel('profile coordinate (nm)');
ylabel('nanosheet height (nm)');
```

In order to calculate the average height of the baseline `z_min`, the operator manually selects two points to define the minimum both at left and right of the peak (Figure B. 3).After that, the right and left minima are averaged.

```
%select points for defining the right minimum

plot(x_axis_profx,z_axis_profx)
uiwait(msgbox('Click 2 points for defining the right minimum'));
[x y] = ginput(2);
hold on;
plot(x, y, 'r+', 'LineWidth', 2);

xFitted = x;
x1 = xFitted(1);
diff_x1 = matrix_centered_profile_x(1,:) - x1;   %matrix diff_x1 = matrix_centered_profile_x to which I subtract x1
[minValue_x1,closestIndex_x1] = min(abs(diff_x1));   %x position which value is the closest to the x1, in pixel
z1 = matrix_centered_profile_x(2,closestIndex_x1);
x2 = xFitted(2);
diff_x2 = matrix_centered_profile_x(1,:) - x2;   %matrix diff_x2 = matrix_centered_profile_x to which I subtract x2
[minValue_x2,closestIndex_x2] = min(abs(diff_x2));   %x position which value is the closest to the x2, in pixel
z2 = matrix_centered_profile_x(2,closestIndex_x2);

if closestIndex_x2<closestIndex_x1
   temp = closestIndex_x2;
   closestIndex_x2 = closestIndex_x1;
```

```
   closestIndex_x1 = temp;
end

z_min_right                              =                              mean
(matrix_centered_profile_x(2,closestIndex_x1:closestIndex_x2));
```

```
%select points for defining the left minimum

plot(x_axis_profx,z_axis_profx)
uiwait(msgbox('Click   2   points   for   defining   the   left
minimum'));
[x y] = ginput(2);
hold on;
plot(x, y, 'r+', 'LineWidth', 2);

xFitted = x;
x1 = xFitted(1);
diff_x1  =  matrix_centered_profile_x(1,:)  -  x1;      %matrix
diff_x1 = matrix_centered_profile_x to which I subtract x1
[minValue_x1,closestIndex_x1] = min(abs(diff_x1));         %x
position which value is the closest to the x1, in pixel
z1 = matrix_centered_profile_x(2,closestIndex_x1);
x2 = xFitted(2);
diff_x2  =  matrix_centered_profile_x(1,:)  -  x2;      %matrix
diff_x2 = matrix_centered_profile_x to which I subtract x2
[minValue_x2,closestIndex_x2] = min(abs(diff_x2));         %x
position which value is the closest to the x2, in pixel
z2 = matrix_centered_profile_x(2,closestIndex_x2);

if closestIndex_x2<closestIndex_x1
   temp = closestIndex_x2;
   closestIndex_x2 = closestIndex_x1;
   closestIndex_x1 = temp;
end
```

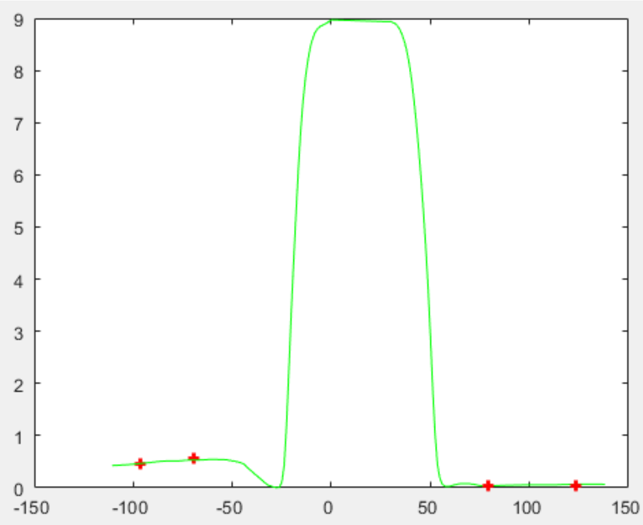

Figure B. 3 Cross-section profile of the nanosheet. The red crosses represent, respectively, the extremes of the segment describing the left and right minima.

```
z_min_left = mean
(matrix_centered_profile_x(2,closestIndex_x1:closestIndex_x2));

z_min = (z_min_right+z_min_left)/2 ;
```

```
%% Step 3: Calculation of the the segments of ascent and descent
profiles
```

In this step, the cross-sectional profile is divided into two branches. For each branch, cross-section segments are calculated and saved into `matrix_ascent_xasc` and `matrix_descent_xdesc`; these segments are useful for the calculations made in Step 4.

The calculation of the segment is done for each branch following the subsequent steps:

1. Creation of a `for` loop from mimimun x position to the maximum x position with steps of 0.05 nm;
2. For each x position (`x_loop_asc`) find the closest measured value `closestIndex_x_step_x_asc` in pixel, then find the corresponding x value in nm `closestIndex_z_step_x_asc_1` and height position `closestValue_z_step_x_asc_1`;

3. If the measured value `closestIndex_x_step_x_asc_1` is greater than the x position searched (`x_loop_asc`), I considered for the calculation of the cross-section segment the previous X value `closestIndex_x_step_x_asc_2`; otherwise, I considered the subsequent value `closestIndex_x_step_x_asc_2`;
4. Once considered the previous or the following value, it is calculated the percentage distance of the z value searched compared to z measured value, and the corresponding abscissae position.

```matlab
% Ascent profile

matrix_profile_asc(2,:) = matrix_profile_asc(2,:) * -1 ;  % I change the sign (as if it were a descent profile)
matrix_profile_asc(1,:) = flip(matrix_profile_asc(1,:));
matrix_profile_asc(2,:) = flip(matrix_profile_asc(2,:));

x_max_asc  =  max  (matrix_profile_asc(2,:));       %maximum  x position in the profile x
x_max_desc  =  max  (matrix_profile_desc(2,:));     %maximum  x position in the profile x

x_min_asc  =  min  (matrix_profile_asc(2,:));       %minimum  x position in the profile x
x_min_desc  =  min  (matrix_profile_desc(2,:));     %minimum  x position in the profile x

x_step = 0.05 ; %nm
index=1;

for x_loop_asc = x_min_asc:x_step:x_max_asc  % nm     (new x values which I calculate)

   diff_x_step_x_asc = matrix_profile_asc(2,:) - x_loop_asc; %matrix diff_x_step_x_asc = matrix ascent to which I subtract the x_loop_asc (new x value which I consider)
   [minValue_x_step_x_asc,closestIndex_x_step_x_asc] = min(abs(diff_x_step_x_asc));       %x position which value is the closest to the x_loop_asc, in pixel
    closestValue_x_step_x_asc_1 = matrix_profile_asc(2,closestIndex_x_step_x_asc); % x position which I search, in nm
    closestValue_z_step_x_asc_1 = matrix_profile_asc(1,closestIndex_x_step_x_asc);  %  z  height of x position, in nm

   if closestValue_x_step_x_asc_1 == x_loop_asc
```

```
       delta_z = 0 ; % searched point coincident with measured point -> percentage = 0%
   else
       if  closestValue_x_step_x_asc_1>x_loop_asc   %closest1h major
            closestValue_x_step_x_asc_2 = closestValue_x_step_x_asc_1;  %I consider closest2
            closestValue_z_step_x_asc_2 = closestValue_z_step_x_asc_1;
            closestValue_x_step_x_asc_1 = matrix_profile_asc(2,closestIndex_x_step_x_asc - 1);
            closestValue_z_step_x_asc_1 = matrix_profile_asc(1,closestIndex_x_step_x_asc - 1) ;
        else
            closestValue_x_step_x_asc_2 = matrix_profile_asc(2,closestIndex_x_step_x_asc  +  1);    %if point closest 1 (measured from AFM) is less than z_loop, it take the subsequent point as closest2
            closestValue_z_step_x_asc_2 = matrix_profile_asc(1,closestIndex_x_step_x_asc + 1) ;
    end
        percent_x = abs((x_loop_asc - closestValue_x_step_x_asc_1) / (closestValue_x_step_x_asc_2 - closestValue_x_step_x_asc_1)*100)  ;    %percentage distance between closest 1 and z_loop
       delta_z= (closestValue_z_step_x_asc_2 - closestValue_z_step_x_asc_1)*percent_x/100  ;   %  x distance from point closest 1
    end

     posz_1=closestValue_z_step_x_asc_1+delta_z  ;     %new z position added to segment delta_z

     matrix_ascent_xasc(1,index)= posz_1 ;
     matrix_ascent_xasc(2,index)= x_loop_asc ;
     index=index+1 ;
end

matrix_profile_asc(1,:) = flip(matrix_profile_asc(1,:));
matrix_profile_asc(2,:) = flip(matrix_profile_asc(2,:));
matrix_profile_asc(2,:) = matrix_profile_asc(2,:) * -1 ;  % I restore the X values of the initial matrix

matrix_ascent_xasc(1,:) = flip(matrix_ascent_xasc(1,:));
matrix_ascent_xasc(2,:) = flip(matrix_ascent_xasc(2,:));
matrix_ascent_xasc(2,:) = matrix_ascent_xasc(2,:) * -1 ; % I change the X sign of the resulting matrix

% Descent profile

x_step = 0.05 ; %nm
```

```
index=1;

for x_loop_desc = x_min_desc:x_step:x_max_desc  % nm

diff_x_step_x_desc = matrix_profile_desc(2,:) - x_loop_desc;
%matrix diff_z_step_c_asc = matrix tip ascent to which I subtract the z_step_c_asc
[minValue_x_step_x_desc,closestIndex_x_step_x_desc] = min(abs(diff_x_step_x_desc));        %z height which value is the closest to the z_step_c_asc in pixel
closestValue_x_step_x_desc_1 = matrix_profile_desc(2,closestIndex_x_step_x_desc);     % x position of z height
closestValue_z_step_x_desc_1 = matrix_profile_desc(1,closestIndex_x_step_x_desc); % z height defined in the line above in nm

    if closestValue_x_step_x_desc_1 == x_loop_desc
       delta_z = 0 ;
    else
        if  closestValue_x_step_x_desc_1>x_loop_desc
            closestValue_x_step_x_desc_2 = closestValue_x_step_x_desc_1;
            closestValue_z_step_x_desc_2 = closestValue_z_step_x_desc_1;
            closestValue_x_step_x_desc_1 = matrix_profile_desc(2,closestIndex_x_step_x_desc - 1);
            closestValue_z_step_x_desc_1 = matrix_profile_desc(1,closestIndex_x_step_x_desc - 1) ;
        else
            closestValue_x_step_x_desc_2 = matrix_profile_desc(2,closestIndex_x_step_x_desc + 1);   %if closest 1 (measured by AFM) is smaller than z_loop, I take the subsequent point
            closestValue_z_step_x_desc_2 = matrix_profile_desc(1,closestIndex_x_step_x_desc + 1) ;
        end
        percent_x = abs((x_loop_desc - closestValue_x_step_x_desc_1) / (closestValue_x_step_x_desc_2 - closestValue_x_step_x_desc_1)*100) ;  %percentage distance between closest 1 and z_loop
        delta_z= (closestValue_z_step_x_desc_2 - closestValue_z_step_x_desc_1)*percent_x/100 ;  % x distance from closest 1
    end

    posz_1=closestValue_z_step_x_desc_1+delta_z  ;       %if closest 1 (measured by AFM) is greater than z_loop, I add the segment delta_z

    matrix_descent_xdesc(1,index)= posz_1 ;
```

```
    matrix_descent_xdesc(2,index)= x_loop_desc ;
    index=index+1 ;

end

matrix_segments_x=[matrix_ascent_xasc(:,1)
matrix_ascent_xasc(:,2)+matrix_descent_xdesc(:,2)] ;
```

%% Step 4: Determination of point P and height h

The model for CSs determination is explained in Section 4.4.2.

At first, the top portion of the profile is calculated in the matrix `mat_n1_n2` and plotted; consider that the top profile is calculated between n1=90% and n2=100% (percentages from the bottom of the plot), reported in Figure B. 4.

More in detail, the matrix is determined in a `for` loop both for ascent and descent branches, in which are considered only the points of the `matrix_ascent_xasc` that are lower than `lim_max` and greater than `lim_min`. Please note that in the calculations of these maximum and minimum limits the baseline `min(matrix_ascent_xasc(1,:))` is considered (and added).

```
%top profile considered - between n1% and n2%
```

```
ind=1 ;

n1=90 ;    %min percentage of the top profile
n2=100;    %max percentage of the top profile

n3=60;     %min percentage of left/right profile
n4=80;     %max percentage of left/right profile

mat_n1_n2 (1,1)=0 ;
mat_n1_n2 (2,2)=0 ;

lim_max = min(matrix_ascent_xasc(1,:)) +
(max(matrix_ascent_xasc(1,:)) -
min(matrix_ascent_xasc(1,:)))/100*n2 ;
lim_min = min(matrix_ascent_xasc(1,:)) +
(max(matrix_ascent_xasc(1,:)) -
min(matrix_ascent_xasc(1,:)))/100*n1;

for i= 1: numel(matrix_ascent_xasc(1,:))
    if (matrix_ascent_xasc (1,i)<= lim_max) &
(matrix_ascent_xasc (1,i)>= lim_min)
        mat_n1_n2 (1, ind)= matrix_ascent_xasc (1,i);
        mat_n1_n2 (2, ind)= matrix_ascent_xasc (2,i);
```

```
            ind=ind+1;
        end
    end

    lim_max = min(matrix_descent_xdesc(1,:)) +
    (max(matrix_descent_xdesc(1,:)) -
    min(matrix_descent_xdesc(1,:)))/100*n2 ;
    lim_min = min(matrix_descent_xdesc(1,:)) +
    (max(matrix_descent_xdesc(1,:)) -
    min(matrix_descent_xdesc(1,:)))/100*n1 ;

    for i= 1: numel(matrix_descent_xdesc(1,:))
        if (matrix_descent_xdesc (1,i)<= lim_max) &
    (matrix_descent_xdesc (1,i)>= lim_min)
            mat_n1_n2 (1, ind)= matrix_descent_xdesc (1,i);
            mat_n1_n2 (2, ind)= matrix_descent_xdesc (2,i);
            ind=ind+1;
        end
    end

    figure
    plot(mat_n1_n2(2,:), mat_n1_n2(1,:),'r','LineWidth',
    2,'Marker','o');
    axis ([-inf inf -inf inf])
    title('top of the profile');
    xlabel('lateral position (nm)');
    ylabel('height (nm)');
```

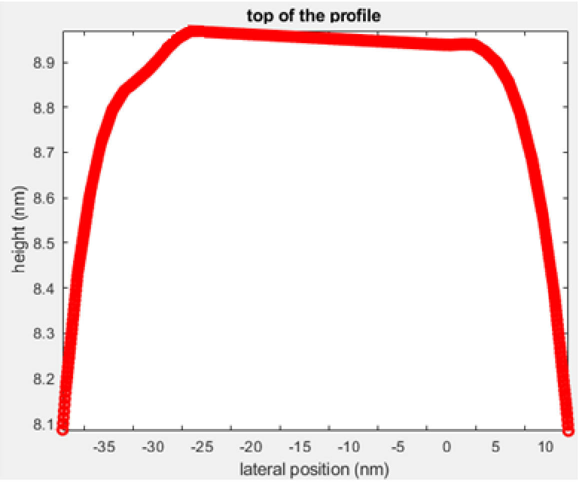

Figure B. 4 Portion of the top profile used to define the linear regression, in order to calculate the point P.

In an analogous way, the left (Figure B. 5) and right (Figure B. 6) profile portions between n3=60% and n4= 80% are calculated, saved into the matrixes `mat_n3_n4_asc` and `mat_n3_n4_desc` and plotted. These portions are used for the calculations of the point P described below.

```
%left profile considered - between n3% and n4%
```

```
ind2=1 ;

mat_n3_n4_asc (1,1)=0 ;
mat_n3_n4_asc (2,2)=0 ;

lim_max_2 = min(matrix_ascent_xasc(1,:)) +
(max(matrix_ascent_xasc(1,:)) -
min(matrix_ascent_xasc(1,:)))/100*n4;
lim_min_2 = min(matrix_ascent_xasc(1,:)) +
(max(matrix_ascent_xasc(1,:)) -
min(matrix_ascent_xasc(1,:)))/100*n3;

for i= 1: numel(matrix_ascent_xasc(1,:))
    if (matrix_ascent_xasc (1,i)<= lim_max_2) &
(matrix_ascent_xasc (1,i)>= lim_min_2)
        mat_n3_n4_asc (1, ind2)= matrix_ascent_xasc (1,i);
        mat_n3_n4_asc (2, ind2)= matrix_ascent_xasc (2,i);
        ind2=ind2+1;
    end
end

figure
plot(mat_n3_n4_asc(2,:), mat_n3_n4_asc(1,:),'r','LineWidth',
2,'Marker','o');
axis ([-inf inf -inf inf])
title('left side of the profile');
xlabel('lateral position (nm)');
ylabel('height (nm)');
```

Annex B. Program Implemented with MATLAB software describing the Geometrical Method for the Analysis of the Critical Sizes of Nanosheets measured by Atomic Force Microscopy

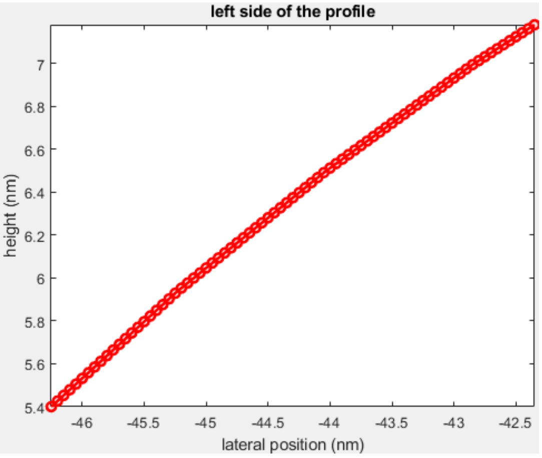

Figure B. 5 Portion of the nanosheet left side profile used to define the linear regression, in order to calculate the point P.

```
%right profile considered - between n3% and n4%

ind3=1 ;

mat_n3_n4_desc (1,1)=0 ;
mat_n3_n4_desc (2,2)=0 ;

lim_max_3 = min(matrix_descent_xdesc(1,:)) +
(max(matrix_descent_xdesc(1,:)) -
min(matrix_descent_xdesc(1,:)))/100*n4;
lim_min_3 = min(matrix_descent_xdesc(1,:)) +
(max(matrix_descent_xdesc(1,:)) -
min(matrix_descent_xdesc(1,:)))/100*n3;

for i= 1: numel(matrix_descent_xdesc(1,:))
    if (matrix_descent_xdesc (1,i)<= lim_max_2) &
(matrix_descent_xdesc (1,i)>= lim_min_2)
        mat_n3_n4_desc (1, ind2)= matrix_descent_xdesc (1,i);
        mat_n3_n4_desc (2, ind2)= matrix_descent_xdesc (2,i);
        ind3=ind3+1;
    end
end

figure
plot(mat_n3_n4_asc(2,:), mat_n3_n4_asc(1,:),'r','LineWidth',
2,'Marker','o');
axis ([-inf inf -inf inf])
title('left side of the profile');
xlabel('lateral position (nm)');
ylabel('height (nm)');
```

Annex B. Program Implemented with MATLAB software describing the Geometrical Method for the Analysis of the Critical Sizes of Nanosheets measured by Atomic Force Microscopy

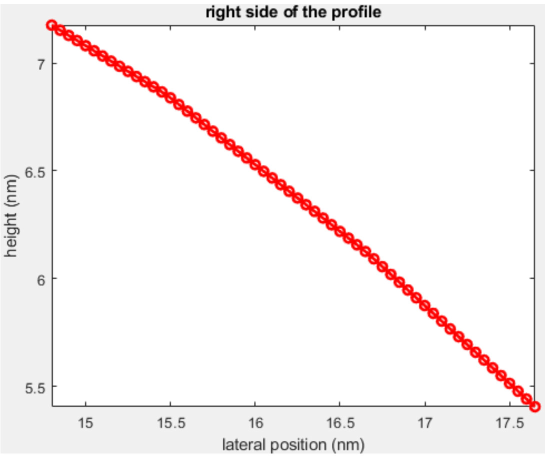

Figure B. 6 Portion of the nanosheet right side profile used to define the linear regression, in order to calculate the point P.

```
%calculation of point P
```

For the calculation of the point P (and subsequently the mean nanosheet height `h_x=z_P`), the intersection is performed between the linear regression lines fitting the plots in Figure B. 4 and Figure B. 5 to obtain P_left, and between the linear regression lines fitting the plots in Figure B. 4 and Figure B. 6 to obtain P_right. After that, the points `new_z_P_asc` and `new_z_P_desc`, that are the measured points in `matrix_ascent_xasc` and `matrix_ascent_xdesc` closest to the calculated `h_x`, are found for allowing the calculation of the lateral size (Step 5).

```
mdl_top_profile =fitlm(mat_n1_n2(2,:),mat_n1_n2(1,:));
q_top_profile=table2array(mdl_top_profile.Coefficients(1,1));
m_top_profile=table2array(mdl_top_profile.Coefficients(2,1));

mdl_left=fitlm(mat_n3_n4_asc(2,:),mat_n3_n4_asc(1,:));
q_left=table2array(mdl_left.Coefficients(1,1));
m_left=table2array(mdl_left.Coefficients(2,1));

mdl_right=fitlm(mat_n3_n4_desc(2,:),mat_n3_n4_desc(1,:));
q_right=table2array(mdl_right.Coefficients(1,1));
m_right=table2array(mdl_right.Coefficients(2,1));

x_P_left = abs((q_left - q_top_profile) / (m_top_profile - m_left));
z_P_left = (m_top_profile * x_P_left + q_top_profile) - z_min;

```

```
x_P_right =(q_right - q_top_profile) / (m_top_profile - m_right);
z_P_right = (m_top_profile * x_P_right + q_top_profile) - z_min;

x_P = (x_P_left + x_P_right)/2;
z_P = (z_P_left + z_P_right)/2;    % calculated nanosheet height
h_x = z_P;

diff_z_P_asc = matrix_ascent_xasc(1,:) - z_P_left;    %matrix diff_z_step_c_asc = matrix ascent to which I subtract the z_P_left
[minValue_z_P_asc,closestIndex_z_P_asc] = min(abs(diff_z_P_asc));       %z height which value is the closest to the z_P_left in pixel
new_z_P_asc = matrix_ascent_xasc(1,closestIndex_z_P_asc); %z height defined in the line above in nm
new_z_P_asc = new_z_P_asc - z_min ;          %new ascent nanosheet height

diff_z_P_desc = matrix_descent_xdesc(1,:) - z_P_right; %matrix diff_z_step_c_asc = matrix descent to which I subtract the z_P_right
[minValue_z_P_asc,closestIndex_z_P_desc] = min(abs(diff_z_P_desc));       %z height which value is the closest to the z_P_right in pixel
new_z_P_desc = matrix_descent_xdesc(1,closestIndex_z_P_desc); %z height defined in the line above in nm
new_z_P_desc = new_z_P_desc - z_min ;       %new descent nanosheet height
```

```
%% Step 5: Calculation of the lateral dimension l_x
```

Figure 4. 14 in Section 4.4.2 shows the sketch of the geometrical approach to determine the nanosheet sizes. Please consider that the code uses slightly different notations; in fact, the segments reported in the Figure 4. 14 as l_{top} here are the segments `g_profx_asc`, while the tip semi-enlargement e is reported in the code as `T_x_asc`.

Once I find the segments `g_profx_asc`/`g_profx_desc` at the height `z_P_asc`/`z_P_desc`, the lateral segment `g_profx` is calculated as the sum of the two segments previously found. After that, the segment `f_max` is calculated as the sum of the two segments `f_max_half_profx_asc` and `f_max_half_profx_desc` at the height `z_half_asc`/`z_half_desc`.

Finally, the lateral segment `l_x` representing the lateral size for the X/Y direction is calculated.

```
% lateral dimension at half height
```

```
g_profx_asc = matrix_ascent_xasc(2,closestIndex_z_P_asc);
g_profx_asc = abs(g_profx_asc) ;
%constant segment 'g_profx_asc' at height new_z_P_asc
g_profx_desc =
matrix_descent_xdesc(2,closestIndex_z_P_desc);   %constant
segment 'g_profx_desc' at height new_z_P_desc
g_profx = abs(g_profx_asc + g_profx_desc) ;

z_half_asc_calc = (new_z_P_asc - z_min_left)/2 + z_min_left
;   %half height of the ascent profile(h/2)
diff_z_half_asc = matrix_ascent_xasc(1,:) - z_half_asc_calc;
[minValue_z_half_asc,closestIndex_z_half_asc] =
min(abs(diff_z_half_asc));
z_half_asc = matrix_ascent_xasc(1,closestIndex_z_half_asc);

z_half_desc_calc = (new_z_P_desc - z_min_right)/2 +
z_min_right ;   %half height of the descent profile(h/2)
diff_z_half_desc = matrix_descent_xdesc(1,:) -
z_half_desc_calc;
[minValue_z_half_desc,closestIndex_z_half_desc] =
min(abs(diff_z_half_desc));
z_half_desc =
matrix_descent_xdesc(1,closestIndex_z_half_desc);

f_max_half_profx_asc = z_half_asc / tand(68.3);     %segment
'f_profx_asc' at h/2
f_max_half_profx_desc = z_half_desc / tand(68.3);   %segment
'f_profx_desc' at h/2
f_max = f_max_half_profx_asc + f_max_half_profx_desc ;

l_x = g_profx + f_max ;
l_prof_x_asc_half = g_profx_asc + f_max_half_profx_asc ;
l_prof_x_desc_half = g_profx_desc + f_max_half_profx_desc ;
```

```
% lateral size for various heights
```

This second part of Step 5 is useful for the calculation of the tip enlargement in Step 6. In fact, both for the ascent and descent profiles, the segments `l_prof_x_asc`/`l_prof_x_desc` are calculated, saved into the matrixes `matrix_l_prof_x_asc`/`matrix_l_prof_x_desc` and plotted (Figure B. 7 and

Figure B. 8). Please note that the segments `f_max_profx_asc`/`f_max_profx_desc` are calculated as reported in Figure 4. 14.

```
id=1 ;

for ii = closestIndex_z_half_asc:closestIndex_z_P_asc

    %ascent CROSS-SECTION x profile

    f_max_profx_asc(id) = (matrix_ascent_xasc
(1,closestIndex_z_P_asc) - matrix_ascent_xasc (1,ii))/
tand(68.3);   %segment 'f_profx_asc' at h/2
    l_prof_x_asc(id)= g_profx_asc + f_max_profx_asc(id) ;
%lateral segment 'l_prof_x_asc'

    id=id+1 ;

end

d= closestIndex_z_half_asc:closestIndex_z_P_asc ;
z_axis_l_prof_x_asc = matrix_ascent_xasc (1,d) ;
matrix_l_prof_x_asc = [z_axis_l_prof_x_asc; l_prof_x_asc] ;

figure
plot(l_prof_x_asc, z_axis_l_prof_x_asc,'b','LineWidth',
2,'Marker','o');
axis ([-inf inf -inf inf])
title('segments l_ asc');
xlabel('segments length (nm)');
ylabel('height (nm)');
```

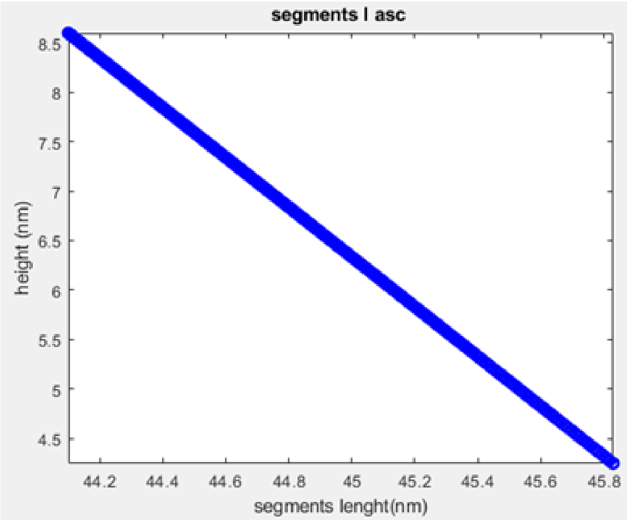

Figure B. 7 Variation of the lateral size ‘l’ at various heights for the nanosheet left side.

```
ix=1;

for iii = closestIndex_z_P_desc:closestIndex_z_half_desc

    %descent CROSS-SECTION x profile

    f_max_profx_desc(ix) = (matrix_descent_xdesc
(1,closestIndex_z_P_desc) - matrix_descent_xdesc(1,iii) )/
tand(68.3);    %segment 'f_profx_desc' at h/2
    l_prof_x_desc(ix)= g_profx_desc + f_max_profx_desc(ix) ;
%lateral segment 'l_prof_x_desc'

    ix=ix+1 ;

end

dd= closestIndex_z_P_desc:closestIndex_z_half_desc ;
z_axis_l_prof_x_desc = matrix_descent_xdesc (1,dd) ;
matrix_l_prof_x_desc = [z_axis_l_prof_x_desc; l_prof_x_desc]
;

figure
plot(l_prof_x_desc, z_axis_l_prof_x_desc,'b','LineWidth',
2,'Marker','o');
axis ([-inf inf -inf inf])
title('segments l_ desc');
xlabel('segments lenght(nm)');
ylabel('height (nm)');
```

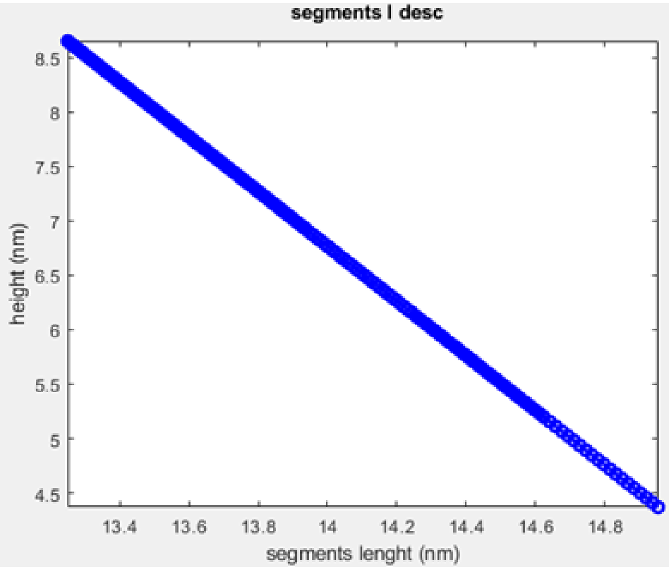

Figure B. 8 Variation of the lateral size ‘l’ at various heights for the nanosheet right side.

%% Step 6: Calculation of the enlargment 'T_x'

In this step, the code that led to the calculation of the tip enlargement profile is reported. For both ascent and descent profiles, two loops are reported.

In the first `while` loop, the segments `T_x_asc`/`T_x_desc` from the baseline to the half height are calculated by subtracting the half lateral CS `l_prof_x_asc_half`/ `l_prof_x_desc_half` to the half ascent/descent cross-section profile.

In the second `while` loop, the segments `T_x_asc`/`T_x_desc` from the half height are calculated to the P_left/P_right height by subtracting the segments `matrix_ascent_profx_f` /`matrix_descent_profx_f` to the half ascent/descent cross-section profile.

In the end, the two segments `T_x_asc` and `T_x_desc` are concatenated and plotted (Figure B. 9).

```
index = 1;
while matrix_ascent_xasc(1,index)< z_half_asc
    T_x_asc(2,index) = matrix_ascent_xasc(2,index) - l_prof_x_asc_half ;   %calculation of enlargement T_x from 0 to h/2
    T_x_asc(1,index) = matrix_ascent_xasc(1,index) ;
    index =index +1;
end

idx = 1;
while matrix_ascent_xasc(1,index)< new_z_P_asc
    matrix_ascent_profx_f(2,idx)=  (new_z_P_asc - matrix_ascent_xasc(1,index)) / tand(68.3) ; %calculate f
    matrix_ascent_profx_f(1,idx)= matrix_ascent_xasc(1,index) ;

    T_x_asc(2,index) = matrix_ascent_xasc(2,index) - g_profx_asc - matrix_ascent_profx_f(2,idx) ;   %calculation of the enlargement T_x from h/2 to new_z_max
    T_x_asc(1,index) = matrix_ascent_xasc(1,index) ;

    index =index +1;
    idx =idx +1;
end

% descent CROSS-SECTION x profile

index = 1;

while matrix_descent_xdesc(1,index) > new_z_P_desc   %I go from z_max to z_max_new (I do not do calculation)
    index =index +1;
```

```
end

idx = 1;
while matrix_descent_xdesc(1,index)> z_half_desc
    matrix_descent_profx_f(2,idx)=  (new_z_P_desc - matrix_descent_xdesc(1,index)) / tand(68.3) ; %calculate f
    matrix_descent_profx_f(1,idx)= matrix_descent_xdesc(1,index) ;

    T_x_desc(2,idx) = matrix_descent_xdesc(2,index) - g_profx_desc - matrix_descent_profx_f(2,idx) ; %calculation of enlargement T_x from h/2 to new_z_max
    T_x_desc(1,idx) = matrix_descent_xdesc(1,index) ;

    index =index +1;
    idx =idx +1;
end

while index < numel(matrix_descent_xdesc)/2
    T_x_desc(2,idx) = matrix_descent_xdesc(2,index) - l_prof_x_desc_half ;   %calculation of the enlargement T_x from 0 to h/2
T_x_desc(1,idx) = matrix_descent_xdesc(1,index) ;
    index =index +1;
    idx =idx +1;
end

T_x_asc (2,:) = T_x_asc(2,:) + max (-T_x_asc(2,:));
T_x_desc (2,:) = T_x_desc(2,:) - min (T_x_desc(2,:));

T_x(2,:) = [(T_x_asc (2,:)), (max(T_x_asc (2,:))+(T_x_desc (2,:)))];
T_x(1,:) = [T_x_asc(1,:), T_x_desc(1,:)];

Figure
plot(T_x(2,:),T_x(1,:),'g','LineWidth', 2);
axis ([-inf inf 1 inf])
title('tip enlargement');
xlabel('profile coordinate (nm)');
ylabel('nanosheet height (nm)');
```

Annex B. Program Implemented with MATLAB software describing the Geometrical Method for the Analysis of the Critical Sizes of Nanosheets measured by Atomic Force Microscopy

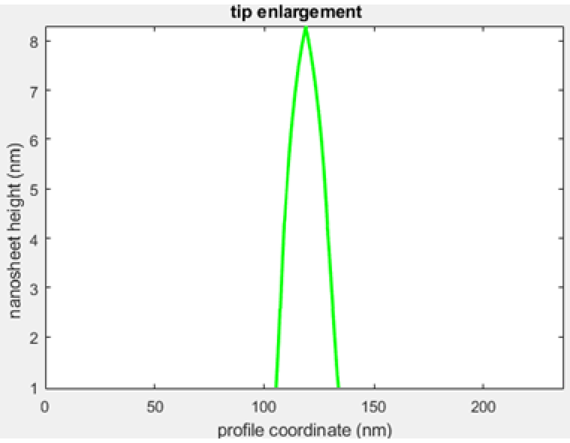

Figure B. 9 Cross-sectional profile of tip enlargement.

Finally, for further comparisons, the tip is centered to its maximum and plotted (Figure B. 10).

```
T_x_asc_2 (2,:) = T_x_asc(2,:) - max (T_x_asc(2,:));
T_x_centered (2,:) = [T_x_asc_2(2,:) T_x_desc(2,:)];
T_x_centered (1,:) = [T_x_asc(1,:) T_x_desc(1,:)];

Figure
plot(T_x_centered(2,:),T_x_centered(1,:),'g','LineWidth',
2);
axis ([-inf inf 1 inf])
title('x-direction tip enlargement');
xlabel('profile coordinate (nm)');
ylabel('nanosheet height (nm)');
```

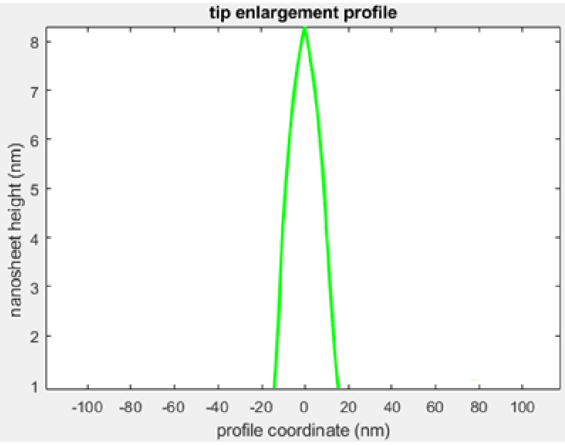

Figure B. 10 Cross-sectional profile of the tip enlargement centered respect to the ordinate axis.

%% Step 7: Save workspace data (.mat) for further analysis

In this last step are reported the instructions needed to choose the folder in which save the MATLAB file for further analysis, *e.g.* in a spreadsheet.

```
%User is prompted to select a destination folder.
destinationpath = uigetdir(file_path, 'Choose output folder for Geometrical Model Tip Reconstruction data');
if destinationpath == 0
    destinationpath = file_path;
end

% Save workspace data (.mat)
k = strfind(file_name,'.');
filetype = file_name(k+1:k+3);
new_file = fullfile(destinationpath,[name '_' filetype '_' datestr(now, 30) 'all.mat']);      %Output name has image name plus date in format YYYYMMDDTHHMMSS
save (new_file) %Outputs all the data in the workspace into "new_file.mat"
```

References

---

[1] G. B. Picotto, M. Vallino, L. Ribotta, Tip–sample characterization in the AFM study of a rod-shaped nanostructure, *Meas. Sci. Technol.* 31 (2020) 084001 (12pp), DOI: 10.1088/1361-6501/ab7bc2

[2] V. Maurino, F. Pellegrino, G. B. Picotto, L. Ribotta, *Ultram.,* 234 (2022) 113480 (13 pp), DOI: 10.1016/j.ultramic.2022.113480

[3] R. Bellotti, G. B. Picotto, L. Ribotta, AFM Measurements and Tip Characterization of Nanoparticles with Different Shapes, *Nanomanuf. Metrol.* (2022) (12 pp), DOI: 10.1007/s41871-022-00125-x

[4] JCGM 200:2012 - International vocabulary of metrology – Basic and general concepts and associated terms (VIM), 3rd edition, 2008

[5] "Metrology – in short" 3rd edition, 2008, EURAMET project 1011

[6] A. J. Lewis, Realising the metre, in Proceedings of the International School of Physics "Enrico Fermi" - Course 206 "New Frontiers for Metrology: From Biology and Chemistry to Quantum and Data Science", edited by M. J. T. Milton, D. S. Wiersma, C. J. Williams, M. Sega (IOS, Amsterdam; SIF, Bologna), 2021, DOI: 10.3254/ENFI210015

[7] The International System of Units, 9th edition, Bureau International de Poids et Mesures (BIPM), 2019, ISBN 978-92-822-2272-0

[8] A. J. Lewis, Dimensional metrology in practice, in Proceedings of the International School of Physics "Enrico Fermi" - Course 206 "New Frontiers for Metrology: From Biology and Chemistry to Quantum and Data Science", edited by M. J. T. Milton, D. S. Wiersma, C. J. Williams, M. Sega (IOS, Amsterdam; SIF, Bologna), 2021, DOI: 10.3254/ENFI210016

[9] R. P. Feynman, There's Plenty of Room at the Bottom, Engineering and Science, 1960, 23, 22-36, ISSN 0013-7812

References

---

[10] https://www.prnewswire.com/news-releases/nanotechnology-market-to-garner-33-63-billion-globally-by-2030-at-36-4-cagr-allied-market-research-301362482.html#:~:text=As%20per%20the%20report%2C%20the,36.4%25%20from%202021%20to%202030, web access January 2022

[11] ISO/TC 229 – Nanotechnologies, International Organization for Standardization, Geneva, 2005, https://www.iso.org/committee/381983.html

[12] R. Bogue, Nanometrology: a critical discipline for the twenty-first century, Sensors Rev, 2007, 27, 3, 189-196, DOI: 10.1108/02602280710758110

[13] R. K. Leach, R. Boyd, T. Burke, H. U. Danzebrink, K. Dirscherl, T. Dziomba, M. Gee, L. Koenders, V. Morazzani, A. Pidduck, D. Roy, W. E. S. Unger, A. Yacoot, The European nanometrology landscape, Nanotechnology 22 (2011) 062001, DOI: 10.1088/0957-4484/22/6/062001

[14] Z. Zhu, J. Meija, S. Tong, A. Zheng, L. Zhou, L. Yang, Determination of the Isotopic Composition of Osmium Using MC-ICPMS. Analytical Chemistry 2018, 90 (15) 9281-9288, DOI: 10.1021/acs.analchem.8b01859

[15] Y. Zhu, T. Narukawa, S.-I. Miyashita, T. Kuroiwa, K. Inagaki, K. Chiba, A. Hioki, Development of a Certified Reference Material (NMIJ CRM 7512-a) for the Determination of Trace Elements in Milk Powder, Analytical Sciences, 2013, 29 (2) 247-53, DOI: 29(2):247-53

[16] N. G. Orji, M. Badaroglu, B. M. Barnes, C. Beitia, B. D. Bunday, U. Celano, R. J. Kline, M. Neisser, Y. Obeng, A. E. Vladar, Metrology for the next generation of semiconductor devices, Nat Electron. 2018; 1, DOI: 10.1038/s41928-018-0150-9

[17] E. M. Perassi, J. C. Hernandez-Garrido, M. Sergio Moreno, E. R. Encina, E. A. Coronado, P. A. Midgley, Using Highly Accurate 3D Nanometrology to Model the Optical Properties of Highly Irregular Nanoparticles: A Powerful Tool for Rational Design of Plasmonic Devices, Nano Lett. 2010, 10, 2097–2104, DOI: 10.1021/nl1005492

[18] D. A. Lucca, K. Herrmann, M. J. Klopfstein, Nanoindentation: Measuring methods and applications, CIRP Annals - Manufacturing Technology 59 (2010) 803–819, DOI: 10.1016/j.cirp.2010.05.009

References

---

[19] N. Ohmae, J. Liu, Nanotribology and Nanoscale Materials Coatings for Lubricants, Reference Module in Materials Science and Materials Engineering, 2016, DOI: 10.1016/B978-0-12-803581-8.00615-9

[20] H. M. C. de Azeredo, C. G. Otoni, O. B. G. Assis, D. S. Corrêa, M. R.de Moura, L. H. C. Mattoso, Nanoparticles and Antimicrobial Food Packaging, Reference Module in Food Science, 2018, DOI: 10.1016/B978-0-08-100596-5.21874-X

[21] S. Beherens, Preparation of functional magnetic nanocomposites and hybrid materials: recent progress and future directions, Nanoscale, 3, 2011, 877–892, DOI: 10.1039/C0NR00634C

[22] W. Poirier, S. Djordjevic, F. Schopfer, O. Thévenot, The ampere and the electrical units in the quantum era, Comptes Rendus Physique, 20, 2019, 92-128, DOI: 10.1016/j.crhy.2019.02.003

[23] A. Duschl, Nanomedicine, Chapter 12 in Immune Rebalancing - The Future of Immunosuppression by D. Boraschi, G. Penton-Rol, 2016, DOI: 10.1016/B978-0-12-803302-9.00012-9

[24] N. Faruqui, A. Kummrow, B. Fu, C. Divieto, F. Rojas, F. Kisulu, J. J. V. Cavalcante, J. Wang, J. Campbell, J. L. Martins, J.-H. Choi, M. P. Sassi, M. Zucco, M. Vonsky, S. Vessillier, S. Zou, S.-I. Fujii, M. G. Ryadnov, Cellular Metrology: Scoping for a Value Proposition in Extra- and Intracellular Measurements, Front. Bioeng. Biotechnol., 2020, DOI: 10.3389/fbioe.2019.00456

[25] M. A. Taylor, W. P. Bowen, Quantum metrology and its application in biology, Physics Reports, 615, 2016, 1-59, DOI: 10.1016/j.physrep.2015.12.002

[26] F. Babick, R. Boyd, A. Braun, I. Busch, H.-U. Danzebrink, L. Depero, K. Dirscherl, T. Dziomba, E. Eriksson, K. Franks, M. Gee, P.-E. Hansen, N. M. Jennett, V. Kestens, L. Koenders, M. Krumrey, J. Lausmaa, R. Leach, L. Pendrill, A. Pidduck, S. Put, G. Roebben, D. Roy, M. Stintz, R. Turan, A. Yacoot, Introductory Guide to Nanometrology, edited by P.-E. Hansen, G. Roebben, Coordination of Nanometrology in Europe project (FP7 CSA-CA 218764), 2010, ISBN: 978-0-9566809-1-4

References

---

[27] S. Rosén, T. R. Thomas, B.-G. Rosén, The Stedman diagram revisited, Surf. Topogr.: Metrol. Prop. 2 (2014) 014005 (5pp), DOI: 10.1088/2051-672X/2/1/014005

[28] R. Herrera-Basurto, B. M. Simonet, Nanometrology, Encyclopedia of Analytical Chemistry, 2013, DOI: 10.1002/9780470027318.a9177

[29] M. Naito, T. Yokoyama, K. Hosokawa, K. Nogi, Chapter 5 – Characterization methods for nanostructure of materials, Nanoparticle Technology Handbook (Third Edition), Elsevier, 2018, ISBN 978-0-444-64110-6

[30] ISO/IEC 17025 - Testing And Calibration Laboratories, International Organization for Standardization, Geneva, https://www.iso.org/ISO-IEC-17025-testing-and-calibration-laboratories.html

[31] A. Henson, Metrological traceabilty: A global perspective, in Proceedings of the International School of Physics "Enrico Fermi" - Course 206 "New Frontiers for Metrology: From Biology and Chemistry to Quantum and Data Science", edited by M. J. T. Milton, D. S. Wiersma, C. J. Williams, M. Sega (IOS, Amsterdam; SIF, Bologna), 2021, DOI: 10.3254/ENFI210027

[32] L. Siekmann, Requirements for Reference (Calibration) Laboratories in Laboratory Medicine, Clin Biochem Rev, 28, 2007, 149-154, PMID: 18392129 PMCID: PMC2282407

[33] PTB Physikalisch-Technische Bundesanstalt Working Group 5.23 AFM Linewidth Metrology, Developments of high resolution CD/3D AFMs, https://www.ptb.de/cms/en/ptb/fachabteilungen/abt5/fb-52/ag-523/forschungsthemen5230.html, web access May 2019

[34] G. Dai, K. Hahm, J. Fluegge, H. Bosse, Accurate and traceable calibration of critical dimensions based on CD-AFM and TEM, Proceedings of the 14th euspen International Conference – Dubrovnik – June 2014

[35] G. Dai, K. Hahm, H. Bosse, R. G. Dixson, Comparison of line width calibration using critical dimension atomic force microscopes between PTB and NIST, Meas. Sci. Technol. 28 (2017) 065010 (12pp), DOI: 10.1088/1361-6501/aa665b

References

---

[36] V. Hackley, Nanoparticle Reference Materials: Lessons Learned and the Case for Number Concentration Measurements, Materials Measurement Science Division of National Institute of Standards & Technology, Nanoparticle concentration – critical needs and state-of-the-art measurements, April 2018, Royal Society of Chemistry

[37] EA-4/14 INF:2003 guide, The Selection and Use of Reference Materials, European co-operation for Accreditation (EA)

[38] T. P. J. Linsinger, G. Roebben, C. Solans, R. Ramsch, Reference materials for measuring the size of nanoparticles, Trends in Analytical Chemistry, 30, 1, 2011, 18-27, DOI: 10.1016/j.trac.2010.09.005

[39] BIPM – Bureau International des Poids et Mesures, Sevres, France, JCTLM database, https://www.bipm.org/jctlm/

[40] COMAR – Code d'Indexation des Matériaux de Référence: International database for certified reference materials, https://www.comar.bam.de/home/login.php

[41] BAM – Bundesanstalt für Materialforschung und -prüfung – German Federal Institute for Materials Research and Testing, Reference Materials Certificates and reports, https://rrr.bam.de/RRR/Navigation/EN/Reference-Materials/RM-Certificates-reports/rm-certificates-reports.html

[42] BAM – Bundesanstalt für Materialforschung und -prüfung – German Federal Institute for Materials Research and Testing, BAM webshop, https://www.webshop.bam.de/

[43] IRMM – Institute for Reference Materials and Measurements, institute of the European Commission's science and knowledge service Joint Research Centre (JRC), https://ec.europa.eu/jrc/en/science-update/welcome-irmm-reference-materials-catalogue

[44] VSL – Dutch Metrology Institute, https://www.vsl.nl/en/services/reference-materials

[45] LGC – Laboratory of the Government Chemist of the United Kingdom, https://www.lgcgroup.com/products/reference-materials/#.W8SxfGj7SUl

References

---

[46] NMIJ – National Metrology Institute of Japan, https://www.nmij.jp/english/service/C/crm/index.php?menu%5B0%5D=42&menu%5B1%5D=9999

[47] NIST National Institute of Standards and Technology, U. S. Department of Commerce https://www.nist.gov/srm/srm-definitions

[48] ISO 17034:2016 - General requirements for the competence of reference material producers, Geneva, https://www.iso.org/standard/29357.html

[49] ISO GUIDE 35:2017 - Reference materials — Guidance for characterization and assessment of homogeneity and stability, Geneva, https://www.iso.org/standard/60281.html

[50] M. Sega, Reference Materials: Preparation, homogeneity, stability and value assignment, in Proceedings of the International School of Physics "Enrico Fermi" - Course 206 "New Frontiers for Metrology: From Biology and Chemistry to Quantum and Data Science", edited by M. J. T. Milton, D. S. Wiersma, C. J. Williams, M. Sega (IOS, Amsterdam; SIF, Bologna), 2021, DOI: 10.3254/ENFI210029

[51] https://www.nanoscale.ptb.de/nanoscale-standards.html, web access May 2020

[52] EMPIR project 15SIB09 – "Traceable three-dimensional nanometrology – 3DNano", Publishable Summary, Euramet, June 2016

[53] ISO Guide 30:2015, Reference Materials — Selected Terms and Definitions, International Organization for Standardization, Geneva, 2020. https://www.iso.org/standard/46209.html, web access May 2021

[54] I. Misumi, Nano dimensional standards, in Nanoscale Standards by Metrological AFM and Other Instruments, IOP Publishing, 2021, DOI: 10.1088/978-0-7503-3191-3ch1

[55] ERM-FD100 colloidal silica (20 nm nominal), Certified reference materials catalogue, IRMM – Institute for Reference Materials and Measurements, institute of the European Commission's science and knowledge service Joint Research Centre (JRC-IRRM), https://crm.jrc.ec.europa.eu/p/40456/40487/By-analyte-

---

group/Particle-pore-size/ERM-FD100-COLLOIDAL-SILICA-20-nm-nominal/ERM-FD100&lang=NL

[56] RM 8011 - Gold Nanoparticles (Nominal 10 nm Diameter), Standard Reference Materials, SRM Online Request System, NIST National Institute of Standards and Technology, U. S. Department of Commerce, https://www-s.nist.gov/srmors/view_detail.cfm?srm=8011

[57] RM 8012 - Gold Nanoparticles, Nominal 30 nm Diameter, Standard Reference Materials, SRM Online Request System, NIST National Institute of Standards and Technology, U. S. Department of Commerce, https://www-s.nist.gov/srmors/view_detail.cfm?srm=8012

[58] RM 8013 - Gold Nanoparticles, Nominal 60 nm Diameter, Standard Reference Materials, SRM Online Request System, NIST National Institute of Standards and Technology, U. S. Department of Commerce, https://www-s.nist.gov/srmors/view_detail.cfm?srm=8013

[59] RM 8017 - Polyvinylpyrrolidone Coated Silver Nanoparticles (Nominal Diameter 75 nm), Standard Reference Materials, SRM Online Request System, NIST National Institute of Standards and Technology, U. S. Department of Commerce, https://www-s.nist.gov/srmors/view_detail.cfm?srm=8017

[60] SRM 1964 - Polystyrene Spheres (Nominal Diameter 60 nm), Standard Reference Materials, SRM Online Request System, NIST National Institute of Standards and Technology, U. S. Department of Commerce, https://www-s.nist.gov/srmors/view_detail.cfm?srm=1964

[61] SRM 1963a - Polystyrene Spheres (Nominal Diameter 100 nm), Certified reference materials catalogue, IRMM – Institute for Reference Materials and Measurements, institute of the European Commission's science and knowledge service Joint Research Centre (JRC-IRRM), https://www-s.nist.gov/srmors/view_detail.cfm?srm=1963A

[62] ERM-FD304 colloidal silica (40 nm nominal), Certified reference materials catalogue, IRMM – Institute for Reference Materials and Measurements, institute of the European Commission's science and knowledge service Joint Research Centre (JRC-IRRM), https://crm.jrc.ec.europa.eu/p/q/ERM-FD304/ERM-FD304-COLLOIDAL-SILICA/ERM-FD304&lang=NL

References

---

[63] ERM-FD102 colloidal silica (bimodal), Certified reference materials catalogue, IRMM – Institute for Reference Materials and Measurements, institute of the European Commission's science and knowledge service Joint Research Centre (JRC-IRRM), https://crm.jrc.ec.europa.eu/p/40456/40487/By-analyte-group/Particle-pore-size/ERM-FD102-COLLOIDAL-SILICA-bimodal/ERM-FD102

[64] Prudent Practices in the Laboratory: Handling and Management of Chemical Hazards, National Research Council (US) Committee on Prudent Practices in the Laboratory, Washington (DC): National Academies Press (US), The National Academies Collection: Reports funded by National Institutes of Health, 2011, DOI: 10.17226/12654

[65] P. Eaton, P. Quaresma, C. Soares, C. Neves, M.P. de Almeida, E. Pereira, P. West, A direct comparison of experimental methods to measure dimensions of synthetic nanoparticles, Ultramicroscopy 182 (2017) 179–190

[66] T. Linsinger, G. Roebben, D. Gilliland, L. Calzolai, F. Rossi, N. Gibson, C. Klein, Requirements on measurements for the implementation of the European Commission definition of the term “nanomaterial”, JRC-IRCCM, 2012, DOI: 10.2787/63490

[67] L. J. Perez-Lorenzo,V- Khanna,T. Meena, J. J. Schmitt, J. Fernandez de la Mora, A high resolution DMA covering the 1–67 nm size range, Aerosol Science and Technology, Volume 54, 2020 - Issue 1DOI: 10.1080/02786826.2019.1684433

[68] S. Da Vela, D. I. Svergun, Methods, development and applications of small-angle X-ray scattering to characterize biological macromolecules in solution, Current Research in Structural Biology, Volume 2, 2020, Pages 164-170, DOI: 10.1016/j.crstbi.2020.08.004

[69] Wikimedia Commons, Electron Interaction with Matter.svg, https://commons.wikimedia.org/wiki/File:Electron_Interaction_with_Matter.svg

[70] ISO 29301:2010 —Microbeam analysis — Analytical transmission electron microscopy — Methods for calibrating image magnification by using reference materials having periodic structures, Geneva, https://www.iso.org/standard/45399.html

References

---

[71] ISO 13322-1:2014 — Particle size analysis — Image analysis methods — Part 1: Static image analysis methods, Geneva, https://www.iso.org/standard/51257.html

[72] P.-J. De Temmerman, J. Lammertyn, B. De Ketelaere, V. Kestens, G. Roebben, E. Verleysen, J. Mast, Measurement uncertainties of size, shape, and surface measurements using transmission electron microscopy of near-monodisperse, nearspherical nanoparticles, J. Nanopart. Res. 16 (2014) 2177, 20p, DOI: 10.1007/s11051-013-2177-1

[73] B. J. Inkson, Scanning electron microscopy (SEM) and transmission electron microscopy (TEM) for materials characterization, in Materials Characterization Using Nondestructive Evaluation (NDE) Methods, 2016, Woodhead Publishing, DOI: 10.1016/B978-0-08-100040-3.00002-X

[74] E. Velichko, S. Makarov, E. Nepomnyashchaya, G. Dong, Molecular Aggregation in Immune System Activation Studied by Dynamic Light Scattering, Biology 9(6):123, 2020, DOI: 10.3390/biology9060123

[75] Otsuka Electronics Co., Ltd, Dynamic Light Scattering Spectrophotometer DLS-8000 series, https://www.otsukael.com/product/detail/productid/23, web access January 2022

[76] W. Wohlleben, V. A. Coleman, D. Gilliland, Chapter 3.3.1 - Analytical centrifugation, Characterization of Nanoparticles – Measurement Processes for Nanoparticles – Micro and Nano Technologies, 2020, 225-247, DOI: 10.1016/B978-0-12-814182-3.00015-8

[77] Centrifugal Sedimentation, Particle Size Distribution Measurement by Centrifugation, Horiba, https://www.horiba.com/int/technology/light-scattering/centrifugal-sedimentation/, web access January 2022

[78] ISO 13318-1, Determination of particle size distribution by centrifugal liquid sedimentation methods – Part 1: General principles and guidelines, International Organization for Standardization, Geneva, 2001, https://www.iso.org/standard/21704.html

[79] ISO 13318-2, Determination of particle size distribution by centrifugal liquid sedimentation methods – Part 2: Photocentrifuge method, International

References

Organization for Standardization, Geneva, 2007, https://www.iso.org/standard/45771.html

[80] D. Intra, N. Tippayawong, An overview of differential mobility analyzers for size classification ofnanometer-sized aerosol particles, Songklanakarin J. Sci. Technol. 30 (2), 243-256, 2008, https://www.researchgate.net/publication/26517300_An_overview_of_differential_mobility_analyzers_for_size_classification_of_nanometer-sized_aerosol_particles

[81] M. L.Ostraat, CHAPTER 6 - Industry-Led Initiative for Occupational Health and Safety, Nanotechnology Environmental Health and Safety - Risks, Regulation and Management, Micro and Nano Technologies, 2010, Pages 181-246, DOI: 10.1016/B978-0-8155-1586-9.10006-4

[82] R. C. Flagan, Continuous-flow differential mobility analysis of nanoparticles and biomolecules, Annu Rev Chem Biomol Eng,. 2014, 5, 255-79, DOI: 10.1146/annurev-chembioeng-061312-103316

[83] K. Vasilatou, F. Gaie-Levrel, N. Clouet-Foraison, V. Delatour, Chapter 3.1.3 - Electrospray-differential mobility analysis (ES-DMA), in Characterization of Nanoparticles - Measurement Processes for Nanoparticles, Micro and Nano Technologies, 2020, Pages 97-116, DOI: 10.1016/B978-0-12-814182-3.00008-0

[84] H. Holmgren, On the Formation and Physical Behaviour of Exhaled Particles, PhD thesis, Department of Chemical and Biological Engineering, CHALMERS UNIVERSITY OF TECHNOLOGY, Goteborg, Sweden 2011, https://www.researchgate.net/publication/260591951_THESIS_FOR_THE_DEGREE_OF_DOCTOR_OF_PHILOSOPHY_On_the_Formation_and_Physical_Behaviour_of_Exhaled_Particles

[85] S. Skou, R. E. Gillilan, N. Ando, Synchrotron-based small-angle X-ray scattering of proteins in solution, Nature Protocols volume 9, pages 1727–1739 (2014), DOI: 10.1038/nprot.2014.116

[86] L. Boldon, F. Laliberte, L. Liu, Review of the fundamental theories behind small angle X-ray scattering, molecular dynamics simulations, and relevant integrated application, Nano Reviews, 6, 1, 25661, (2015), DOI: 10.3402/nano.v6.25661

---

[87] J. C. Riviere, S. Myhra, Handbook of Surface and Interface Analysis – Methods for Problem-Solving, Second Edition, 2009, CRC Press, ISBN:9781420007800

[88] G. Binnig, H. Rohrer, C. Gerber, E. Weibel, Surface Studies by Scanning Tunneling Microscopy, 1982, Phys. Rev. Lett., 49, 57, DOI: 10.1103/PhysRevLett.49.57

[89] R. Young, J. Ward, and F. Scire, The Topografiner: An Instrument for Measuring Surface Microtopography, 1972, Rev. Sci. Instrum., 43, 999-1011, DOI: 10.1063/1.1685846

[90] G. Binnig, C. F. Quate, C. Gerber, Atomic Force Microscope, 1986, Phys. Rev. Lett. 56, 930, DOI: 10.1103/PhysRevLett.56.930

[91] E. Betzig, A. Lewis, A. Harootunian, M. Isaacson, E. Kratschmer, Near Field Scanning Optical Microscopy (NSOM), 1986, Biophys. J. 49 (1): 269–79, DOI:10.1016/s0006-3495(86)83640-2

[92] A. J. Bard, F. R. F. Fan, J. Kwak, O. Lev, Scanning electrochemical microscopy. Introduction and principles, Analytical Chemistry,1989, 61 (2): 132–138, DOI: 10.1021/ac00177a011

[93] True Non-Contact™ Mode, Park AFM Systems, https://www.parksystems.com/park-spm-modes/91-standard-imaging-mode/217-true-non-contact-mode, web access October 2021

[94] Atomic force microscopy introduction, Dissemination of IT for the Promotion of Materials Science (DoITPoMS), University of Cambridge, https://www.doitpoms.ac.uk/tlplib/afm/intro.php, web access January 2020

[95] What is Atomic Force Microscopy (AFM), NanoandMore Gmbh, https://www.nanoandmore.com/what-is-atomic-force-microscopy, web access November 2021

[96] P. A. F. Garrillo, Development of highly resolved and photo-modulated Kelvin probe microscopy techniques for the study of photovoltaic systems, Doctoral thesis, Université Grenoble Alpes, 2018, https://www.researchgate.net/publication/330179783_Development_of_highly_resolved_and_photo-

---

modulated_Kelvin_probe_microscopy_techniques_for_the_study_of_photovoltaic_systems

[97] B. Voigtlander, Atomic Force Microscopy, Second Edition, NanoScience and Technology Series, Springer, 2019, ISBN 978-3-030-13653-6, DOI: 10.1007/978-3-030-13654-3

[98] Park Systems AFM configurations, https://www.parksystems.com/park-afm-options, web access December 2021

[99] Y. Hua, C. Coggins, S. Park, S, Park, Advanced 3D metrology atomic force microscope with crosstalk eliminated, Proc. SPIE 7729, Scanning Microscopy 2010, 77290N (3 June 2010); https://doi.org/10.1117/12.853679

[100] Atomic Force Microscopy Feedback, Dissemination of IT for the Promotion of Materials Science (DoITPoMS), University of Cambridge, https://www.doitpoms.ac.uk/tlplib/afm/feedback_circuit.php, web access January 2020

[101] F. Marinello, Atomic Force Microscopy in nanometrology: modeling and enhancement of the instrument, PhD thesis, University of Padova, 2007, http://hdl.handle.net/11577/3425597

[102] V. Korpelainen, Traceability for nanometre scale measurements: Atomic force microscopes in dimensional nanometrology, PhD Dissertation, University of Helsinki, 2014, ISBN 978-952-6682-21-1, https://cris.vtt.fi/en/publications/traceability-for-nanometre-scale-measurements-atomic-force-micros

[103] A. Yacoot, L. Koenders, Recent developments in dimensional nanometrology using AFMs, 2011, Meas. Sci. Technol., 22 ,122001, 12pp, DOI:10.1088/0957-0233/22/12/122001

[104] B. J. Eves, Design of a large measurement-volume metrological atomic force microscope (AFM), Meas. Sci. Technol. 20 (2009) 084003 (5pp), DOI:10.1088/0957-0233/20/8/084003

[105] J. A. Kramar, R. Dixson, N. G. Orji, Scanning probe microscope dimensional metrology at NIST, Meas. Sci. Technol. 22 (2011) 024001 (11pp) doi:10.1088/0957-0233/22/2/024001

References

---

[106] J. Herrmann, M. Lawn, C. Freund, J. Miles, V. Coleman, Å. Jämting, Development of a Scanning Probe Microscope for Traceable Nanoscale Length Metrology, Proceedings of the euspen International Conference, Delft, 2010

[107] B. Babic, C. H. Freund, J. Herrmann, M. A. Lawn, J. Miles, Metrological scanning probe microscope based on a quartz tuning fork detector, J. Micro/Nanolith. MEMS MOEMS, 2012, 11, 1, 011003, DOI: 10.1117/12.884567

[108] NMI Australia's new Metrological Scanning Probe Microscope, 2013, https://www.youtube.com/watch?v=OFWNHTIm_O8, web access September 2021

[109] M. Lu, S. Gao, Q. Jin, J. Cui, H. Du, H. Gao, An atomic force microscope head designed for nanometrology, Meas. Sci. Technol., 2007, 18, 1735–1739, DOI:10.1088/0957-0233/18/6/S11

[110] J.-A. Kim, J. W. Kim, B. C. Park, T. B. Eom, Measurement of microscope calibration standards in nanometrology using a metrological atomic force microscope, Meas. Sci. Technol., 2006, 17, 1792–1800, DOI:10.1088/0957-0233/17/7/018

[111] J.-A. Kim, J. W. Kim, C.-H. Kang, T. B. Eom, Metrological Atomic Force Microscope Using a Large Range Scanning Dual Stage, International Journal of Precision Engineering and Manufacturing, 2009, 10(5):11-17, DOI: 10.1007/s12541-009-0087-z

[112] R. Kizu, I. Misumi, A. Hirai, K. Kinoshita, S. Gonda, Development of a metrological atomic force microscope with a tip-tilting mechanism for 3D nanometrology, Measurement Science and Technology, 2018, 29, 7, 075005, DOI: 10.1088/1361-6501/aabe1a

[113] S. H. Wang, G. Xu, S. L. Tan, Development of a metrological atomic force microscope for nano-scale standards calibration, Proc. SPIE 7155, Ninth International Symposium on Laser Metrology, 2008, 71550I, DOI: 10.1117/12.814517

[114] H.-M. Tai, Instrumentation in Precision Metrology, 2008, https://www.slideshare.net/CHENHuiMei/2008-tech-instrumentation-in-precision-metrology, web access September 2021

References

---

[115] V. P. Gavrilenko, Yu. A. Novikov, A. V. Rakov, P. A. Todua, Nanoscale dimensional metrology in Russia, 2009, Proc. SPIE 7405, Instrumentation, Metrology, and Standards for Nanomanufacturing III, 740504, DOI: 10.1117/12.826164

[116] J. Piot, J. Qian, H. Pirée, G. Kotte, J. Petry et al. Design of a sample holder for a metrological atomic force microscope. In Euspen 2010 - Conference Proceedings, volume 1, pages 2241–4, 2010

[117] P. Klapetek, M. Valtr, V. Ducho, J. Sobota, Voice coil-based scanning probe microscopy, Nanoscale Research Letters 2012, 7:332, DOI: 10.1186/1556-276X-7-332

[118] V. Korpelainen, J. Seppä and A. Lassila, Design and characterization of MIKES metrological atomic force microscope, Precision Engineering, 2010, 34, 2, 735-744, DOI: 10.1016/j.precisioneng.2010.04.002

[119] S. Ducourtieux, B. Poyet, Development of a metrological atomic force microscope with minimized Abbe error and differential interferometerbased real-time position control, Meas. Sci. Technol., 2011, 22, 094010,15pp, DOI:10.1088/0957-0233/22/9/094010

[120] O. Jusko, X. Zhao, H. Wolff, G. Wilkening, Design and three dimensional calibration of a measuring scanning tunneling microscope for metrological applications, 1994, Review of Scientific Instruments 65, 2514, DOI:10.1063/1.1144643

[121] M. Bienias, S. Gao, K. Hasche, R. Seemann, K. Thiele, A metrological scanning force microscope used for coating thickness and other topographical measurements, Applied Physics A, 1998, 66, 837–S842, DOI: 10.1007/s003390051252

[122] K. Hasche, K. Herrmann, W. Mirandé, R. Seemann, L. Vitushkin, M. Xu, G. Yu, Calibrated scanning force microscope with capabilities in the subnanometre range, Surf. Interface Anal., 2002; 33, 71–74, DOI: 10.1002/sia.1164

[123] G. Dai, L. Koenders, F. Pohlenz, T. Dziomba, H.-U. Danzebrink, Accurate and traceable calibration of one-dimensional gratings, Meas. Sci. Technol., 2005, 16, 1241–9, DOI: 10.1088/0957-0233/16/6/001

References

---

[124] Low Noise 3D/CD-AFM, PTB - Physikalisch-Technische Bundesanstalt, Precision Engineering Department, Dimensional Nanometrology group, https://www.ptb.de/cms/en/ptb/fachabteilungen/abt5/fb-52/ag-523/low-noise-3dcd-afm.html

[125] G. Dai, W. Hässler-Grohne, D. Hueser, H. Wolff, J. Flügge, H. Bosse, New developments at Physikalisch Technische Bundesanstalt in three-dimensional atomic force microscopy with tapping and torsion atomic force microscopy mode and vector approach probing strategy, Journal of Micro/Nanolithography, MEMS, and MOEMS, 2012, 11(1), 011004, DOI:10.1117/1.JMM.11.1.011004

[126] G. Dai, K. Hahm, F. Scholze, M.-A. Henn, H. Gross, J. Fluegge, H. Bosse, Measurements of CD and sidewall profile of EUV photomask structures using CD-AFM and tilting-AFM, Meas. Sci. Technol., 2014, 25, 044002, DOI: 10.1088/0957-0233/25/4/044002

[127] HIGH-SPEED AFM, PTB - Physikalisch-Technische Bundesanstalt, Precision Engineering Department, Dimensional Nanometrology group, https://www.ptb.de/cms/en/ptb/fachabteilungen/abt5/fb-52/ag-523/high-speed-afm.html

[128] G. Dai, F. Zhu, J. Fluegge, High-speed metrological large range AFM, Meas. Sci. Technol. 26 (2015) 095402 (10pp), DOI: 10.1088/0957-0233/26/9/095402

[129] G. B. Picotto, M. Pisani, A sample scanning system with nanometric accuracy for quantitative SPM measurements, Ultramicroscopy, Volume 86, Issues 1–2, January 2001, Pages 247-254, DOI: 10.1016/S0304-3991(00)00112-1

[130] C. Werner, P.C.J.N. Rosielle, M. Steinbuch, Design of a long stroke translation stage for AFM, International Journal of Machine Tools & Manufacture, 2010, 50, 183–190, DOI: 10.1016/j.ijmachtools.2009.10.012

[131] R. J. Merry, M. J. Ronde, R. Van-de-molengraft, K. R. Koops, and M. Steinbuch, Directional Repetitive Control of a Metrological AFM, IEEE Transactions on Control Systems Technology, 2011, 19, 6, 1622-1629, DOI : 10.1109/TCST.2010.2091642

References

[132] F. Meli, R, Thalmann, Long-range AFM profiler used for accurate pitch measurements, Meas. Sci. Technol., 1998, 9, 1087, DOI: 10.1088/0957-0233/9/7/014

[133] F. Meli, A. Küng, Realization of a Large Sample 3D Metrology AFM with Differential Jamin Interferometers, Proceedings of the 11th euspen International Conference – Como – May 2011

[134] Dimensional nano and sub nanometrology, NPL – National Physical Laboratory, https://www.npl.co.uk/dimensional/nano-and-sub-nanometrology

[135] J. Haycocks, K. Jackson, Traceable calibration of transfer standards for scanning probe microscopy, Precision Engineering, 2005, 29, 2, 168-175, DOI: 10.1016/j.precisioneng.2004.06.002

[136] E. Heaps, A. Yacoot, H. Dongmo, L. Picco, O. D. Payton, F. Russell-Pavier, P. Klapetek, Bringing real-time traceability to high-speed atomic force microscopy, Meas. Sci. Technol., 2020, 31, 074005, 11pp, DOI:10.1088/1361-6501/ab7ca9

[137] Y. Wu, E. Wirthmann, U. Klöpzig, T. Hausotte, Investigation of a metrological atomic force microscope system with a combined cantilever position, bending and torsion detection system, J. Sens. Sens. Syst., 2021, 171–177, DOI: 10.5194/jsss-10-171-2021

[138] Automated AFM Metrology, Bruker, https://www.bruker.com/en/products-and-solutions/semiconductor-solutions/automated-afm-metrology.html, web access January 2022

[139] The leading nano metrology tool for failure analysis and large sample research, Park Systems, https://parksystems.com/applications/manufacturing/semiconductor/188-chemical-mechanical-polishing-cmp-metrology-with-advanced-afm-surface-profiler?highlight=WyJtZXRyb2xvZ3kiXQ==, web access December 2021

[140] C. Werner, A 3D translation stage for metrological AFM, Technische Universiteit Eindhoven., Doctorate Thesis, 2010, DOI: 10.6100/IR692270

[141] ISO 1:2016 — Geometrical product specifications (GPS) — Standard reference temperature for the specification of geometrical and dimensional

properties, International Organization for Standardization, Geneva, https://www.iso.org/standard/67630.html

[142] Y. Wang, H. Wang, S. Bi, Real time drift measurement for colloidal probe atomic force microscope: a visual sensing approach; AIP Advances, 2014, 4, 057130, DOI: 10.1063/1.4880242

[143] P. Rahe1, J. Schütte, W. Schniederberend, M. Reichling, M. Abe, Y. Sugimoto, A. Kühnle, Flexible drift-compensation system for precise 3D force mapping in severe drift environments, Review of Scientific Instruments 82, 063704 (2011) DOI:10.1063/1.3600453

[144] Q. Yang, S. Jagannathan, E. W. Bohannan, Automatic Drift Compensation Using Phase Correlation Method for Nanomanipulation, IEEE Transactions on Nanotechnology, 2008, 7, 2, DOI: 10.1109/TNANO.2007.915021

[145] F. Marinello, P. Bariani, L. De Chiffre, E. Savio, Fast technique for AFM vertical drift compensation, Meas. Sci. Technol., 2007, 18, 689, DOI: 10.1088/0957-0233/18/3/019

[146] T. R. Meyer, D. Ziegler, C. Brune, A. Chen, R. Farnham, N. Huynh, J-M Chang, A. L. Bertozzi, P. D. Ashby, Height drift correction in non-raster atomic force microscopy, Ultramicroscopy, 2014, 137, 48-54, DOI: 10.1016/j.ultramic.2013.10.014

[147] J. Degenhardt, R. Tutsch, G. Dai, Flexible correction of 3D non-linear drift in SPM measurements by data fusion, Meas. Sci. Technol. 32 (2021) 035005 (11pp) DOI: 10.1088/1361-6501/abc9f8

[148] Abbe Error/Offset, CIRP Encyclopedia of Production Engineering, Springer, DOI: 10.1007/978-3-642-35950-7

[149] N.G. Orji, H. Itoh, C. Wang, R.G. Dixson, P.S. Walecki, S.W. Schmidt, B. Irmer, Tip characterization method using multi-feature characterizer for CD-AFM, Ultramicroscopy 162 (2016) 25–34, DOI: 10.1016/j.ultramic.2015.12.003

[150] R. Kizu, I. Misumi, A. Hirai, K. Kinoshita, S. Gonda, Linewidth calibration using a metrological atomic force microscope with a tip-tilting mechanism, 2019 *Meas. Sci. Technol.* **30** 015004, DOI: 10.1088/1361-6501/aaf02a

References

---

[151] EMPIR project 20IND08 MetExSPM - Traceability of localised functional properties of nanostructures with high speed scanning probe microscopy, https://www.ptb.de/empir2021/metexspm/home/

[152] A.P.E. Research company, Trieste, Italy, http://www.aperesearch.com/default.html

[153] M. Bisi, E. Massa, A. Pasquini, G. B. Picotto, and M. Pisani, Nanometrology at the IMGC, in Nanoscale Calibration Standards and Methods: Dimensional and Related Measurements in the Micro and Nanometer Range, Book by Günter Wilkening and Ludger Koenders 2005, DOI: 10.1002/3527606661.ch2

[154] V. Ferro, A. Sacchi, G. Saggese, Impianti straordinari di condizionamento per Galleria misure di Lunghezze, Consiglio Nazionale delle Ricerche – Istituto di Metrologia "Gustavo Colonnetti", 6 febbraio 1970

[155] SPIP - Scanning Probe Image Processor v. 5.1.3, Image Metrology, https://www.imagemet.com/products_/spip/

[156] Y. Wu, Z. Fan, Y. Fang, C Liu, An Effective Correction Method for AFM Image Distortion due to Hysteresis and Thermal Drift, IEEE Transactions on Instrumentation and Measurement, 70, 2020, DOI: 10.1109/TIM.2020.3038007

[157] Z.-H. Xu, X.-D. Li, M. Sutton, N. Li, Drift and spatial distortion elimination in atomic force microscopy images by the digital image correlation technique, The Journal of Strain Analysis for Engineering Design, 2008 43(8):729-743, DOI: 10.1243/03093247JSA400

[158] A. Delvallée, N. Feltin, S. Ducourtieux, M. Trabelsi, J. F. Hochepied, Direct comparison of AFM and SEM measurements on the same set of nanoparticles, 2015 Meas. Sci. Technol. 26 085601, DOI: 10.1088/0957-0233/26/8/085601

[159] HOPG Substrates – Highly Ordered Pyrolytic Graphite, Micro to Nano - Innovative Microscopy Supplies, https://www.microtonano.com/HOPG-highly-ordered-pyrolytic-graphite-substrate-sample-for-SPM-AFM-STM.php

[160] HOPG, Nano and More GmbH, https://www.nanoandmore.com/AFM-Accessories-HOPG

[161] J. D. Kwon, Nanoparticle Growth Studies on Highly Oriented Pyrolytic Graphite (HOPG) and Photocatalytic studies on bimetallic system supported on

---

HOPG, 2014, UC Irvine. ProQuest ID: Kwon_uci_0030D_13113. Merritt ID: ark:/13030/m5f493f8. Retrieved from https://escholarship.org/uc/item/23d1g39v

[162] I. Lee, K-Y Chan, D. Lee Phillips, Atomic force microscopy of platinum nanoparticles prepared on highly oriented pyrolytic graphite, 75, 2, 11998, 69-76, DOI: 10.1016/S0304-3991(98)00055-2

[163] K. Xu, P. Cao, J. R. Heath, Graphene visualizes the first water adlayers on mica at ambient conditions, 2010, 329 (5996):1188-91, DOI: 10.1126/science.1192907

[164] JCGM 100:2008, Evaluation of measurement data — Guide to the expression of uncertainty in measurement, https://www.bipm.org/en/publications/guides/gum.html

[165] Fukuzawa K. (2012) AFM Probes. In: Bhushan B. (eds) Encyclopedia of Nanotechnology. Springer, Dordrecht. DOI: 10.1007/978-90-481-9751-4_109

[166] AFM Probe Selection Guide- How to choose an AFM probe, Park Systems, 2008

[167] LiteScope™ NenoVision, https://www.nenovision.com/litescopetm/main-benefits/

[168] A. Yacoot, L. Koenders, Aspects of scanning force microscope probes and their effects on dimensional measurements, J. Phys. D: Appl. Phys., 41, 2008, DOI: 10.1088/0022-3727/41/10/103001

[169] µmasch, https://www.spmtips.com/afm-probes.afm

[170] AFM Info, NanoAndMore GmbH, https://www.nanoandmore.com/afm-info

[171] A. Dulebo, M. Febvre, How To Choose an AFM Probe?, Bruker online webinar, 21/04/2020

[172] J. P. Cleveland, S. Manne, D. Bocek, P. K. Hansma, A Nondestructive Method for Determining the Spring Constant of Cantilevers for Scanning Force Microscopy, The Review of scientific instruments, 1993, 64, 2, 403 – 405, DOI: 10.1063/1.1144209

References

---

[173] J. E. Sader, J. W. M. Chon, P. Mulvaney, Calibration of rectangular atomic force microscope cantilevers, Review of Scientific Instruments 70, 3967 (1999); DOI: 10.1063/1.1150021

[174] J. L. Hutter, J. Bechhoefer, Calibration of atomic-force microscope tips, Review of Scientific Instruments, Volume 64, Issue 7, July 1993, pp.1868-1873, DOI: 10.1063/1.1143970

[175] C. A Clifford, M. P. Seah, Improved methods and uncertainty analysis in the calibration of the spring constant of an atomic force microscope cantilever using static experimental methods, Meas. Sci. Technol. 2009 20 125501 DOI: 10.1088/0957-0233/20/12/125501

[176] A. D. Slattery, A. J. Blanch, J. S. Quinton, C. T. Gibson, Calibration of atomic force microscope cantilevers using standard and inverted static methods assisted by FIB-milled spatial markers, Nanotechnology 2013 24 015710 DOI: 10.1088/0957-4484/24/1/015710

[177] A. D. Slattery, J. S. Quinton, C. T. Gibson, Atomic force microscope cantilever calibration using a focused ion beam, Nanotechnology 23 (2012) 285704 (14pp) DOI:10.1088/0957-4484/23/28/285704

[178] J. E. Sader, R. Borgani, C. T. Gibson, D. B. Haviland, M. J. Higgins, Jason I. Kilpatrick, J. Lu, P. Mulvaney, C. J. Shearer, A. D. Slattery, P. Thorén, J. Tran, H. Zhang, H. Zhang, T. Zheng, A virtual instrument to standardise the calibration of atomic force microscope cantilevers, Review of Scientific Instruments 87, 093711 (2016) DOI:10.1063/1.4962866

[179] K. L. Johnson, Contact mechanics, Cambridge University Press, 1985, DOI: 10.1017/CBO9781139171731

[180] Cantilever-sample interaction potential. Afm operation modes, NT-MDT Spectrum Instruments, https://www.ntmdt-si.com/resources/spm-theory/theoretical-background-of-spm/2-scanning-force-microscopy-(sfm)/22-cantilever-sample-force-interaction/221-cantilever-sample-interaction-potential-afm-operation-modes, web access November 2021

[181] The nature of adhesion, NT-MDT Spectrum Instruments, https://www.ntmdt-si.com/resources/spm-theory/theoretical-background-of-spm/2-scanning-force-microscopy-(sfm)/22-cantilever-sample-force-

---

interaction/227-adhesion-forces/2271-the-nature-of-adhesion, web access November 2021

[182] S. Ebnesajjad, Chapter 3 - Surface Tension and Its Measurement, Handbook of Adhesives and Surface Preparation – Technology, Applications and Manufacturing – Plastics Design Library, 2011, Pages 21-30, DOI: 10.1016/B978-1-4377-4461-3.10003-3

[183] F. M.Borodich, Chapter Three - The Hertz-Type and Adhesive Contact Problems for Depth-Sensing Indentation, Advances in Applied Mechanics, 47, 2014, 225-366, DOI: 10.1016/B978-0-12-800130-1.00003-5

[184] A. Nicolet, F. Meli, Spherical polystyrene particle deformation measured with the AFM, Meas. Sci. Technol. 28 (2017) 034003 (9pp) DOI: 10.1088/1361-6501/28/3/034003

[185] R. O'Rorke, T. Steele, H. Taylor, Bioinspired fibrillar adhesives: A review of analytical models and experimental evidence for adhesion enhancement by surface patterns, Journal of Adhesion Science and Technology 30(4), 2015, DOI: 10.1080/01694243.2015.1101183

[186] A. Y. Shu, N. Yu, K. M. Lee, A. A. Polycarpou, H. T. Johnson, Crystallite coalescence during film growth based on improved contact mechanics adhesion models, Journal of Applied Physics 96(3):1348-1359, 2004, DOI: 10.1063/1.1766099

[187] M. K. Chaudhury, T. Weaver, Adhesive contact of cylindrical lens and a flat sheet, Journal of Applied Physics 80, 30 (1996) DOI:10.1063/1.362819

[188] H. Hertz, On the contact of elastic solids, In: Miscellaneous Papers, Chapter V, 1896, pp.146-1621896., translated by D. E. Jones, G. A. Schott., London: Macmillan.

[189] Adhesion contact mechanics, Polymer Database, https://polymerdatabase.com/polymer%20physics/Adhesion%20Contact%20Mechanics.html

[190] A. Kruusing, Handbook of Liquids-Assisted Laser Processing, Elsevier, 2008, pages 25-29, ISBN 978-0444547347

References

---

[191] K. L. Johnson, K. Kendall, A. D. Roberts, Surface energy and the contact of elastic solids, Proc. R. Soc. Lond. A, 1971, 324, 301–13, DOI: 10.1098/rspa.1971.0141

[192] B. V. Derjaguin, V. M. Muller, Y. P Toporov, Effect of contact deformations on the adhesion of particles, Journal of Colloid and Interface Science, 53, 2, 1975, 314-326, DOI: 10.1016/0021-9797(75)90018-1

[193] D. S. Rimai, L. P. DeMejo, R. C. Bowen, Mechanics of particle adhesion, Fundamentals of Adhesion and Interfaces, De Gruyter, 1-23, 1993, DOI: 10.1515/9783112318515-002

[194] D. Maugis, H. M. Pollock, Surface forces, deformation and adherence at metal microcontacts, Acta Metallurgica, 32, 9, 1984, 1323-1334, DOI: 10.1016/0001-6160(84)90078-6

[195] M. J. Puttock, E. G. Thwaite, Elastic compression of spheres and cylinders at point and line contact, National Standards Laboratory Technical Paper No. 25, 1969

[196] M.T. Postek, Critical issues in scanning electron microscope metrology, J. Res. Natl Inst. Stand Technol., 1994, 99, 641

[197] G. Raina, Atomic Force Microscopy as a Nanometrology Tool: Some Issues and Future Targets, MAPAN-Journal of Metrology Society of India (December 2013) 28(4):311–319, -DOI 10.1007/s12647-013-0085-6

[198] D. Keller, Reconstruction of STM and AFM images distorted by finite-size tips, Surface Science, 253, 1-3, 1991, 353-364, DOI: 10.1016/0039-6028(91)90606-S

[199] J. S. Villarrubia, Algorithms for Scanned Probe Microscope Image Simulation, Surface Reconstruction, and Tip Estimation, J. Res. Natl. Inst. Stand. Technol., 1997, 102(4):425-4544, DOI: 10.6028/jres.102.030.

[200] P. M. Williams, K. M. Shakesheff, M. C. Davies, D. E. Jackson, C. J. Roberts, S. J. B. Tendier, Blind reconstruction of scanning probe image data, Journal of Vacuum Science and Technology B: Microelectronics and Nanometer Structures, 1996, 14, 2, 1557 – 1562, DOI: 10.1116/1.589138

References

---

[201] L. S. Dongmo, J. S. Villarrubia, S. N. Jones, T. B. Renegar, M. T. Postek, J. F. Song, Experimental test of blind tip reconstruction for scanning probe microscopy, Ultramicroscopy, 85, 3, 2000, 141-153, DOI: 10.1016/S0304-3991(00)00051-6

[202] B. A. Todd, S. J. Eppell, A method to improve the quantitative analysis of SFM images at the nanoscale, Surface Science, 491, 3, 2001, 473-483, DOI: 10.1016/S0039-6028(01)01313-9

[203] H. G. Abdelhady, S. Allen, S. J. Ebbens, C. Madden, N. Patel, C. J. Roberts, J. Zhang, Towards nanoscale metrology for biomolecular imaging by atomic force microscopy, 2005, Nanotechnology, 16, 6, DOI: 10.1088/0957-4484/16/6/058

[204] D. Tranchida, S. Piccarolo, R. A. C. Deblieck, Some experimental issues of AFM tip blind estimation: the effect of noise and resolution, 2006, Measurement Science and Technology, 17, 2630, DOI: 10.1088/0957-0233/17/10/014

[205] E. E. Flater, G. E. Zacharakis-Jutz, B. A. Dumba, I. A. White, C. A. Clifford, Towards easy and reliable AFM tip shape determination using blind tip reconstruction, Ultramicroscopy, 2014, 146, 130-143, DOI: 10.1016/j.ultramic.2013.06.022

[206] G. Dai, L. Xu, K. Hahm, Accurate tip characterization in critical dimension atomic force microscopy, Meas. Sci. Technol. 31 (2020) 074011 (12pp) https://doi.org/10.1088/1361-6501/ab7fd2

[207] J. Wan, L. Xu, S. Wu, X. Hu, Investigation on Blind Tip Reconstruction Errors Caused by Sample Features, Sensors (Basel). 2014 Dec; 14(12): 23159–23175, DOI: 10.3390/s141223159

[208] D. Keller, F. S. Franke, Envelope reconstruction of probe microscope images, Surf. Sci., 1993, 294, 409–19, DOI: 10.1016/0039-6028(93)90126-5

[209] A. D. Slattery, A. J. Blanch, J. S. Quinton, C. T. Gibson, Efficient attachment of carbon nanotubes to conventional and high-frequency AFM probes enhanced by electron beam processes Nanotechnology 2013, 24, 235705, DOI: 10.1088/0957-4484/24/23/235705

[210] K. A. Ramirez-Aguilar, K. L. Rowlen, Tip Characterization from AFM Images of Nanometric Spherical Particles, Langmuir 1998, 14, 9, 2562–2566, DOI: 10.1021/la971277o

References

---

[211] M-H Trinh, M. Odorico, L. Bellanger, M. Jacquemond, P. Parot, J-L Pellequer, Tobacco mosaic virus as an AFM tip calibrator, Journal of Molecular Recognition, 2011, 24, 503-510, DOI: 10.1002/jmr.1118

[212] H. R. Gelderblom, Structure and Classification of Viruses, In book: Medical Microbiology, Edition: 4th, Chapter: 41, Publisher: University of Texas Medical Branch at Galveston, Editors: Samuel Baron

[213] J. M. Alonso, M. Ł.Górzny, A. M. Bittner, The physics of tobacco mosaic virus and virus-based devices in biotechnology, Trends in Biotechnology, 31, 9, 2013, 530-538, DOI: 10.1016/j.tibtech.2013.05.013

[214] K. Namba, G. Stubbs, Structure of tobacco mosaic virus at 3.6 Å resolution: implications for assembly, Science, 21, 1986, DOI: 10.1126/science.3952490

[215] P. J. G. Butler, Self-assembly of tobacco mosaic virus: the role of an intermediate aggregate in generating both specificity and speed, Phil.Trans. R. Soc. Lond. B (1999) 354, 537-550, DOI: 10.1098/rstb.1999.0405

[216] A. Klug, The tobacco mosaic virus particle: structure and assembly, Phil.Trans. R. Soc. Lond. B, 1999; 354, 531–535, DOI: 10.1098/rstb.1999.0404

[217] G. Stubbs, Fibre diffraction studies of filamentous viruses, Rep. Prog. Phys., 64, 1389-1425, 2001, DOI: 10.1088/0034-4885/64/11/201

[218] M. Finch, V. L. Chi, R. M. Taylor, M. Falvo, S. Washburn, R. Superfine, Surface Modification Tools in a Virtual Environment Interface to a Scanning Probe Microscope, Proceedings of the 1995 symposium on Interactive 3D graphics,1995, DOI: 10.1145/199404.199406

[219] Y. Lin, H. Komatsu, J. Ma, P. H. Axelsenb, Z. Fakhraai, Quantitative analysis of amyloid polymorphism using height histograms to correct for tip convolution effects in atomic force microscopy imaging, Royal Society of Chemistry Advances, 2016, 6, 114286, DOI: 10.1039/c6ra24031c

[220] C. Godon, J. Teulon, M. Odorico, C. Basset, M. Meillan, L. Vellutini, S. Chen, J. Pellequer, Conditions to minimize soft single biomolecule deformation when imaging with atomic force microscopy, Journal of Structural Biology, 197, 3, 2017, 322-329, DOI: 10.1016/j.jsb.2016.12.011

References

---

[221] O. V. Sinitsyna, N. O. Kalinina, K. McGeachy, E. Whale, D. Hepworth, A. J. Love, M. E. Taliansky, I. V. Yaminsky, Interaction between nanocellulose and tobacco mosaic viruslike particles: an atomic force microscopy study, Cellulose (2020), DOI: 10.1007/s10570-020-02978-1

[222] Y. Zhang, R. Potter, W. Zhang, Z. Fakhaai, Using tobacco mosaic virus to probe enhanced surface diffusion of molecular glasses, Soft Matter, 2016, 12, 9115-9120, DOI: 10.1039/C6SM01566B

[223] N. Stitz, S. Eiben, P. Atanasova, N. Domingo, A. Leineweber, Z. Burghard, J. Bill, Piezoelectric Templates – New Views on Biomineralization and Biomimetics, Scientific Reports, 6, Article number: 26518 (2016) DOI: 10.1038/srep26518

[224] F. A. Schabert, J. P. Rabe, Vertical dimension of hydrated biological samples in tapping mode scanning force microscopy, 70, 3, 1996, 1514-1520, DOI: 10.1016/S0006-3495(96)79713-8

[225] A. Castellanos-Gomez, M. Poot, A. Amor-Amorós, G. A. Steele, H. S. J. van der Zant, N. Agraït, G. Rubio-Bollinger, Mechanical properties of freely suspended atomically thin dielectric layers of mica, Nano Research, 5, 550–557, 2012, DOI: 10.1007/s12274-012-0240-3

[226] M. A. Hopcroft, W. D. Nix, T. W. Kenny, What is the Young's Modulus of Silicon?, Journal of Microelectromechanical Systems, 19, 2, 2010, DOI: 10.1109/JMEMS.2009.2039697

[227] Y. Zhao, Z. Ge, J. Fang, Elastic modulus of viral nanotubes, Physical Review E, 78, 031914, 2008 DOI: 10.1103/PhysRevE.78.031914

[228] W. N. Sharpe, B. Yuan, R. Vaidyanathan, R. L. Edwards, Measurements Of Young's Modulus, Poisson's Ratio, And Tensile Strength Of Polysilicon, Proceedings of the Tenth IEEE International Workshop on Microelectromechanical Systems, Nagoya, Japan, 424-429 (1997)

[229] W. C. Oliver, G. M. Pharr, Measurement of hardness and elastic modulus by instrumented indentation: Advances in understanding and refinements to methodology, Journal of Materials Research volume 19, 3, 2004, DOI: 10.1557/jmr.2004.19.1.3

References

---

[230] M. R. Falvo, S. Washburn, R. Superfine, M. Finch, F. P. Brooks Jr., V. Chi, R. M. Taylor II, Manipulation of Individual Viruses: Friction and Mechanical Properties, Biophysical Journal, 72, 1396-1403, 1996, DOI: 10.1016/S0006-3495(97)78786-1

[231] O. I. Kiselyova, M. O. Gallyamov, N. S. Nasikan, I. V. Yaminsky, O. V. Karpova, V. K. Novikov, Scanning Probe Microscopy of Biomacromolecules: Nucleic Acids, Proteins And Their Complexes, in Frontiers of Multifunctional Nanosystems by E. Buzaneva, P. Scharff, Frontiers of Multifunctional Nanosystems, NATO Science Series (Series II: Mathematics, Physics and Chemistry), 57, 321-330, 2002, DOI: 10.1007/978-94-010-0341-4_24

[232] A. Schmatulla, N. Maghelli, O. Marti, Micromechanical properties of tobacco mosaic viruses, Journal of Microscopy, 225, 3, 2007, 264–268, DOI: 10.1111/j.1365-2818.2007.01741.x

[233] H. Wang, X. Wang, T. Li, B. Lee, Nanomechanical characterization of rod-like superlattice assembled from tobacco mosaic viruses, Journal of Applied Physics, 113, 024308 (2013)

[234] M. Ciavarella, J. Joe, A. Papangelo, J. R. Barber, The role of adhesion in contact mechanics, Journal of The Royal Society Interface, 16, 151, 2019, DOI: 10.1098/rsif.2018.0738

[235] D. Imbraguglio, A. M. Giovannozzi, A. M. Rossi, Nanometrology, Proceedings of the International School of Physics “Enrico Fermi” – Course 185 “Metrology and Physical Constants”, edited by E. Bava, M. Kuhne, A. M. Rossi (IOS, Amsterdam; SIF, Bologna) 2013, DOI 10.3254/978-1-61499-326-1-193

[236] ISO/TS 80004-1:2010, Nanotechnologies – Vocabulary – Part 1: Core terms

[237] W. J. Stark, P. R. Stoessel, W. Wohlleben, A. Hafner, Industrial applications of nanoparticles, Chem. Soc. Rev., 2015, 44, 5793-5805, DOI: 10.1039/C4CS00362D

[238] A. Przyklenk, A. Balsamo, D. O’Connor, A. Evans, T. Yandayan, S. A. Akgöz, O. Flys, V. Zeleny, D. Czułek, D. Phillips, F. Meli, C. S. Ragusa, H.Bosse, AdvManuNet: Support for a European Metrology Network for Advanced

Manufacturing, euspen's 21st International Conference & Exhibition, Copenhagen, DK, June 2021

[239] ISO/TC 213 – Dimensional and geometrical product specifications and verification, https://www.iso.org/committee/54924.html

[240] Introduction to Roughness, Keyence, https://www.keyence.com/ss/products/microscope/roughness/, web access June 2020

[241] ISO 21920-2:2021 — Geometrical product specifications (GPS) — Surface texture: Profile — Part 2: Terms, definitions and surface texture parameters, Geneva, https://www.iso.org/standard/72226.html

[242] ISO 25178-2:2021 — Geometrical product specifications (GPS) — Surface texture: Areal — Part 2: Terms, definitions and surface texture parameters, Geneva, https://www.iso.org/standard/74591.html

[243] F. Marinello, A. La Storia, G. Mauriello, D. Passeri, Atomic Force microscopy techniques to investigate activated food packaging materials, Trends in Food Science & Technology, 87, 2019, 84-93, DOI: 10.1016/j.tifs.2018.05.028

[244] Roughness Parameters, https://www.keyence.com/ss/products/microscope/roughness/line/parameters.jsp

[245] E. C. T. Ba, M. Rosa Dumont, P. S. Martins, R. M. Drumond, M. P. Martins da Cruz, V. Ferreira Vieira, Investigation of the effects of skewness Rsk and kurtosis Rku on tribological behavior in a pin-on-disc test of surfaces machined by conventional milling and turning processes, Mat. Res. 24 (2) 2021, DOI:10.1590/1980-5373-MR-2020-0435

[246] Texture Parameters, https://www.olympus-ims.com/en/metrology/surface-roughness-measurement-portal/parameters/#!cms[focus]=cmsContent14709

[247] ASTM E2859 - 11(2017), Standard Guide for Size Measurement of Nanoparticles Using Atomic Force Microscopy, American Society for Testing and Materials (ASTM)

[248] R. D. Boyd, A. Cuenat, F. Meli, T. Klein, C. G. Frase, G. Gleber, M. Krumrey, A. Duta, S. Duta, R. Hogstrom, E. Prieto, Good Practice Guide for the

References

Determination of the Size and Size Distribution of Spherical Nanoparticle Samples, National Physical Laboratory, 2011

[249] Calibration and measurement capabilities in the context of the CIPM MRA - Guidelines for their review, acceptance and maintenance, CIPM MRA-G-13, Version 1.1, 30/03/2021

[250] F. Meli, T. Klein, E. Buhr, C. G. Frase, G. Gleber, M. Krumrey, A. Duta, S. Duta, V. Korpelainen, R., G. B. Picotto, R. D. Boyd, A. Cuenat, Traceable size determination of nanoparticles, a comparison among European metrology institutes, Meas. Sci. Technol.,2012, 23, 125005, DOI: 10.1088/0957-0233/23/12/125005

[251] H. –L. Lin, W.-E. Fu, H.-F. Weng, I. Misumi, K. Sugawara, S. Gonda, K. Takahashi, K. Takahata, K. Ehara, T. Takatsuji, T. Fujimoto, J. Salas, K. Dirscherl, J. Garnaes, J. Damasceno, J. C. V. de Oliveira, E. Emanuele, G. B. Picotto, C. S. Kim, S. J. Cho, C. Motzkus, F. Meli, S. Gao, Y. Shi, J. Liu, K. JÄmting, H. J. Catchpoole, M. A. Lawn, J. Herrmann, V. A. Coleman, L. Adlem, O. A. Kruger, J. Buajarern, E. Buhr, H.-U. Danzebrink, M. Krumrey, H. Bosse, Nanoparticle Characterization - Supplementary Comparison on Nanoparticle Size, Metrologia, 2019, 56, 04004, DOI: 10.1088/0026-1394/56/1A/04004

[252] KCDB new INRiM CMC, https://www.bipm.org/kcdb/cmc/search?domain=PHYSICS&areaId=3&keywords=particle&specificPart.branch=12&specificPart.service=-1&specificPart.subService=-1&specificPart.individualService=-1&_countries=1&publicDateFrom=&publicDateTo=&unit=&minValue=&maxValue=&minUncertainty=&maxUncertainty=#uncert-equation-26918

[253] N. Sebaihi, J. Pétry, R. Koops, M. Valtr, P. Klapetek, G. Dai, T. Hausotte, U. Klöpzig, Y. Wu, V. Korpelainen, Good practice guide for dimensional metrology at the nanometer scale in general and for using the developed reference standards and methodologies in particular, EMPIR 15SIB09 Traceable three-dimensional nanometrology (3DNano) project, 2019, https://www.ptb.de/emrp/3738.html

[254] EMPIR 15 SIB 09 project "Traceable three-dimensional nanometrology (3DNano)", https://www.ptb.de/emrp/15sib09-home.html

References

---

[255] EU seventh framework programme, project number: 604577, call identifier: FP7-NMP-2013_LARGE-7, “Shape-engineered TiO_2 nanoparticles for metrology of functional properties: setting design rules from material synthesis to nanostructured devices (SETNanoMetro)”, http://www.metecnetwork.eu/setnanometro-project/index.html

[256] EMPIR 17NRM04 project “Improved traceability chain of nanoparticle size measurements (nPSize)”, https://www.bam.de/Content/EN/Projects/nPSize/npsize.html

[257] S. Banerjee, D. D. Dionysiou, S. C. Pillai, Self-cleaning applications of TiO_2 by photo-induced hydrophilicity and photocatalysis, *Applied Catalysis B: Environmental*, 176–177, 2015, 396-428, DOI: 10.1016/j.apcatb.2015.03.058

[258] F. Pellegrino, F. Sordello, M. Minella, C. Minero, V. Maurino, The Role of Surface Texture on the Photocatalytic H_2 Production on TiO_2, Catalysts, 2019, 9, 32, DOI: 10.3390/catal9010032

[259] U. Mansfeld, F. Pellegrino, V. Maurino, S. Marguet, F. Testard, O. Tachè, V-D Hodoroaba, New Reference Material Candidates For Traceable Size Measurement Of Non-Spherical Nanoparticles. 18th European Conference On Applications Of Surface And Interface Analysis (ECASIA 19), Sep 2019, Dresden, Germany

[260] L. Mino, F. Pellegrino, S. Rades, J. Radnik, Joerg; V.-D. Hodoroaba, G. Spoto, V. Maurino, G. Martra, Beyond shape engineering of TiO_2 nanoparticles: post-synthesis treatment dependence of surface hydration, hydroxylation, Lewis acidity and photocatalytic activity of TiO_2 anatase nanoparticles with dominant {001} or {101} facets, *ACS Applied Nano Materials*, 2018, 1 (9), pp 5355–5365, DOI: 10.1021/acsanm.8b01477

[261] F. Pellegrino, F. Sordello, L. Mino, C. Minero, V.-D. Hodoroaba, G. Martra, V. Maurino, Formic Acid Photoreforming for Hydrogen Production on Shape-Controlled Anatase TiO_2 Nanoparticles: Assessment of the Role of Fluorides, {101}/{001} Surfaces Ratio, and Platinization, *ACS Catal.* 2019, 9, 6692−6697, DOI: 10.1021/acscatal.9b01861

[262] F. Pellegrino, R. Isopescu, L. Pellutiè, F. Sordello, A. M. Rossi, E. Ortel, G. Martra, V.-D. Hodoroaba, V. Maurino, Machine learning approach for elucidating and predicting the role of synthesis parameters on the shape and size of

TiO_2 nanoparticles, Scientific Reports, 2020, 10:18910, DOI: 10.1038/s41598-020-75967-w

[263] U. Diebold, The surface science of titanium dioxide, *Surface Science Reports*, 48, 5-8, 2003, DOI: 10.1016/S0167-5729(02)00100-0

[264] H. G. Yang, C. H. Sun, S. Z. Qiao, J. Zou, G. Liu, S. C. Smith, H. M. Cheng, G. Q. Lu, Anatase TiO_2 single crystals with a large percentage of reactive facets, *Nature*, 453, 638–641, 2008, DOI: 10.1038/nature06964

[265] ISO 5436-2:2012 — Geometrical product specifications (GPS) — Surface texture: Profile method; Measurement standards — Part 2: Software measurement standards, Geneva, https://www.iso.org/standard/61261.html, web access January 2021

[266] L. Crouzier, N. Feltin, A. Delvallée, F. Pellegrino, V. Maurino, G. Cios, T. Tokarski, C. Salzmann, J. Deumer, C. Gollwitzer, V-D Hodoroaba, Correlative Analysis of the Dimensional Properties of Bipyramidal Titania Nanoparticles by Complementing Electron Microscopy with Other Methods, Nanomaterials 2021, 11(12), 3359, DOI:10.3390/nano11123359

[267] V. Swamy, E. Holbig, L. S. Dubrovinsky, V. Prakapenka, B. C. Muddle, Mechanical properties of bulk and nanoscale TiO_2 phases, Journal of Physics and Chemistry of Solids, 2008, 2332-2335, DOI: 10.1016/j.jpcs.2008.04.018

[268] L. Borgese, M. Gelfi, E. Bontempi, P. Goudeau, G. Geandier, D. Thiaudière, L. E. Depero, Young modulus and Poisson ratio measurements of TiO_2 thin films deposited with Atomic Layer Deposition, Surface and Coatings Technology, 206, 8–9, 2012, 2459-2463

[269] Z. Zhu, X. Fu, D. Ren, Y. Wan, J. Wang, A Method for Measurement of Nonlinearity of Laser Interferometer Based on Optical Frequency Tuning, Sensors 2017, 17, 2721, DOI: 10.3390/s17122721

[270] L. C. Lipus, G. Budzyn, B. Acko,Analysis of laser interferometer measurement uncertainty by simulating errorsources, Int. Journal of Simulation Modelling, 2021, 20, 2, 339-350, DOI:10.2507/IJSIMM20-2-563

References

---

[271] S. Rades, E. Ortel, V.-D. Hodoroaba, ILC on shape of bipyramidal TiO_2 NPs by TEM, Tokyo, June 2016, https://opus4.kobv.de/opus4-bam/frontdoor/index/index/docId/38900, web access December 2020

[272] E. Gualtieri, N. Pugno, A. Rota, A. Spagni, E. Lepore, S. Valeri, Role of Roughness Parameters on the Tribology of Randomly Nano-Textured Silicon Surface, Journal of Nanoscience and Nanotechnology, 11, 9244–9250, 2011, DOI: 10.1166/jnn.2011.4296

[273] L. Románszki, S. Klébert, K. Héberger, Estimating Nanoscale Surface Roughness of Polyethylene Terephthalate Fibers, ACS Omega, 2020, 5, 7, 3670–3677, DOI: 10.1021/acsomega.9b04211

[274] F. Borghi, V. Vyas, A. Podestà, P. Milani, Nanoscale Roughness and Morphology Affect the IsoElectric Point of Titania Surfaces, PLoS ONE, 2013, 8,7, e68655, DOI:10.1371/journal.pone.0068655

[275] A. Borras, A. R. Gonzalez-Elipe, Wetting Properties of Polycrystalline TiO_2 Surfaces: A Scaling Approach to the Roughness Factors, Langmuir, 2010, 2010, 26(20), 15875–15882, DOI: 10.1021/la101975e

[276] Q. Lu, J. Wang, A. Faghihnejad, H. Zeng, Y. Liu, Understanding the molecular interactions of lipopolysaccharides duringE.coliinitial adhesion with a surface forces apparatus, Soft Matter, 2011, 7, 19, 9366-93792011, DOI: 10.1039/c1sm05554b

[277] M. Setvín, B. Daniel, V. Mansfeldova, L. Kavan, P. Scheiber, M. Fidler, M. Schmid, U. Diebold, Surface preparation of TiO_2 anatase (101): Pitfalls and how to avoid them, Surface Science, 2014, 626, 61-67, DOI: 10.1016/j.susc.2014.04.001

[278] F. Pellegrino, E. Morra, L. Mino, G. Martra, M. Chiesa, V. Maurino, Surface and Bulk Distribution of Fluorides and Ti^{3+} Species in TiO_2 Nanosheets: Implications on Charge Carrier Dynamics and Photocatalysis, The Journal of Physical Chemistry C, 2020, 124, 5, 3141-3149

[279] Z-Measurement Based on ISO 5436 Profile Analysis, http://www.imagemet.com/WebHelp6/Default.htm#Zcalibration/Z_Calibration_based_on_ISO_5436_Profile_Analysis.htm